

CRYOGENIC OPTICS AND DETECTORS FOR
NEXT-GENERATION MICROWAVE COSMOLOGY
AND ASTROPHYSICS OBSERVATORIES

A Dissertation

Presented to the Faculty of the Graduate School

of Cornell University

in Partial Fulfillment of the Requirements for the Degree of

Doctor of Philosophy

by

Nicholas Flood Cothard

August 2021

© 2021 Nicholas Flood Cothard

ALL RIGHTS RESERVED

CRYOGENIC OPTICS AND DETECTORS FOR NEXT-GENERATION
MICROWAVE COSMOLOGY AND ASTROPHYSICS OBSERVATORIES

Nicholas Flood Cothard, Ph.D.

Cornell University 2021

Millimeter and sub-millimeter observatories provide a unique and powerful window into the origins, content, and evolution of the universe. In our current era of precision cosmology, measurements of the cosmic microwave background (CMB) yield constraints on frontier physics such as dark energy, the sum of the neutrino masses, and models of inflation. Measurements of the CMB also reveal the astrophysics of galaxy clusters and can then be used to glean information about the early universe.

The early universe can also be studied with millimeter-wave observations of redshifted spectral line emissions from early star-forming galaxies during the Epoch of Reionization (EoR). A relatively new method, called spectral line intensity mapping (LIM), can be used to tomographically map the EoR. LIM observations of the EoR will reveal properties of the reionization sources and how reionization impacted the evolution of the intergalactic medium (IGM) into the large-scale structure we see today.

In order to improve CMB observations and enable new LIM measurements, microwave observatories require high-throughput cryogenic optics and interferometry, and ultra-sensitive superconducting detectors. This dissertation presents developments of these technologies for three projects: the Atacama Cosmology Telescope (ACT), the CCAT-prime Observatory, and the Simons Observatory (SO). We begin with a presentation of in-situ warm spillover beam measurements of the

Advanced ACT receiver, which have been used to improve the optical designs of future telescopes. We then discuss the design, models, and fabrication development of metamaterial-based, silicon-substrate, Fabry-Perot interferometers for CCAT-prime's [CII] LIM instrument. We then describe the characterization of prototype superconducting transition edge sensors (TES) for Simons Observatory including, critical temperature, saturation power, time constant, and complex impedance measurements. The dissertation concludes with a brief discussion of the cosmology and astrophysics science goals that these technologies will enable when they are deployed on microwave telescopes in the coming years.

BIOGRAPHICAL SKETCH

Nicholas Cothard grew up in Elmhurst, Illinois. In 2015, he graduated from the University of Rochester in Rochester, NY earning a Bachelor of Science in Physics with highest distinction. While at the Rochester, he had the opportunity to work on multiple research projects. Throughout his undergraduate career, he worked as a student researcher at Fermilab searching Tevatron CDF collider data for magnetic monopoles (none were found!). In the summer of 2013, he received an NSF Research Experience for Undergraduates at SRI International in Menlo Park, CA where he worked on the Compact Echelle Spectrograph for Aeronomical Research. In the summer of 2014, he received the DOE National Undergraduate Fellowship in Plasma Physics and worked on fast ion loss measurement hardware and analysis codes in the DIII-D Tokamak fusion reactor at General Atomics in San Diego, CA.

In the fall of 2015, Nicholas began graduate school in the field of Applied Physics at Cornell University, and the following spring, he joined the research groups of Mike Niemack and Gordon Stacey. Over his six years at Cornell, he worked with multiple collaborations, including the Atacama Cosmology Telescope (ACT), CCAT-prime, Simons Observatory (SO), and CMB Stage-4 (CMB-S4). His technology contributions in the far-IR and millimeter bands ranged from characterizing receiver optics, to designing Fabry-Perot interferometers, to developing superconducting detectors. He was also often found playing with one of the lab's three He3/He4 dilution refrigerators and working on improving other lab infrastructure. His graduate work was financially supported through the Kavli Institute at Cornell for Nanoscale Science's Watt W Webb Graduate Fellowship and through a NASA Space Technology Research Fellowship. After leaving Cornell, Nicholas will continue working on far-IR detectors and optics as a NASA Postdoctoral Fellow at Goddard Space Flight Center.

To Mom and Dad. For their devotion, which got me here.

To Jenn. For everything. I love you.

ACKNOWLEDGEMENTS

The academic journey which led to this thesis would have been nothing without the support of my incredible colleagues, friends, and family. Here, I attempt to acknowledge and thank those who have had the largest influence on these pages.

I owe an immeasurable amount of gratitude to my advisors, Mike Niemack and Gordon Stacey. Mike, your excitement for our work is infectious. Thank you for bringing me into our field, trusting me with our detectors and dilution refrigerators, and showing me how to see the bigger picture. Gordon, your excitement for our work is also infectious. Thank you for your guidance and incredibly insightful conversations, whether it be about intuitive Fabry-Perot models, spectrometer designs, or the Chicago Cubs. Both of you have been fantastic to work with and wonderful mentors. Thank you both for your support and encouragement, your technical insights, and your professional guidance in our fields.

The work presented in this thesis would not have been successful without the technical support from many collaborators in ACT, CCAT-prime, and SO. To Hannes Hubmayr, who has been a mentor for all things superconducting, who continually encouraged me to dig deeper for a more complete picture of our devices, and who always welcomed me for each visit to NIST: thank you. To Ed Wollack, my NASA Space Technology Research Fellowship advisor, who gave me professional guidance and shared his incredibly vast knowledge on far-IR and millimeter optics: thank you. To Team Toco (circa 2017-2018), namely Max Fanhanel and Felipe Carrero, who taught me how to drive stick, how to work (and breathe) at 17,000 feet, and supported my beam measurements presented in Chapter 2: thank you. To the many colleagues and friends I made in these collaborations along the way: Suzanne Staggs, Mark Devlin, Alex Van Engelen, Patty Ho, Shannon Duff, Kevin Crowley, Ben Westbrook, Sarah-Marie Bruno, Erin Healy, Yuhan Wang, Max Silva-

Fever, Joe Seibert, and countless more: thank you.

And now for some huge thank yous to my groupmates who provided a tremendous amount of support both inside and outside of the lab. To the grad students – Brian, Pato, Paul, Jason, Eve, Cody, Zach, and Bugao: thank you for sharing the grad school experience with me, for always being willing to help with whatever was needed in the lab, for being my comrades-in-arms, and for being some of the greatest friends ever. To the postdocs and technical staff – Shawn, Francesco, Thomas, Steve, Yaqiong, and Thuong: thank you for your endless help in the lab and for transferring vast amounts of technical, professional, and life knowledge to me.

I had a great deal of support outside of research as well. To the friends I made in Ithaca – Tanner, Berit, Sasank, Josephine, Kyle, and Ari: thank you for making my time in Ithaca more special and for giving me fantastic reasons to enjoy the other parts of life. To Jenn’s family, the Goldreiches – Matt, Kathy, and Jon: thank you for being like a second family for me and for all of your excitement and encouragement towards my career. To the friends that have endured my time away from home – Alex, Sam, and Nolan: thank you for your unending support and understanding, and for being a constant, wonderful, cherished presence in my life.

I also want to acknowledge a few of the most important teachers and mentors I had prior to grad school. I am indebted to Jonathan Lewis at Fermilab who took the risky move of giving me my very first research experience the summer before freshman year of college: thank you. To my undergraduate research mentors at Fermilab, SRI International, and General Atomics – Homer Wolfe, Daniel Matsiev, and David Pace: thank you. To some of the most insightful, kind, and devoted teachers, professors, and mentors – Dave Aggen, Aakash Shah, Frank Wolfs, and

Lynne Orr, and Janet Fogg: thank you. And finally, to one of the most influential directresses in my life, Mrs. Carmen: thank you for your devotion, your compassion, and for showing me the fundamental tools to explore this universe.

And finally, to my family. To Steven: thank you for your excitement about my work, for our conversations about all things sci-fi, and for being my brother. To Ellen Kay, Uncle Tom, Nancy, Ethan, Old Grandma, and New Grandma: thank you for your unending support, love, and encouragement. I would get in trouble with Jenn if I didn't mention the pets – Pharaoh, Clementine, Charlie, Taran, Toby, Delta, PJ, Scooter, and Chowdy: thank you for your presence.

To Mom and Dad: you are the pillars of my life. None of this would have been possible without your endless love and support. I can't say this one enough: Thank you.

And lastly, to Jenn, without whom I may not have stumbled my way into these wonderful labs. Even when things get crazy, you keep me sane, you make me happy, you love me, and you support me every step of the way. Thank you.

TABLE OF CONTENTS

Biographical Sketch	iii
Dedication	iv
Acknowledgements	v
Table of Contents	viii
List of Tables	x
List of Figures	xi
1 Introduction	1
1.1 The Expanding Universe	1
1.2 The Cosmic Microwave Background Radiation	4
1.2.1 Blackbody Spectrum	5
1.2.2 Anisotropies	6
1.2.3 Power Spectra	8
1.2.4 Current efforts in CMB cosmology	12
1.3 The Epoch of Reionization	15
1.3.1 Line Intensity Mapping	17
1.3.2 Probes of the EoR	19
1.3.3 Astrophysics and Cosmology from LIM	21
1.4 Summary	23
2 Characterizing the AdvACT Receiver Optics	24
2.1 The Atacama Cosmology Telescope and Receivers	24
2.2 Telescope Beam and Spillover Systematics	27
2.3 AdvACT Receiver Beam Mapping	31
2.3.1 Measurements Methods	32
2.3.2 Analysis Methods	36
2.3.3 Results	41
2.3.4 Comparison to Models	50
2.3.5 Baffle experiments	52
2.4 Impact on Future Receiver Designs	56
2.5 Conclusion	59
3 Fabry-Perot Interferometers	60
3.1 CCAT-prime and EoR-Spec	61
3.2 FPI Background	64
3.2.1 Theory	64
3.2.2 Free-Standing Metal-Mesh Mirrors	69
3.2.3 Silicon Substrate-Based Mirrors	71
3.2.4 The EoR-Spec FPI	73
3.3 Silicon-Based Metamaterial Anti-Reflection Coatings	75
3.3.1 Dielectric Theory for ARCs	77
3.3.2 Metamaterial Approximations for Silicon ARCs	86

3.3.3	Electromagnetic Simulations of Silicon ARCs	90
3.4	Silicon Substrate-Based FPI Mirrors	101
3.4.1	Frequency Selective Metal Mesh Reflectors	102
3.4.2	Mesh Designs for Wide-Bandwidth Interferometers	105
3.4.3	Electromagnetic Simulations of Single FPI Mirrors	110
3.4.4	Electromagnetic Simulations of Silicon Substrate-Based FPIs	113
3.4.5	Ohmic and Dielectric Losses	118
3.5	Prototype Device Fabrication and Characterization	123
3.5.1	Deep Reactive Ion Etching for sub-mm ARCs	124
3.5.2	DRIE ARC Characterization	127
3.5.3	Metal Mesh Fabrication	131
3.5.4	Early Device Measurements	133
3.6	Future Paths	136
3.6.1	Next Steps Towards EoR-Spec	136
3.6.2	Prospects for Future Silicon-based sub-mm Devices	138
3.7	Conclusion	141
4	Transition Edge Sensors for Simons Observatory	143
4.1	Simons Observatory	143
4.2	Transition Edge Sensor Design Overview	146
4.2.1	TES Pixel Design	147
4.2.2	TES Model	148
4.2.3	SO detector parameters	155
4.3	TES Characterization Methods	158
4.3.1	R vs T Critical Temperatures	160
4.3.2	I-V Curve Saturation Powers	162
4.3.3	Bias Step Time Constants	166
4.3.4	Complex Impedance	170
4.3.5	Comparison of $f_{3\text{dB},\text{eff}}$ Measurements	179
4.4	Conclusion	181
5	Conclusions	183
5.1	The Atacama Cosmology Telescope	183
5.2	The Simons Observatory	184
5.3	The CCAT-Prime Collaboration	188
5.4	Conclusion	192
Bibliography		193

LIST OF TABLES

1.1	Best fit Λ CDM parameters from ACTPol DR4 2020 [9]	12
2.1	Fit parameters for the Eccosorb-Robot beam maps	47
3.1	Double-layer ARC parameters, optimized via EM simulation parameter sweeps	99
3.2	SSB FPI CST model parameters	117
4.1	Target saturation powers and time constants for SO TESs	156
4.2	Table of best-fit parameters from I-V and P_{sat} analysis.	166

LIST OF FIGURES

1.1	Full-sky CMB temperature and polarization maps from Planck 2018	7
1.2	CMB power spectra from ACTPol DR4	10
1.3	History of the universe and line intensity mapping illustration	18
2.1	Panoramic photographs of the Atacama Cosmology Telescope	25
2.2	Screenshot of Zemax ray traces of ACT	28
2.3	AdvACT optics tube ray trace	29
2.4	Photograph illustrating Eccosorb-Stick beam mapping method	33
2.5	Photographs illustrating Eccosorb-Robot beam mapping method	35
2.6	AdvACT MF2 detector array map	37
2.7	Eccosorb-Stick TODs at various angles from the boresight	38
2.8	Eccosorb-Robot TODs and FFTs at various angles	40
2.9	Beam maps from Eccosorb-Stick method at multiple vertical angles	41
2.10	Fitted beam map from Eccosorb-Stick method	42
2.11	Encircled energy of the Eccosorb-Stick beam map	43
2.12	Comparison of Eccosorb-Robot and Eccosorb-Stick beam maps	45
2.13	Comparison of Eccosorb-Robot and Eccosorb-Stick encircled energies	46
2.14	Comparison of TES bias powers to Eccosorb signal amplitude	48
2.15	Comparison of harmonic and fundamental amplitudes	49
2.16	Comparison of Eccosorb-Robot beam map to diffractive simulation	51
2.17	Comparison of beam measurements to scattering ray trace	52
2.18	Photograph illustrating Eccosorb baffle measurement	53
2.19	Differential bias powers of Eccosorb baffles	55
2.20	Comparison of the Eccosorb baffle and Eccosorb-Robot results	56
3.1	Renderings and raytraces of FYST, Prime-Cam, and EoR-Spec	62
3.2	Reflection and transmission of a plane wave in a FPI	65
3.3	Airy function for an ideal FPI as a function of physical parameters	68
3.4	Photographs of inductive and capacitive metal meshes	70
3.5	Photograph prototype SSB mirrors with ARCs and gold meshes	72
3.6	EoR-Spec principle of operation	74
3.7	Waves in a multilayer dielectric medium	78
3.8	Dielectric model for single, double, and triple layer ARCs	82
3.9	Dielectric model double-layer ARC parameter sweep for ϵ_1 and ϵ_2	83
3.10	Dielectric model double-layer ARC parameter sweep for d_1 and d_2	85
3.11	Metamaterial geometry and approximate capacitive circuits	87
3.12	Effective refractive index of artificial dielectrics	89
3.13	Screenshot of the 3D ARC unit cell in CST-MWS	91
3.14	Comparison of dielectric theory to EM simulations for ARCs	93
3.15	Double-layer ARC CST simulations, sweeping over pitch	94
3.16	Double-layer ARC CST simulations, sweeping over target indices	95
3.17	Double-layer ARC CST simulations, sweeping over hole widths	96

3.18	Double-layer ARC CST simulations, sweeping over hole depths	97
3.19	Double-layer ARC CST simulations, sweeping over angle of incidence	100
3.20	Double-layer ARC CST simulations, sweeping over sidewall taper	101
3.21	Illustrations of SSB FPI and metal mesh geometries and models	102
3.22	CST simulation of inductive and capacitive metal meshes	105
3.23	CST simulation sweep of inductive and capacitive designs	108
3.24	Mesh design optimization with geometric mean reflectance	109
3.25	Screenshots of the single mirror designs in CST	111
3.26	Simulated reflectance of inductive and capacitive FPI mirrors	112
3.27	CST transmittance simulation of bare and metalized silicon wafers	114
3.28	Screenshot of full SSB FPI model in CST	115
3.29	CST transmittance simulation of the full scanning SSB FPI model	116
3.30	Full SSB FPI simulations, sweeping over angles of incidence	118
3.31	CST simulation of a fixed FPI with varying Ohmic losses	120
3.32	Dielectric loss in silicon at 300 K and 10 K	123
3.33	Double-layer metamaterial ARC DRIE recipe	125
3.34	SEM image of first DRIE-based double-layer metamaterial ARC	127
3.35	Profilometer data of the first DRIE-based double-layer ARC	128
3.36	SEM image of mm-wave DRIE-based ARC with strong fences	129
3.37	SEM image of 100 μm band DRIE-based ARC with clean sidewalls	131
3.38	Inductive and capacitive metal mesh microfabrication recipe	132
3.39	Microscope photos of inductive and capacitive meshes	133
3.40	FTS measurements of warm, 315 GHz fixed FPI	134
3.41	FTS measurements of 18 K, 3 THz fixed FPI	136
4.1	Renderings of Simons Observatory LAT, SAT, and receivers	144
4.2	Photographs of SO pixels and arrays	145
4.3	Photograph of SO MF single pixel illustrating microwave components	147
4.4	TES bolometer photograph and electrothermal model illustration	150
4.5	Photographs of prototype TESs showing P_{sat} and $f_{3\text{dB},\text{eff}}$ splits	157
4.6	Photograph of SO TESs on AdvACT MCE single pixel board	159
4.7	R-T curve of TES and T_c -check pad at multiple excitation currents	161
4.8	I-V and R-P curves of a SOSP3 MF TES at multiple T_{bath}	163
4.9	TES saturation power vs bath temperature with fits	164
4.10	TES parameters as a function of n extracted from P_{sat} fits	165
4.11	Example bias step time stream and time constant fits	168
4.12	Bias step time constant measurements as a function of P_{bias}	169
4.13	Example complex impedance time streams and sinusoidal fits	173
4.14	Complex impedance transfer functions for MF-150 GHz bolometer	174
4.15	Normal and superconducting transfer functions, \hat{V}_{th} , and Z_{eq}	175
4.16	TES complex impedance measurements and fits	177
4.17	Extracted bolometer parameters from complex impedance fits	178
4.18	Comparison of bias step and complex impedance measured $f_{3\text{dB},\text{eff}}$	180

5.1	Simons Observatory forecasted constraints on H_0	185
5.2	Simons Observatory simulated B-mode measurements	187
5.3	Simulated EoR-Spec redshift slice and power spectrum sensitivity	190

CHAPTER 1

INTRODUCTION

This dissertation describes the author’s scientific contributions to far-infrared and millimeter-wave telescope instrumentation through applied physics. Before diving into the technical work, it is important to set the stage in the relevant fields of observational cosmology and astrophysics. This chapter provides an overview of the motivations behind the development of these telescope technologies.

1.1 The Expanding Universe

Observational evidence of the expansion of the universe dates back to the early 1900s when Slipher interpreted redshift measurements of nearby galaxies as Doppler shifts due to their motions away from Earth [128, 129]. Using distance measurements to Cepheid variable stars [89] in nearby galaxies, Hubble refined this observation by noting that redshifts appeared to increase roughly linearly with distance [76]. This gave rise to Hubble’s law, $z = \frac{H_0}{c}r$, which quantifies the recession rate that we measure today as Hubble’s constant, H_0 , in terms of the measured redshift, $z \equiv (\lambda_{\text{obs}} - \lambda_{\text{emit}})/\lambda_{\text{emit}}$, the distance to the galaxy, r , and the speed of light, c . At the time of this discovery, the implication that space is expanding was at odds with the accepted cosmological model of a static universe. These observations gave rise to the Big Bang theory which asserted that the universe expanded from a hot, dense, ionized state in which matter and radiation were in thermal equilibrium.

Today, the prevailing model of cosmology is Λ CDM, which is a parameterization of the Big Bang theory. This model is well described in many texts [45, 123, 154].

The evolution of this expansion under Λ CDM is governed by the energy density constituents of the universe, namely: radiation (including relativistic particles), matter (including ordinary matter as well as cold dark matter, CDM, which does not interact electromagnetically), and dark energy (in the form of a cosmological constant, Λ). These energy densities drive the evolution of space and have turned subtle matter overdensities in the primordial plasma into the large scale structure of galaxies and clusters that we observe today. Observational evidence of the big bang exists in the form of a nearly isotropic blackbody radiation filling all of space that is known as the cosmic microwave background (CMB).

Λ CDM relies on the Cosmological Principle which states that on large scales, the universe looks the same in all directions (it is isotropic) from every location (it is homogeneous). To describe the evolution of the universe under the Cosmological Principle, Λ CDM uses the Friedmann-Lemaître-Robertson-Walker (FLRW) metric solutions to Einstein's theory of general relativity [55, 91, 121, 153]. The FLRW metric uses the scale factor $a(t)$ to quantify the expansion of space as a function of the proper time, t . The scale factor today is conventionally defined such that $a_0 = a(t_0) = 1$ and is related to redshift via $a(t) = a_0/(1+z)$. Evolving with the energy densities of the universe, $a(t)$ is effectively a cosmological clock. The evolution of the scale factor is described by the Friedmann equation [154]:

$$\left(\frac{\dot{a}(t)}{a(t)}\right)^2 \equiv H(t)^2 = \frac{8\pi G}{3}\rho(t) - \frac{k}{a(t)^2}, \quad (1.1)$$

where $H(t)$ is the Hubble parameter (note $H(t_0) = H_0$), \dot{a} is the time derivative of the scale factor, G is Newton's constant, ρ is the energy density of the universe, and k describes the curvature of spacetime. The Friedmann equation is often rewritten in terms of the constituent energy densities [154] such that:

$$H(t)^2 = H_0^2 \left(\frac{\Omega_r}{a^4} + \frac{\Omega_m}{a^3} + \frac{\Omega_k}{a^2} + \Omega_\Lambda \right), \quad (1.2)$$

where $\Omega_k = -k/H_0^2$ and the other $\Omega_i = \rho_i/\rho_c$ (for $i = r, m, \Lambda$) are the energy densities divided by the critical density $\rho_c = \frac{3}{8\pi G}H_0^2$ which is the total energy density required for a flat spacetime. Each energy density scales with $a(t)$ differently, as defined by each components equation of state [45]. This means that the expansion dynamics of the universe are directly tied to the evolution of the energy densities.

Λ CDM has been widely successful at explaining observations of the CMB and large scale structure. However, multiple questions still remain. For example, the source of the initial perturbations which seeded large scale structure is still unknown. Further, the observed isotropy of the CMB across large-angular scales violates causality since those regions of the sky have never been in thermal contact. This is known as the horizon problem. Additionally, since the curvature density scales as $1/a^2$, a flat spacetime today implies an extremely flat spacetime in the past, which requires the initial total energy density to be “finely-tuned” [123]. This is known as the flatness problem.

Inflation is a group of models which attempt to explain these problems by positing that in the very earliest moments of the universe, the scale factor underwent rapid, exponential growth, driven by the existence of an inflaton field [154]. Regions that were in causal contact at the beginning of inflation are driven out of contact during the exponential expansion, solving the horizon problem. During inflation’s exponential expansion, the Hubble parameter would have been roughly constant, requiring that the any curvature be decreasing rapidly to zero like $1/a^2$, solving the flatness problem. Further, during inflation, small-scale quantum fluctuations expand to large-scale perturbations, seeding the inhomogeneities that we see in the CMB, and the large scale structure of the universe.

We have no means to directly observe inflation. However, inflation is predicted

to produce primordial gravitational waves, which would cause tensor perturbations to the spacetime metric, that would be the only source of primordial B-mode polarization patterns in the CMB (more on polarization later in Section 1.2.3). The amplitude of the primordial B-mode signal is characterized by the tensor-to-scalar ratio, r . Thus far, there is no evidence of such primordial gravitational waves, but constraints have been placed such that $r \lesssim 0.05$ [145]. Complicated by contamination from gravitational lensing and dust emission, measurements of the faint primordial B-mode signal remains an active goal of many contemporary CMB observatories [1, 3].

Another unanswered question in Λ CDM is the nature of dark energy. Fitting to Λ CDM, recent CMB measurements find the dark energy density to be $\Omega_\Lambda = 0.68$, making up 68% of the universe's total energy density [7]. Further, the CMB measurements are corroborated by supernovae observations [87]. These measurements indicate that the expansion of spacetime is accelerating and suggest that the acceleration is exponential. Understanding the source and manifestation of dark energy remains one of the modern mysteries that cosmologists aim to unravel through observations.

1.2 The Cosmic Microwave Background Radiation

In the big bang model, the universe was once hot, dense, and ionized. The universe was opaque due to the high density of free charges and the resulting high photon scattering rate. The high rate of interactions meant that the photon-baryon fluid was in thermal equilibrium, forming a primordial plasma. Density perturbations propagated through the plasma like acoustic waves coupling over-

and under-densities of matter to the photon distribution. As the universe expanded and the energy densities became more dilute, the components of the universe began to freeze out and decouple from the plasma. Eventually, electrons combined with baryons, forming atoms (primarily neutral hydrogen¹). As the plasma became less ionized, the mean free path of photons increased until the photons could free-stream into the universe. This occurred between $z = 1400$ and $z = 1100$, when the temperature had dropped to $T \approx 3000$ K, and is known as the epoch of recombination. The photons released from the surface of last scattering² encode the density fluctuations of the acoustic waves at the time of recombination. As the universe continued expanding and cooling, the photons were redshifted into millimeter wavelengths and comprise what we now call the CMB and observe with microwave telescopes.

1.2.1 Blackbody Spectrum

Before recombination, CMB photons were in thermal equilibrium with the primordial plasma. We therefore expect their temperature to follow that of a redshifted blackbody spectrum. The first measurements of the CMB were made in 1964 by Penzias and Wilson at Bell Labs, who measured an isotropic sky temperature of 3.5 K [115], suggesting a radiation background [41]. A few decades later, in 1990s the Far-InfraRed Absolute Spectrophotometer [53] on the Cosmic Background Explorer (COBE) used a Fourier transform spectrometer to measure the spectral profile of the radiation, finding a stunning agreement to a thermal blackbody with temperature 2.725 ± 0.002 K [99]. A decade later, combining the COBE black-

¹Hydrogen was by far the dominant product, followed by ^4He ($\approx 25\%$ by mass), and smaller abundances of deuterium, ^3He , tritium, lithium, and beryllium were also produced.

²Since the process of recombination was not instantaneous, the surface of last scattering can be thought of as a shroud of last scattering.

body measurements with measurements from the Wilkinson Microwave Anisotropy Probe (WMAP) modestly improved the constraint on the black body temperature to 2.7260 ± 0.0013 K [52]. COBE was also equipped to measure the spatial fluctuations of the CMB across the sky. With a relatively large 10° resolution, COBE found the fluctuations to be roughly a part in $\mathcal{O}(10^5)$ [130]. The observations that the CMB is a nearly perfect and isotropic blackbody strongly support the big bang theory by implying that the universe was once indeed hot, dense, opaque and highly homogeneous.

1.2.2 Anisotropies

As a snapshot of the density fluctuations during the epoch of recombination, the CMB is rich with information about the early universe. Characterizing the anisotropies in the CMB is the subject of modern CMB observations. With a statistical understanding of their properties, Λ CDM parameters can be constrained.

The COBE, WMAP, and *Planck* satellites have all mapped the CMB across the full sky. Figure 1.1 shows the most recent all-sky CMB anisotropy map from *Planck* in temperature and polarization [7]. The data plotted are fluctuations about the mean CMB blackbody temperature. The temperature anisotropies are a result of density fluctuations at the time of recombination³. The polarization anisotropies describe the velocity field of the primordial plasma and may also contain information about primordial gravitational waves. Thus, the anisotropies directly probe the energy densities and kinematics of the early universe. In the next section, we will see how Λ CDM cosmology can be retrieved from these fluctuations.

³Cooler regions correspond to overdense regions, where the photons had to escape a larger gravitational potential, losing energy. This is called the Sachs-Wolfe effect.

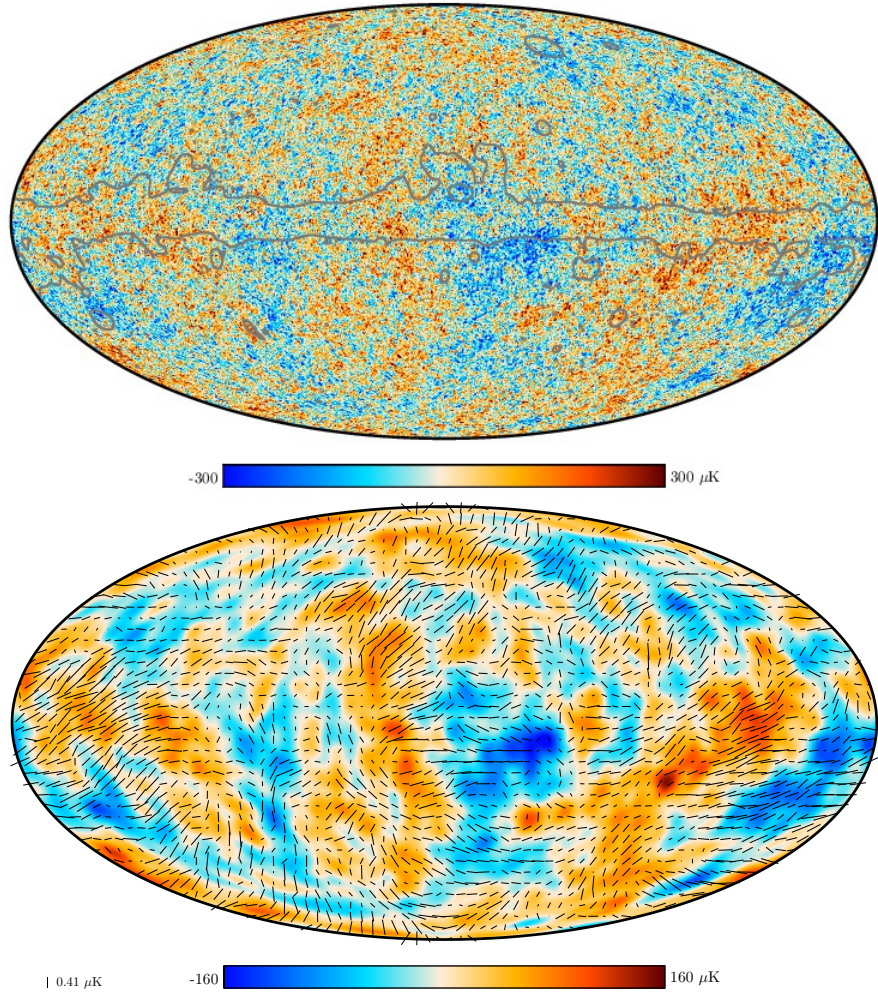


Figure 1.1: Figure from [7]. Full-sky CMB temperature (upper panel) and polarization (lower panel) anisotropy maps from the 2018 data release of the *Planck* collaboration. Galactic (area outlined with gray line in temperature map) foreground emission is removed. Polarization anisotropies are shown as the black rods (indicating the magnitude and direction of the electric field) superimposed on top of the temperature map, smoothed to 5° resolution for visibility.

So far, we've talked only about fluctuations due to the primordial plasma itself, which we call the primary CMB anisotropies. We expect the CMB to interact with matter on its way from the surface of last scattering to our telescopes. We observe these interactions as small angular scale distortions in the primary CMB,

called secondary anisotropies. Secondary anisotropies are not just contamination – we can glean a great deal of cosmology and astrophysics from them. For example, CMB photons can interact with high-energy free electrons in galaxy clusters, which will impart a spectral distortion on the CMB spectrum via inverse Compton scattering. This is called the Sunyaev-Zel'dovich (SZ) effect. Another example is the gravitational lensing of the CMB which occurs as trajectories of CMB photons are distorted by large masses such as galaxy clusters or dark matter halos, leaving a distortion in the primary CMB. These secondary anisotropies occur on small scales, and so are actively being measured by new, high-resolution ground-based CMB observatories. We discuss recent measurements of these effects below.

1.2.3 Power Spectra

Maps of the CMB anisotropies can be decomposed into spherical harmonics

$$\Delta T(\hat{n}) = \sum_{\ell m} a_{\ell m} Y_{\ell}^m(\hat{n}), \quad (1.3)$$

where $\Delta T(\hat{n})$ represents the deviation from the CMB mean temperature in a direction \hat{n} on the celestial sphere, and $a_{\ell m}$ are the harmonic coefficients. Since the CMB is isotropic and largely Gaussian [12], we can explore the angular power spectrum C_{ℓ} by comparing the amplitude ΔT at two points on the celestial sphere, \hat{n} and \hat{n}' such that

$$\langle \Delta T(\hat{n}) \Delta T(\hat{n}') \rangle = \sum_{\ell m} C_{\ell} Y_{\ell}^m(\hat{n}) Y_{\ell}^{-m}(\hat{n}'), \quad (1.4)$$

where the power spectrum C_{ℓ} is given by [154]

$$\delta_{\ell\ell'} \delta_{mm'} C_{\ell} = \langle a_{\ell m} a_{\ell' m'}^* \rangle, \quad (1.5)$$

where the angle brackets indicate an average of all m since we expect the fluctuations to have no preferred direction (isotropy).

So far, we have discussed the power spectrum of CMB temperature anisotropies. An analogous analysis can be performed for the CMB polarization anisotropies as is described in [154]. The CMB is expected to be linearly polarized, sourced from Thomson scattering of quadrupolar anisotropies in the last scattering surface. These polarizations can be described by the Stokes Q and U parameters, and decomposed into coordinate-system-independent E and B-modes [163]. Following the electromagnetic analogy, E-modes consist of curl-free polarization patterns, while B-modes are divergence free. The primordial quadrupolar anisotropies can only source E-modes, and the B-modes can only be sourced by primordial gravitational waves. Power spectra for each component as well as cross-spectra between components can be obtained and are denoted C_ℓ^{XY} , where the X and Y can be T , E , or B (in reference to temperature, E-modes, and B-modes).

Figure 1.2 shows recent power spectra measurements from the Atacama Cosmology Telescope (ACT) DR4 (for data release four) overplotted with other contemporary measurements [25]. ACT is a 6 m aperture ground-based CMB telescope which observes a large fraction of the sky from Chile and will be described further in Chapter 2. Note that the ACT data accesses higher multipole moments (smaller angular scale) than Planck due to its higher spatial resolution, but Planck can access lower ℓ since it can map the entire sky. The power spectrum here is reparameterized as

$$D_\ell \equiv \frac{\ell(\ell+1)}{2\pi} C_\ell \quad (1.6)$$

to aid visualization. It is evident that the temperature, E-mode, and B-mode signals are separated by many orders of magnitude in amplitude. Note that the

B-mode data shown here is due to gravitational lensing of E-modes. An example expectation primordial B-modes is shown with a dashed line in the bottom left, assuming $r = 0.1$ which is higher than current constraints [145].

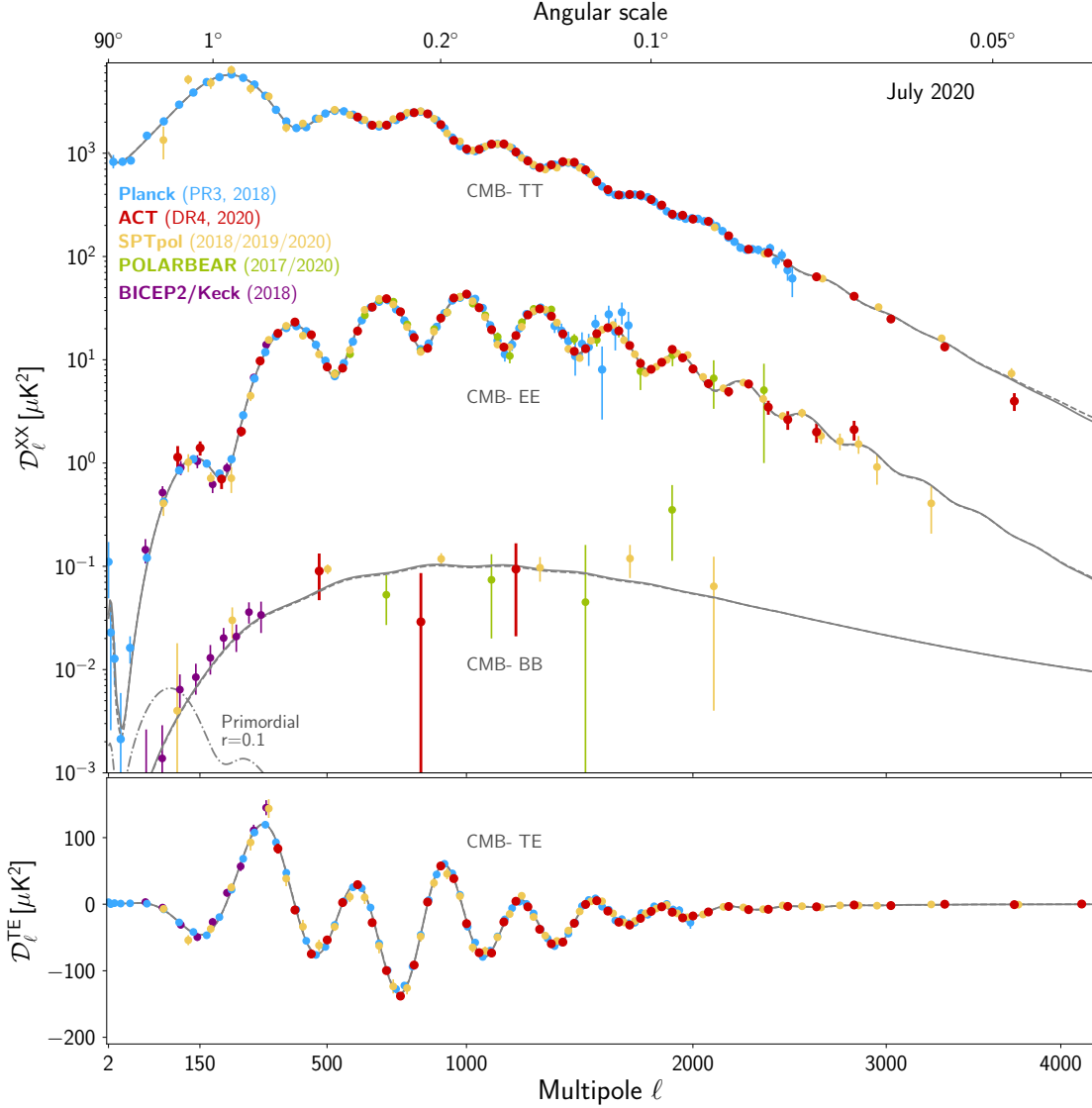


Figure 1.2: Figure from [25]. A compilation of power spectra measurements of CMB temperature and polarization anisotropies. Best fit Λ CDM models to the Planck and ACT+WMAP data are plotted as the gray dashed and solid lines respectively. The expected B-mode signal from primordial gravitational waves corresponding to $r = 0.1$ is also plotted as the dot-dashed line in the lower right.

The power spectrum encodes a variety of fundamental physics from the early universe and has powerfully constrained Λ CDM [113]. A series of acoustic peaks is apparent in the power spectra above $\ell \sim 100$. These are called baryon acoustic oscillations (BAO) and arise from the dynamics of the density fluctuations described above. The BAO retain a snapshot of how the gravitational compression of matter overdensities interacted with the photon pressure, setting up acoustic waves. The lowest- ℓ peak corresponds to a wave which has undergone a single compression and thus corresponds to the sound horizon at the time of last scattering, which we see is on the scale of 1 degree today. Harmonics of this wave constitute the other peaks, representing waves that have undergone compression and rarefaction, and so on. The location and sizes of these peaks provide a cosmological ruler and are used to constrain cosmological parameters. The first two peaks constrain the total matter and baryon densities. Above $\ell \sim 1000$, the length scales of the acoustic peaks are shorter than the photon diffusion length, and so are suppressed. Below $\ell \sim 100$, the spectrum is relatively flat since modes here are outside the sound horizon and are dominated by the Sachs-Wolfe effect.

The power spectra can be fit to the parameters of the Λ CDM model. Many of the parameters are degenerate with each other. It is remarkable that the model can be fully described by merely six parameters. Best-fit Λ CDM parameters for ACT power spectra shown above are presented in [9]. Table 1.1 gives the six independent parameters as a couple derived parameters measured by ACT [9].

The six independent parameters can be used to calculate all other quantities in Λ CDM. The independent parameters are the baryon density, $\Omega_b h^2$, the cold dark matter density, $\Omega_c h^2$,⁴ the angular scale of the acoustic horizon at decoupling, θ_{MC} ,

⁴These parameterizations of the densities incorporate the Hubble constant through the reduced Hubble constant: $h = H_0/(100 \text{ km/sec/Mpc})$.

Parameter	Value	Uncertainty
Fitted		
$100\Omega_bh^2$	2.239	± 0.021
$100\Omega_ch^2$	12.00	± 0.29
$10^4\theta_{\text{MC}}$	104.170	± 0.067
τ	0.061	± 0.012
n_s	0.9729	± 0.0061
$\ln(10^{10}A_s)$	3.064	± 0.024
Derived		
H_0 [km/s/Mpc]	67.6	± 1.1
Ω_Λ	0.687	± 0.016

Table 1.1: Best fit Λ CDM parameters from ACTPol DR4 2020 [9]. The six fitted parameters are shown along with two derived parameters.

the optical depth through reionization, τ , the scalar spectral index, n_s , and the amplitude of the scalar density perturbations, A_s . The Hubble constant, H_0 , and the dark energy density are be derived from these. Many other parameters such as the age of the universe $t_0 \approx 13.8 \times 10^9$ years and the age at decoupling $t_* \approx 380,000$ years, can also be calculated.

1.2.4 Current efforts in CMB cosmology

Modern high-precision CMB measurements have revealed beautiful temperature and E-mode power spectra. A great deal of fundamental physics is being constrained with these measurements, and there is still much to discover. Here we highlight some of the most recent ACT results and some remaining open questions.

As described above, ACT measurements have produced constraints on Λ CDM using primary anisotropies. In combination with full sky measurements of WMAP and Planck, the DR4 measurements greatly constrain our understanding of the primordial universe [9, 25]. ACT has also released additional data for DR5, enabling

many secondary anisotropy analyses [109].

Recent analyses of secondary anisotropies include measurements of the thermal and kinematic SZ effects [21, 151], revealing optical depths of galaxy clusters and probing their baryon content. These measurements can reveal a great deal of astrophysical information about galaxy cluster formation and evolution, as well as cosmological information such has the sum of the neutrino masses and dark energy [104, 105]. Additional analyses of secondary anisotropies include measurements of CMB gravitational lensing. These measurements are used to constrain the lensing B-mode signal, probe dark matter halos, and measure the mass of distant galaxy clusters [13, 49, 97].

The data and maps from these surveys are becoming more widely useful for local astrophysics and time domain astronomy. For example, polarization maps of the galactic center at CMB frequencies reveal structure and magnetic field gradients [65]. Similarly, with ground-based telescopes observing nearly 24 hours per day, time domain astrophysical events are being observed and are of increasing interest, such as blazars [111]. In a recent application closer to home, data from ACT was used in the search for Planet-9, where in the millimeter wavelengths, observations have a great deal of constraining power over optical measurements⁵, yet have thus far returned null results [110]. Further, ACT uses observations of planets to characterize its beam and measures their microwave temperatures [67].

Returning to CMB observations, even with the exquisite modern constraints on Λ CDM [8, 9], there is still a great deal to investigate. As described above, there are multiple issues that Λ CDM does not explain, such as the horizon and flatness problems or the source of the primordial perturbations. We described how

⁵The intensity of reflected sunlight from Planet-9 would fall as $1/r^4$ whereas thermal emission in the millimeter would be much more forgiving, falling as $1/r^2$ [110].

inflation presents an attractive solution to these problems. However, primordial B-modes remain undetected [11].

Measuring inflationary B-modes would be a huge milestone for CMB cosmology, providing critical evidence for inflation. Gravitational lensing of E-modes into B-modes and polarized dust emission obfuscate the inflationary signal [81]. Removal of these foregrounds is the aim of many current and new experiments [1, 3]. Improving measurements of the lensing B-mode spectrum will enable delensing of CMB maps. Foregrounds are sourced from free electron synchrotron emission and dust thermal emission, both of which have strong frequency dependencies and contaminate the B-mode signal [2]. Using maps at multiple frequencies, it is possible to constrain dust and synchrotron models and clean them from the primary CMB signal. Thus, to improve constraints on inflation, the field is driven towards higher-sensitivity, large-scale, multi-frequency surveys with excellent polarization calibration.

Another issue in modern cosmology is the discordance of Hubble constant measurements between early-time CMB measurements and late-time distance-ladder measurements. A review of this so-called Hubble-tension is provided in [148]. Fitting CMB power spectra to Λ CDM gives an indirect measurement of the Hubble constant. From *Plank* data, $H_0 = 67.4 \pm 0.5$ km/s/Mpc [8]. From ACTPol+WMAP data, $H_0 = 67.6 \pm 1.1$ km/s/Mpc [9]. Direct distance-ladder measurements of Cepheids and supernovae give a Hubble constant of roughly $H_0 = 74.03 \pm 1.42$ km/s/Mpc [120]. The *Planck* and Cepheid-supernovae measurements differ by $> 4\sigma$ [119]. As the Hubble tension is explored further in the next decade, it could reveal systematic issues with the measurement approaches, or (more excitingly) it could lead to departures from Λ CDM. In the latter case, it

could suggest new cosmological models such as, evolving dark energy or modified gravity, for example.

The Hubble tension and inflationary B-modes are only two examples of the interesting physics that will come from CMB cosmology in the next decades. Experiments aim to constrain a variety of fundamental physics [1, 3, 90, 131]. For example, we may see constraints on the nature of dark matter, which has proven difficult to detect directly due to interacting only gravitationally on large scales. Similarly, the nature of dark energy is relatively unknown other than that it is necessary to explain the recent acceleration of the expansion of the universe. We may discover the physical source of the cosmological constant or we may find that it has a subtle evolution over time. Further, neutrinos are expected to impact the SZ and CMB lensing effects because of their mass, and so more precise measurements will enable constraints on the sum of the neutrino masses. The list continues and it is clear that CMB measurements will continue to be an invaluable source of fundamental physics.

1.3 The Epoch of Reionization

Following recombination, neutral matter (primarily in the form of hydrogen and helium) fills the universe. This epoch is called the “Dark Ages” since visible photons aren’t being produced⁶. Without the previously-coupled photon pressure, baryonic matter slowly gravitationally collapses into dark matter overdensities. Over time, as the baryonic matter collapses, the first stars and galaxies form, pro-

⁶The term “Dark Ages” is a bit of a misnomer to since the universe was filled with the CMB which was then in the optical and near-IR. And also because the neutral hydrogen can be traced by its 21 cm hyperfine splitting emission.

ducing high-energy radiation, and tracing the underlying dark matter distribution. This radiation begins ionizing the neutral hydrogen of the universe, marking the beginning of the epoch of reionization (EoR) [123].

Compared to the CMB, the EoR is largely unexplored and occurred over a large span of cosmic time ($6 \lesssim z \lesssim 11$) [50]. The first sources of reionization are not well characterized but are hypothesized to be a combination of ultraviolet light from the first stars and black hole accretion in active galactic nuclei [14]. Targeted studies of individual, bright, high-redshift galaxies with the Hubble Space Telescope (HST)⁷ and the Atacama Large Millimeter Array (ALMA)⁸ suggest that cosmic reionization is primarily driven by the starlight from stars within the first galaxies that form in the universe [118]. However, the overall process of reionization remains poorly understood since it is thought to be driven by a multitude of intrinsically faint sources. Observations of the EoR will reveal properties of the first sources of light and how reionization impacted the evolution of the intergalactic medium (IGM) into the large scale structure we see today.

In the current model of the EoR, the first luminous sources heat the gas around them, creating a “bubble” of ionized gas, surrounded by the neutral IGM [86]. As more sources develop, more bubbles are generated, expanding the regions of ionized space until all of IGM became reionized. Figure 1.3 illustrates the evolution of the universe, highlighting these bubbles and the transition to fully ionized IGM during reionization between redshifts 15 and 6. From an observational standpoint, the star-forming/ionizing regions contain astrophysical processes which generate specific spectral lines. Different spectral lines can be used to trace different processes and regions around the ionizing sources. The neutral IGM can also be traced

⁷HST: https://www.nasa.gov/mission_pages/hubble/main/index.html

⁸ALMA: <https://www.almaobservatory.org/en/home/>

by observing the hyperfine transition of neutral hydrogen. Thus, the EoR can be characterized by observing the various redshifted spectral lines corresponding to the different regions and processes during this epoch.

Observations of these lines would enable many investigations into fundamental questions about the EoR [85]. For example, when did the EoR begin and how did the process of reionization evolve over time? How did the evolution of reionization impact the formation of large-scale structure? Further, what were the properties of the different ionization sources and how did they each contribute to different stages of reionization? Did first generation stars and galaxies contribute differently than later generations? What was the cosmic star-formation rate during the EoR?

Clearly, probing the EoR on a variety of scales and frequencies will illuminate a great deal of unexplored astrophysics and cosmology. Targeted measurements of individual clusters or sources are difficult at these high redshifts due to their intrinsic faintness. The luminosities during the EoR decay not only due to the distance, but also due to the lower star formation rate in the earliest times of the universe. In the next section, we will discuss a new measurement method predicted to overcome these challenges and well-suited for studying the clustering signals of early star-forming regions in the EoR.

1.3.1 Line Intensity Mapping

Line intensity mapping (LIM) is a relatively new method for observing large-scale structure and evolution in the early universe [86]. Rather than performing high-resolution, targeted observations of individual high-redshift reionization sources, LIM uses low-resolution measurements of the aggregate emission of many sources.

Figure 1.3 illustrates how LIM measures the spatial fluctuations of spectral line emission in distinct “slices” of redshift.

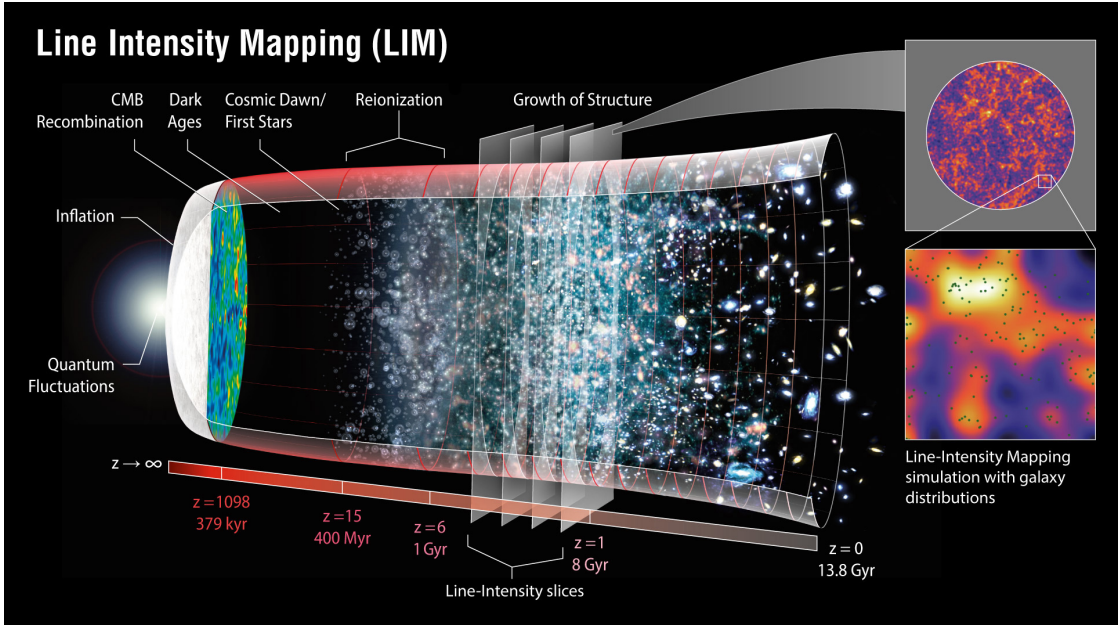


Figure 1.3: Illustration of the history of the universe and how line intensity mapping can be used to probe the epoch of reionization and the growth of structure. As shown, reionization begins as bubbles of ionized gas form around ionization sources which develop in gravitationally collapsing matter overdensities. As collapse continues, large-scale structure forms and the neutral hydrogen in the IGM becomes fully ionized. LIM maps specific ionization processes throughout EoR and the growth of structure as a function of redshift. This results in many redshift “slices” which generate a three-dimensional datacube. LIM intentionally under-resolves the ionization sources, measuring the aggregate signal of the brightest and faintest sources as shown by the example slices on the right. Figure from [NASA/LAMBDA Archive/WMAP Science Team](#).

This method has multiple advantages for EoR applications. Unlike targeted studies which can only access the brightest of sources, LIM is sensitive to all sources regardless of their individual luminosities. This enables observations of faint and extended sources that cannot be accessed through traditional observations. In turn, this enables more comprehensive studies of the processes that occur during

reionization and galaxy assembly. Further, the fluctuations that LIM observes are correlated with the underlying dark matter distribution and can therefore be used as a cosmological probe of large-scale structure-formation.

Since high angular-resolution is not required by LIM, it can potentially cover large sky areas very quickly, compared to long-baseline interferometric observatories such as ALMA. This gives LIM a large mapping-speed efficiency advantage over traditional observations. LIM measurements prefer wide field of view instruments with high surface brightness sensitivity and modest frequency resolution.

Mapping spectral lines as a function of redshift, enables tomographic imaging of the formation of structure and the processes of reionization. Figure 1.3 illustrates how LIM can be used to tomographically measure structure in many redshift slices. Mapping multiple spectral lines at many different redshifts produces a hyperspectral-spatial datacube containing vasts amount of astrophysics and cosmology. Spectral LIM observations of different sources of emission or absorption can be used to trace the evolutions of different processes during the EoR. LIM can probe both the properties of star-forming regions and the neutral hydrogen IGM around the ionized bubbles. Further, correlations between different lines will illuminate the interplay between various processes and the formation of structure.

1.3.2 Probes of the EoR

The most common LIM experiments are designed to measure the 21 cm HI line. Before reionization occurred, neutral hydrogen was everywhere, but concentrated around dark matter halos. Thus, this line is expected to trace the formation of

structure at the earliest times of the EoR. As the ionization bubbles grow and expand during EoR, the HI line will be able to constrain the size and distributions of the bubbles through cosmic time. HI measurements are difficult to make, as they are highly susceptible to radio frequency interference (RFI) and strong galactic synchrotron foregrounds. Multiple 21 cm experiments already exist and many are being proposed and built. For example, the Square Kilometer Array (SKA) Observatory⁹ is a consortium of previously independent precursor HI radio observatories.

Many millimeter and sub-millimeter spectral lines can be used to directly probe the ionization regions [37]. For example, the [CII] fine structure line represents cooling radiation of the gas heated by starlight and is an exceptionally bright and efficient tracer of star forming regions [132, 133]. CO rotational lines at the same wavelength as EoR [CII], can be used to trace lower redshift cold molecular clouds, enabling studies into the properties of the interstellar medium, and constraining future star formation [93]. The [OIII] fine structure line, like the [CII] line, also traces early star-forming regions but is expected to be less bright than lower-redshift [CII] at a given wavelength [134], since the [OIII] will be emitted at roughly twice the redshift of [CII] emitters.

All of these millimeter and sub-millimeter lines are brighter than the 21 cm HI line. This gives them the advantage of being observable by a single telescope rather than an array. Equally important, is that millimeter and sub-millimeter are able to resolve the cosmic web with telescope apertures of only a few meters in diameter, as opposed to the several kilometer arrays that are necessary for the radio emission. Similarly, since the wavelengths are of order 600 times shorter, the apertures of millimeter and sub-millimeter telescopes need only be a few meters in

⁹SKA: <https://www.skatelescope.org/>

diameter

However, the measurements still must contend with significant foregrounds and atmospheric absorption. Successful surveys of these lines will enable many analyses and cross-correlations with other lines, revealing a plethora of EoR physics and astrophysics.

1.3.3 Astrophysics and Cosmology from LIM

EoR LIM surveys of the HI 21 cm, [CII], [OIII], CO, H α , Ly α lines will be highly complementary and useful for cross-correlation analyses [46, 85, 86, 125]. For example, the HI 21 cm line emission from neutral hydrogen is expected to anti-correlate with [CII] and [OIII], since the latter two lines will trace gas heated and ionized by starlight. Analyses such as this could dramatically improve our understanding of the interplay between the IGM and ionizing sources. Correlating the brightness and three-dimensional spatial distributions of different probes will reveal properties of the radiation fields, such as the numbers, types, and spatial distribution of young massive stars within ionizing galaxies. The combined probes will explore the growth of ionization, the production of metals, and the evolution of reionization bubbles [86]. Further, with unbiased measurements of sources at all scales and at many wavelengths, LIM will produce excellent constraints on the cosmic star formation rate and efficiency, while also characterizing the properties of the ISM.

In addition to astrophysics and EoR observations, LIM also has many cosmological applications [85]. By intensity mapping aggregate line emissions over large co-moving spatial scales, LIM will reveal the growth of density fluctuations. This

enables probes into the primordial matter power spectrum which in turn enables tests of Λ CDM and its extensions. LIM measurements can also probe the BAO as well as gas abundances, enabling simultaneous measurements of large-scale structure and galaxy evolution [17]. Further, when combined with measurements of CMB secondary anisotropies, LIM could provide redshift and gas content information for CMB lensing and SZ cluster analyses.

With sufficiently precise measurements and foreground removal, constraints could be placed on fundamental physics including models of inflation, dark energy, and the sum of the neutrino masses [85]. By probing galaxies at high redshifts, LIM could help address the Hubble tension by providing intermediate measurements between the CMB and late-time distance ladder measurements. Further, LIM could help constrain models for dark energy by investigating the potential time dependence of the cosmological constant. LIM has also been forecasted to help place constraints on primordial non-Gaussianity, which would in turn help constrain certain models of inflation [43].

While some of these results could be obtained through pointed measurements of individual galaxies, intensity mapping provides a more efficient measurement. Rather than using the largest aperture telescopes and very long integration times for individual sources, LIM experiments will be sensitive to the aggregate signal of all bright and faint sources. In Chapter 3, we will talk about an instrument to perform LIM of the EoR that the author helped develop. Then, in Chapter 5, we will discuss forecasts and sensitivity models for this instrument in constraining properties of the EoR.

1.4 Summary

The fields of CMB cosmology and EoR LIM have many open questions. In order to address these questions, new millimeter and sub-millimeter high-throughput and high-sensitivity observatories are needed. In Chapter 2, measurements of the Atacama Cosmology Telescope’s millimeter-wave receiver beam are presented and the impact of the measurements on future observatories is discussed. In Chapter 3, models and fabrication methods are presented for silicon-substrate metamaterial-based Fabry-Perot interferometers that will be used in CCAT-prime’s upcoming LIM instrument, EoR-spec. In Chapter 4, superconducting transition edge sensor characterization methods and analyses are presented for the upcoming Simons Observatory. In Chapter 5, we conclude with a brief discussion of the next generation of observatories that will use these technologies and present a glimpse of the expected science outcomes of each project.

CHAPTER 2

CHARACTERIZING THE ADVACT RECEIVER OPTICS

In this chapter, we describe measurements of the receiver beam of the Atacama Cosmology Telescope and how they are being used to optimize new telescopes. We begin Section 2.1 with a brief overview of the telescope and its instrumentation. In Section 2.2 we motivate measurements of the receiver beam with a discussion of the implications of warm spillover in the instrument sidelobes. Section 2.3 describes the measurement, analysis, and results of two beam mapping experiments performed by the author and provides a brief comparison to optical models. Finally, we close the chapter in Section 2.4 with a discussion of how these measurements have affected the design of multiple upcoming telescopes and receivers.

2.1 The Atacama Cosmology Telescope and Receivers

The Atacama Cosmology Telescope¹ (ACT) is a 6 meter aperture, millimeter-wave (mm-wave) telescope designed to map the CMB with arcminute resolution [141]. The off-axis Gregorian telescope was built in 2007 at an altitude of 5190 meters on a plateau on the side of Cerro Toco in the Atacama Desert in northern Chile. Its high-altitude and extremely dry climate give ACT one of the best terrestrial mm-wave observing sites in the world. The two-mirror telescope is designed to provide a few square degree diffraction limited field of view to its cryogenic camera/receiver. With its field of view and high angular resolution, ACT is optimized to study the small-scale primary and secondary anisotropies of the CMB and provide datasets that are complementary to larger-scale space-based observations. Figure 2.1 shows panoramic views of ACT. The upper panel shows the telescope situated on the

¹<https://act.princeton.edu/>

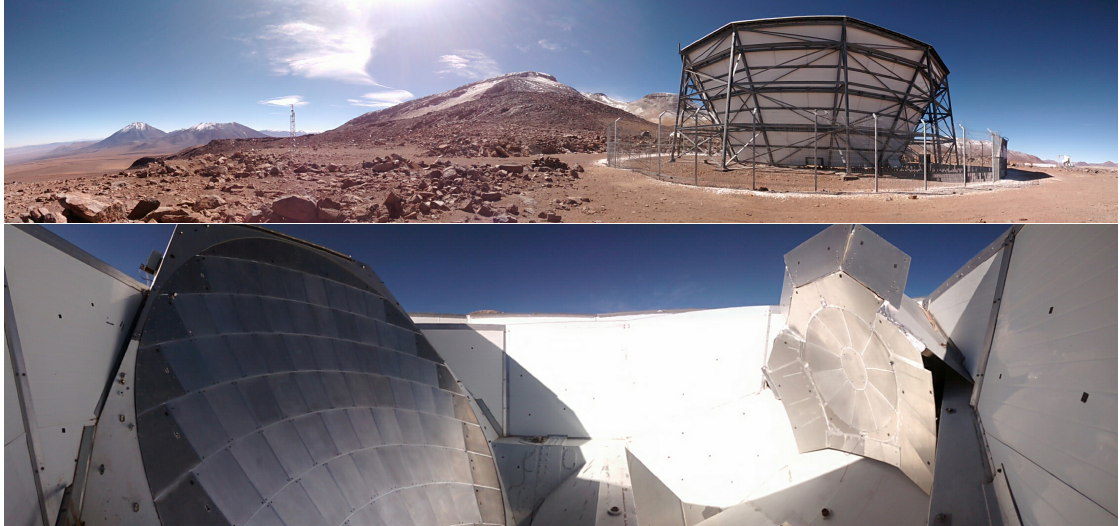


Figure 2.1: Panoramic photographs of ACT. The upper panel shows the exterior of ACT’s stationary ground screen situated on a plateau beneath the summit of Cerro Toco (shown center). The ground screen is designed to prevent radiation from bouncing from the ground into the telescope structure. The lower panel shows ACT’s multi-paneled 6 m primary mirror and secondary mirror situated inside a co-moving ground screen (white). The secondary mirror is surrounded by metal baffling. The receiver is not shown but is just below the middle of the panorama.

plateau, surrounded by a stationary ground-screen to block contaminating signals. Cerro Toco’s summit can be seen behind and to the left of ACT while to the right, additional mm-wave telescopes such as the Cosmology Large Angular Scale Surveyor (CLASS) and Simons Array (formerly POLARBEAR) are present. The lower panel shows ACT’s multi-panel primary and secondary mirrors inside a co-moving ground screen. A reflective baffle surrounds the secondary mirror to minimize radiation from the warm telescope structure near the main beam.

The original ACT receiver was the millimeter bolometric array camera (MBAC), which was sensitive to CMB temperature in three bands: 150, 220, and 280 GHz [54, 140]. In 2013, MBAC was upgraded to the ACTPol receiver which contained higher-sensitivity, polarization-sensitive, transition-edge sensor

(TES) arrays (150 GHz) as well as the first dichroic array (90 and 150 GHz) [38, 144]. ACTPol also had improved cryogenics and high-efficiency metamaterial anti-reflection coatings on its silicon lenses [39]. The third and current generation instrument, Advanced ACTPol (AdvACT), was deployed in 2016 using the same cryostat as ACTPol. AdvACT improved array sensitivities and increased the number of pixels using monolithic large-format dichoric polarimeter arrays [48, 70]. AdvACT was originally deployed with a high-frequency (150 and 220 GHz) module and two mid-frequency (90 and 150 GHz) modules named HF, MF1, and MF2. In 2020, MF2 was replaced with a low-frequency array (27 and 39 GHz), LF. AdvACT is currently observing with HF, MF1, and LF, each of which have their own silicon lenses, anti-reflection coatings, and bandpass filters tuned for each band [24, 75, 92, 127].

The AdvACT upgrade extended ACT’s frequency coverage and increased its total number of detectors and overall sensitivity. With these improvements, AdvACT’s sky coverage was also increased in order to use its data for lower angular scale science [136]. In good weather, ACT observes almost 24 hours per day and is operated and monitored by a team of remote observing coordinators² who take 24 hour shifts monitoring the telescope, running observation schedules, and interfacing with the local site crew, Team Toco. As discussed in the previous chapter, many cosmology and astrophysics science results based on ACT data are being published. As the data is being used for broader applications and increasingly precise measurements, an understanding of the telescope systematics becomes increasingly important. In this chapter we focus on one type of systematic: contaminating optical spillover. As ACT’s survey areas expand, wide scans become more susceptible to passing near bright sources such as the sun, moon, or galaxy. An understand-

²The author is a member of ACT’s remote observing coordinator team

ing of how the receiver responds to rays that are not part of the primary optical path (stray light) can inform mapping efficiencies and survey strategies. Further, the empirical knowledge of ACT’s receiver design and stray light response is also valuable for aiding the design of future instruments.

2.2 Telescope Beam and Spillover Systematics

Stray light that enters the receiver and causes extra loading on the detectors has a strong impact on the overall sensitivity of a CMB instrument. Understanding the receiver beam can therefore lead to an improved understanding of instrument systematics. ACT uses optical photogrammetry measurements to regularly characterize the location of each of the mirror panels with respect to the receiver. These measurements have been used to construct ray trace and physical optics models of the telescope [59].

Figure 2.2 shows a Zemax ray trace model of ACT’s mirrors to three fields on the sky (green, red, and blue). This model operates in the time reverse sense, launching rays from the telescope focal plane (right in front of the receiver) at angles according to a prescription based on measurements of the receiver beam. In the left panel, the majority of the rays can be seen to be sent properly to the secondary, primary, and sky. However, there are two stray rays (green and blue) that are not directed properly to the fields on the sky. The right panel shows a cross section view of the telescope in which the three fields are launched from the Gregorian focal plane and then sent through the telescope (the green field has been cut out of view by the cross section). The stray rays depend on the receiver beam model that is used.

The receiver beam is a function of the optics inside the cryostat. All three arrays in AdvACT have their own set of cold optics, but each has the same general design. At 100 mK, the detector antennas are coupled to feedhorns which launch beams out of the receiver. The beams are truncated by a cold Lyot stop which is painted black to intentionally have rays outside the main beam terminate on a cold surface, minimizing detector loading. The truncated beam then continues through the reimaging optics and filter stacks until it reaches the window and is sent to the secondary. However, the Lyot stop absorption is never perfect and some rays will scatter off it, bounce around in the optics tube, and then escape through the cryostat window at wide angles. Effects like this, combined with diffraction mean that the receiver beam will have sensitivity to power at angles wider than the secondary mirror. A simple model for AdvACT’s receiver beam profile is a Gaussian directed towards the secondary mirror which is truncated at the edge of

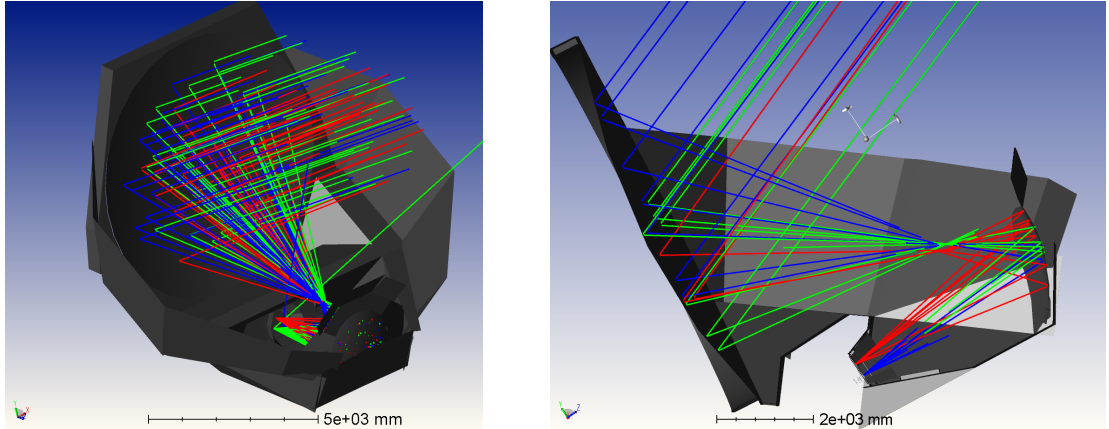


Figure 2.2: A 3D model of ACT in Zemax, showing ray traces of three fields (green, red, and blue), corresponding to the center of the three optics tubes in AdvACT. 30 rays per field are shown. The rays are launched probabilistically based on a prescription for the receiver beam profile. Two rays (green and blue) in the left panel can be seen to miss the secondary mirror, contributing to a sidelobe in the telescope’s overall beam pattern. Figure from [59].

the secondary by a few orders of magnitude to an exponential fall-off:

$$B(\theta) = \begin{cases} A_G \exp\left(\frac{-(\theta - c_G)^2}{\sigma_G^2}\right) & \text{for } \theta < 11.3^\circ \\ A_E \exp\left(\frac{-|\theta - c_E|}{\sigma_E}\right) & \text{for } \theta > 11.3^\circ, \end{cases} \quad (2.1)$$

where c_G , σ_G , c_E , and σ_E define the centers and widths of the Gaussian and exponential beam respectively, A_E/A_G represents the relative amplitude of the exponential to the Gaussian, and 11.3° is the Lyot stop truncation angle (defined by the diameter of the stop) used in ACT.

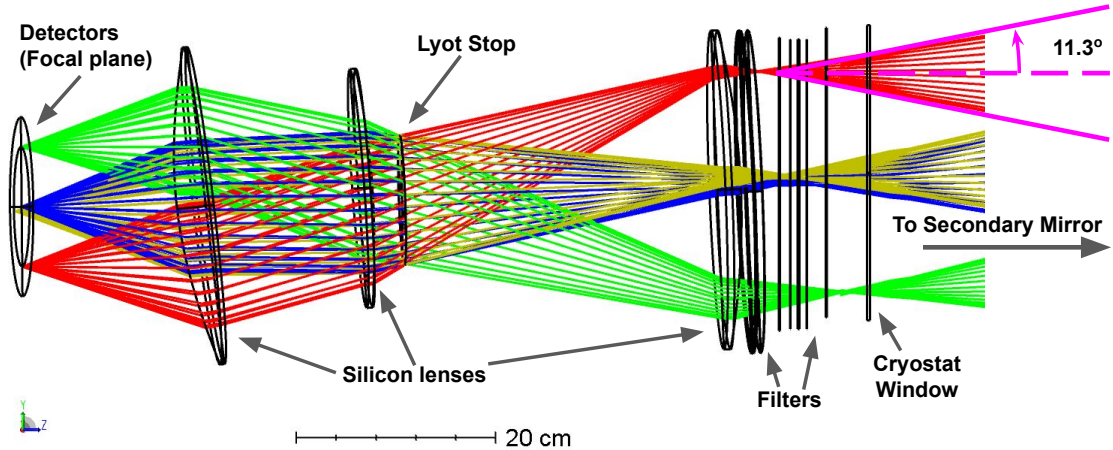


Figure 2.3: Ray trace of AdvACT optics tube. Four fields (blue, yellow, green, red) from the focal plane (left) are imaged in the time reverse sense (left to right) through two lenses, a Lyot stop, a third lens, a filter stack, and then finally the cryostat window. The Lyot stop diameter controls the divergence angle of the outgoing beam, which is 11.3° in the AdvACT case. Ray trace courtesy of Dr. Patricio Gallardo.

Figure 2.3 shows a ray trace of an AdvACT optics tube for four fields (Blue, yellow, green and red) on the focal plane (left). The exiting beam has a half-angle of 11.3° and goes to the telescope's secondary mirror. The rays shown indicate the extent of the Gaussian beam, which is constrained by the radius of the Lyot stop. Outside the Gaussian beam, the rays are either clipped by the Lyot stop or are scattered around the optics tube via reflections off the sidewalls (not shown).

To study how stray light impacts telescope sensitivity, we are interested in the exponential part of the beam. In particular, A_E and σ_E which characterize the amplitude and fall-off of the portion of the beam which does not go to the secondary. The fraction of the beam power which does not go to the secondary is called the spillover fraction. The spillover can either go to the sky (directly or via reflections around the telescope structure) or it can be absorbed by the warm telescope structure. The optical load from the telescope structure or sources in the sky can then produce a time-varying thermal load on the bolometers, increasing the photon noise of the detectors and impacting the overall sensitivity of the telescope.

The sensitivity of the telescope can be quantified as the noise equivalent temperature of the detector arrays,

$$\text{NET}_{\text{arr}} \propto \frac{\text{NET}_{\text{det}}}{\sqrt{N_{\text{det}}}} \propto \frac{\sqrt{\text{NEP}_{\text{ph}}^2 + \text{NEP}_g^2 + \text{NEP}_{\text{read}}^2}}{\sqrt{N_{\text{det}}}} \quad (2.2)$$

which is proportional to the quadrature sum of the photon noise, the bolometer thermal carrier noise, and the readout noise. Note that there can be other contributions to the detector noise, but the thermal carrier noise, NEP_g , is typically the largest. A common metric for performance of an instrument is the mapping speed $MS = 1/\text{NET}_{\text{arr}}^2$ which scales linearly with the number of detectors. It has been shown that the mapping speed of an ACT-like CMB telescope is a very steep function of the spillover fraction, falling by as much as 25% for a one percent spillover [74].

This steep fall-off in mapping speed motivates careful characterization of the receiver beam. An ideal, diffraction based model of ACT's cold optics suggest that the spillover fraction should be significantly less than 1% (we will discuss this model more in Section 2.3.4). However, as mentioned previously, in practice, internal reflection on the Lyot stop and scattering from cold surfaces will

increase the spillover fraction. A measurement of the receiver beam map will inform the spillover fraction and could help optimize baffling around the telescope structure and observing strategies. Measurements along these lines were performed on MBAC and noted a larger-than-expected response to far-angle rays [58]. The MBAC measurements resulted in increased baffling around the secondary mirror which reduced the average detector optical load by sending spillover to the sky rather than to the telescope structure. In the next section, we will discuss receiver beam map measurements of AdvACT’s MF2 array.

2.3 AdvACT Receiver Beam Mapping

The author traveled to ACT three times between May 2017 and June 2018 to gather and improve beam mapping data. These measurements are difficult to perform because it is easy to contaminate the spillover with spurious signals from human beings or the apparatus used for beam mapping. The measurements are further complicated on days with high precipitable water vapor (PWV), during the inevitable yet random power outages, and when travel plans must be postponed for global pandemics. Nevertheless, during each trip, the measurements improved and the measurement technique matured³.

In this section, we discuss two methods that the author used to measure the receiver beam of AdvACT’s MF2 array. We describe the data collection procedures, analysis routines, and results of both measurement methods. We then take the results from the preferred method and compare it to physical optics and ray

³Acquiring these data was a team effort. The author thanks Brian Koopman, Pato Gallardo, Mike Niemack, Felipe Carrero, Max Fankhanel, Gerrit Farren, and Bruce Partridge for assisting with the design and implementation of these measurements.

trace simulations of ideal and realistic receiver models. We then discuss a third method which was explored to validate the other methods.

2.3.1 Measurements Methods

The two measurement methods used will be referred to as the Eccosorb-Stick and Eccosorb-Robot methods.

Eccosorb-Stick Method

The first method that we attempted was to wave a $3'' \times 3''$ square of Eccosorb⁴ HR-25 in front of the MF2 window. Figure 2.4 illustrates the measurement method. The Eccosorb was mounted on the end a ~ 1.5 m long aluminum rod which was partially painted black. Accurate positioning of the Eccosorb was achieved by using a semicircular (~ 1.25 m in radius) hexcell arch mounted horizontally in front of the MF2 window. The arch was centered and leveled on MF2's central axis. Angular intervals every five degrees from the central axis were marked on the arch, providing an angular ruler from -60° to $+60^\circ$.

During measurements, the author stood as far as possible away from the receiver. A companion sat in the receiver cabin (pictured as the black opening on the floor of the telescope in Figure 2.4) and operated the data acquisition. 80 seconds of data were recorded for every 5° increment between -60° and $+60^\circ$. During each acquisition, the companion in the receiver cabin ran a timer and yelled “go!” every 4 seconds. Upon each “go!”, the author would move the Eccosorb square to the specific angle marker on the arch and then quickly remove it, away from the

⁴<https://www.laird.com/products/microwave-absorbers/microwave-absorbing-foams>



Figure 2.4: Photograph of the author performing Eccosorb-Stick beam mapping measurements of AdvACT’s MF2 array (the top receiver window). The author stands far to the side of the beam, against the bulkhead wall and moved the Eccosorb HR-25 block into and out of the the beam. A hexcell arch with every 5° marked from -60° to $+60^\circ$ is used as a ruler/guide for Eccosorb placement. The arch is centered and leveled with the MF2 optical axis. Note the hexcell receiver baffle installed around the windows to prevent warm spillover at wide angles.

beam. The author kept the Eccosorb against the white wall where he was leaning in order to remove it from view of the wide-angle beam.

An 80 second acquisition was recorded for all angles on the arch. In general, we went $\theta = 0^\circ \rightarrow 60^\circ$ and then $\theta = 0^\circ \rightarrow -60^\circ$ in 5° increments. Between each dataset/angle, a bias step was run on the MF2 array, collecting time constant calibration date. IV-curve measurements⁵ were taken three times throughout the entire sweep: before the first acquisition at 0° , before the second acquisition at

0° , and after the final acquisition at -60° . The IV curves provide calibration data and set the detector bias powers for the current optical loading conditions. In total, to sweep across all angles, approximately 34 minutes of data were taken and over 500 “go!”s were yelled. In practice, with the addition of the calibration data time, it took well over an hour for a complete set of measurements.

Multiple complete sets of data were taken during each of the author’s trips to Chile. Some data were taken with the receiver baffle (see hexcell baffle surrounding cryostat windows in Figure 2.4) installed, but many sets were taken without the baffle in order to test the beam at high angles. Additionally, the hex cell arch could be tilted vertically with respect to MF2’s central optical axis. Full horizontal sweep datasets were measured for vertical angles of -5° , 0° , and $+5^\circ$ with the Eccosorb-Stick method.

Eccosorb-Robot Method

The second beam mapping method was designed to eliminate potential sources of beam contamination (for example: the moving human in the telescope structure) and to enable simpler data analysis methods. The Eccosorb-Robot method utilized the same hexcell arch used for the Eccosorb-Stick method. A dual-axis stepper motor was used to spin a pair of Eccosorb AN-72 paddles such that the camera saw a time-varying cross section of the Eccosorb. The stepper motor was shielded inside a metal box and behind the arch to mitigate potential RF interference during data acquisition. Neglecting any angle-of-incidence dependence of the AN-72’s reflectivity, the thermal cross-section of the paddles as seen by the detectors should vary like $P(t) \propto |\cos(\omega t)|$.

⁵IV-curves will be described in detail in Chapter 4.



Figure 2.5: Photographs of the Eccosorb-Robot method. Two Eccosorb AN-72 paddles were rotated by a stepper motor at each of the 5° increments on the same hexcell arch used in the Eccosorb-Stick method. The upper panel shows the arch and robot directly in front of the MF2 window. The bottom left panel shows the robot mounted at -55° from MF2's central optical axis. The lower right panel shows the view of the arch, robot, and secondary mirror from the perspective of MF2. The 3" square paddles horizontally span $\sim 3^\circ$ of the receiver beam.

At every 5° angle on the arch, a 180 second acquisition was acquired on MF2 with the double-sided paddles spinning at 0.8 Hz (200 steps per full rotation). We expect the detectors to see a 1.6 Hz signal, corresponding to both sides of

the Eccosorb paddles. The positions on the arch were swept over in the same manner as the Eccosorb-Stick method. Bias step and IV-curve data were acquired in between the acquisitions in the same manner as well.

The robot measurements were first attempted in January 2018, but due to poor weather and high PWV, very few detectors were responsive. In addition, during the first iteration of these measurements, the sheets of AN-72 were taped to 3D-printed PLA paddles which mounted to the stepper motor. Due to poor thermal management of the stepper motor at the high altitude site, the PLA paddles began to soften and warp during the measurements. When the author returned again in May 2018, the weather was much more cooperative and aluminum paddles were successfully used in place of the PLA, producing a much higher quality dataset.

2.3.2 Analysis Methods

In this subsection, we describe the two analysis routines that were developed for both data acquisition methods. For both methods, we restrict ourselves to using detectors with antennas within 10 cm of the center of the array. Figure 2.6 illustrates the relative location of the antennas used for these analysis. Each dot corresponds to one antenna which is coupled to four detectors (two for each polarization and two for each frequency – 90 and 150 GHz). Detectors connected to the blue antennas are unused in this analysis. We do this so that we are only measuring beams which are near the center of the cryostat window. The window is roughly at an image of the focal plane and so detectors at larger radii on the array have beams at larger radii on the cryostat window, and their beams will be off-centered from the arch. Additional detectors were cut if they were unresponsive or if they were ramping.

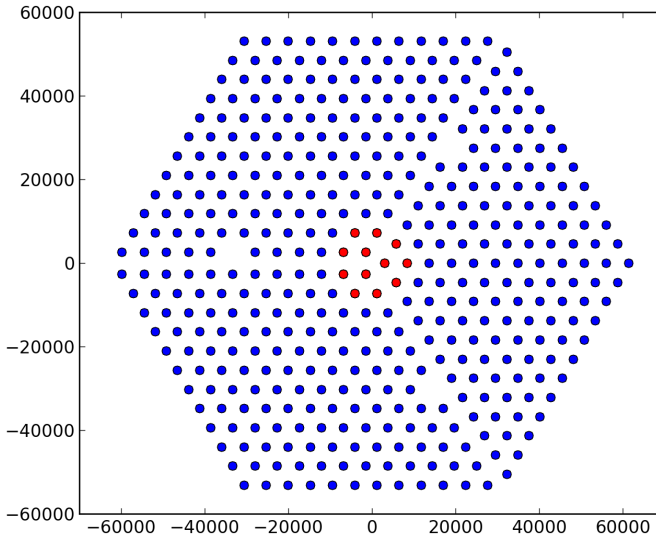


Figure 2.6: Map of AdvACT’s MF2 detector array in units of microns. Each dot corresponds to one antenna, with four detectors (two polarizations, two frequencies). Only detectors within 10 mm of the array center (highlighted in red) were used for the analysis.

Eccosorb-Stick analysis

Each time-ordered data (TOD) from the Eccosorb-Stick method consisted of common mode (atmospheric drift) with interruptions every 4 seconds when the Eccosorb was moved into the beam. The detector response to the Eccosorb loading is a dip in the TOD when plotted in DAC units. Each 80 second TOD was split into 20 chunks for each four second interval. Figure 2.7 shows TODs for a single detector at multiple Eccosorb angles on the arch. As the Eccosorb is moved to larger angles, the detector’s response is diminished and the common mode becomes dominant. For each 4 second chunk, the mean detector response to the common mode was estimated as the mean of the first and last data point in the chunk. The detector’s response to the Eccosorb was then taken as the maximum deviation from the estimated common mode during the 4 second chunk. The maximum deviation

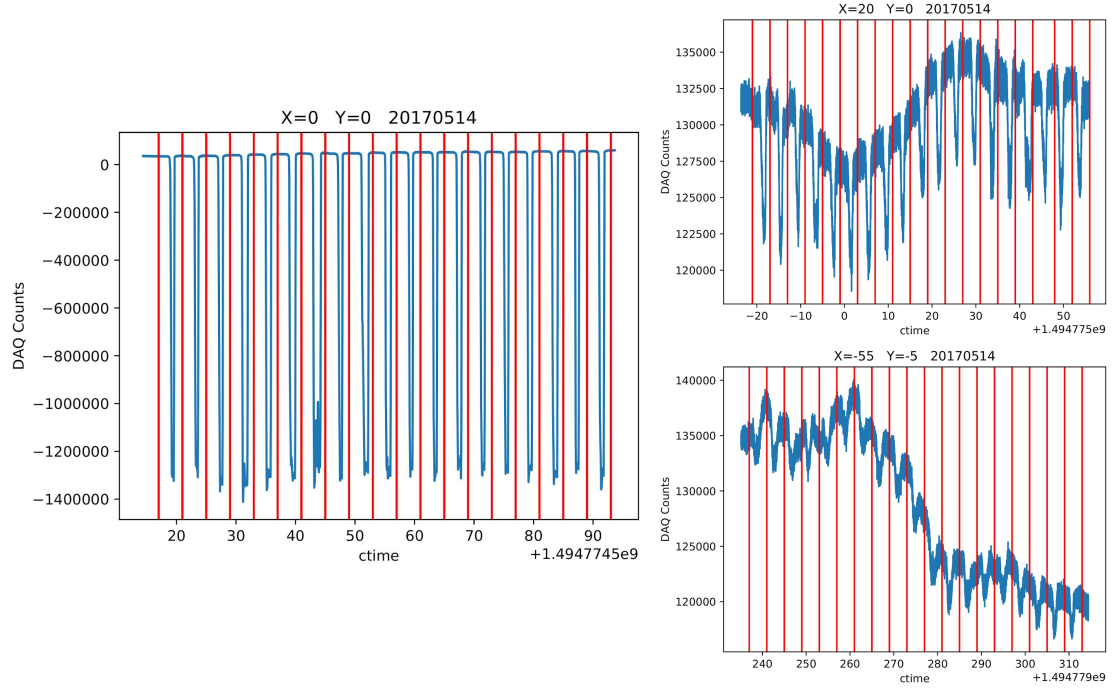


Figure 2.7: Example time streams for one detector during the Eccosorb-Stick measurements. The left panel shows the detector response when the paddle was placed at $\theta = 0^\circ$. The upper and lower right panels correspond to $\theta = 20^\circ$ and $\theta = 55^\circ$ respectively. Red lines indicate four second intervals in the 80 second time stream. The dips in the time stream correspond to loading from the Eccosorb. They are dips rather than spikes because these data have not been converted to units of power. The dips are smaller compared to the common mode for larger angles from the boresight.

is calculated for each chunk and each detector.

We average the maximum-deviation over each chunk and each detector to determine the beam's sensitivity at a given angle. The standard deviation between detectors is taken as the statistical uncertainty. This method becomes limited at large angles when the signal-to-noise ratio of the Eccosorb motion is order unity.

Eccosorb-Robot analysis

Each TOD from the Eccosorb-Robot method consisted of common mode drift modulated by the rotating Eccosorb paddle. Rather than doing the data analysis in the time domain, we instead search for the 1.6 Hz signal in the frequency domain. Figure 2.8 show example TODs (left) and fast Fourier transforms (FFTs, right) for 150 GHz detectors with 10 mm of the array center. Each row in the figure corresponds to a different angle where where the robot was installed: $\theta = 0^\circ$ (upper row), 20° (middle row), and 55° (bottom row). We only show the first 8 seconds of each time stream to make the 1.6 Hz modulate signal as visible for the reader. A band between 1.55 and 1.65 Hz is highlighted in the FFTs. Harmonics at 3.2 and 4.8 Hz are visible. In the $\theta = 0^\circ$ FFT, there is also signal at 0.8 Hz and its harmonics, suggesting that the two sides of the Eccosorb paddles produced slightly different loadings.

To extract the relative receiver beam response at each angle, we compared the power in the 1.6 Hz tone at each angle. The power in the 1.6 Hz tone was computed at each angle, by integrating the power spectral density (PSD) from 1.55 to 1.65 Hz for each detector. The relative beam response at a particular angle is then taken to be the PSD integral averaged over all of the sampled detectors. The uncertainty on this method is estimated as the standard deviation of the integral over the sampled detectors. The 90 and 150 GHz detectors and beams were treated separately.

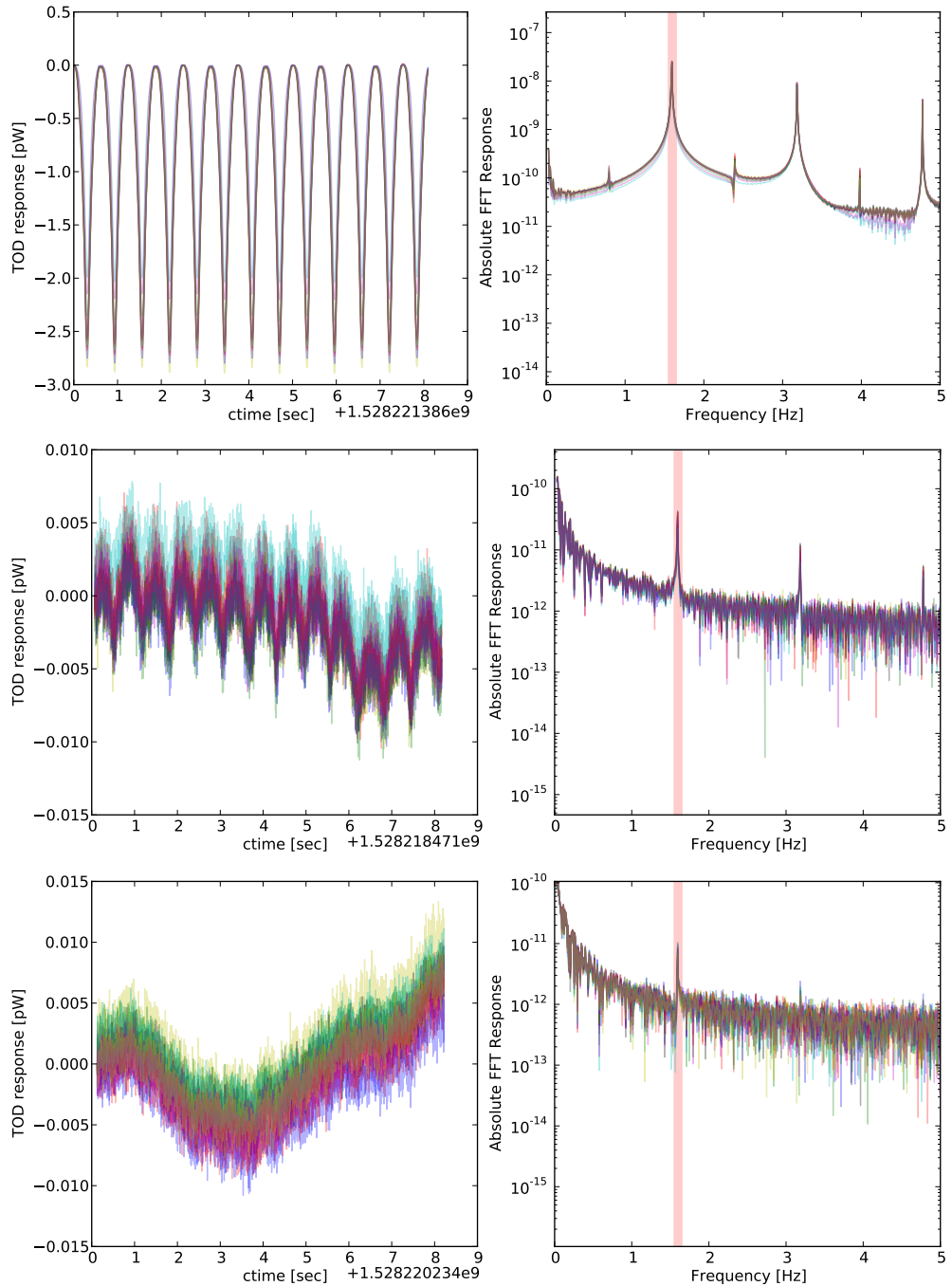


Figure 2.8: Example Eccosorb-Robot TODs (left column) and their FFTs (right column) of 150 GHz TESs for $\theta = 0^\circ$ (upper row), 20° (middle row), and 55° (bottom row). Only the first 8 seconds of each time stream is shown in order to see the modulated signal. A pink band is drawn on the FFTs between 1.55 and 1.65 Hz.

2.3.3 Results

Eccosorb-Stick Results

Figure 2.9 shows the 90 (left) and 150 GHz (right) beam maps of MF2 that was measured using the Eccosorb-Stick method. The x-axis represents the horizontal angle on the hexcell arch where the Eccosorb was placed. The y-axis represents the mean absolute value of the maximum-deviation of the between the Eccosorb and the common mode, averaged over all 4 second chunks and all detectors within 10 mm of the array center, in units of DAC, which are linear with power (when not saturated). The legend indicates the vertical angle of the arch with respect to MF2's central axis ($y = [-5^\circ, 0^\circ, +5^\circ]$). The legend also indicates in which datasets the hexcell receiver baffle was installed ($b = 1$) or removed ($b = 0$).

In this data, we note that the center of the beam looks roughly Gaussian and

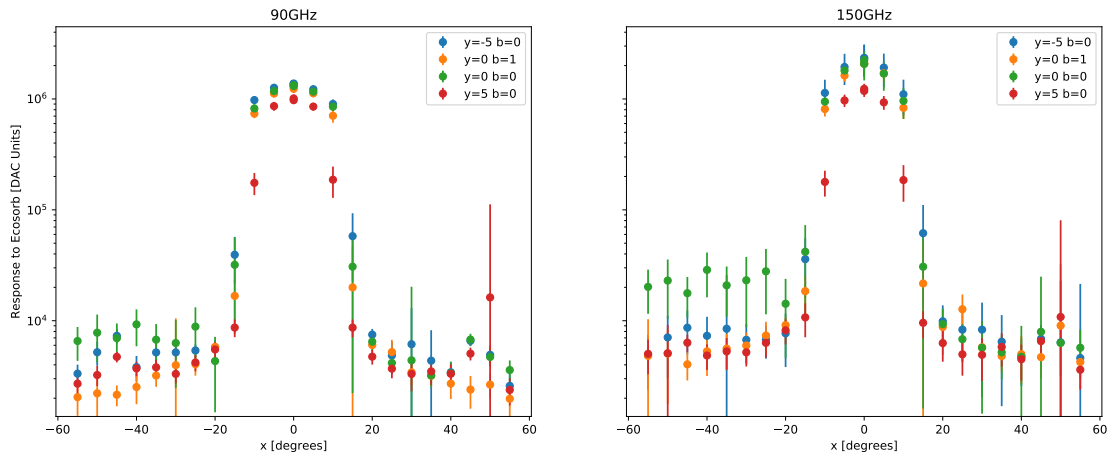


Figure 2.9: Beam map from Eccosorb-Stick method. Multiple datasets are plotted. Three different hexcell vertical angles were measured: $y = [-5^\circ, 0^\circ, +5^\circ]$. One dataset was also taken with the receiver baffle installed ($b = 1$). All datasets shown were measured in May 2017. Note that this data suggests that the sidelobe power is roughly two orders of magnitude below the main beam amplitude.

that the tails look roughly exponential, as expected. The cut-off angle around 11.3° which is determined by the diameter of the Lyot stop is also evident. Further, the exponential tails appear to be roughly two orders of magnitude lower than the main beam. We also note that in the datasets where the receiver baffle was removed (blue, green, and red), data beyond $|\theta| > 40^\circ$ appears to be elevated. We believe that this is due to spurious loading from the author who held the Eccosorb-Stick differently for these angles, and could have contributed to the detector loading. This suggests that at far angles, we do not have enough sensitivity to distinguish the Eccosorb from other thermal fluctuations during the experiment.

Figure 2.10 shows a fit of the dataset where the receiver baffle was installed. We fit the beam to the piece-wise Equation 2.1, but we exclude the data at $\theta = \pm 15^\circ$ since it appears to be sensitive to the transition. The fitted parameter values are shown in the legend. We note that the 150 GHz Gaussian beam is narrower than the 90 GHz Gaussian beam. This meets expectations since we expect the diffraction limited feedhorn beam size to scale with wavelength.

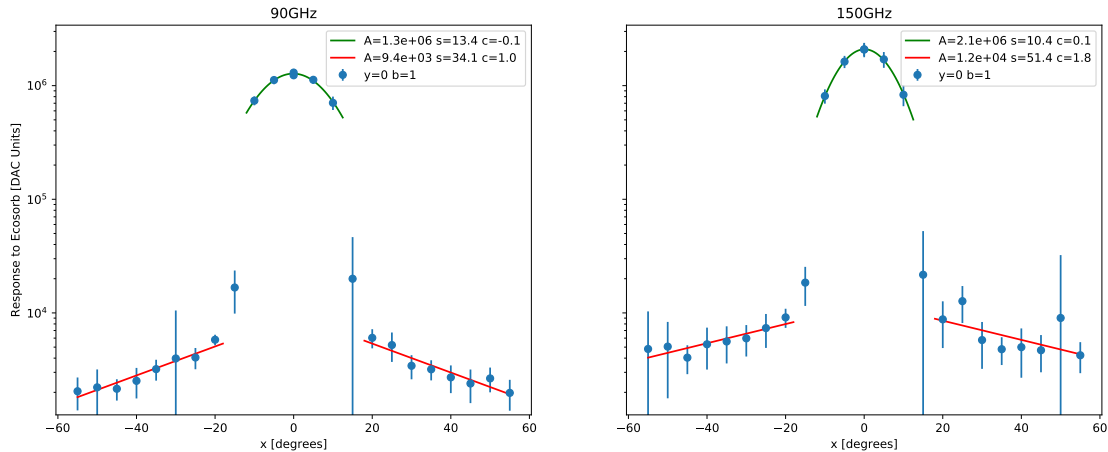


Figure 2.10: The $y = 0^\circ$, $b = 1$ dataset from Figure 2.9 is fit to the piece wise beam profile (Equation 2.1). The $x = 15^\circ$ was excluded from the fit. Fit parameters are given in the legend.

From the fitted beam function, we can estimate the spillover fraction by computing the encircled energy⁶. The encircled energy $EE(\theta)$ of our receiver beam profile $B(\theta)$ is the fraction of optical power that is contained within a circle of radius θ on a hemisphere centered on the receiver's central axis. We can compute it with

$$EE(\theta) = \frac{2\pi \int_0^\theta B(\theta') \sin(\theta') d\theta'}{2\pi \int_0^{\pi/2} B(\theta') \sin(\theta') d\theta'} \quad (2.3)$$

where we assume that the beam is azimuthally symmetric. The integral is normalized such that the total encircled energy emanating from the receiver (over the entire hemisphere centered on the receiver window) is equal to 1.

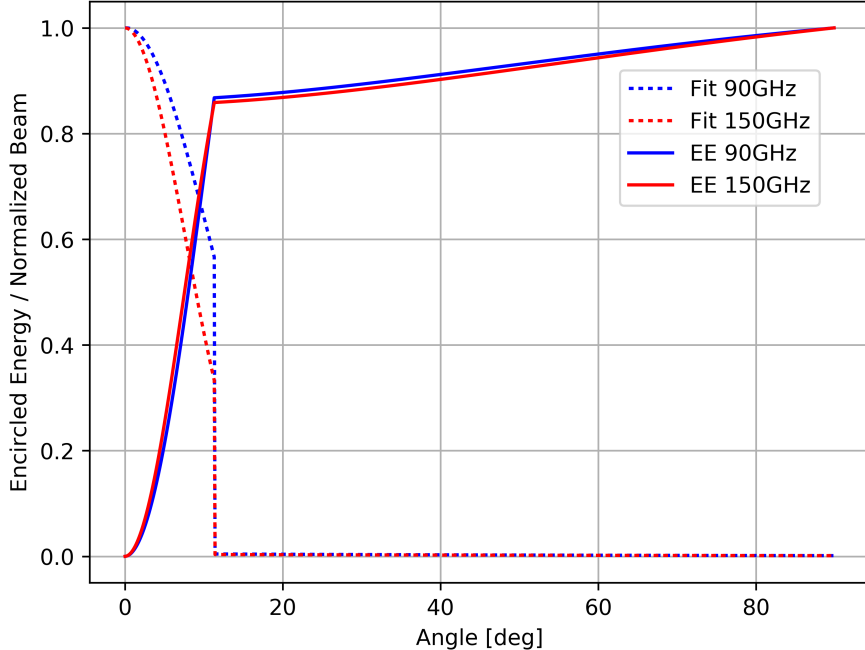


Figure 2.11: The encircled energy (solid) and normalized beam (dotted) are shown as a function of θ from the center of the optical axis. The beam shown here is an extrapolation of the fitted beam in Figure 2.10. The encircled energy at 11.3° gives the spillover fraction from this dataset to be about $\sim 13\%$.

Figure 2.11 plots the fitted piece-wise beam function (dotted) and the encircled

⁶We use the term “encircled energy” here in convention with our publications, but more specifically, we mean the “encircled optical power”

energy (solid) for both frequencies. For the beam function, we extrapolated the fits shown in Figure 2.10 up to 11.3° and down to 90° . Since $EE(\theta)$ is a function of $\sin(\theta)$, a large fraction of the encircled energy remains in the spillover ($\theta > 11.3^\circ$) even though the amplitude of the exponential tail is much lower than the Gaussian central beam. From this plot, we roughly estimate a $\sim 13\%$ spillover fraction for this data (taken in May 2017) using the Eccosorb-Stick method. This result is much higher than expected. Based on the data shown above, we hypothesize that this method does not provide enough sensitivity at high angles to distinguish between the waving Eccosorb and other thermal fluctuations near the receiver.

In 2018, the author repeated the Eccosorb-Stick measurements. The results gave similar beam maps and encircled energies, and agreed with the roughly $\sim 13\%$ spillover fraction.

Eccosorb-Robot Results

Figure 2.12 compares beam maps measured using the Eccosorb-Robot method (blue) and the Eccosorb-Stick (orange). In these plots, both beam maps are normalized such that $B(0^\circ) = 1$. The beams from both methods were fit and the fit parameters are in the figure legends. For both datasets presented, the receiver baffle was removed and the arch was leveled vertically with the optical axis of MF2 ($y = 0^\circ$).

It is clear that the amplitude of the exponential tails is much lower for the Eccosorb-Robot method. Further, the fall-off of the exponential tails is faster for the Eccosorb-Robot method. We also note that the uncertainties (blue errorbars) on the Eccosorb-Robot are not visible for almost all angles. This suggests that the each sampled detector had a nearly identical frequency response to the Eccosorb-

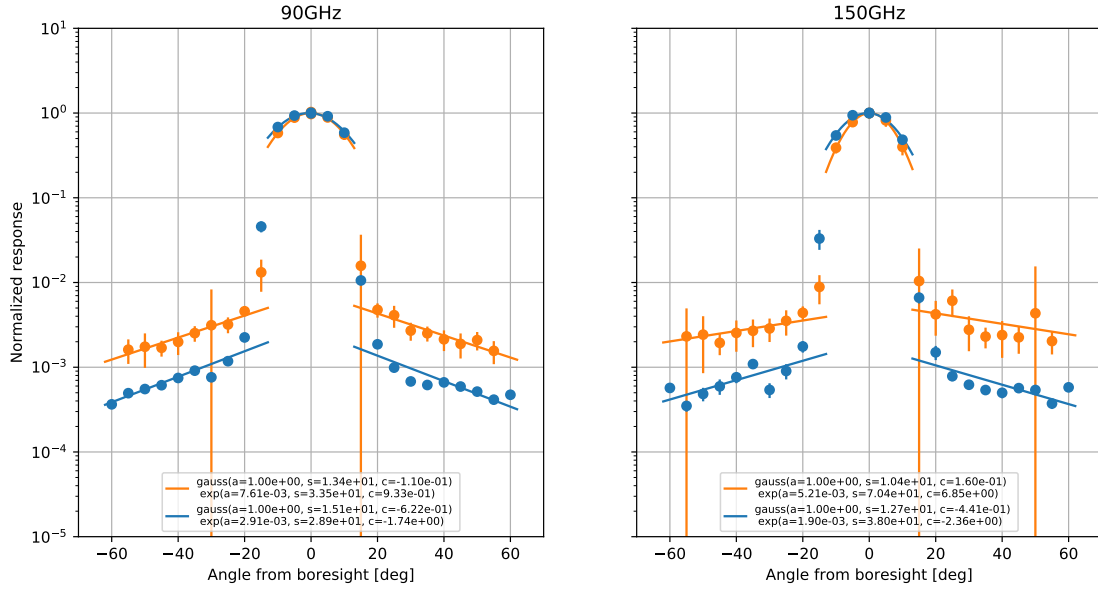


Figure 2.12: Beam map from the Eccosorb-Robot method (blue) compared to a beam map from the Eccosorb-Stick method (orange) for both 90 and 150 GHz separately. Both beams are normalized to 1 and fit parameters are given in the legend. Note that the Eccosorb-Robot method has much lower power in the exponential tail. Also note the wider Gaussian main beam which could suggest detector compression near the central angles.

Robot. We note, however, that the width of the Gaussian portion of the Eccosorb-Robot beam is significantly wider than the Eccosorb-Stick beam. One possible explanation for this is detector compression: the detector's response may be slightly non-linear for the central angles. This could occur if the optical power from the Eccosorb-Robot is of order the detector's electrical bias power. As discussed below, compression would have the affect of artificially inflating the observed power in the exponential portion of the beam.

Figure 2.13 compares the encircled energy of the Eccosorb-Robot (dotted) and Eccosorb-Stick (solid) beams. The encircled energy was calculated using the same method as described above for the Eccosorb-Stick method. The fitted beam parameters listed in Figure 2.12 were used for the beam extrapolation. From this result,

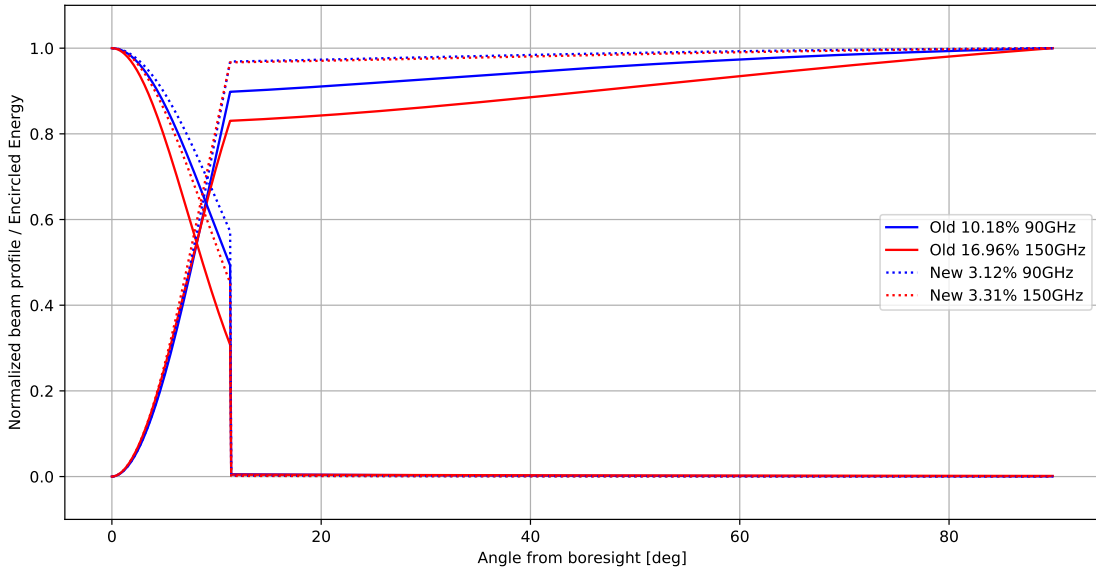


Figure 2.13: Encircled energy from the Eccosorb-Robot method (dotted) and from the Eccosorb-Stick method (solid), for 90 GHz (left) and 150 GHz (right) detectors separately. The fitted beam functions from Figure 2.12 were extrapolated for the encircled energy calculation. From this, we determine the spillover fraction for the Eccosorb-Robot data to be $\sim 3\%$, compared to $\sim 13\%$ for the Eccosorb-Stick data.

we see that the encircled energy at 11.3° gives a spillover fraction of roughly $\sim 3\%$ for the Eccosorb-Robot method, approximately five times lower than the Eccosorb-Stick method. We conclude that the spectral analysis of the Eccosorb-Robot method was able to achieve higher sensitivity at far angles than the Eccosorb-Stick robot, and that the reduction of spurious thermal sources near the receiver may have also improved the results. Table 2.1 gives the best fit parameters for the Eccosorb-Robot beam map presented in Figure 2.12.

We now investigate the possibility of detector compression in the main Gaussian beam data from the Eccosorb-Robot method. If the detector compression occurred, then we expect that the amplitude of the $P(t) \propto |\cos(\omega t)|$ signal from the Eccosorb to be artificially deflated. In our beam fitting, this would have the

Parameter	90 GHz	150 GHz
A_G	1	1
σ_G	15.1°	12.7°
c_G	-0.62°	-0.44°
A_E	$2.91\text{e-}3$	$1.90\text{e-}3$
σ_E	28.9°	38.0°
c_E	-1.74°	-2.36°
$1 - EE(11.3^\circ)$	3.12%	3.31%

Table 2.1: Best fit parameters for the Eccosorb-Robot beam map and the spillover fraction, using Equations 2.1 and 2.3.

effect of artificially inflating A_E , the relative amplitude of the exponential portion of the piece-wise beam function (Equation 2.1). This would in turn inflate the spillover fraction by placing more power in the exponential tails.

One method to look for detector compression is to compare the Eccosorb's signal amplitude to the detector bias power. We expect that if the optical power on a TES is of order the electrical bias power on the TES, then the detectors could be nearing the saturation power of the bolometer, where its response can begin to become non-linear. To examine this, Figure 2.14 (bottom left), plots the fitted signal amplitude (in pW) versus the TES bias power for each detector in an Eccosorb-Robot time stream at $\theta = 0^\circ$. The upper right histogram shows the ratio of the signal amplitude to the bias powers. We see for 90 GHz detectors, that the signal amplitude is roughly a third of the bias power, while for the 150 GHz detectors, the signal amplitude is roughly 90% of the bias powers. This suggests potential compression, especially in the 150 GHz detectors.

Another method to search for signs of compression is to look at the amplitude of the 1.6 Hz signal's harmonics. We expect the power in the harmonics to increase in the event of amplitude compression. This is because the sinusoidal response will be come more flat-topped with compression. Figure 2.15 plots the ratio of the

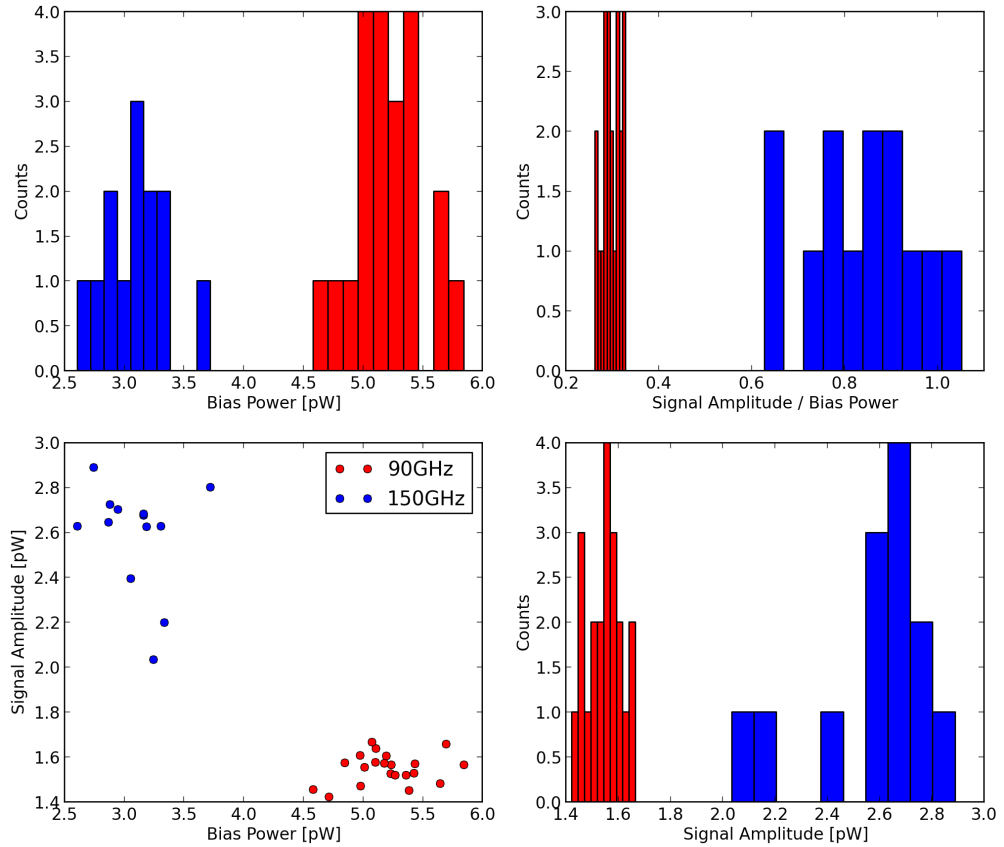


Figure 2.14: Comparison of the spinning Eccosorb signal amplitude to the TES bias power. The lower left panel shows a scatter plot for each of the detectors from a $\theta = 0^\circ$ TOD. The upper left and lower right panels show histograms of the scatter plot axes. The upper right plot shows a histogram of the ratio of signal amplitude to bias power. We see that the 90 GHz (150 GHz) detectors see an amplitude that is $\sim 30\%$ ($\sim 90\%$) of the bias power, suggesting modest compression, especially for the 150 GHz detectors.

second and third harmonics to the fundamental 1.6 Hz tone (A_2/A_1 and A_3/A_1 , respectively) for both frequencies over all angles of a Eccosorb-Robot dataset. Each point represents an average over all sampled detectors, with error bars representing the standard deviation between detectors. For the 90 GHz detectors in particular, we see the ratios of the harmonic amplitudes to the fundamental increase slightly for the center ± 10 degrees. The signal to noise ratio is worse for the 150 GHz

detectors, but a bump at $\theta = 0^\circ$ is clear. Thus, we believe that there is modest compression of the main Gaussian beam amplitude in the beam map. We therefore claim that our 3% spillover fraction amplitude is an upper limit.

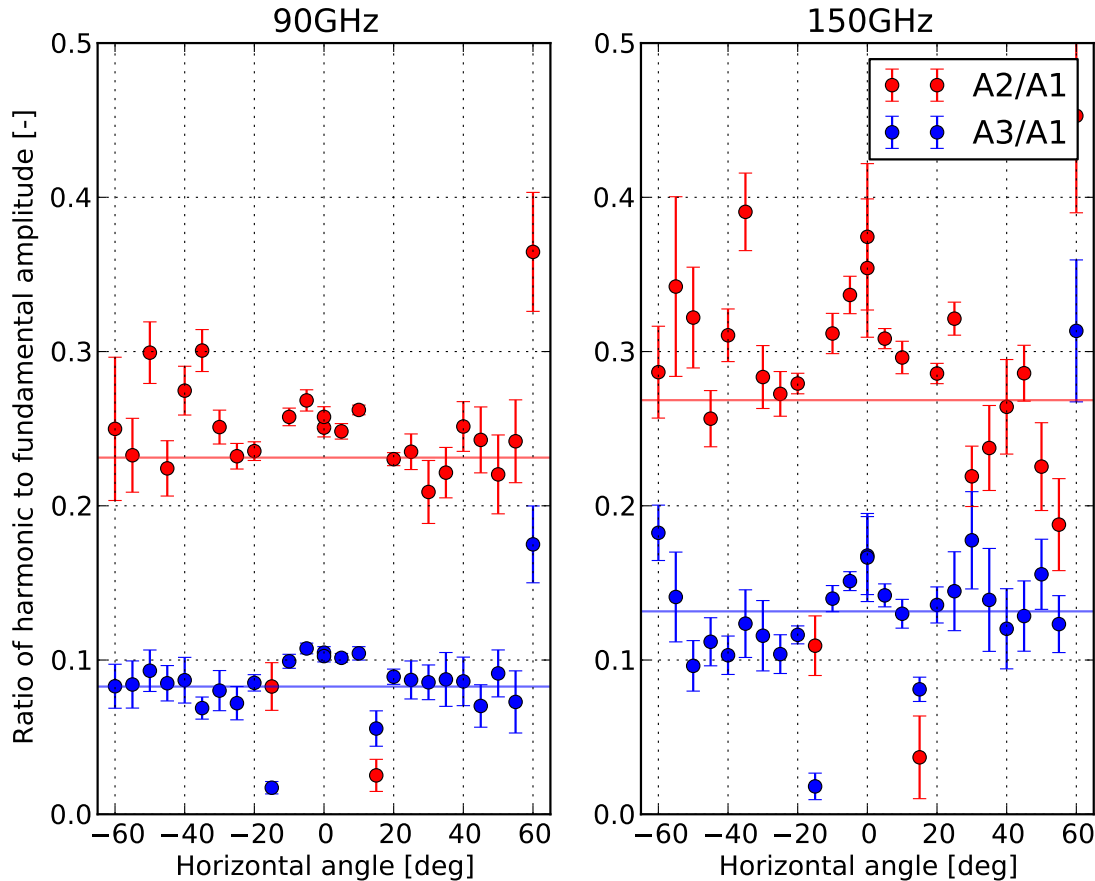


Figure 2.15: Comparison of the amplitudes of the second and third harmonic amplitudes to the amplitude of the fundamental as a function of θ . At each angle, we take the mean peak value of resonance in the FFT, averaging over all sampled detectors. The errorbars represent the standard deviation between detectors. The 90 GHz (left) and 150 GHz (right) detectors are treated separately. We plot the ratio of the second and third harmonic amplitude to that of the fundamental, $A2/A1$ (red) and $A3/A1$ (blue) respectively. The red and blue horizontal lines show the mean ratio for data where $|\theta| > 10^\circ$, illustrating that the data in the main beam ($\theta \leq 10^\circ$) is slightly higher, suggesting modest compression.

Future measurements should consider ways to minimize detector compression

such as using smaller pieces of Eccosorb, to reduce the detector loading. If a smaller piece of Eccosorb makes the signal difficult to see at wide angles, then longer time streams could be used to integrate the periodic signal to greater depth. The author planned to return to Chile in summer 2020 to perform additional measurements on the MF1, HF, and LF arrays, but these plans were canceled due to the COVID-19 pandemic. The data would still be useful, however, and will hopefully be measured and improved in the future.

2.3.4 Comparison to Models

Here, we compare our Eccosorb-Robot beam map to physical optics (diffraction) and ray trace simulations. Figure 2.16 (left) overplots the beam map (from Figure 2.12) with a physical optics simulation of an AdvACT-like optics tube with perfectly absorbing sidewalls and Lyot stop. The simulation shown here were built and run by colleague Dr. Patricio Gallardo using GRASP⁷. We note that the nearfield simulation matches the measurements fairly well. However, the diffractive simulation does not explain the wide angle response. In fact, it suggests that if the spillover was entirely from diffraction, then we would expect the nearfield amplitude of the exponential should be two orders of magnitude lower than the measurements. This is much lower than can be explained by detector compression.

Figure 2.17 (left) over plots our beam measurements (from Figure 2.12) with a ray trace simulation of an ACT optics tube. The ray trace simulation shown here was built and run by collaborator Dr. Simon Dicker at UPenn using Zemax⁸. In the ray trace model, the optics tube sidewalls were modeled as 70% absorbing and

⁷url`https://www.ticra.com/software/grasp/`

⁸`https://www.zemax.com/products/opticstudio`

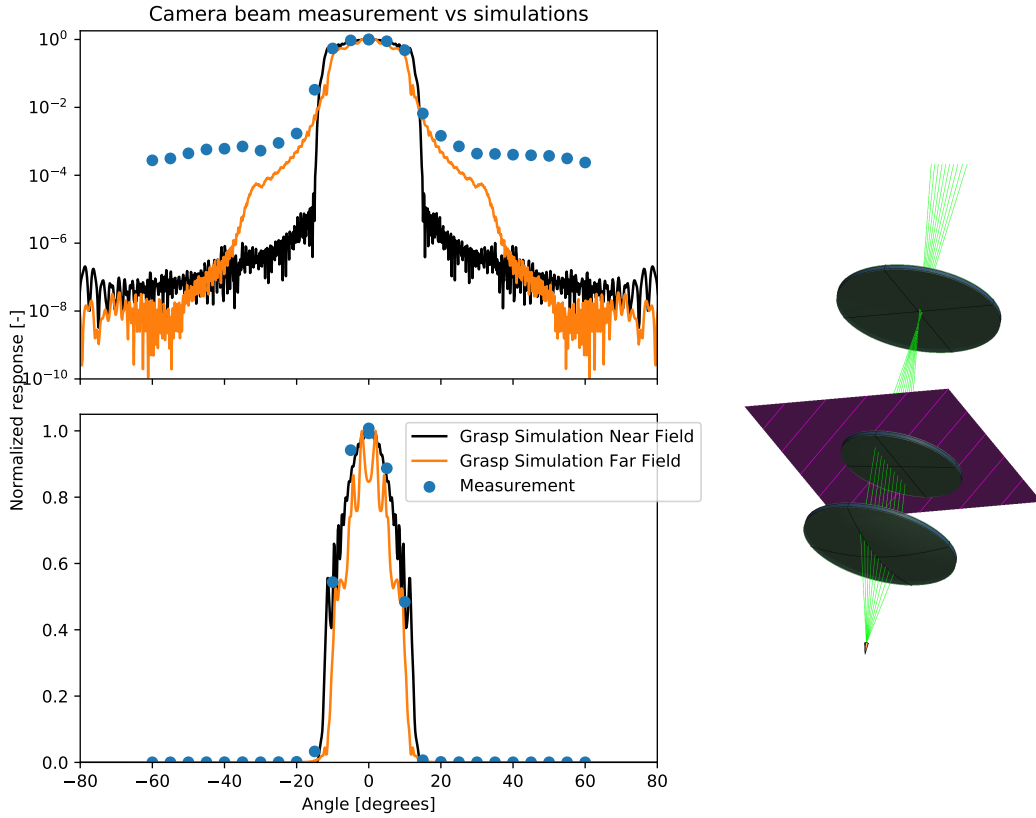


Figure 2.16: Comparison of the Eccosorb-Robot beam map (blue dots) to a physical optics simulation of an AdvACT-like optics tube with perfectly absorbing sidewall. The exponential tails in the simulated beam are due purely to diffraction. The near field Gaussian main beam agrees well with the measurements, but the diffractive spillover is two orders of magnitude lower in amplitude. A screenshot of the model is down to the right. GRASP simulation data courtesy of Dr. Patricio Gallardo.

30% scattering, the lenses were modeled with a realistic three-layer anti-reflection coating, the windows and filters were 2% reflective, and the lens/filter holders were set to 100% reflective. With this more realistic model of the optics tube, we see that the amplitude of the nearfield sidelobes are in rough agreement with the Eccosorb-Robot beam map. We note that our measured sidelobes are marginally larger than the simulation. This can be controlled by the choice of transmission/reflection/absorption parameters for the optics tube components, but could

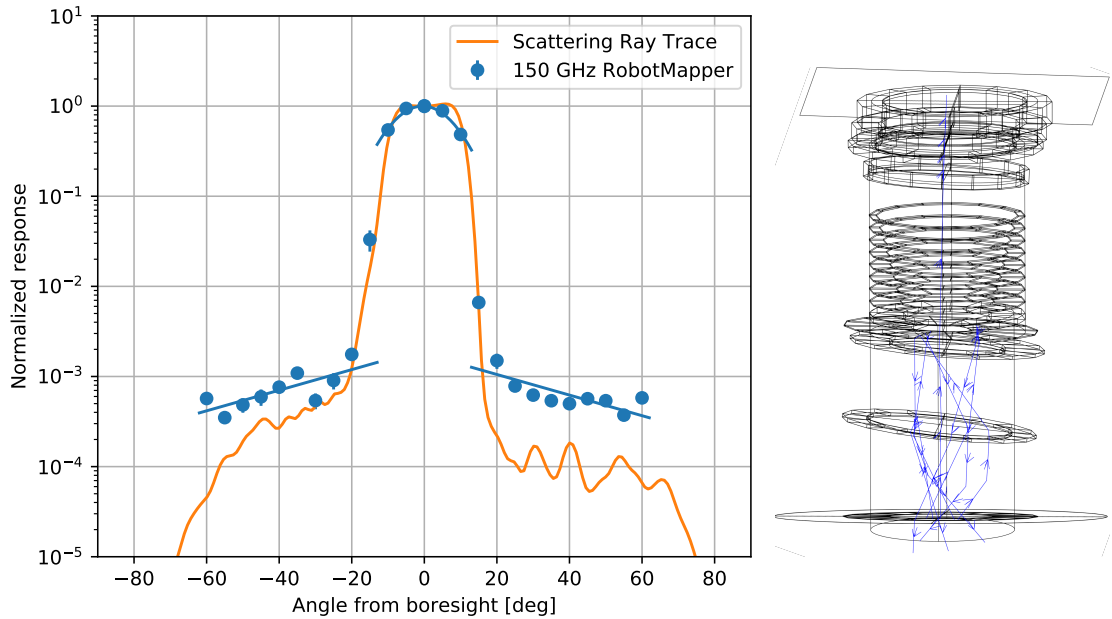


Figure 2.17: Comparison of the Eccosorb-Robot and Eccosorb-Stick beam maps to a ray trace simulation of an AdvACT-like optics tube with partially reflecting and scattering surfaces. Rays are allowed to partially scatter off the optics tube sidewalls, reflect off of lens and filter holders, and partially reflect at lens surfaces. We see that the elevated sidelobe power in the Eccosorb-Robot method could be explained by some combination of the reflective and scattering effects. Zemax ray trace simulation courtesy of Dr. Simon Dicker.

also be explained by modest detector compression. With this comparison, we conclude that higher than expected scattering/reflections on surfaces inside the optics tube can account for the few percent spillover fraction.

2.3.5 Baffle experiments

Here, we discuss a different measurement method that was explored for measuring the spillover fraction and as a cross-check for the arch-based methods. Figure 2.18 illustrates the method. Sheets of Eccosorb AN-72 were used to line the interior

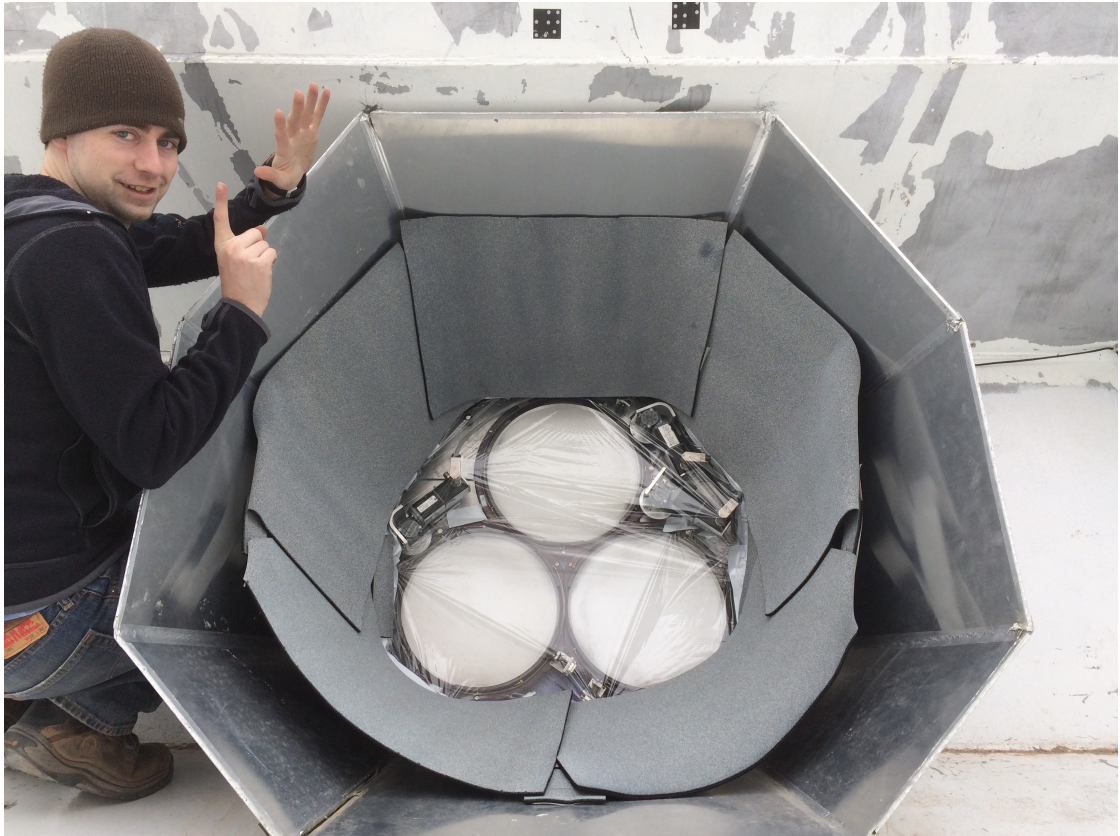


Figure 2.18: Photograph illustrating the Eccosorb baffle measurement method. A “cone” of Eccosorb was constructed inside the receiver baffle. Plastic wrap was laid on top of the windows to prevent Eccosorb dust from accumulating on the windows which could impede future observations. The configuration shown fills $\sim 55^\circ < \theta < 90^\circ$ of the beam with Eccosorb, where θ is defined from the boresight axis at the center of all three arrays. Two other configurations were used corresponding to 67° and 48° . IV-curves were taken with and without the Eccosorb baffles to estimate their optical loading. The author is shown noting the current configuration.

of the receiver baffle in a cone-like shape. Thin plastic wrap was laid over the receiver windows to protect them from accumulating Eccosorb dust. Three Eccosorb configurations were used, each with a slightly different height, filling the receiver baffle. From the center of all three arrays, the heights of the Eccosorb baffle cones correspond to $\theta = 67^\circ$, 55° , and 48° , where θ is the angle from the boresight of the camera (the same angle used on the hexcell arch). The Eccosorb baffle shown in

Figure 2.18 corresponds to the middle case, which fills the $55^\circ < \theta < 90^\circ$ beam with Eccosorb. These measurements were performed in Jan 2018 when the PWV was high⁹. IV-curves were taken with and without the Eccosorb baffles to estimate the amount of optical loading that they produced on the detectors. It is expected that the larger the Eccosorb baffle (larger solid angle), the larger the optical loading.

For each IV-curve taken, we obtain calculate the bias power which optimally places us in the middle of the TES transition. We can infer the optical loading from the Eccosorb baffle by taking the difference of the bias powers with and without the Eccosorb baffle installed. Figure 2.19 shows the differential bias power produced by each Eccosorb baffle. For illustration purposes, we show only the MF1 (upper row) and MF2 (lower row) arrays and only the 90 GHz data. Multiple datasets were taken over multiple days but we only show the data from January 22 2018. We select detectors within the center half of the two arrays, with respect to the central boresight axis of the entire three-tube cryostat. This is because we expect the beams of the outermost detectors to intercept the Eccosorb baffle more than the central beams. As expected, the mean differential bias power declines for smaller Eccosorb baffle sizes.

We now wish to compare the optical loading estimates from the Eccosorb baffle method to the encircled energy from the Eccosorb-Robot method. In the limit that the Eccosorb baffles do not drive the detectors non-linear, we expect the optical loading from the Eccosorb baffles to follow $P_{\text{EccoBaffle}} \propto 1 - EE(\theta)$. In Figure 2.20, we plot the MF2 Eccosorb-Robot 90 GHz beam (green line) and $1 - EE(\theta)$ for that beam (blue line). We also overplot the MF2 90 GHz mean differential bias powers from Figure 2.19, scaled such that the blue dot intercepts the blue line. From this

⁹The author thanks Mike Niemack, Roberto Puddu, and Felipe Carrero for helping with the design and implementation of these measurements.

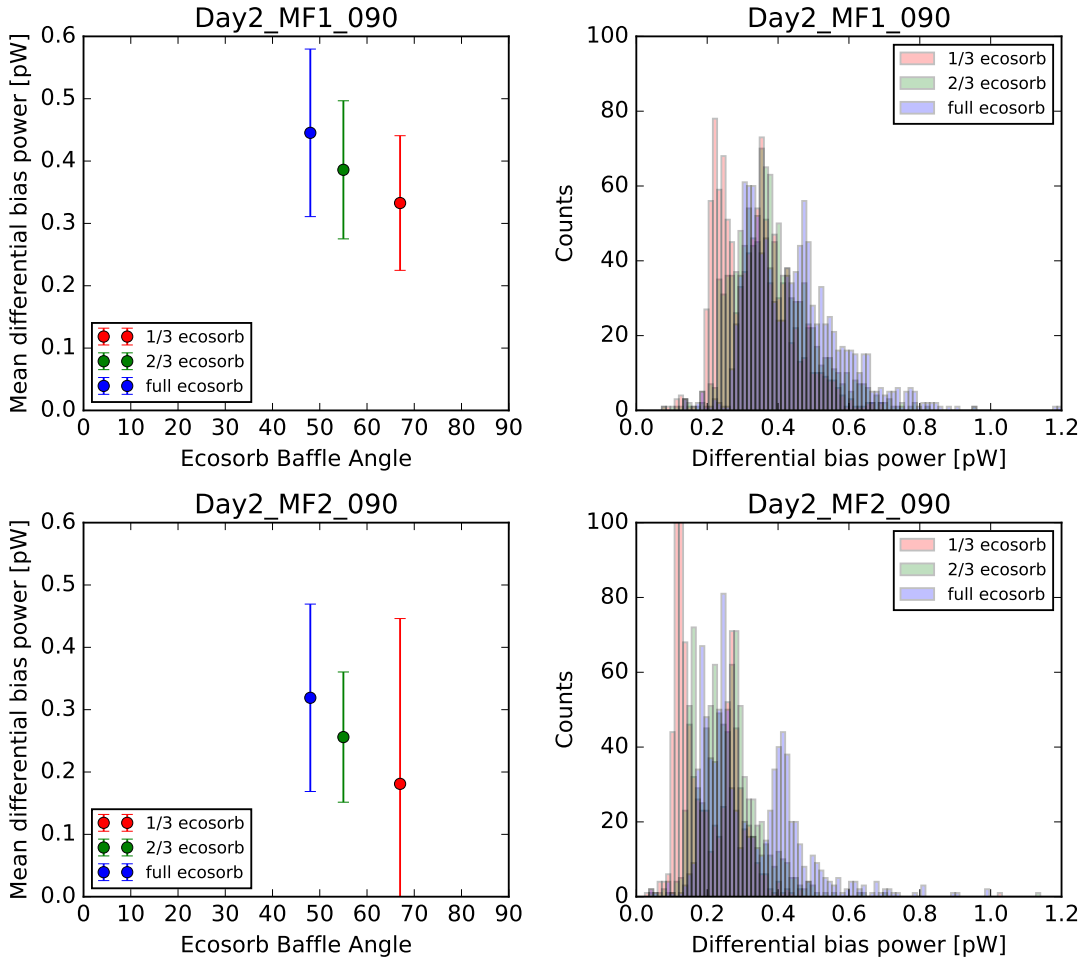


Figure 2.19: Mean differential bias power for the three different Eccosorb baffle sizes for MF1 (upper row) and MF2 (lower row). Data was taken on January 22 2018. IV-curves were taken with and without the Eccosorb baffles. We can infer the optical loading of the Eccosorb baffles by looking at the difference between the bias powers with and without the Eccosorb baffles. The bias powers were computed for the central half of detectors via IV-analysis. We exclude the outer half of detectors because we expect their beams to significantly intercept the Eccosorb.

rough scaling, we see that the Eccosorb baffle data is roughly proportional to the encircled energy from the Eccosorb-Robot method at large angles. We take this as modest confirmation that we know the slope of the encircled energy, but we do not extract any new information about the absolute level of the spillover fraction.

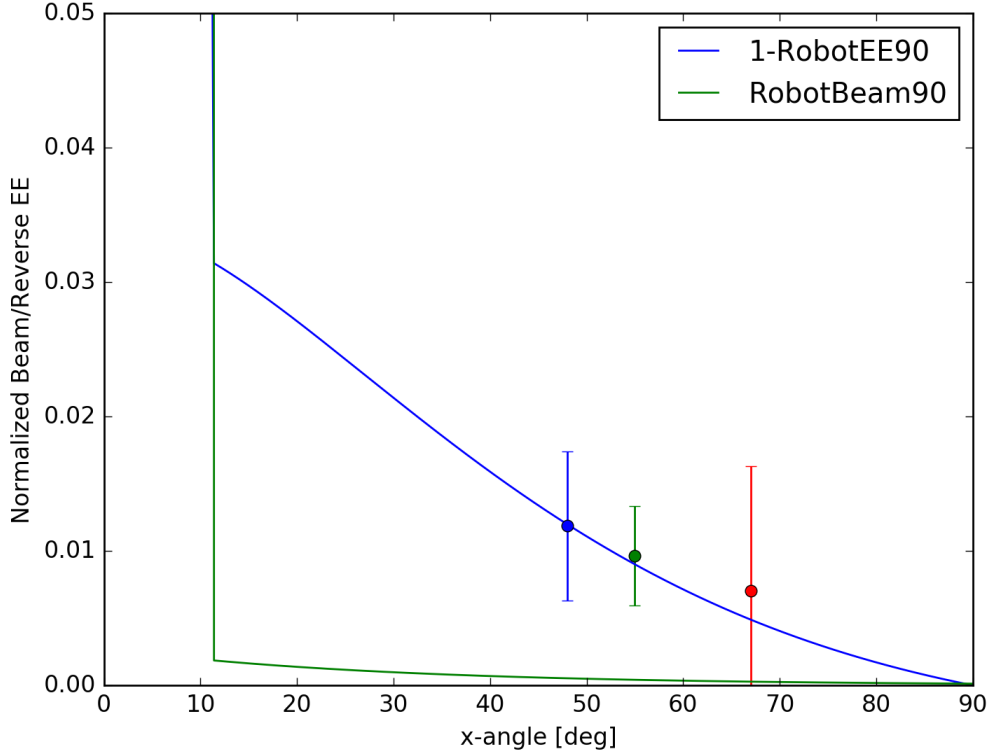


Figure 2.20: A rough comparison of the Eccosorb baffle and Eccosorb-Robot results. We plot $1 - EE(\theta)$ for the 90GHz Eccosorb-Robot beam (solid blue line) as well as the beam itself (solid green line). We overplot the MF2 90 GHz mean differential bias powers from Figure 2.19 but scale them arbitrarily such that the 48° data point intercepts the $1 - EE(\theta)$ curve. We see that the other data points roughly lie on the same line. This only suggests that we roughly know the fall-off of the encircled energy at large angles from the main beam. It does not provide information about the absolute level of spillover fraction.

2.4 Impact on Future Receiver Designs

The Eccosorb-Robot results presented above for AdvACT’s MF2 optics tube give a spillover fraction of at most 3%. We compared this result to optics tube models which showed that the excess spillover fraction can be explained scattering and reflections within the optics tube but could not be explained by a purely diffractive model of an ideal optics tube. In this section, we discuss ways in which these results

have impacted other analyses and projects.

The Eccosorb-Robot beam map has been used as a direct input for Zemax ray tracing simulations of ACT. These simulations are presented (along with the beam map) in Gallardo et al [59]. In the ray trace model (shown in Figure 2.2), the rays are launched in the time reverse sense from the camera aperture, using our beam map as a probability distribution for the ray vectors. The model assumes that the beam is azimuthally symmetric and polarization independent. The telescope’s mirrors, baffles, and warm structure are included in the model. The distribution of rays ending in the far-field on the sky gives the telescope’s overall beam pattern. Dr. Patricio Gallardo built and ran this simulation to study the baffling of the mirrors and investigate ways in which spillover could potentially create large enough sidelobes that could impact observations. He was able to correlate specific features in the sidelobe pattern to specific baffling elements around the mirrors [62]. Further, using sun and moon sidelobe maps produced by Dr. Sigurd Naess, Dr. Gallardo was able to find common sidelobe patterns between his simulation and the real maps.

Our beam map results have also been used for systematics modeling for the Simons Observatory (SO), a multi-telescope CMB observatory currently being built on the same plateau as ACT. The SO detectors and optics tubes will be very similar to those used in ACT. SO is working to improve the optics tube design but is taking our beam measurements and 3% spillover fraction as a baseline worst-case scenario input for systematics modeling. The Eccosorb-Robot beam map is used in [60] to study the warm spillover fraction, or the number of rays which are specifically trapped in the SO large aperture telescope’s (LAT) warm structure. It was found that without any receiver or mirror baffling, the number of rays which

terminate in the structure is about $\sim 1.9\%$, whereas the addition of a parabolic receiver baffle reduces it to $\sim 1\%$, and also adding baffling around the mirrors reduces it to $\sim 0.4\%$. As mentioned above, the relative mapping speed of an ACT or SO-like telescope is a steep function of the warm spillover [74]. According to BoloCalc simulations [74], a warm spillover fraction of 2% reduces the telescope mapping speed to between 50% and 80% of the ideal case (lower frequencies are worse). Thus, in this worst case scenario, adding the baffles modeled in [60] could substantially improve the relative mapping speed.

In Gudmundsson et al [66], our beam map is used to simulate the performance of different receiver baffle designs for SO’s LAT. In particular, paraboloid and conical baffles are examined. It was found that the conical baffle was more efficient at directing rays from the entire telescope focal plane to the sky. They estimate that the baffle could reduce the warm spillover by roughly half a percent which would improve the relative mapping speed by roughly 10-15%. However, the baffle would create a circularly symmetric sidelobe pattern at roughly $7^\circ - 8^\circ$ away from the main beam accounting for almost 1% of the total power on the sky.

So far, we have only discussed methods to reduce the impact of spillover by steering it away from warm structures. There has also been significant effort within SO to design the optics tubes to minimize spillover before it leaves the receiver. SO’s cold optics designs are presented in Dicker et al [42]. The SO optics tubes will utilize injection molded carbon-loaded plastic absorbing tiles with metamaterial anti-reflection coatings in order to turn scattering sidewalls into highly absorptive sidewalls [159]. These tiles will mitigate internal reflections within the optics tube module, and are likely to significantly reduce the spillover fraction.

Other collaborations that the author works with, are also making use of these

beam measurements as worst-case spillover performances. CCAT-prime plans to make use of SO’s absorbing tiles as they develop and deploy their optics tubes in Prime-Cam [149] and Mod-Cam [47]. CMB-S4 has used the beam profile to design baffling options and forecast the telescope sidelobe patterns and power.

2.5 Conclusion

In this chapter, we discussed cryogenic receiver beam measurements and spillover for AdvACT’s MF2 array. We motivated the study of the receiver beam profile and spillover by reviewing the systematic effect of warm spill on sensitivities and mapping speeds. We described two methods to measure the beam profile, and the corresponding results. We compared these results to simulations and concluded that the 3% spillover fraction that we measured is likely sourced from internal reflections on the sidewalls and structures in the optics tube. A third measurement was presented to probe the wide-angle response of the beams by using Eccosorb baffles. And finally, we discussed multiple ways in which these measurements have been used in the author’s collaborations to understand and improve the performance of current and future millimeter wave telescopes.

CHAPTER 3

FABRY-PEROT INTERFEROMETERS

Spectrometers have long been a critical tool for studying astrophysical objects by separating light from a source into its constituent wavelengths. Spectral measurements can reveal a great deal of information about the physical properties and motions of celestial objects and about intervening material between the source and observer. Many different types of spectrometers exist and are specialized for different types of measurements.

In this chapter, we focus on the development of a high-throughput, wide-bandwidth, far-IR and mm-wave Fabry-Perot interferometer (FPI) based spectrometers [22, 108, 116]. We begin Section 3.1 with an overview of the primary application of this work, LIM with CCAT-prime. Section 3.2, describes the relevant background and theory for FPIs in the far-IR and introduces new silicon substrate-based mirror designs. Section 3.3 discusses the theory, simulation, and design of metamaterial silicon anti-reflection coatings (ARCs) which are critical for silicon-based FPIs. Section 3.4 focuses on the design and modeling of full silicon-based FPIs. Section 3.5 describes the fabrication methods for the silicon ARCs and metal mesh reflectors used in silicon-based FPIs. We close the chapter in Section 3.6 with a discussion of future work and prospects for EoR-spec as well

as additional applications for these silicon-based technologies.

3.1 CCAT-prime and EoR-Spec

The CCAT-prime Collaboration¹ is building the Fred Young Sub-millimeter Telescope (FYST²) at an altitude of 5600 m on Cerro Chajnantor in the Atacama Desert in northern Chile [114]. With its high altitude and exceptionally dry site, FYST will enable some of the world’s best ground-based sub-mm observations, addressing a wide range of astrophysical questions from star and galaxy formation to CMB cosmology [131]. FYST is currently being constructed in Germany by Vertex Antennentechnik GmbH³. With a 6 m aperture crossed Dragone design [112], FYST will provide high-spatial resolution over a large 8 degree diameter field-of-view. Figure 3.1 *top left* and *center* show a rendering and ray trace of the telescope structure and optics. Modestly slowed down due to the global coronavirus pandemic, CCAT-prime plans to have first light with FYST in 2023.

Positioned at FYST’s focal plane, Prime-Cam will be one of CCAT-prime’s cryogenic receivers [149]. As shown in Figure 3.1 *top right*, Prime-Cam will contain seven cryogenic optics tube modules. The cryostat will be backed by CryoMech pulse-tube cryocoolers and a single Bluefors dilution refrigerator, providing continuous 100 mK cooling power for the detector arrays of all seven modules. The modules will be optimized for a variety of science goals [23]. The baseline plan is for five modules containing broadband polarization-sensitive microwave kinetic inductance detector (MKID) arrays at five frequencies: 220, 280, 350, 410, and 860 GHz. The remaining two modules will combine MKIDs and FPIs as imaging spec-

¹<https://www.ccatobservatory.org/index.cfm>

²Despite many CMB instruments being named after body parts or animals (BICEP, ABS, QUADE, POLARBEAR, SPIDER, MUSTANG), FYST is pronounced “feast,” not “fist.”

³<https://www.vertexant.com/>

trometers for line intensity mapping between 210 and 420 GHz. Each module will contain a series of cryogenic sub-mm and mm-wave filters and lenses, re-imaging ~ 1.3 degree diameter of the telescope's field of view onto the detector arrays. The optical design of the modules evolved from the Simons Observatory project's design [42] which uses three silicon lenses at different temperatures in the cryostat. Each spectrometer module will include a fourth lens to appropriately collimate the beam for the cryogenic FPI which will be placed at the pupil (Figure 3.1 *bottom*).

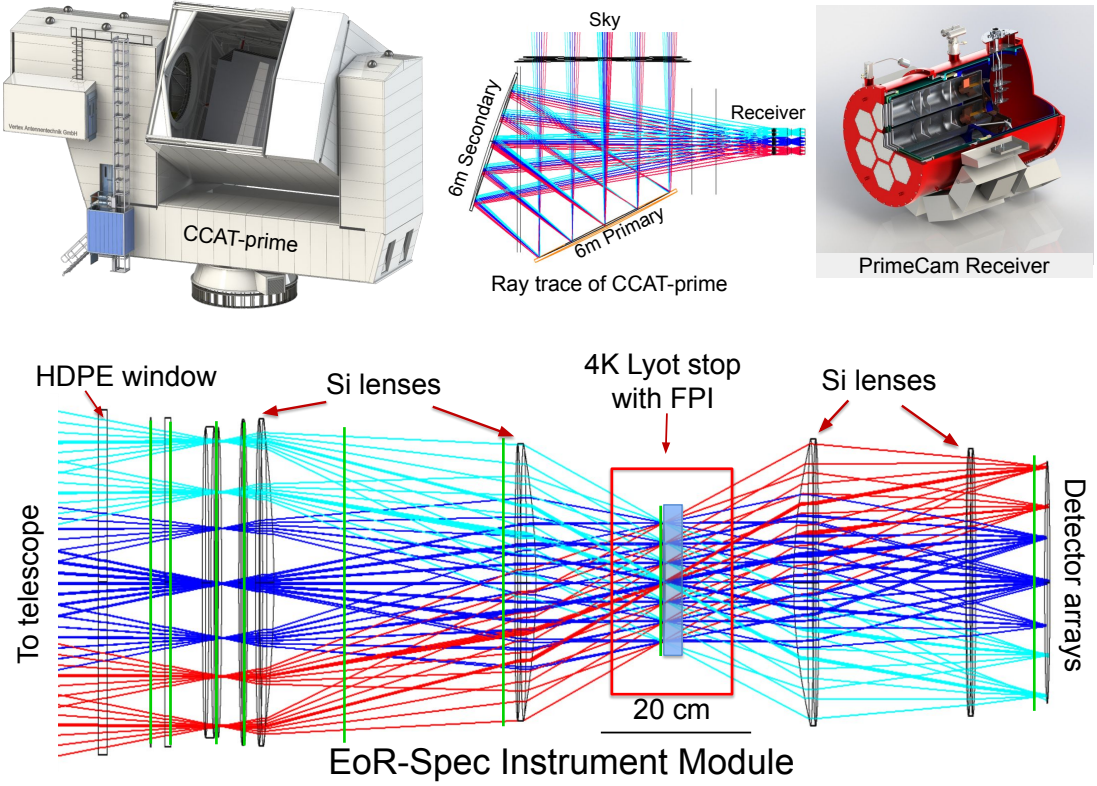


Figure 3.1: Rendering of FYST (*top left*) and Prime-Cam receiver (*top right*). Ray traces of the telescope (*top center*) and EoR-Spec instrument module (*bottom*). The instrument module uses anti-reflection coated silicon lenses to re-image the sky onto the detector arrays. A fourth lens is included to optimize the beam collimation through the FPI at the Lyot stop. The sky is then reimaged onto broadband MKID arrays.

The spectrometer modules compose CCAT-prime's *Epoch of Reionization Spectrometer* (EoR-Spec). EoR-Spec is optimized to measure the redshifted $158\ \mu\text{m}$

[CII] fine-structure line emission of early star-forming regions between $3.5 \leq z \leq 8$, corresponding to frequencies 420 – 210 GHz. The [CII] line of cooling emission from star forming regions is an exceptionally bright and efficient tracer of early structure formation and reionization [132, 133]. At lower redshifts, EoR-Spec will observe galaxies near the period of peak star formation when most stars in today’s universe were formed. At higher redshifts, EoR-Spec will trace the late stages of reionization, the early stages of galaxy assembly, and the large-scale, three-dimensional clustering of star-forming galaxies.

The scanning FPI in EoR-Spec will act as a tunable narrow bandpass filter, permitting the detector arrays to image [CII] emission in thin slices of redshifts. During observations, the telescope will be scanned across a patch of the sky with the FPI in a fixed position. After the telescope scans the patch several times, the FPI position will be stepped, shifting the resonant frequencies of the interferometer. The sky patch will then be re-scanned, imaging it at slightly different redshift. This process will be repeated, mapping the patch at many redshifts. A spatial-spectral data cube is constructed by spatially mapping the sky at each step of the FPI’s frequency range until the entire spectrum is obtained to the required depth. This observing technique is known as spectral line intensity mapping (LIM), as described above in Section 1.3.1. With the large-field of view, and a beam size well-matched to the expected EoR clustering scale, the combination of FYST and EoR-Spec will be well tuned for [CII] LIM.

The rest of this chapter focuses on the author’s contributions to the design, simulation, and fabrication of silicon substrate-based (SSB) FPIs for EoR-Spec. Section 3.2.4 discusses how the FPI will be used for EoR-Spec’s LIM observations.

3.2 FPI Background

3.2.1 Theory

A Fabry-Perot Interferometer consists of two parallel, reflective surfaces, forming an optically resonant cavity [116]. The distance and index of refraction between the reflective surfaces determines a fundamental resonant frequency of the cavity. Waves of any integer multiple of fundamental frequency will constructively interfere while all other frequencies destructively interfere. Due to this interference, only radiation of the resonant frequencies will be transmitted through the FPI. The spectral profile of an FPI can be quantified and optimized in terms multiple different parameters. In this section, we briefly review the formalism for modeling FPIs by following the derivations in Born & Wolf [19] and Yeh [161].

Figure 3.2 describes a FPI with cavity length h and cavity index n surrounded by a medium with index n' . A plane wave with freespace wavelength λ_0 is incident on the first surface at an angle θ' and is transmitted through the cavity at an angle θ . At the first surface, the plane wave is partially transmitted and partially reflected. The transmitted portion continues to be reflected and transmitted inside the cavity. The total transmitted and reflected amplitudes can be determined by summing the amplitudes of each reflected and transmitted ray. Let r_1 , t_1 , r_2 , and t_2 be the amplitude reflection and transmission coefficients for the first and second surfaces respectively⁴. Let $A_0 = Ae^{i\omega t}$ be the complex amplitude of the incident wave. The complex amplitude of the p^{th} transmitted wave is then:

$$A_{t,p} = t_1(r_2r_1)^pt_2e^{ip\delta}A_0 = t_1t_2(r_1r_2e^{i\delta})^pA_0, \quad (3.1)$$

⁴Note that for both surfaces, in the limit of no absorption, conservation of energy requires that $r_i^2 + t_i^2 = 1$. But in general, $r_i + t_i \neq 1$

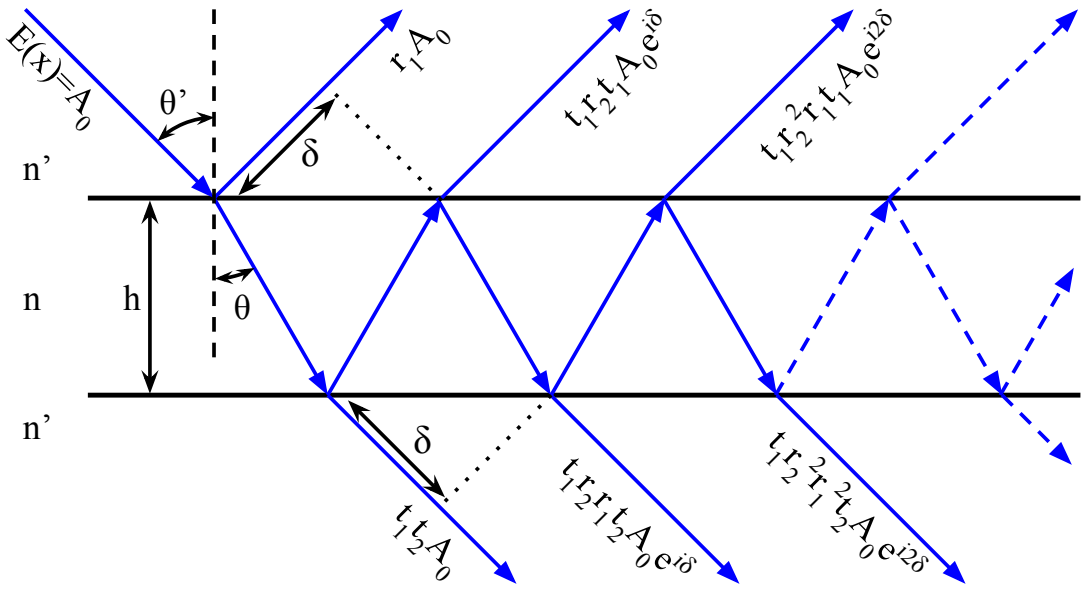


Figure 3.2: Reflection and transmission of a plane wave $E(x) = A_0$ incident on a FPI. The wave is incident at an angle θ' from a surrounding medium with refractive index n' . The wave is transmitted at an angle θ into a cavity with length h and refractive index n before it is re-transmitted into the surrounding medium. The parallel reflective plates have reflection and transmission amplitude coefficients r_1 , t_1 , r_2 , and t_2 . The amplitude of each successive ray is a function of these coefficients. The phase of each successive ray is shifted geometrically by a difference in path length δ .

where $p = 0, 1, 2, \dots$ and δ is the phase shift between each successive ray. In the limit that $p \rightarrow \infty$, then the total complex amplitude of the transmitted rays is an infinite geometric series and can be written:

$$A_t = \sum_{p=1}^{\infty} A_{t,p} = \frac{t_1 t_2}{1 - r_1 r_2 e^{i\delta}} A_0. \quad (3.2)$$

The total transmitted intensity is then

$$I_t = A_t A_t^\dagger = \frac{T_1 T_2}{(1 - \sqrt{R_1 R_2})^2 + 4\sqrt{R_1 R_2} \sin^2(\delta/2)} I_0, \quad (3.3)$$

where we have replaced the reflection and transmission amplitude coefficients with their appropriate intensity coefficients⁵: $R_i = |r_i|^2$ and $T_i = |t_i|^2$. Equation 3.3

⁵Note again that in the limit of no absorption, the reflectance and transmittance of each

is known as an Airy function [10]. The transmittance is maximal when $\delta = 2\pi m$ where m is an integer. m is known as the order of the transmission fringe.

The geometric phase shift δ is given by the optical path length difference between each transmitted ray which can be shown to be:

$$\delta = \frac{4\pi}{\lambda_0} nh \cos \theta. \quad (3.4)$$

We can rewrite this using the interference order $m = \delta/2\pi$, such that the resonant frequencies of the FPI are given as:

$$f_m = \frac{c}{\lambda_m} = \frac{mc}{2nh} \frac{1}{\cos \theta}. \quad (3.5)$$

Here, we note that the FPI resonant frequencies are linear with m . Thus, the spacing between fringes, known as the free spectral range, is a constant in frequency space: $\Delta f_{\text{FSR}} = \frac{f_m}{m} = \frac{c}{2nh} \frac{1}{\cos \theta}$. We also note that as the angle of incidence increases, the resonant wavelength becomes shorter and so tilting an FPI will blue-shift the resonant frequencies.

In addition to the geometric phase shift, there is also a reflective phase shift at the surface of both mirrors, ϕ_i , where we use the subscript i to denote which surface the reflection occurs at. The phase shift induced by metalized mirrors can be frequency dependant and can vary depending on the material and geometry of the reflective film. If the two FPI mirrors are not identical, then the phase shift that they induce will also likely not be identical. Rather than accounting for these reflective phase shifts in the Airy formula (Eq 3.3), we can instead think of them as a change in cavity length where $h \rightarrow h + \sum_i \Delta h_i$ with $\Delta h_i = \phi_i \frac{\lambda}{2\pi} \cos \theta$.

For the sake of providing a broad overview, we will make the simplifying approximation that the two reflective surfaces have the same reflectance, transmittance,

reflector must sum to unity $R_i + T_i = 1$ for conservation of energy. If we include absorptance, then $R_i + T_i + A_i = 1$.

and absorptance such that $R_1 = R_2 = \mathcal{R}$, $T_1 = T_2 = \mathcal{T}$, and $A_1 = A_2 = \mathcal{A}$. With this, we can rewrite the Airy function (Equation 3.3) as

$$I_t = \frac{\mathcal{T}^2}{(1 - \mathcal{R})^2 + 4\mathcal{R} \sin^2(\delta/2)} I_i. \quad (3.6)$$

We then substitute $\mathcal{T} = 1 - \mathcal{R} - \mathcal{A}$ and $\mathcal{F} = \frac{\pi\sqrt{\mathcal{R}}}{1-\mathcal{R}}$ such that

$$\frac{I_t}{I_i} = \left(1 - \frac{\mathcal{A}}{1 - \mathcal{R}}\right)^2 \frac{1}{1 + \frac{4}{\pi^2} \mathcal{F}^2 \sin^2(\delta/2)}, \quad (3.7)$$

where \mathcal{F} is known as the reflective finesse which we will come back to shortly. Note that the peak transmittance when $\delta = 2\pi m$ is simply

$$\left(\frac{I_t}{I_i}\right)_{\max} = \left(1 - \frac{\mathcal{A}}{1 - \mathcal{R}}\right)^2. \quad (3.8)$$

To investigate the width of the FPI fringes (transmission peaks), let us examine the full width half maximum (FWHM) of the Airy function, $\delta_{\text{FWHM}} = 2\delta_{\text{HWHM}}$ by solving for the half width half maximum (HWHM) in equation 3.7:

$$\frac{1}{1 + \frac{4}{\pi^2} \mathcal{F}^2 \sin^2(\delta_{\text{HWHM}}/2)} = \frac{1}{2}, \quad (3.9)$$

from which it follows that

$$\delta_{\text{FWHM}} = 2\delta_{\text{HWHM}} = 4 \sin^{-1}(\pi/2\mathcal{F}) \approx \frac{2\pi}{\mathcal{F}}, \quad (3.10)$$

where we have assumed that \mathcal{F} is much larger than $\pi/2$.

Thus, if we take the ratio of the distance between each peak ($\Delta\delta_m = 2\pi$) to the FWHM of the peak, we obtain the reflective finesse, \mathcal{F} :

$$\frac{2\pi}{\delta_{\text{FWHM}}} = \frac{\Delta f_{\text{FSR}}}{\Delta f_{\text{FWHM}}} = \mathcal{F} = \frac{\pi\sqrt{\mathcal{R}}}{1 - \mathcal{R}}. \quad (3.11)$$

The finesse and maximum transmittance are the primary figures of merit for a FPI since they describe the width and peak of the fringes. Now, if we multiple through by m , we get

$$m\mathcal{F} = \frac{m\Delta f_{\text{FSR}}}{\Delta f_{\text{FWHM}}} = \frac{f_m}{\Delta f_{\text{FWHM}}} = RP, \quad (3.12)$$

the spectral resolving power. For the m^{th} fringe, $RP = m\mathcal{F}$ of the m^{th} . For a grating, the RP is equivalent to the number of wavelengths in the path length difference and so by analogy, for a FPI, the finesse can be thought of as the average number of round trip path lengths made by a photon in the cavity. This approximation holds up surprisingly well, and as we will see in Section 3.4.5, it is useful for estimating the amount of power lost due to absorption in the cavity.

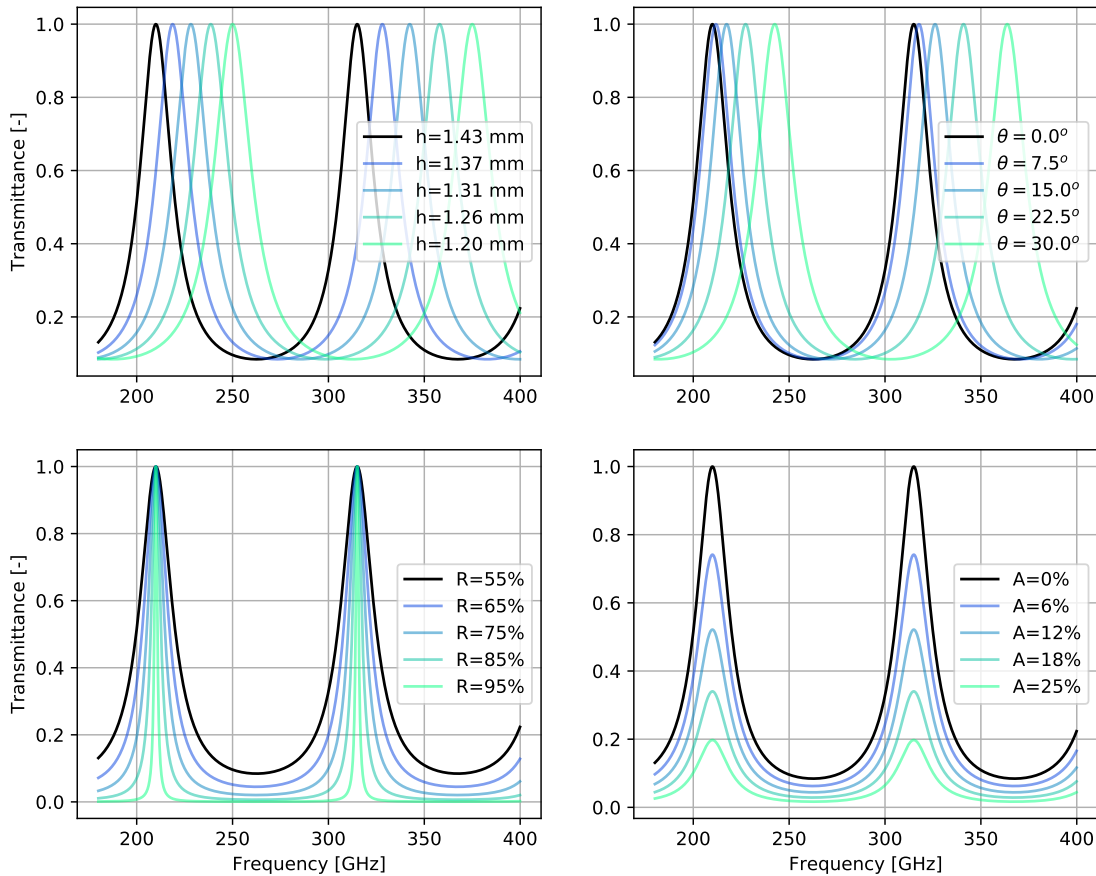


Figure 3.3: Airy function (Equation 3.7) plotted as a function of frequency for many cavity lengths (*upper left*), angles of transmission (*upper right*), mirror reflectances (*lower left*), and mirror absorptances (*upper right*). The nominal configuration is plotted in black in each subplot and corresponds to a freespace ($n = 1$) cavity with length $h = 1.43$ mm, $\theta = 0^\circ$, $\mathcal{R} = 0.55$, and $\mathcal{A} = 0$. In each plot, only one parameter is changed at a time.

Figure 3.3 plots the transmittance of Equation 3.7 and illustrates how changing some of the physical FPI parameters affects its transmittance. Decreasing the cavity length h linearly blue-shifts the fringes whereas increasing the angle of the rays inside the cavity θ , blue-shifts them with a $\cos \theta$ dependence. Increasing the reflectance of the mirrors \mathcal{R} increased the finesse and resolving power of the fringes. Increasing the absorptance of the meshes while holding the reflectivity constant decreases the peak transmittance.

3.2.2 Free-Standing Metal-Mesh Mirrors

As shown in the previous section, the finesse of an ideal FPI is function of the mirror reflectances. The design of the reflectors is therefore critical to the design of a FPI-based spectrometer. The reflectances of the mirrors must be tuned to achieve the desired resolving power of the FPI. The reflectances must also not be too large or the maximum transmittance will rapidly decline if there is any mirror absorption. In the far-IR, the most commonly used mirror technology is the metal mesh.

A metal mesh is any patterned metal film such as a wire-grid or an array of metal patches suspended on a dielectric substrate. For wavelengths shorter than the grid constant of the mesh (the distance between identical elements, also known as the pitch), metal meshes behave as frequency selective surfaces with frequency dependent reflection and transmission profiles. The geometric design of a mesh impacts its optical properties [4]. Multiple mesh designs have been empirically modeled [146, 147] and used as far-IR filters and FPI mirrors [117, 124] since the 1960s. Models for metal meshes typically take the form of transmission line approximations which relate the mesh geometry to an LRC filter. Mesh geometries

can be designed to produce low-pass, high-pass, band-pass, and even band-notch optical filters. Additionally, stacking multiple filters in succession can be used to create filters with complex shapes or sharp-edge cutoffs. We explore the design of metal meshes further in Section 3.4.

For far-IR instrumentation, there are two primary designs for metal mesh filters. The first are free-standing, stretched, two-dimensional, conductive wire grids which behave as a high-frequency-pass filters (and are known as inductive meshes). The second are two dimensional square arrays of disconnected metal patches suspended on a thin dielectric film such as Mylar which behave as low-frequency-pass filters (and are known as capacitive meshes). Figure 3.4 shows photographs of free-standing inductive meshes in a far-IR FPI (left) and hot-pressed, stacked, capacitive meshes for mm-wave filtering (right).

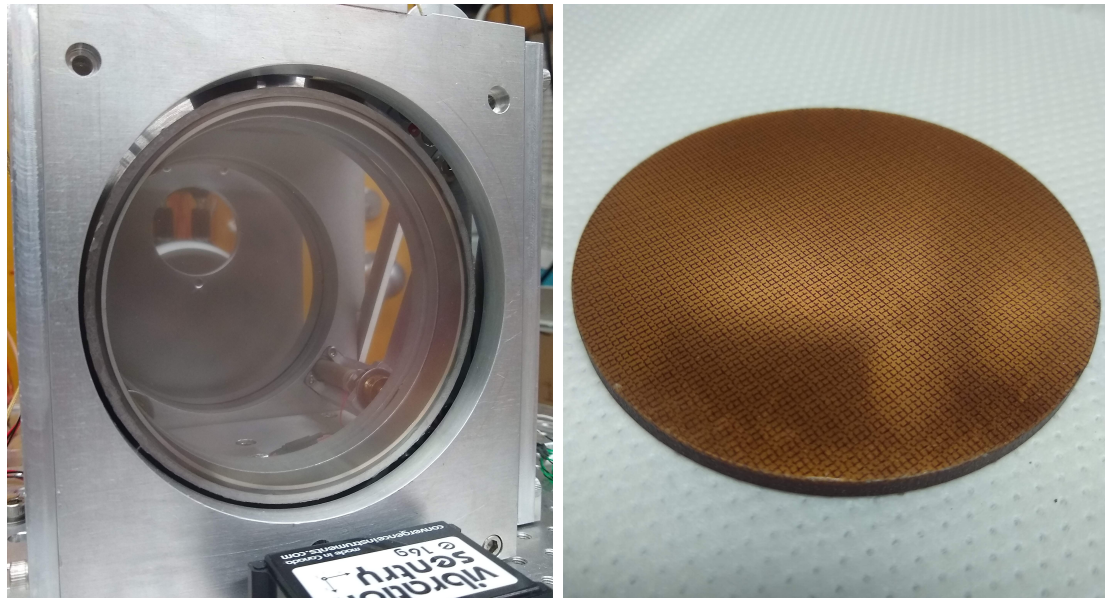


Figure 3.4: Photographs of free-standing inductive (left) and hot-pressed capacitive metal meshes (right). The inductive meshes are stretched on metal rings and assembled into a far-IR high-resolution FPI. The capacitive mesh is stacked in series with many other meshes, separated by low-loss dielectric, forming a bandpass filter for mm-wave instruments.

Since the grid constant must be small compared to the wavelength, far-IR meshes are generally very fragile. Their strength can be improved by increasing the wire or film thickness but doing so increases absorption and decreases the overall performance when used with a FPI. Inductive meshes are typically made by flashing gold on a nickle wire mesh, which results in a surface roughness of $\sim 1 \mu\text{m}$ which for high-frequency applications can cause different positions in the FPI cavity to resonate at different wavelengths. Capacitive meshes, which are fabricated on thin dielectric films, suffer from poor thermal conduction and thermal contraction which can cause the mesh film to deform, droop, or wrinkle. Additionally, a FPI consisting of either inductive-only or capacitive-only meshes will have a strong frequency-dependent finesse, limiting its bandwidth to roughly less than $\sim 1 : 1.6$. This is a limiting factor for instruments which require wide-band spectroscopy in order to accomplish their science goals, such as EoR-Spec which requires a full octave (1 : 2) of bandwidth to observe between 210 and 420 GHz.

3.2.3 Silicon Substrate-Based Mirrors

Making FPI mirrors on a solid substrate would ameliorate the issues faced by free-standing meshes. However, many substrates are lossy in the sub-mm and so choosing the substrate material must be done carefully [5]. High-purity, undoped, high-resistivity silicon is a good low-loss dielectric material that behaves well at wavelengths longer than $\sim 20 \mu\text{m}$ ($\sim 15 \text{ THz}$). Shorter wavelengths are affected by absorption bands in the lattice structure [6]. High purity silicon has a high index of refraction and low-loss tangent, [157] in the sub-mm and millimeter wavelengths. Silicon's crystalline structure makes it a good thermal conductor and pushes drum vibration resonances to higher frequencies than free-standing meshes. Therefore,

silicon substrate-based (SSB) mirrors minimize the fragility and flatness issues of free-standing meshes.

Being widely used in the semiconductor industry, high-resistivity silicon is commercially available and easy to process with microfabrication techniques. Using mature lithographic and thin film deposition processes in a cleanroom, arbitrarily shaped metal meshes can be patterned on silicon. This enables a broad range of metal mesh design options for the frequency selective transmittance profile of each silicon-based filter (see Section 3.4).

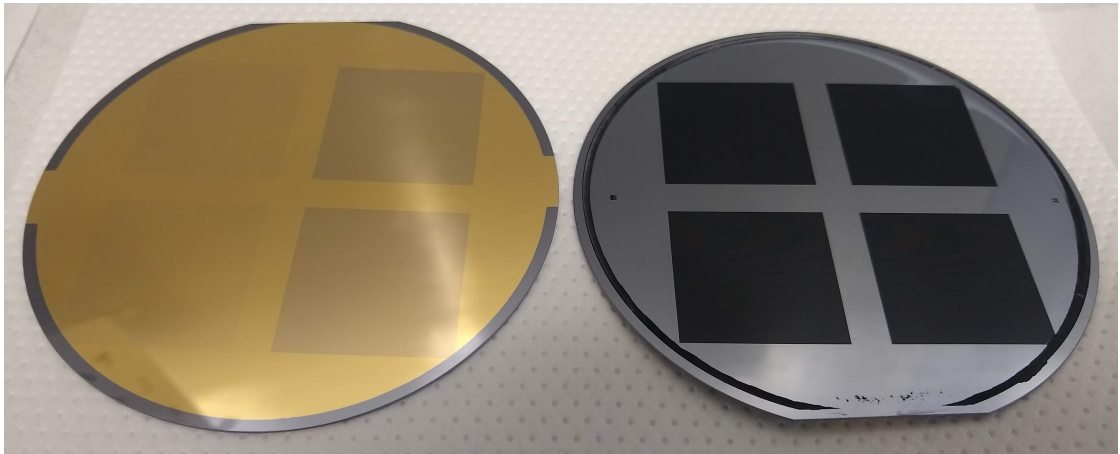


Figure 3.5: Photograph of SSB prototype mirrors. The left and right images show the front and backsides of two prototype samples. Capacitive and gold meshes were patterned on the left wafer. Double layer ARCs were etched into the right wafer. Samples courtesy of Bugao Zou.

However, as a dielectric with a relatively high index of refraction, SSB mirrors require an anti-reflection coating (ARC) in order to minimize Fresnel reflections. Small Fresnel reflections of the order a few percent on the non-metallized side of the silicon substrate can cause parasitic resonances in the FPI transmittance. Therefore, a highly efficient wide-bandwidth ARC is required for EoR-Spec's SSB FPI mirrors (see Section 3.3). Figure 3.5 shows two SSB mirror prototypes with lithographically patterned gold meshes (left) and plasma etched ARCs (right).

3.2.4 The EoR-Spec FPI

As discussed in Section 3.1, EoR-Spec will be a LIM instrument which will observe redshifted $158\ \mu\text{m}$ [CII] emission from the EoR. EoR-Spec will be enabled by a scanning SSB FPI operated with a finesse of about $\mathcal{F} \sim 50$. The SSB mirrors will have a double layer silicon metamaterial ARCs and inductive and capacitive metal mesh reflectors which will work in tandem to flatten the Finesse across EoR-Spec’s octave of bandwidth (210–420 GHz).

EoR-Spec will use arrays of MKIDs in two bands: 210–315 and 315–420 GHz. The FPI will be operated such that when the second order ($m = 2$) fringe is centered at 210 GHz, the third order ($m = 3$) fringe is centered at 315 GHz. Thus, when scanning the FPI, two frequencies will be mapped simultaneously – one by each band of detector. Figure 3.6 illustrates the operating principles of EoR-Spec. The detector bandpasses are shown in green and purple between 210 and 420 GHz. A two-layer metamaterial ARC is shown as the broadband yellow line with high transmission efficiency in the EoR-Spec band. Electromagnetically simulated second and third order SSB FPI fringes are plotted in red. Scanning the cavity length of the FPI will move the fringes through the bandpasses, enabling LIM measurements. The redshift of the [CII] line is shown on the top axis for reference. EoR-Spec’s optics will couple off-axis detectors to beams that go through the FPI at off-axis angles. This means that off-axis pixels will see slightly higher frequency fringes than on-axis pixels. This is illustrated in the figure by the pink bands.

The ARC on the SSB mirrors is required to have an octave of bandwidth in order to reduce parasitic resonances and optimize the transmitted fringe power. Similarly, the metal meshes must be designed to provide reasonable finesse across the entire bandwidth. These two requirements motivate careful modelling and

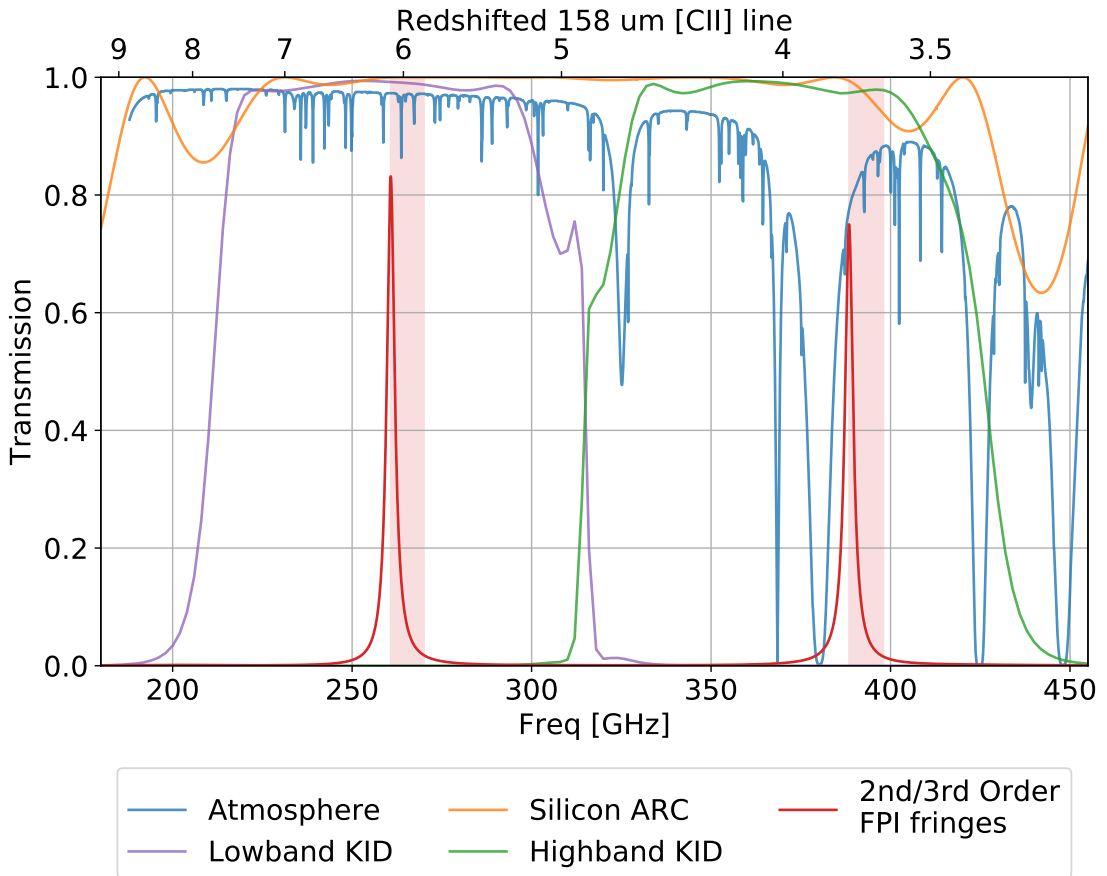


Figure 3.6: Transmittance plot illustrating the operating principles of EoR-Spec over the redshifted [CII] line between 210–420 GHz corresponding to redshifts 8–3.5. The first quartile telluric transmittance is plotted in blue, showing the atmospheric absorption. Nominal low (purple) and high (green) bandpasses are shown for the MKID detectors, splitting the 210–420 GHz octave in half. Simulated two-layer broadband ARC transmittance is shown in yellow. Second and third order simulated SSB FPI fringes are shown in red, one in each detector bandpass. Pink bands demonstrate how off-axis pixels will see blue-shifted fringes. As the FPI cavity length is scanned, the fringes will move left and right, sampling narrow bandpasses of the [CII] emission at a time, building a tomographic view of the EoR. Figure from [32].

optimization of the SSB mirrors. The rest of this chapter focuses on the design of the ARCs and SSB metal mesh reflectors.

3.3 Silicon-Based Metamaterial Anti-Reflection Coatings

As mentioned above, high-purity silicon is an excellent refractive media for the far-IR and millimeter because of it's low loss tangent and high index of refraction [157]. While its high index of refraction makes designing powered optics simpler, it also meands that there will be a large Fresnel reflection at each silicon surface. At normal incidence, the reflected power between two dielectrics with indices of refraction n_1 and n_2 is

$$R = \left| \frac{n_1 - n_2}{n_1 + n_2} \right|^2. \quad (3.13)$$

This is a result of the impedance mismatch between the dielectric media. With an index of about $n_{\text{Si}} \approx 3.4$, every silicon-vacuum interface will suffer a 30% reflection.

For cryogenic re-imaging silicon lenses, these reflections can cause ghost images that bounce around the interior of the optics module before ending at a detector. For a silicon-based FPI, having multiple parallel reflective surfaces can lead to parasitic resonances in which undesired resonances are formed between the coupled cavities. Therefore, in order to use silicon effectively as a cryogenic refractive media, an anti-reflection coating (ARC) technology for silicon is required.

Multiple approaches for silicon ARCs have been explored and fielded. The simplest solution is to apply a uniform dielectric film with a precisely controlled index of refraction and thickness onto the silicon surface. However, finding a material with the ideal index and low loss-tangent is challenging. Additionally, spraying or stretching/adhering a dielectric film on silicon such that it doesn't delaminate under cryocycling is challenging. Nonetheless, these approaches have worked in the past and been fielded in instruments such as MBAC, POLARBEAR, BICEP [54, 80, 88, 122]. For the application of SSB mirrors for FPIs, any mismatch be-

tween the coefficients of thermal expansion (CTEs) of the silicon and the dielectric film will cause film stress upon cooling and would warp the mirrors which already have a tight tolerance on flatness.

Another method which has been developed extensively over the past decade is using subwavelength structures to create a metamaterial artificial dielectric. The design of the subwavelength geometry controls its effective dielectric constant, enabling highly tunable artificial dielectric layers. For example, a single layer of silicon pillars will have a constant index of refraction between that of silicon and vacuum depending on the area fill fraction of the pillar footprint. Alternatively, a gradient indexed metamaterial layer can be created by constructing silicon pyramids or cones. Because the metamaterial ARC is made of the same material as the substrate, delamination and warping due to mismatched CTEs is no longer a concern. The challenge of this technology is to precisely inscribe or etch the silicon surface with the repeating geometry of the metamaterial. If the features are on the order of a wavelength or greater, they will cause incident radiation to diffract or scatter off the metamaterial structures.

Two previously explored methods for fabricating metamaterial ARCs include cutting it onto the silicon surface using a dicing saw blade and ablating it using a laser [39, 162]. Both methods have produced successful prototypes, but to-date, the dicing saw method remains the most popular and has produced many multi-layer ARCs and half-wave plates for experiments that this author collaborates with [34, 64]. The dicing saw method is limited to longer wavelengths due to the physical constraints on the blade size. Recent demonstrations of the laser method have shown success but are limited to gradient index designs and have yet to be fielded [155].

A third method for fabricating metamaterial ARCs is to use deep reactive ion etching (DRIE), which is a common nanofabrication plasma etching technique. In this method, a plasma is accelerated at the silicon surface, bombarding it with ions which break silicon bonds. Etch masks such as patterned photoresist or SiO_2 can be used to protect areas of the silicon surface, enabling selective vertical etching of metamaterial geometries. The primary benefit of DRIE-based metamaterial ARCs is that they can access much higher frequencies (well into the THz) than the dicing saw method. A secondary benefit is that the total fabrication time is much less than a dicing saw since the entire surface of the optical element is etched simultaneously rather than being traced out multiple times with a single blade. Our group has developed this method at the Cornell Nanofabrication Facility (CNF) and produced some of the first silicon-based single and double layer ARCs fabricated with DRIE [61]. We discuss the fabrication process and characterization of early plasma etched ARCs in section 3.5.

EoR-Spec plans to use double-layer DRIE-based metamaterial ARCs in order to provide sub-percent reflectance to the mirror substrates over an octave of bandwidth. In the following subsections, we develop and optimize the design of EoR-Spec’s ARCs by following a design flow from analytic ARC theory, to approximate metamaterial models, and then finally through full electromagnetic simulations of the subwavelength structures.

3.3.1 Dielectric Theory for ARCs

We begin the ARC design process with an analytic model of layered, homogeneous dielectrics. A general solution for the transmission of waves through homogeneous layered dielectric media is presented in Yeh [161]. Here, we present a brief overview

of the matrix formulation of transmittance and reflectance derived in Yeh §5.1.3.

Consider a multilayer structure of N homogenous dielectrics, each with a unique complex index of refraction n_i and thickness d_i . The structure is bounded by the incident medium, n_0 , and the substrate medium n_s as shown in Figure 3.7.

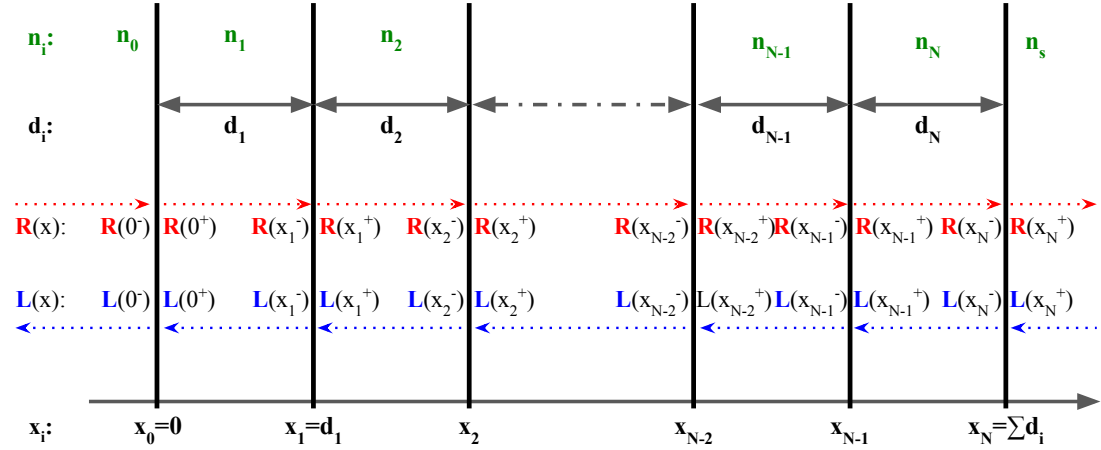


Figure 3.7: A multilayer system of dielectrics between two media with indices n_0 and n_s . The refractive index and depth of each layer is n_i and d_i . Right and left traveling wafers represented by $R(x)$ and $L(x)$ represent a general solution for the electric field everywhere.

Consider a plane wave incident on the boundary between the incident medium (n_0) and the first dielectric layer (n_1). The general solution for the electric field on both sides of the interface can be written as the superposition of right and left-traveling waves:

$$E(x) = Re^{-ik_xx} + Le^{ik_xx} = R(x) + L(x). \quad (3.14)$$

We require that the right and left waves satisfy boundary conditions at the interface $x = 0$. Specifically, Fresnel's reflection and transmission equations dictate the relationship between the field amplitudes when the two media are dielectrics. For transverse electric (TE) waves (when the electric field vector is perpendicular with

the normal vector of the dielectric surface) this amounts to:

$$\begin{aligned} L(0^-) + R(0^-) &= L(0^+) + R(0^+) \\ n_1(L(0^-) - R(0^-)) \cos \theta_1 &= n_2(L(0^+) - R(0^+)) \cos \theta_2, \end{aligned} \quad (3.15)$$

where 0^- and 0^+ represent the x coordinates infinitesimally to the left and right of $x = 0$ respectively. Written in matrix form, these equations are:

$$D_1 \begin{pmatrix} L(0^-) \\ R(0^-) \end{pmatrix} = D_2 \begin{pmatrix} L(0^+) \\ R(0^+) \end{pmatrix}, \quad (3.16)$$

where D_i is called the dynamical matrix of the TE wave in medium i :

$$D_i^{TE} = \begin{pmatrix} 1 & 1 \\ n_i \cos \theta_i & -n_i \cos \theta_i \end{pmatrix}. \quad (3.17)$$

Following a similar approach, the dynamical matrix of a TM wave in medium i is:

$$D_i^{TM} = \begin{pmatrix} \cos \theta_i & \cos \theta_i \\ n_i & -n_i \end{pmatrix}. \quad (3.18)$$

Using this approach, we can relate the electric fields on both sides of the boundary using simple matrix arithmetic:

$$\begin{pmatrix} L(0^-) \\ R(0^-) \end{pmatrix} = D_1^{-1} D_2 \begin{pmatrix} L(0^+) \\ R(0^+) \end{pmatrix}. \quad (3.19)$$

Thus, if we know the indices of both media and the angle of incidence, we can solve for the electric field at the boundary. This formalism can be extended to the entire system of stacked homogeneous dielectric layers shown in Figure 3.7 if we introduce a propagation matrix to account for the phase shift between successive layers. Let P_i be the propagation matrix for the wave traveling through layer i

with index n_i and thickness d_i at an angle θ_i to the normal:

$$P_i = \begin{pmatrix} e^{i\phi_i} & 0 \\ 0 & e^{-i\phi_i} \end{pmatrix}, \quad (3.20)$$

where ϕ_i is the phase shift in layer i given by

$$\phi_i = k_{ix}d_i = \frac{n_i d_i}{\lambda_0} \cos \theta_i. \quad (3.21)$$

Thus, if we know the index, thickness, and angle of incidence in each layer, we can determine the electric field amplitudes on both sides of the system. For example, consider a thin dielectric film with index n_f and thickness d between two media with indices n_0 and n_s . The field amplitudes through the system can be written

$$\begin{pmatrix} L(0^-) \\ R(0^-) \end{pmatrix} = D_0^{-1} D_f P_f D_f^{-1} D_s \begin{pmatrix} L(d^+) \\ R(d^+) \end{pmatrix}. \quad (3.22)$$

This easily extends to any number of dielectric layers

$$\begin{pmatrix} L^- \\ R^- \end{pmatrix} = D_0^{-1} \left[\prod_{l=1}^N D_l P_l D_l^{-1} \right] D_s \begin{pmatrix} L^+ \\ R^+ \end{pmatrix} = \begin{pmatrix} M_{11} & M_{12} \\ M_{21} & M_{22} \end{pmatrix} \begin{pmatrix} L^+ \\ R^+ \end{pmatrix}. \quad (3.23)$$

And so, if the matrix M is known for the system of dielectrics, then the reflected and transmitted electric fields can be computed. An incident wave from the left will have reflection and transmission coefficients

$$r = \begin{pmatrix} L(0^-) \\ R(0^-) \end{pmatrix} \quad \text{and} \quad t = \begin{pmatrix} R(X_N^+) \\ R(0^-) \end{pmatrix}. \quad (3.24)$$

It can be shown⁶ that these coefficients are equivalent to

$$r = \frac{M_{21}}{M_{11}} \quad \text{and} \quad t = \frac{1}{M_{11}}, \quad (3.25)$$

⁶See §5.2 of Yeh [161]

and the reflectance and transmittance are then given by

$$R = \left| \frac{M_{21}}{M_{11}} \right|^2 \quad \text{and} \quad T = \frac{n_s \cos \theta_s}{n_0 \cos \theta_0} \left| \frac{1}{M_{11}} \right|^2. \quad (3.26)$$

Using a computer to perform the matrix multiplication for us, this formalism makes it simple to compute the transmittance of multi-layer dielectric systems. Dr. Patricio Gallardo wrote an implementation⁷ of this method assuming normal incidence which I helped test, correct, and improve. Using Gallardo's *chal* code, I have modeled double layer ARCs for silicon substrates.

For a single layer quarter-wave depth ARC with index n_1 and thickness $\lambda_0/4n_1$, the reflectance at normal incidence reduces simply to

$$R = \left(\frac{n_0 n_s - n_1^2}{n_0 n_s + n_1^2} \right)^2 \quad (3.27)$$

and thus can be totally eliminated at λ_0 if the ARC index is $n_1 = \sqrt{n_0 n_s}$. The blue line in Figure 3.8 shows the transmittance of an optimal single layer ARC tuned for a band center of 315 GHz. However, notice that the fractional bandwidth above 99% transmittance is small at $\sim 1.2 : 1$.

A multi-layer ARC does not simplify quite as nicely as a single layer. Adding additional layers enables higher transmittances over broader bandwidths. Choosing the indices of each layer is a multi-parameter optimization problem. Generally, if lower transmittances can be accepted, broader bandwidths can be achieved. Similarly, higher in-band transmittance can be achieved at the cost of a narrower bandwidth.

For a double-layer quarter-wave depth ARC with indices n_1 and n_2 ($n_0 < n_1 <$

⁷<https://github.com/patogallardo/chal>

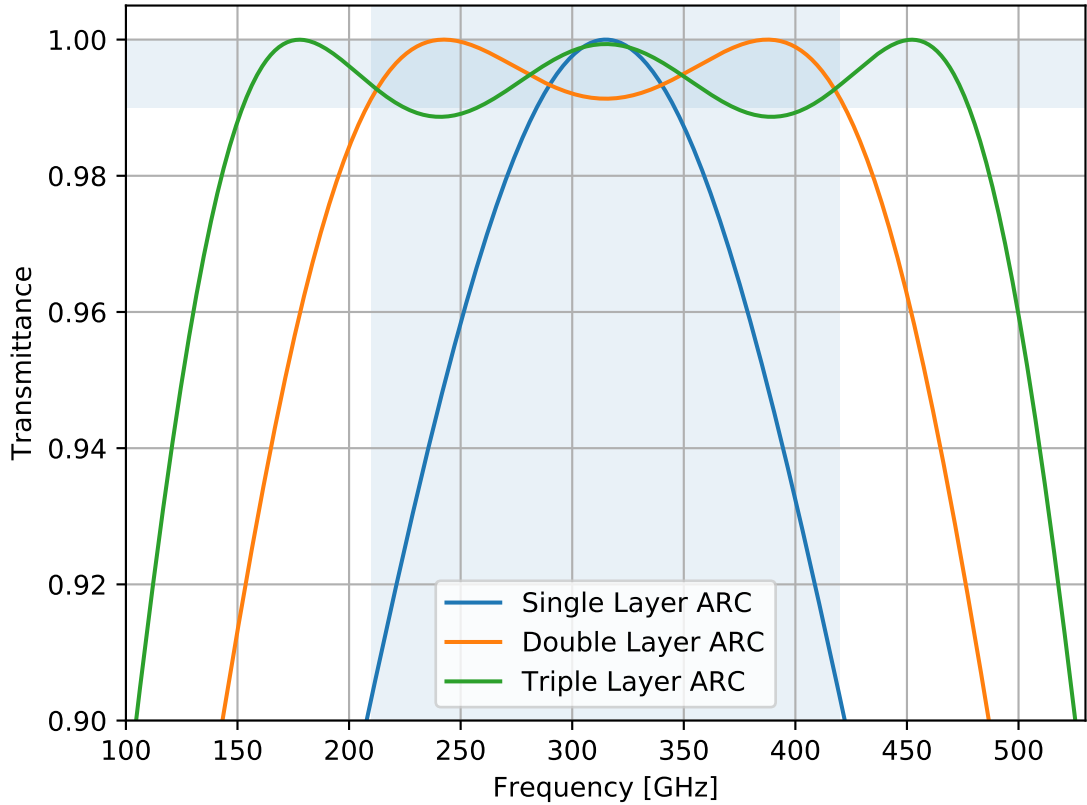


Figure 3.8: Dielectric model of the transmittance of a single, double, and triple layer ARCs centered at 315 GHz. Increasing the number of layers dramatically increases the bandwidth of the ARC.

$n_2 < n_3$), the reflectance at normal incidence reduces to

$$R = \left(\frac{n_0 n_2^2 - n_s n_1^2}{n_0 n_2^2 + n_s n_1^2} \right)^2 \quad (3.28)$$

and so, the reflectance will be eliminated at λ_0 when $(n_2/n_1)^2 = n_s/n_0$. However, note that satisfying this condition maximizes the reflectance at the center of the band but does not optimize the bandwidth. Figure 3.8 also shows the transmittance of a double and triple layer ARC that have been roughly optimized to produce a minimum transmittance of 99% over as wide a bandwidth as possible. The double and triple layer ARCs have bandwidths above 99% transmittance of roughly $\sim 2.0 : 1$ and $\sim 3.2 : 1$ respectively. While a triple-layer ARC would be

best for EoR-Spec's requirements, the fabrication methods for a three-layer ARC using DRIE still need development. In order to optimize EoR-Spec's performance, a careful optimization of a double-layer ARC is required.

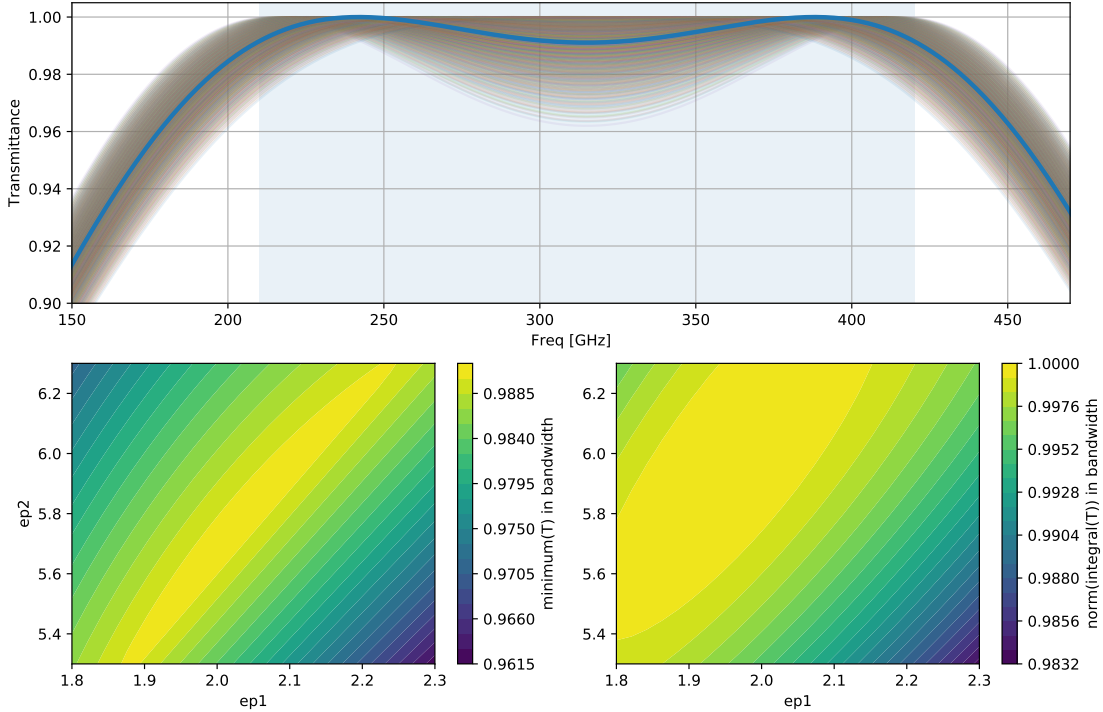


Figure 3.9: Dielectric model calculations for double-layer ARCs, sweeping over target dielectric constants for both layers. The thickness of each layer is a quarter wavelength in the index of the layer. The substrate dielectric constant is set to $\epsilon_s = 11.7$. The upper panel overplots all simulated transmittances. The lower left panel plots the minimum transmittance within the EoR-Spec bandwidth over the entire parameter sweep. The lower right panel plots the integral of the transmittance over the EoR-Spec bandwidth, normalized to the best performing simulation. From this, we select a roughly optimal design: $\epsilon_1 = 2.0$ and $\epsilon_2 = 5.7$. The transmittance of this design is highlighted in the upper panel.

In Figure 3.9, we used the dielectric model presented above to simulate double-layer ARC performances over two dimensional parameter space of refractive indices. The substrate dielectric constant is set to that of silicon in the millimeter: $\epsilon_s = 11.7$. The upper panel of the figure shows all of the simulated profiles over

plotted on one another. The lower panels are contour plots of two merit functions used to evaluate the ARC performance. The parameter space is denoted in terms of the relative dielectric constant of each layer $\epsilon_i = n_i^2$ instead of the refractive index. The merit function used in lower left panel is the minimum transmittance within the EoR-Spec band for a given simulation. Ideally, we want the minimum transmittance to be $> 99\%$ within the entire octave but this is difficult to accomplish except in the highest bin of the contour plot. The merit function used in the lower right panel is a proxy for bandwidth: the integral over the transmittance profile within the EoR-Spec band, normalized to the best performing simulation in the sweep. This merit function will tend to reject results with a large dip in the middle of the band but will award balanced results where the dip is roughly equal to drop at the edges of the bandwidth. The two merit functions do not agree in general but they have a similar behavior. Based on these results, we can select a rough estimate for the target dielectric constants of our double-layer ARC, and then continue to optimize it with this analytic dielectric model and electromagnetic simulation techniques. We select $\epsilon_1 = 2.0$ and $\epsilon_2 = 5.7$ which roughly balances the two merit functions. The transmittance of this design is highlighted in the upper panel of the figure.

Figure 3.10 takes this design and then runs a parameter sweep over the layer depths. The nominal depth of each layer is a quarter wavelength in the index of the layer. Small changes to these values can shift and stretch the transmittance, increasing the minimum in-band transmittance or increasing the bandwidth. The panels in the figure are laid out in the same format as in Figure 3.9, with the same merit functions. The parameter values d_1 and d_2 are fractional changes to the nominal quarter wavelength depths. From the minimum in-band transmittance merit function (lower left), we see the two layer depths can vary as long as they

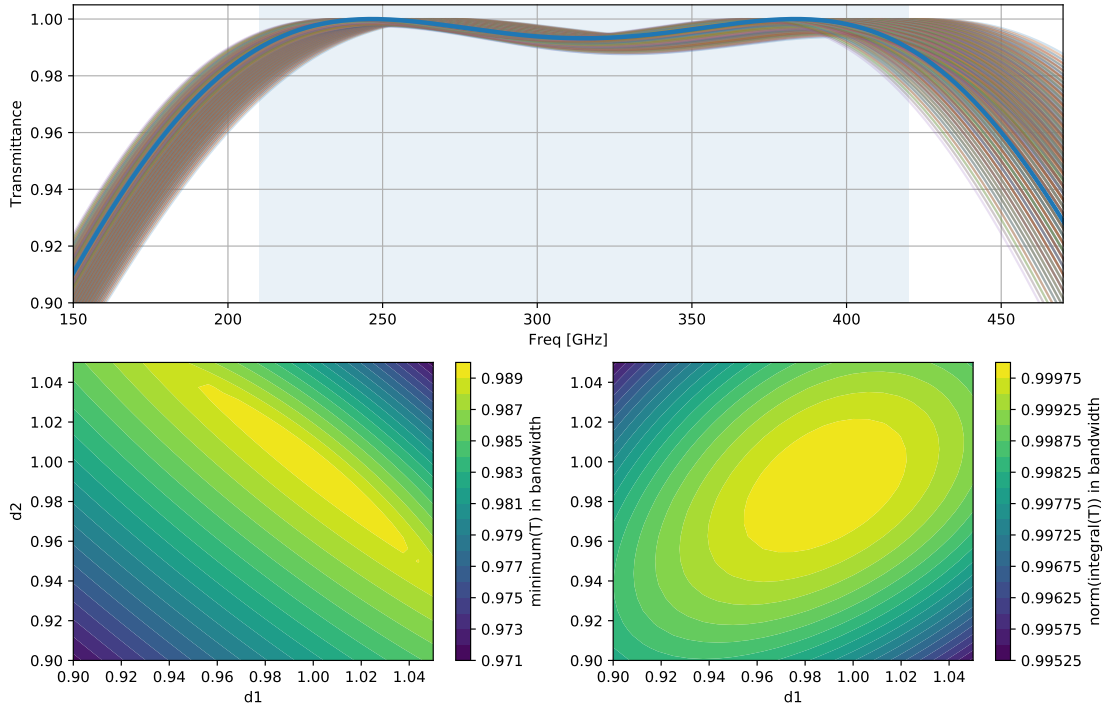


Figure 3.10: Dielectric model calculations for double-layer ARCs, sweeping over the layer depths. For these simulations, we take $\epsilon_1 = 2.0$ and $\epsilon_2 = 5.7$ from the previous figure as the nominal design and then sweep over fractional changes to the quarter wavelength depths. The upper panel overplots all simulated transmittances. The lower left panel plots the minimum transmittance within the EoR-Spec bandwidth over the entire parameter sweep. The lower right panel plots the integral of the transmittance over the EoR-Spec bandwidth, normalized to the best performing simulation. From this, we remain with the nominal design: $d_1 = d_2 = 1$. The transmittance of this design is highlighted in the upper panel.

are inversely varied with respect to the other. From this plot, it is clear that the nominal $d_1 = d_2 = 1$ provides the best in-band transmittance. In the other merit function (lower right), where we integrated the in-band transmittance, we see a different behavior. The integrated transmittance is fairly tolerant to depth deviations and may even suggest that the optimal layer depth for the EoR-Spec band is closer to $d_1 = d_2 = 0.99$. However, since the integrated transmittance is relatively tolerant compared to the minimum transmittance, we will continue using

$d_1 = d_2 = 1$ for our nominal, dielectric model design.

The powerful matrix formalism for layered dielectric media that we developed here has many applications. The model accepts complex refractive indices and is therefore not limited to lossless optical devices. The author has applied this model and code to study many other sub-mm devices such as gradient index ARCs, silicon-cavity FPI etalons, and high-reflectance Bragg mirrors. However, for SSB FPIs which rely on metamaterial-based ARCs, we need a model to connect the target refractive indices we identified in this subsection to the metamaterial geometry that must be fabricated.

3.3.2 Metamaterial Approximations for Silicon ARCs

In the previous section, we discussed a dielectric theory for multi-layer ARCs that assumes each layer is homogeneous. This theory provides a guide for the desired indices of refraction for our multi-layer metamaterial ARCs. The next step in designing our silicon-based ARCs is to determine a metamaterial geometry that will produce the desired effective index of refraction for each layer. In this section, we go through the capacitive models that we use for estimating the metamaterial geometry.

We begin with a discussion of a capacitive model for artificial dielectrics that was developed in Biber et al 2003 [18]. This model assumes that (1) the metamaterial structures are dielectric, (2) the unit cell of the structures have a four-fold symmetric design, (3) the unit cell periodicity is significantly less than the incident wavelength (in the dielectric medium), and (4) the electric field vector is perpendicular to the surface (i.e. TE modes). Figure 3.11 shows illustrations of the unit

cell structures (*top*) and equivalent capacitive circuits (*bottom*) for metamaterial designs based on dielectric pillars (*left*) and holes (*right*).

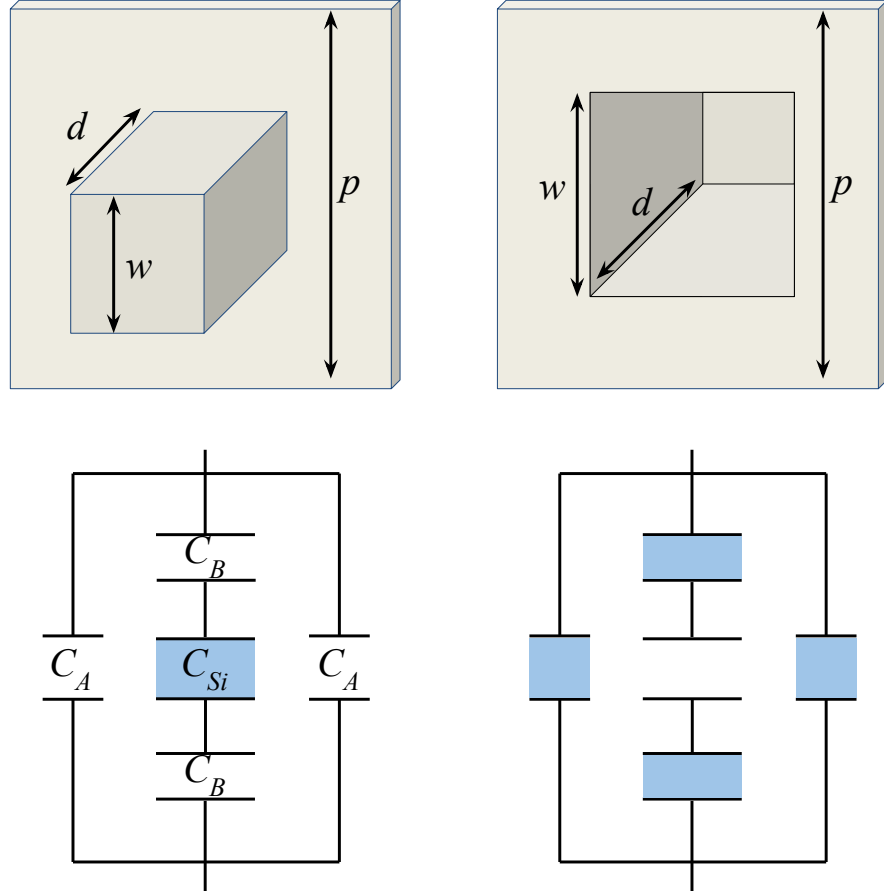


Figure 3.11: Illustrations of the metamaterial geometry (upper) and effective capacitive circuit models (lower) for subwavelength pillars (left) and holes (right) geometries. In the circuit models, a capacitor symbol with a blue shading indicates a parallel plate capacitor loaded with a dielectric constant of silicon ϵ_{Si} , whereas the white capacitor symbols are parallel plate capacitors with the dielectric constant of free-space.

The effective dielectric constant for such designs can be estimated by determining the total capacitance of the equivalent circuit. Consider the case of silicon pillars of width w , periodicity (pitch) p , height d , and relative dielectric constant $\epsilon_{Si} \approx 11.7$, surrounded by vacuum with relative dielectric constant $\epsilon_{vac} = 1$. We

can write the total capacitance of the equivalent circuit shown in Figure 3.11 *lower left*:

$$C_{\text{tot}} = 2C_A + \left(\frac{2}{C_B} + \frac{1}{C_{\text{Si}}} \right)^{-1}. \quad (3.29)$$

Using the equation for a parallel plate capacitor of area A , separation s , and relative dielectric constant in between the plates ϵ_r , $C = \epsilon_0 \epsilon_r \frac{A}{s}$ we can write each capacitance separately:

$$\begin{aligned} C_A &= \epsilon_0 \epsilon_{\text{vac}} \frac{d(p-w)}{2p} = \epsilon_0 \epsilon_{\text{vac}} \frac{d(1-r)}{2}, \\ C_B &= \epsilon_0 \epsilon_{\text{vac}} \frac{2dw}{p-w} = 2\epsilon_0 \epsilon_{\text{vac}} d \frac{r}{1-r}, \\ C_{\text{Si}} &= \epsilon_0 \epsilon_{\text{Si}} \frac{dw}{w} = \epsilon_0 \epsilon_{\text{Si}} d, \end{aligned} \quad (3.30)$$

where we defined $r = w/p$. Another common parameterization instead of r is the silicon area fill fraction f_{Si} . For pillars $f_{\text{Si}} = r^2$ and for holes $f_{\text{Si}} = 1 - r^2$. Plugging these in to Equation 3.29 yields

$$C_{\text{tot,pillars}} = \epsilon_0 \epsilon_{\text{vac}} d \left[1 - r + \left(\frac{1-r}{r} + \frac{\epsilon_{\text{vac}}}{\epsilon_{\text{Si}}} \right)^{-1} \right]. \quad (3.31)$$

Note that this equation only holds for the pillar metamaterial geometry. An analogous equation can be derived for a metamaterial geometry of holes, or equivalently, we can simply swap the instances of ϵ_{vac} and ϵ_{Si} in Equation 3.31:

$$C_{\text{tot,holes}} = \epsilon_0 \epsilon_{\text{Si}} d \left[1 - r + \left(\frac{1-r}{r} + \frac{\epsilon_{\text{Si}}}{\epsilon_{\text{vac}}} \right)^{-1} \right]. \quad (3.32)$$

The effective index of refraction for either geometry can then be determined from Equations 3.31 and 3.32 using

$$n_{\text{eff}} = \sqrt{\epsilon_{\text{eff}}} = \sqrt{\frac{C_{\text{tot}}}{\epsilon_0 d}}. \quad (3.33)$$

Figure 3.12 plots n_{eff} as a function of the silicon area fill fraction f_{Si} for both silicon pillars and holes (solid lines). Thus, this model is useful for roughly estimating the area fill ratio of silicon to vacuum, and thus the geometry of these

metamaterial designs. It is also useful for giving physical insight and intuition for the design of artificial dielectrics.

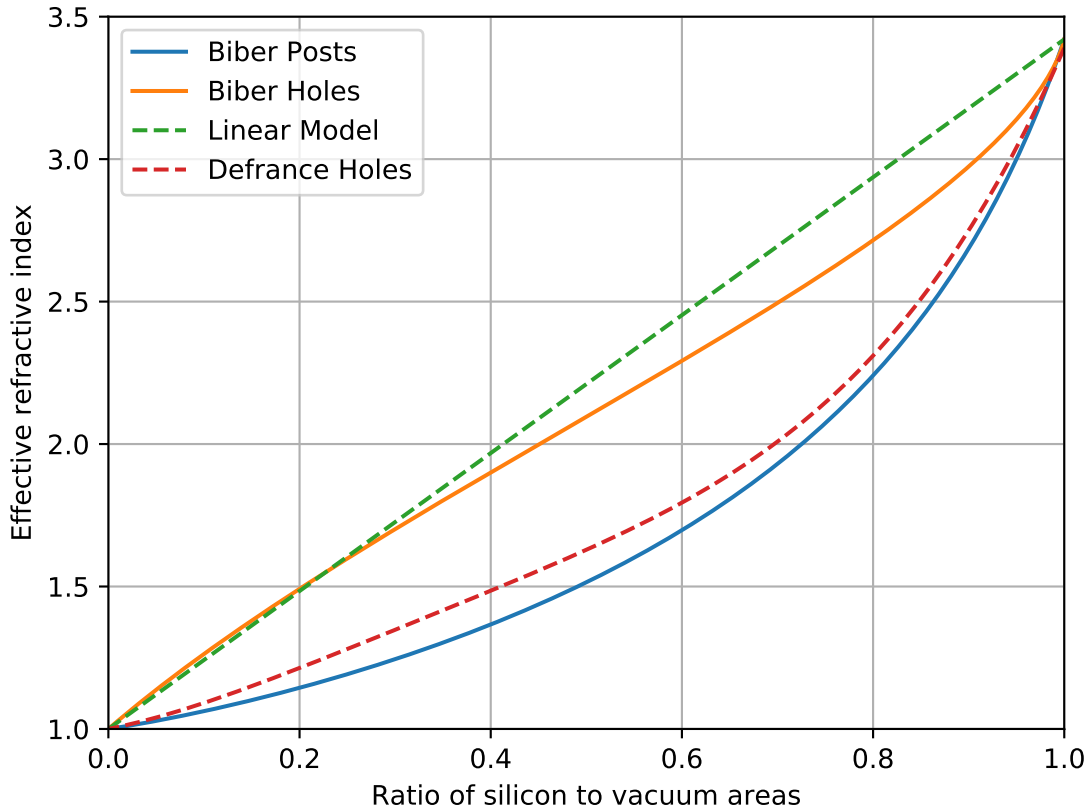


Figure 3.12: The effective index of refraction for artificial dielectrics based on sub-wavelength holes and pillars as a function of the area fill fraction of silicon to vacuum, f_{Si} . The capacitive circuit approximations from Biber et al 2003 [18] are plotted as solid lines. The dashed lines are the relations determined through empirical electromagnetic simulations from Defrance et al 2018 [40].

Following the increase in computing power over the past two decades, electromagnetic (EM) simulation packages such as Computer Simulation Technology Microwave Studio⁸ (CST) or ANSYS High Frequency Structure Simulator⁹ (HFSS) have made it easier to calculate the expected metamaterial response by solving

⁸<https://www.3ds.com/products-services/simulia/products/cst-studio-suite/>

⁹<https://www.ansys.com/products/electronics/ansys-hfss>

Maxwell's equations. Using iterative modeling, a metamaterial design can be determined via brute force rather than using approximate physical models such as the capacitive model above. Recent works such as Defrance et al 2018 [40] have compared EM simulations of silicon pillars and holes to the predictions of Biber's capacitive model. Defrance finds that a simple linear function and a quartic polynomial function more readily describe the behavior of pillar and hole geometries respectively. These functions are over plotted in Figure 3.12 (dashed lines) where it is clear that the capacitive model and the EM simulations are in relative agreement even though the capacitive model tends to slightly under estimate the EM simulations. The functional form of the linear and polynomial functions found by Defrance et al are:

$$\begin{aligned} n_{\text{eff, pillars}} &= 4.9f_{\text{Si}}^4 - 6.28f_{\text{Si}}^3 + 3.11f_{\text{Si}}^2 + 0.66f_{\text{Si}} + 1 \\ n_{\text{eff, holes}} &= f_{\text{Si}}(n_{\text{Si}} - 1) + 1. \end{aligned} \quad (3.34)$$

Using these models and the target dielectric constants determined in the previous section, we can select initial metamaterial geometries. In the next section, we use electromagnetic simulations to evaluate and re-optimize the design of our metamaterial geometry.

3.3.3 Electromagnetic Simulations of Silicon ARCs

To design our FPI metamaterial ARCs, we use the models described in the previous two sections to estimate the metamaterial geometry, and then optimize it by iterating over electromagnetic simulations in CST. We use CST's frequency domain solver for periodic structures which is a 3D finite element-based full-wave solver. Figure 3.13 shows a screenshot of an example unit cell of a double layer ARC in CST.

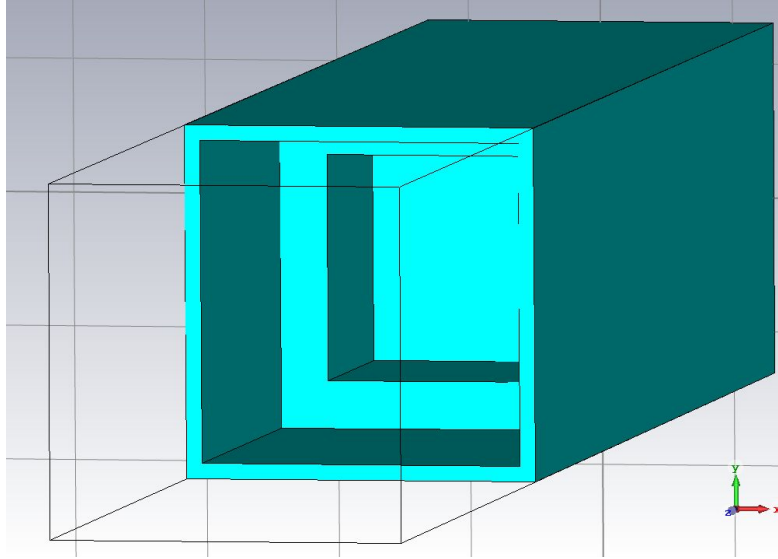


Figure 3.13: Screenshot of a unit cell of the 3D unit cell double-layer metamaterial ARC. Periodic boundary conditions are set on the lateral sides of the unit cell. Floquet ports are defined above and behind (in the silicon) the unit cell to simulate the transmittance through a double-layer coating without other contaminating reflections.

To simulate the transmittance and reflectance of the two layer ARC structure, a pair of Floquet ports are defined along the normal axis of the structure: the first port is placed some distance before the first metamaterial layer in free space, the second port is placed within the silicon such that reflections off the back of the silicon are not measured. Periodic boundary conditions are applied on all four lateral sides of the cell, implying an infinitely repeating cell structure. The important parameters of the 3D unit cell ARC model include the pitch, hole widths, and layer depths. The hole widths and layer depths are determined using the ARC parameters defined using the dielectric theory and metamaterial approximations in the preceding sections. The pitch only needs be shorter than the shortest wavelength in the EoR-Spec band in the silicon medium, but the pitch can and should be optimized. We run a series of parameter sweeps to optimize and characterize the ARC performance as well as to understand how fabrication defects impact the

final ARC performance.

Before diving into ARC parameter sweeps and optimizations, we first compare the expected theoretical performance theory (Equation 3.26) to CST’s simulated transmittance. Figure 3.14 shows the analytic and simulated transmittances for a two-layer ARC designed for a center frequency of 315 GHz with target indices $n_1 = 2.0$ and $n_2 = 5.8$, and quarter-wave layer depths. The CST model uses the metamaterial hole geometry with f_{Si} should be 17.1% and 58.2% for both layers respectively (Equataion 3.34). It is evident that the analytic dielectric prescription and the EM simulations agree on the general form of the transmittance, but that there are discrepancies between the models. The transmittance in the middle of the band is significantly worse in the EM simulation, dropping below our target $T = 0.99$ for minimizing parasitic FPI resonances. The two models disagree on the overall bandwidth, with the EM simulations being centered at a slightly lower frequency than the dielectric model. From this result, it is clear that the metamaterial design requires fine-tuning beyond the effective capacitive model.

Optimizing the ARC metamaterial geometry through EM simulation sweeps is time consuming but has been found to give results consistent with lab measurements [38, 40, 61]. We take the nominal design from the dielectric and capacitor models and perturb various geometric parameters such as the pitch, target, dielectric constant, hole width, and depth of each layer.

First, we sweep over the pitch of the metamaterial structure. Fabrication requires that the pitch of both ARC layers are identical and so, we simulate the ARC performance over a one dimensional sweep of pitches. Figure 3.15 shows the CST simulated ARC transmittance as a function of pitch. As the pitch is increased, the ARC performance is reduced at higher frequencies, and eventually

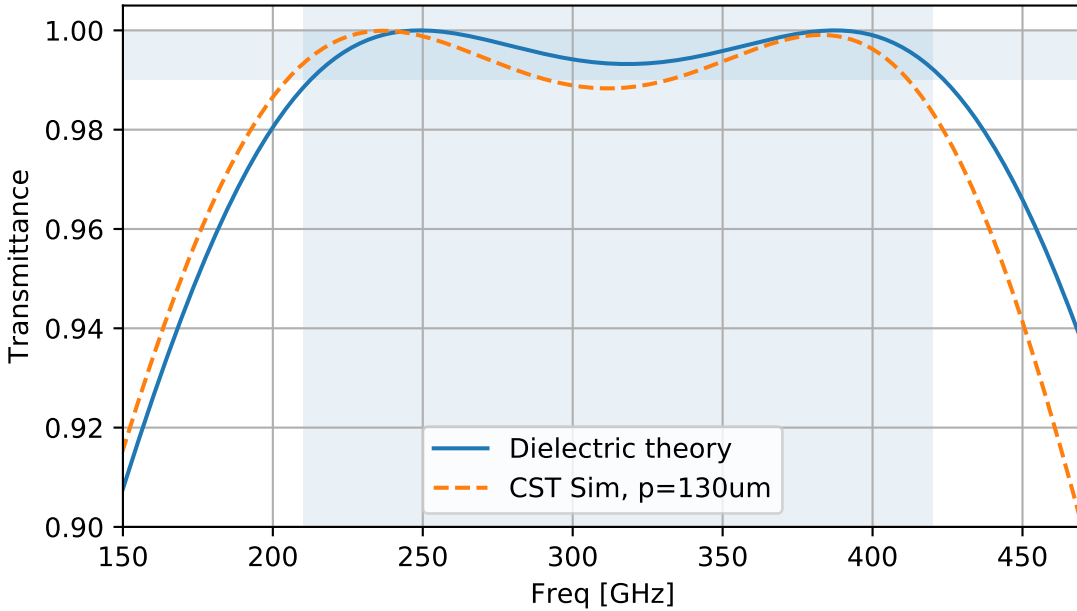


Figure 3.14: Comparison of analytic (Section 3.3.1) and CST simulated transmittance for a double layer ARC with target dielectric constants $\epsilon_1 = 2.0$ and $\epsilon_2 = 5.8$. The metamaterial hole geometry used in the CST model was computed with Equation 3.34 and the layer thicknesses were set to a quarter wavelength in the layer indices.

begins diffracting when the metamaterial structures are no longer subwavelength. For the simulations shown here, diffraction occurs when $p/\lambda_0 \gtrsim 0.30$.¹⁰ We see that the ARC performance is stable in the EoR-Spec band (210 – 420 GHz) for pitches $\lesssim 65 \mu\text{m}$. Pitches as high as $130 \mu\text{m}$ are also stable, with higher transmittances in the middle of the band, but smaller bandwidths. The layer depths are driven by the quarter wave thickness requirement and so are roughly around $100 \mu\text{m}$ and $160 \mu\text{m}$ for the lower and upper layers respectively. For fabrication, a higher width to depth ratio is desirable. If the pitch is too small, then the aspect ratio of the holes becomes too high for plasma etching. Therefore, we will constrain our EM ARC models to pitches between roughly $65\text{-}130 \mu\text{m}$.¹¹

¹⁰Note that this roughly agrees but is less conservative than the limit discussed in Datta et al 2013 [38] which says diffraction occurs when $p/\lambda_0 \gtrsim 1/(n_s + n_0) = 0.23$.

¹¹This corresponds to $p/\lambda_0 \approx 7\text{-}14\%$, agreeing with the quasi-static limit $p/\lambda_0 \ll 0.1$ described

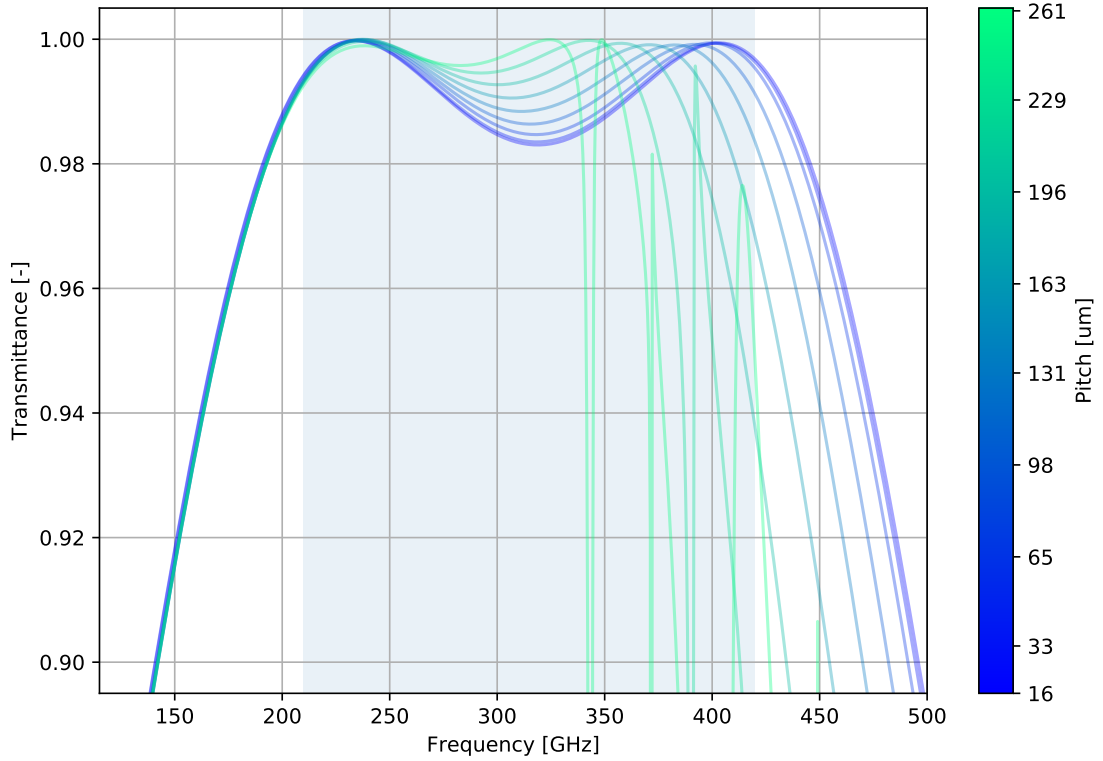


Figure 3.15: CST transmittance simulations of a double-layer metamaterial ARC with target dielectric constants $\epsilon_1 = 2.0$ and $\epsilon_2 = 5.8$ and a varied pitch. At larger pitches, the metamaterial structures are no longer subwavelength and begin to diffract. The bandwidth is maximal for pitches $\lesssim 65 \mu\text{m}$ but is still acceptable up to $130 \mu\text{m}$.

Next, we sweep over small variations of the target dielectric constant of both layers to optimize the transmittance and bandwidth. When we perturb the target dielectric constant we simultaneously change the hole width and depth of each layer since both depend on the target index via Equation 3.34 and $d_i = \lambda/4n_i$. For these simulations, we choose $p = 65.33 \mu\text{m}$. Figure 3.16 shows the sweep results. The upper panel overplots all of the simulations in the sweep while the lower plots evaluate each simulation in terms of its minimum in-band transmittance (left) and its normalized integrated in-band transmittance (right). We search for the

in Datta et al 2013 [39] for which the performance converges to the homogeneous approximation.

parameter set which maximizes both merit functions.

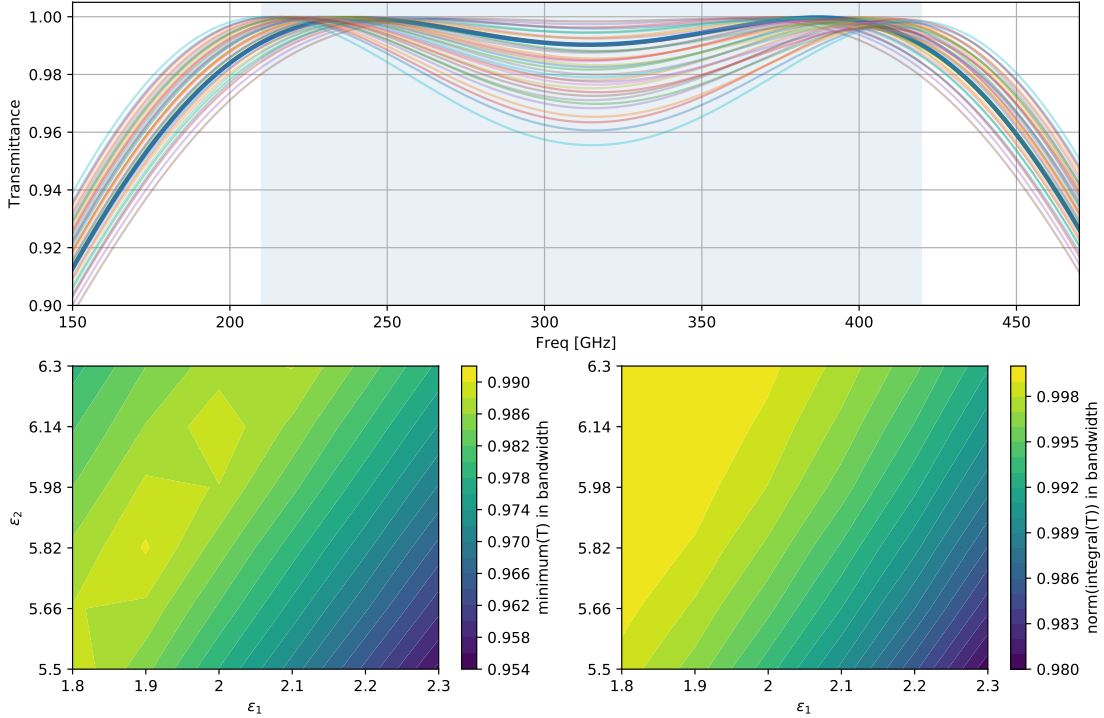


Figure 3.16: CST transmittance simulations of double-layer metamaterial ARCs, with varied target dielectric constants. The pitch of these simulations is held constant at $65.33\ \mu\text{m}$. The layer depths are a quarter wavelength in the index of each layer. The hole widths are determined for a given dielectric constant using Equation 3.34. The upper panel overplots all simulated transmittances. The lower panels plot the minimum in-band transmittance and the integrated in-band transmittance over the dielectric constant parameter space. The transmittance when $\epsilon_1 \approx 1.90$ and $\epsilon_2 \approx 5.82$ is highlighted in the upper panel.

Comparing the results of this CST parameter sweep to the parameter search we performed with the dielectric theory (see Figure 3.9), we see a similar structure, but a slightly different optimal set of dielectric constants at $\epsilon_1 \approx 1.90$ and $\epsilon_2 \approx 5.82$. The transmittance profile for this combination of dielectric constants is bolded above the rest. We carry these new dielectric constants forward into our depth and hole width optimizations.

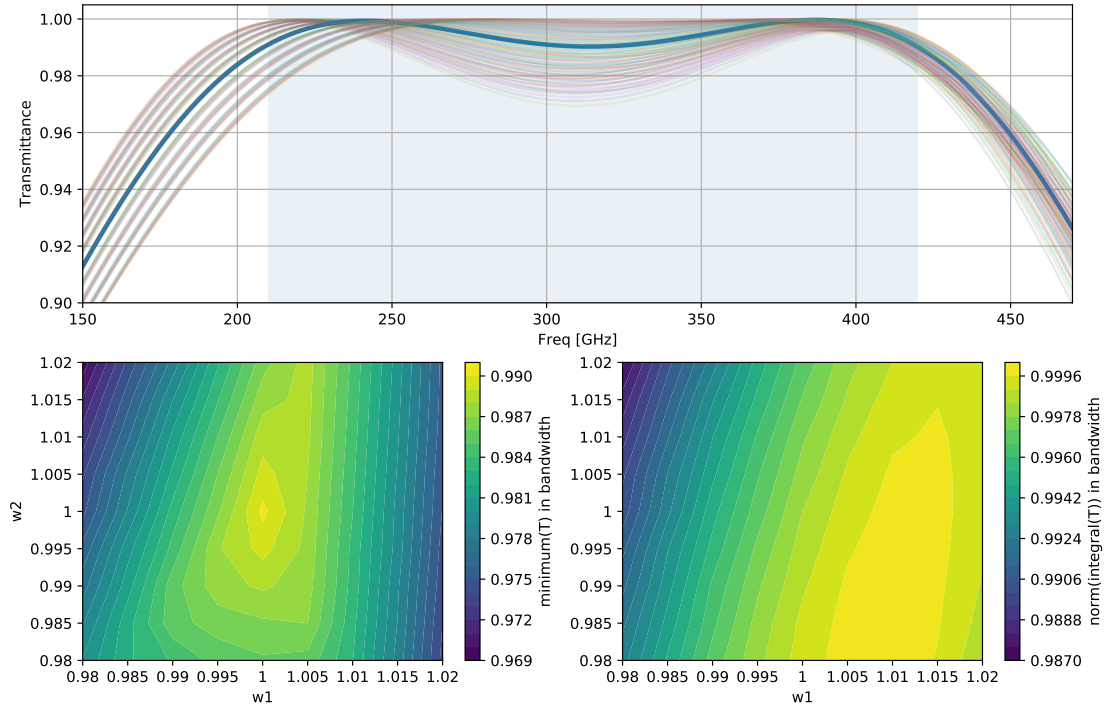


Figure 3.17: CST transmittance simulation sweep of double layer metamaterial ARCs, with varied hole widths. The nominal design uses $\epsilon_1 \approx 1.90$ and $\epsilon_2 \approx 5.82$ and quarterwave layer depths. The upper panel plots all simulated transmittances. The lower panels plot the minimum in-band transmittance and the integrated in-band transmittance over the fractional width parameter space. The fractional width is defined as the fractional deviation from the width given by Equation 3.34 for the target index of each layer. The transmittance when $w_1 = w_2 = 1$ is highlighted in the upper panel.

Figure 3.17 shows the sweep results when the hole width of each layer is perturbed by up to $\pm 2\%$. The x and y-axes of the lower panels are fractional changes to the hole widths away from the nominal values which are determined for $\epsilon_1 \approx 1.90$ and $\epsilon_2 \approx 5.82$ using Equation 3.34. During the hole width sweep, all other parameters were held at their nominal values. The transmittance with $w_1 = w_2 = 1$ is bolded in the upper panel. However, based on the sum of the in-band transmittance plot (lower right), we find that the best performance is not necessarily at $w_1 = w_2 = 1$. From the lower right panel, it is also evident that the

ARC performance is strongly dependant on the width of the upper ($i = 1$) layer width, but much less so on the lower ($i = 2$) layer. Percent-level deviations in the upper layer hole width can have a one percent decline in the minimum in-band transmittance. By prioritizing the minimum in-band transmittance merit function, we select to remain with the nominal $w_1 = w_2 = 1$ design.

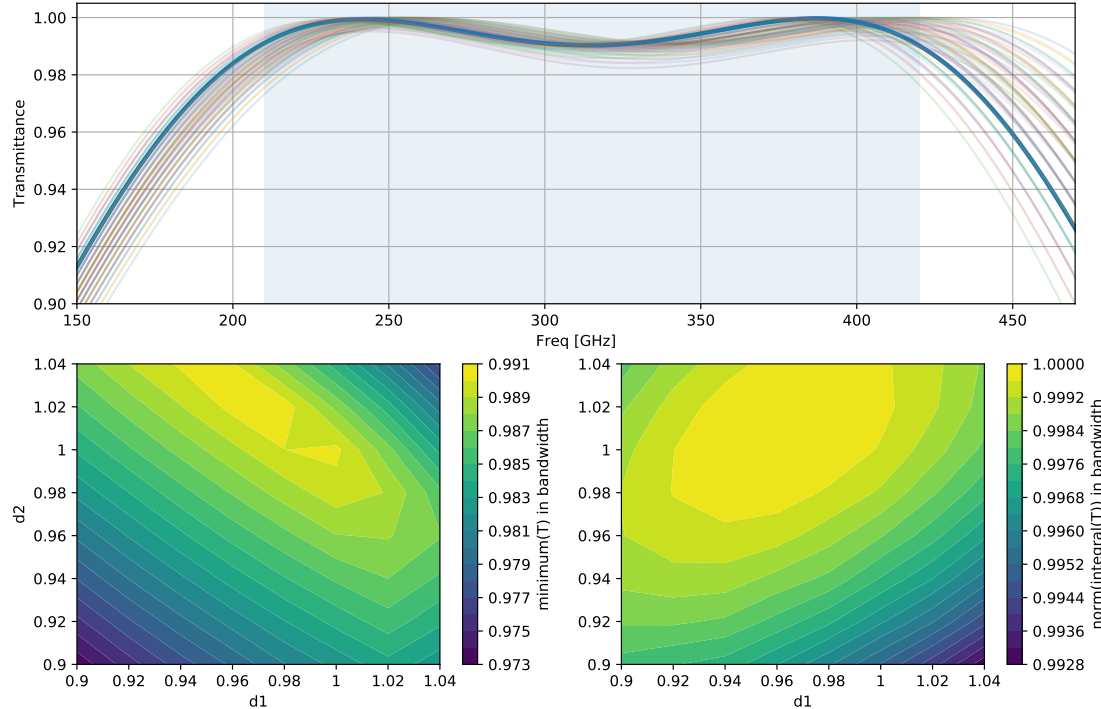


Figure 3.18: CST transmittance simulation sweep of double layer metamaterial ARCs, with varied hole depths. The nominal design uses $\epsilon_1 \approx 1.90$ and $\epsilon_2 \approx 5.82$ to determine the hole widths which are held constant in this parameter sweep. The upper panel plots all simulated transmittances. The lower panels plot the minimum in-band transmittance and the integrated in-band transmittance over the fractional depth parameter space. The fractional depth is defined as the fractional deviation from the quarter wavelength depth given the target index of the layer. The transmittance when $d_1 = d_2 = 1$ is highlighted in the upper panel.

Figure 3.18 shows the sweep results when the depth of each layer is perturbed by $\pm 4.0\%$. The x and y-axes of the lower panels are fractional changes to the

layer depth away from the nominal quarter wavelength depth. During the layer depth sweep, all other parameters (such as the pitch, target index, and widths) were held at their nominal values. The nominal transmittance with $d_1 = d_2 = 1$ is bolded in the upper panel. Comparing the results of this CST parameter sweep to the parameter search we performed with the dielectric theory (see Figure 3.10), the structure of the merit functions look similar. The optimal performance again is not necessarily at $d_1 = d_2 = 1$. The integrated in-band merit function (lower right panel) suggests that the optimal performance tends to prefer upper layer depths that are slightly smaller than nominal. Further, from the minimum transmittance merit function (lower left panel) we note that if d_1 is smaller than the nominal design, then d_2 prefers to be larger, and vice versa. The minimum in-band transmittance is relatively tolerant to deviations of up to a few percent, which would cause a $\lesssim 0.5\%$ decrease in transmittance. We choose $d_1 = 0.97$ and $d_2 = 1.02$ to optimize the minimum in-band transmittance.

The process of optimizing w_i and d_i can be iterative. Choosing the hole widths will affect the performance of a depth sweep and vice versa. Some eyeballing must be done in order to choose from the width and depth sweeps. The two merit functions plotted do not tend to agree on an optimal design. There may also be other merit functions that were not explored which could lead to more optimal designs. This is suggested as future work if stricter requirements for two-layer metamaterial ARCs are needed. Table 3.1 records the optimal values given from the sweep over dielectric constants above, and taking $w_1 = w_2 = 1$, $d_1 = 0.97$, $d_2 = 1.02$ as an optimal configuration.

Figure 3.19 plots the transmittance of the optimized ARC defined in Table 3.1 as a function of angle of incidence. The ARC performs well for a wide range

Parameter	Value
Metamaterial structure pitch	65.33 μm
Target upper layer dielectric constant	1.90
Target lower layer dielectric constant	5.82
Substrate dielectric constant	11.7
Upper layer hole width	60.01 μm
Lower layer hole width	42.16 μm
Upper layer depth	167.48 μm
Lower layer depth	100.63 μm

Table 3.1: Double-layer ARC parameters, optimized via EM simulation parameter sweeps. The metamaterial pitch was chosen to optimize the ARC bandwidth. The target indices were then chosen to minimize the in-band reflectances. The hole widths were determined via Equation 3.34 and the hole depths are quarter wavelength, in the layer index. Via parameter sweeps, the nominal hole widths and depths were found to satisfy the performance requirements.

of angles. As the angle of incidence increases, the bandwidth and band-center are blue-shifted. At 30° , the transmittance at 210 GHz degrades by roughly one percent while the higher frequencies see a modest boost in transmittance. At 40° , the transmittance near band-center falls below 99%, the low frequency end of the bandpass has shifted significantly to higher frequencies, and the bandwidth is diminished. Off-axis beams will pass through EoR-Spec’s FPI at angles up to $\sim 27^\circ/2 = 13.5^\circ$, so this understanding of the ARC performance will be valuable for determining the optics design of the rest of the module.

Lastly, we also use CST to simulate the effects of fabrication defects on the ARC performance. Various physical defects can be added to the 3D model of the metamaterial structure. For example, the deep silicon etching process that we have developed does not always produce perfectly vertical sidewalls. We can use a CST model to place a tolerance on the sidewall taper angle. Figure 3.20 shows a simulation sweep over which the sidewalls of the holes are tapered inwards (so

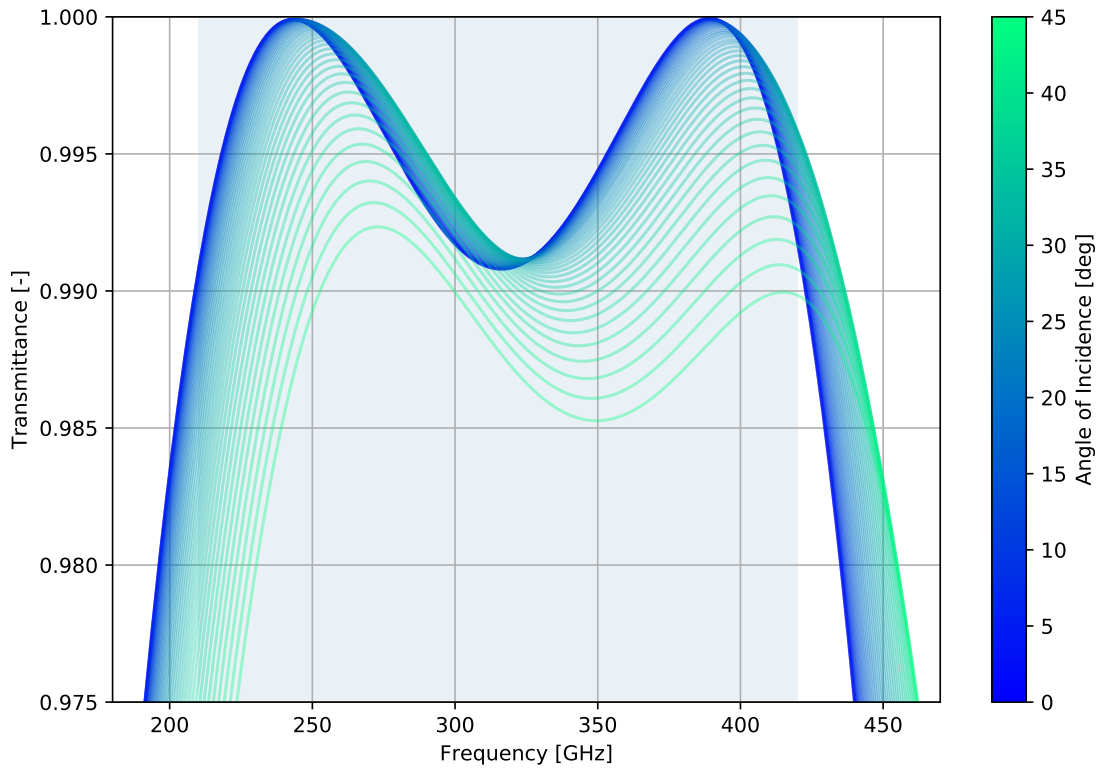


Figure 3.19: CST transmittance simulation sweep of double layer metamaterial ARCs, with varied angles of incidence. Nominal design parameters are taken from Table 3.1. As the angle of incidence is increased, the bandpass is blue-shifted. The ARC performance remains adequate up to about 30°. Beyond that, the bandwidth is minimized and the transmittance near the band-center drops precipitously.

that the hole width gets narrower as the depth increases). It is not surprising that the transmittance is strongly affected by the sidewall taper because we already saw that small changes in the hole width affect the ARC performance (i.e., Figure 3.18). However, if the deep silicon etching process produces consistently tapered sidewalls, then an optimal ARC design can be found by re-sweeping the hole width and layer depths, holding the sidewall taper as a constant in the EM model.

With a well-performing double-layer ARC design, we now move on to developing a design for the metal mesh reflectors. Once both components are designed, we

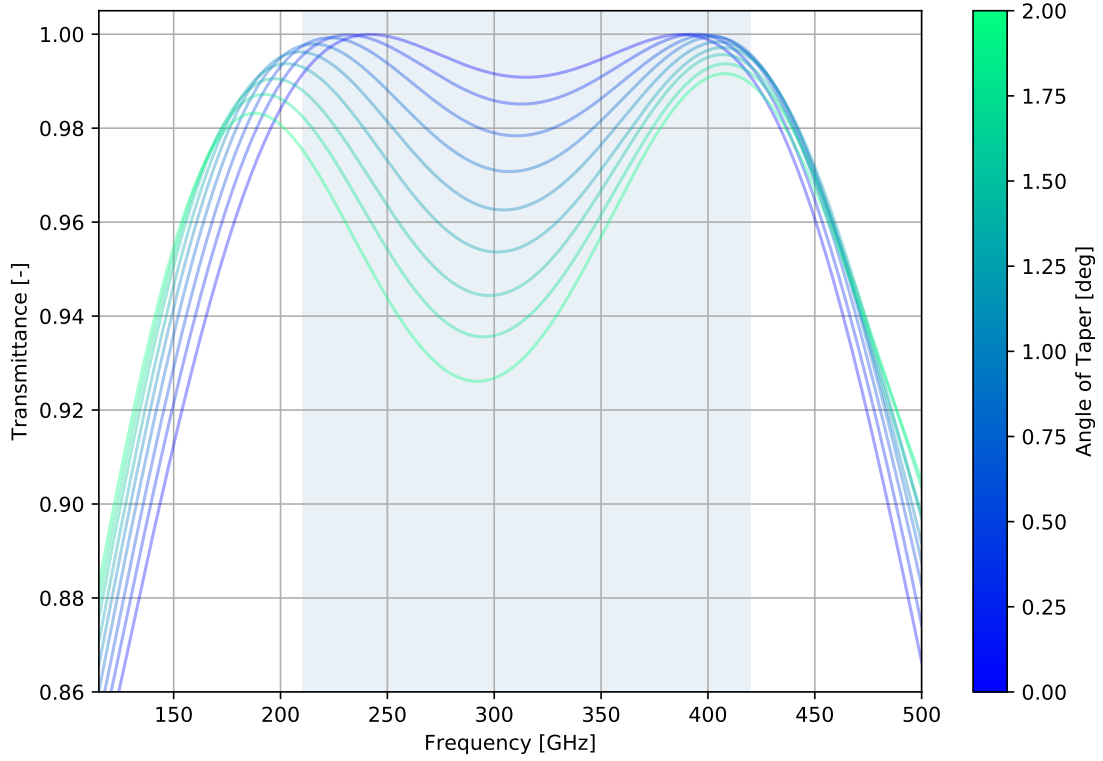


Figure 3.20: CST transmittance simulation sweep of double layer metamaterial ARCs, with varied sidewall taper angles. Nominal design parameters are taken from Table 3.1. As the sidewall taper angle is increased, the transmittance is reduced throughout the band.

will generate EM simulations combining an approximate model for the ARCs and the reflectors and then evaluate the performance of a model of an entire mirror.

3.4 Silicon Substrate-Based FPI Mirrors

A cryogenic silicon substrate scanning FPI consists of two silicon mirrors, each coated with one reflective surface and one anti-reflective surface. In this section, we discuss models and EM simulations of silicon-based metal mesh reflectors, single FPI mirrors, and the full EoR-Spec silicon-based scanning FPI. We also discuss

Ohmic and dielectric losses in these silicon-based devices.

Figure 3.21 shows an illustration of a silicon substrate-based FPI. The ARC on the outer surface of each mirror is critical for minimizing Fresnel reflections which could generate parasitic resonances in the FPI transmittance. Each inner mirror surface is coated with a thin, lithographically patterned mesh like the inductive and capacitive designs shown here.

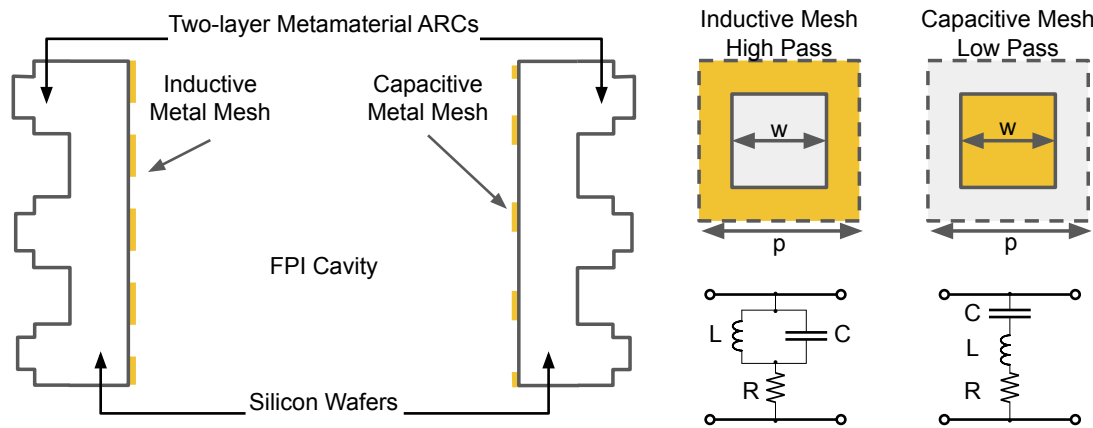


Figure 3.21: *Left:* SSB FPI illustration, showing metamaterial ARCs and metal meshes on silicon wafers, forming an etalon. *Right:* Illustration of basic metal mesh unit cells and corresponding equivalent circuit models.

3.4.1 Frequency Selective Metal Mesh Reflectors

Metal meshes have been used as reflective filters and polarizers for microwave and infrared instruments since the mid-1900s [117, 147]. For applications in the fields of astronomy and cosmology, simple inductive and capacitive filters are the most common and are often stacked (in the direction of wave propagation) in order to produce sharp cutoff or bandpass filters [4]. In defense and security applications, more complex shapes and cascaded filters (generally termed frequency selective

surfaces) are used for bandpass and bandstop filters to minimize the radar cross-sections of planes and ships [106]. Empirical studies have related the geometric properties of meshes to lumped-element circuit parameters to develop transmission line models for the transmittance, reflectance, and absorptance of metal meshes [98, 146, 147].

For simple inductive and capacitive meshes such as those shown in Figure 3.21, transmission line models have been built based on experimental data. In the 1960s, Ulrich developed the multi-element equivalent circuit representations shown in Figure 3.21, and constructed models for their transmittance [147]. Fitting his models to transmittance and reflectance data for a variety of capacitive meshes in the sub-mm, Ulrich empirically related the mesh geometry (characterized by the ratio of the square width to the pitch, w/g) to an effective capacitance so long as $w/p > 0.7$. The data for inductive meshes did not fit as well to Ulrich's model, though this may be due to the relatively thick metal wires that were used at the time for structural integrity of freestanding inductive meshes [108]. Ulrich also established a relationships for the resonant frequency and resistive loss term for capacitive meshes based on w/p and the resistivity of the mesh material (Section 3.4.5).

Since the 1960s, improvements have been made to the transmission line approach [124] and have expanded it to a variety of different mesh geometries for various applications [31, 98, 106]. Significant effort has also gone into analytically solving the behavior of metal meshes via electromagnetics with Maxwell's equations [16, 95, 103]. Modern metal mesh design is primarily performed using software packages that numerically solve Maxwell's equations for a given unit-cell of the structure.

EM modeling of metal meshes via CST is similar to that of metamaterial ARCs (Section 3.3.3). Important design considerations are the ratio of the square width to the pitch, w/p , the ratio of the pitch to the wavelength, p/λ , and the thickness of the mesh. As with ARCs, the metal mesh pitch must be less than the wavelength of incident radiation such that $p < \lambda/n$ where n is the index of refraction of the dielectric substrate. When this is not satisfied, the mesh can diffract incident radiation. Additionally, the thickness of metal mesh must be much less than a wavelength but also greater than the skin depth of the metal. A final constraint is related to fabrication: the method we currently use for patterning these meshes on silicon is limited to minimum feature sizes of $\approx 1\ \mu\text{m}$, setting physical limits on w and p .

Figure 3.22 shows CST transmittance simulations of inductive and capacitive meshes designed for EoR-Spec. These meshes consist of a $100\ \mu\text{m}$ thick layer of cryogenic gold ($\rho_{\text{Au},1\text{K}} = 2.2 \times 10^{-10}\ \Omega \cdot \text{m}$) [68] on top of a $10\ \text{nm}$ thick adhesion layer of chromium ($\rho_{\text{Cr}} = 1.25 \times 10^7\ \Omega \cdot \text{m}$) that is necessary for fabrication. The chromium layer's thickness is well below a skin depth, so it is not expected to significantly contribute to the reflectance or absorptance of the mirrors. Decreasing (increasing) the pitch of either geometry would stretch (compress) their transmittance profiles to the right (left). Changing the ratio of the square width to the pitch, w/p , would change the shape of the filter and move the cutoff frequency. Thus, the design of metal mesh reflectors for FPI mirrors comes down to optimizing w/p and p/λ for the desired reflectance and bandwidth.

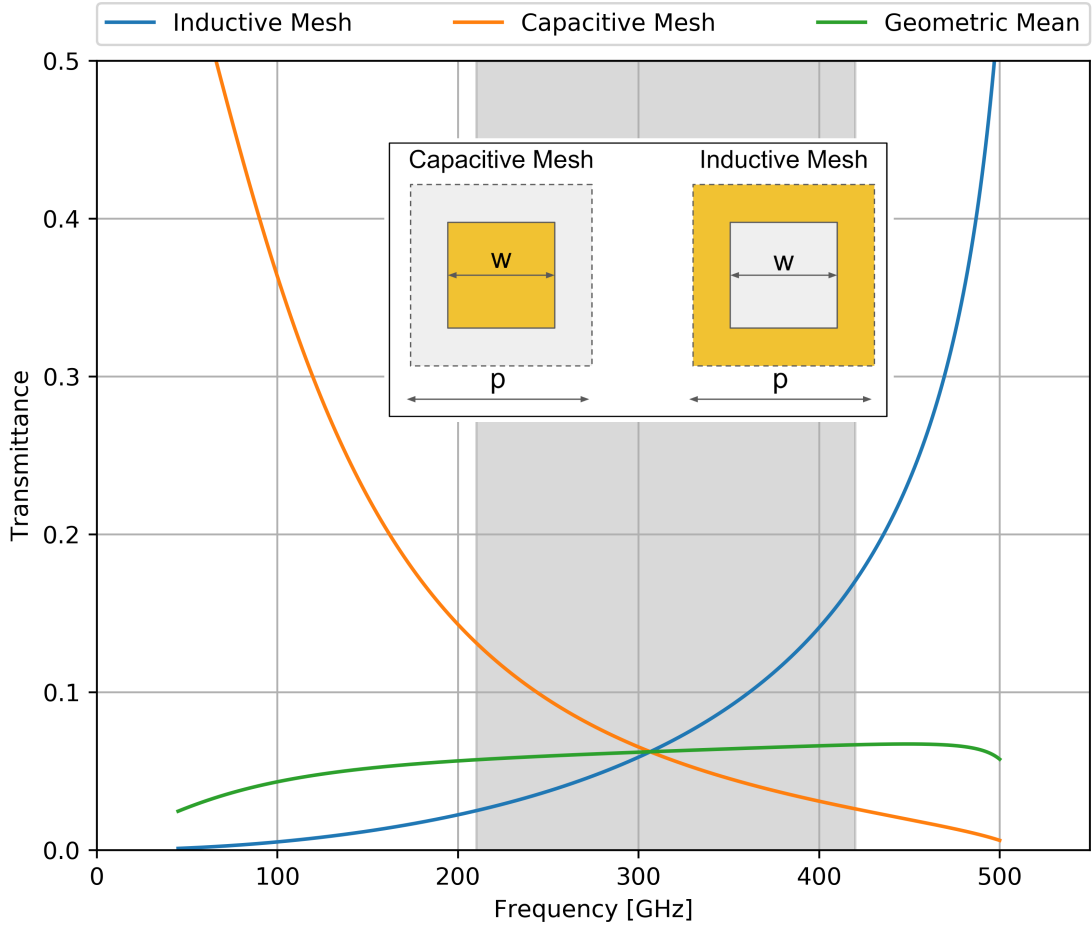


Figure 3.22: CST transmittance simulations of inductive and capacitive gold meshes on silicon substrates ($\epsilon_{\text{Si}} = 11.7$). The inductive (capacitive) design produces a high-pass (low-pass) filter shape. The geometric mean transmittance is shown in green. For these simulations, $p = 171.29 \mu\text{m}$, $w_{\text{cap}} = w/p = 0.96$, $w_{\text{ind}} = w/p = 0.59$, and the gold resistivity is $\rho_{\text{Au},1\text{K}} = 2.2 \times 10^{-10} \Omega \cdot \text{m}$.

3.4.2 Mesh Designs for Wide-Bandwidth Interferometers

As shown in Figure 3.22, the reflectances of inductive and capacitive meshes have strong frequency dependencies. Since the finesse of a FPI is a function of the reflectance, the finesse of a FPI based on these filters will also have a strong dependence on frequency. For wide-band spectrometry, such as EoR-Spec's pro-

posed LIM measurements, having a frequency dependent finesse (and thus resolving power) is not desirable. When the reflectance is too high, the finesse will increase and mesh absorption will cause a loss of transmitted power. When it is too low, the spectral resolving power will decrease beyond usefulness.

Ideally, for EoR-Spec, the FPI will have a flat finesse of $\mathcal{F} \sim 50$ over the octave 210–420 GHz such that the resolving power of both the second and third order fringes stays constant (with resolving powers of 100 and 150 respectively) across the band. A finesse of 50 corresponds to a mirror reflectance of $\mathcal{R} \sim 94\%$. It is impossible to achieve such a reflectance over an octave of bandwidth using either a pair of inductive mirrors or a pair of capacitive mirrors. However, recall in Section 3.2.1 when we made the simplifying assumption that $R_1 = R_2 = \mathcal{R}$ and defined $\mathcal{F} = \frac{\pi\sqrt{\mathcal{R}}}{1-\mathcal{R}}$. If we relax this assumption and say that we have an asymmetric FPI ($R_1 \neq R_2$), then we can rewrite the finesse such that it is a function of the geometric mean of the mesh reflectances, $\mathcal{F} = \frac{\pi\sqrt[4]{R_1 R_2}}{1-\sqrt{R_1 R_2}}$. This is not strictly valid because for such an asymmetric FPI, the relation $1 = \mathcal{T} + \mathcal{R} + \mathcal{A}$ no longer holds¹² and we can no longer define \mathcal{F} as we did in Equation 3.7. Nevertheless, this approximation provides a rough guide for mesh design which relates the finesse to the geometric mean of the two mirror reflectances ($\sqrt{R_1 R_2}$). The geometric mean of the inductive and capacitive mesh reflectances is plotted in Figure 3.22 and for these particular meshes, provides a flat transmittance between 5% and 6%, corresponding to 95% and 94% reflectance if the absorptance is negligible.

In addition to simple square inductive and capacitive geometries, we have investigated the use of other mesh designs for FPI mirrors. For example, a square inductive mesh loaded with square patches, or loaded with square annuli. Both

¹²It is true that $1 = T_i + R_i + A_i$ for both meshes ($i = 1, 2$) independently, but it is not required that $1 = \sqrt{T_1 T_2} + \sqrt{R_1 R_2} + \sqrt{A_1 A_2}$.

of these designs create resonant features with relatively narrow bandpasses. The complementary designs, a square annulus, and a loaded square annulus were also investigated but unsurprisingly also had narrowband features [106]. Additionally, we investigated capacitive square cross meshes and square inductive meshes loaded with crosses. Among all of these geometries, no configurations with a flat reflectance of $\sim 95\%$ were found over a wide bandwidth.

Other methods for designing a metal mesh with the requisite reflectance profile include testing arbitrary patterns within a unit cell of the mesh. Such a process would typically be prohibitively time consuming and complex but recent studies have employed machine learning techniques to develop filter designs for a desired transmittance profile [142, 143]. These methods have shown success for designing sharp cutoff filters of different types but have yet to be fully explored and applied to the partially reflective filters required for FPIs.

In order to optimize the inductive and capacitive meshes for use in EoR-Spec, we first simulate single meshes of both types on silicon, for a variety of w/p ratios. Figure 3.23 shows the reflectance of many inductive and capacitive meshes as a function of normalized frequency in the dielectric medium, $\omega = p/(\lambda/n)$. Each curve corresponds to a single w_{ind} and w_{cap} which are defined as the ratios of the square width to the pitch w/p for inductive and capacitive meshes respectively. With the reflectance of both types of meshes, we can then compute the geometric mean reflectance, and look for a combination that is relatively flat over an octave and about 95% reflective.

The upper panel of Figure 3.24 shows the geometric mean of every combination of inductive-capacitive meshes that were shown in Figure 3.23. A band between 94 and 96 % reflectance is shown corresponding to finesse of 50 and 77 respectively.

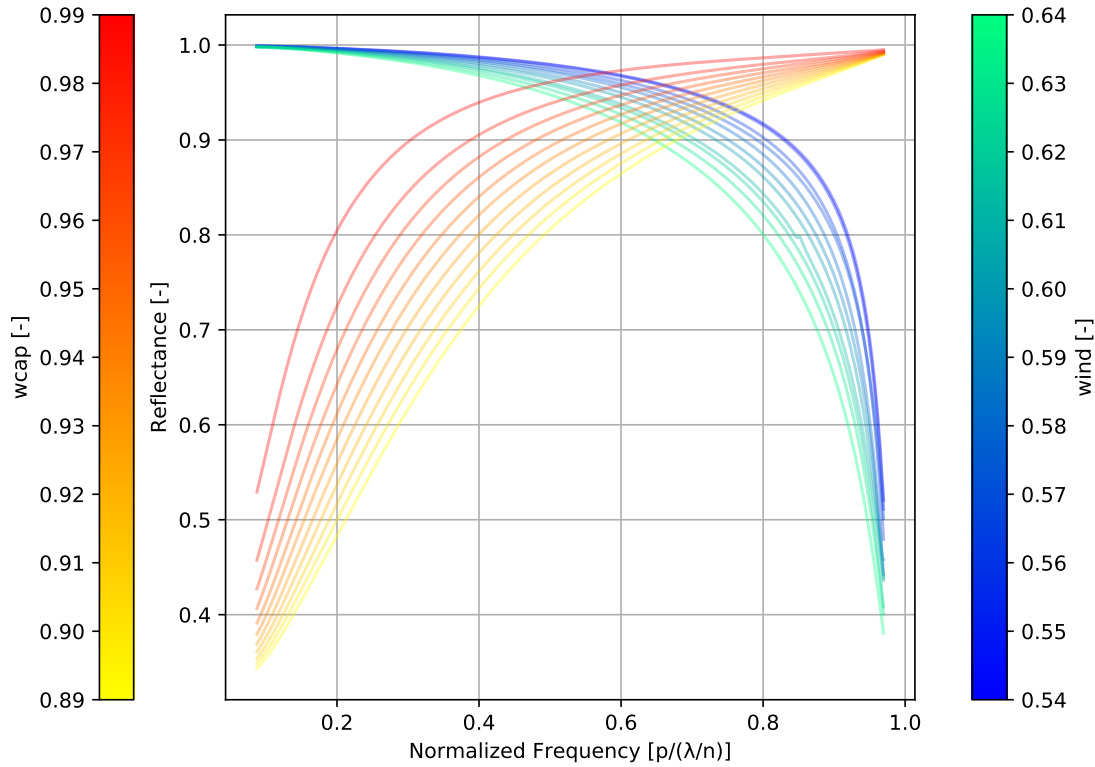


Figure 3.23: CST reflectance simulations of square inductive and capacitive metal mesh designs for a variety of linear fill ratios, w/p , plotted as a function of the normalized dimensionless frequency, $\omega = p/(\lambda/n)$. The inductive designs are the high-pass filters in blue-green. The capacitive designs are the low-pass filters in yellow-red. w_{ind} and w_{cap} are the ratios of the square width to the pitch, w/p , for inductive and capacitive geometries respectively.

The lower panels show the bandwidth and maximum finesse as a function of w_{ind} and w_{cap} . The bandwidth of each combination is computed as the ratio of highest and lowest frequencies where the reflectance is above 94% and is shown in the lower left panel. The lower right panel takes the maximum reflectance of each combination and plots the corresponding finesse as a function of w_{ind} and w_{cap} .

In order to achieve EoR-Spec's octave of bandwidth with $\mathcal{F} \approx 50$, we want to pick a combination of w_{ind} and w_{cap} that provides a bandwidth of at least 2 while minimizing the maximum finesse. There is some flexibility in this choice,

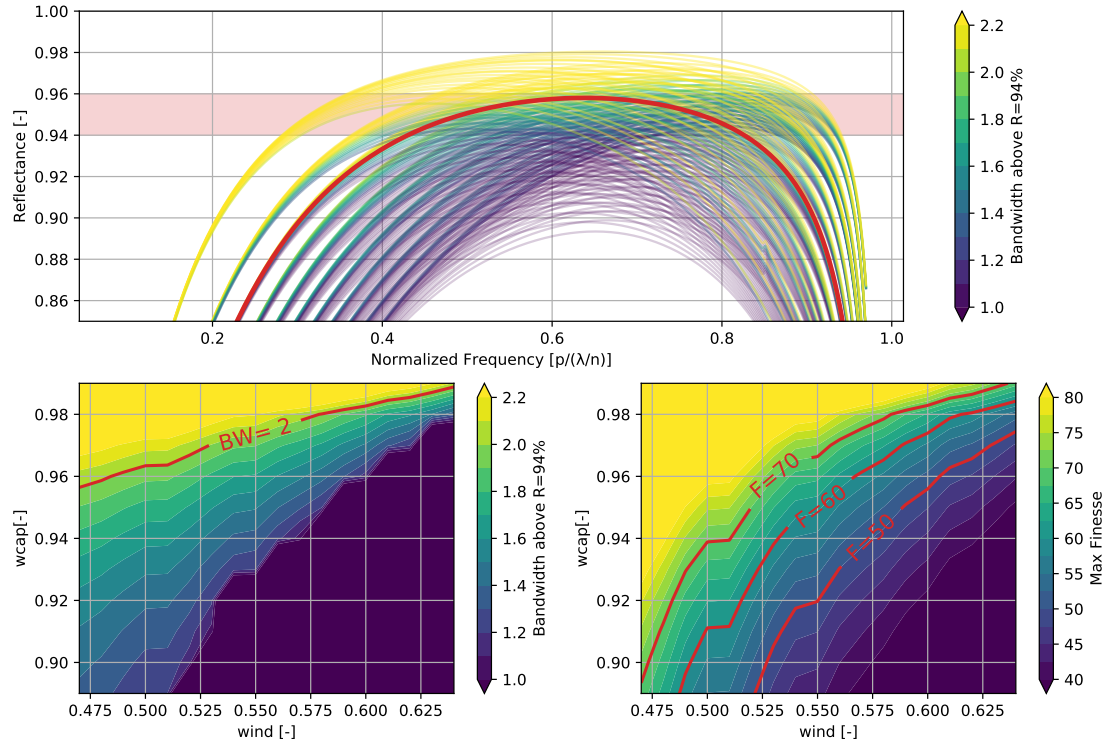


Figure 3.24: Inductive and capacitive mesh optimization using the geometric mean reflectance. The upper panel plots the geometric mean of every combination of w_{ind} and w_{cap} in Figure 3.23 as a function of the dimensionless normalized frequency. A pink band indicates the desired reflectance range, 94–96%. The color of each line indicates the bandwidth above $R = 0.94$. The lower panels plot the bandwidth and maximum finesse of each combination for the entire parameter space. The reflectance for $w_{\text{ind}} = 0.54$ and $w_{\text{cap}} = 0.97$ is highlighted in the upper panel.

since there are many curves with bandwidth around 2. For example, $w_{\text{ind}} = 0.54$ and $w_{\text{cap}} = 0.97$ work reasonably well with a maximum finesse of about 73 and a bandwidth with $R > 0.94\%$ just under 2. This combination of w_{ind} and w_{cap} is highlighted in bold red in the upper panel and the center of its $R > 0.94\%$ bandpass is at a normalized frequency of $\omega = 0.628$. Using $\omega = p/(\lambda/n)$, and placing the center frequency at 315 GHz, we arrive at the target pitch for these meshes at $p \approx 175 \mu\text{m}$. We could have chosen a combination with a higher bandwidth and

lower finesse if we went to higher w_{ind} and w_{cap} but we want to avoid very high values of w_{cap} for fabrication limitations. Below, this mesh design is combined with an ARC design and the performance of both inductive and capacitive mirrors is confirmed.

3.4.3 Electromagnetic Simulations of Single FPI Mirrors

After determining the ARC and metal mesh geometries through the parameter sweeps described above, we build and simulate models of single FPI mirrors. Simulating the mirrors separately prior to simulating the full FPI is useful for confirming the ARC and metal mesh performances and for understanding the mirror performance in-band and out-of-band.

A model of a single mirror is effectively a model of a simple low or high pass filter in series with a wide-bandpass filter. However, the ARC and metal meshes do not necessarily have the same pitch, and so combining the CST models of each is non-trivial. In order to build a unit cell containing both models, one would need to either force both designs to use the same pitch, or to construct a model with a unit cell size equal to the least common multiple of the ARC and mesh pitches. Forcing the ARC and metal meshes to have the same pitch is, in general, not an option. As we saw in the previous subsection, the metal mesh pitch is set to $p = 175 \mu\text{m}$ by the bandwidth optimization of the effective reflectance. Similarly, as we saw in Figure 3.15, the ARC pitch is constrained to $p \lesssim 130 \mu\text{m}$ by the ARC bandwidth optimization. Instead of forcing the same pitch, if the EM model of the ARC is sufficiently similar to the homogeneous approximation, a homogeneous ARC model can be used in place of the metamaterial model. The homogeneous model, with indices equal to the effective indices of the metamaterial layers, can

then use the same pitch as the metal meshes.

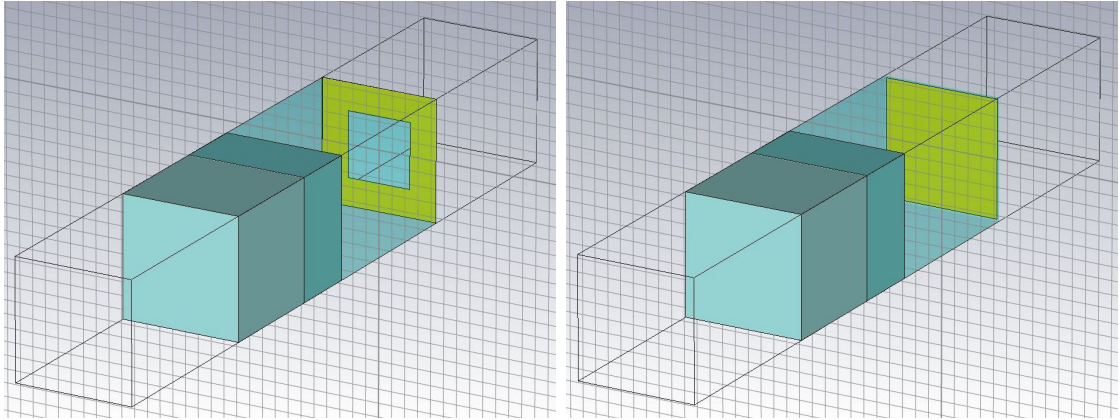


Figure 3.25: Screenshots of the single mirror designs in CST including the homogeneous approximation for the ARC on the front side of a silicon substrate (transparent) and metal meshes on the backside. Periodic boundary conditions are set on the lateral sides of the unit cell. Floquet ports (hidden) are defined in free space some distance away from both surfaces.

Figure 3.25 shows screenshots of the inductive and capacitive single mirror models in CST. Note that the Floquet ports (hidden) are located in freespace, some distance away from the top ARC and metal mesh surfaces. The left most two layers comprise the homogeneous ARC. The silicon substrate was made transparent in order to illustrate the metal meshes beyond it.

Figure 3.26 shows the reflectance of these CST models. The mesh resistivity assumes that of gold at 1 K, ($\rho_{\text{Au},1\text{K}} = 2.2 \times 10^{-10} \Omega \cdot \text{m}$), and the silicon is assumed to be lossless ($\text{Im}(\epsilon_{\text{Si}}) = 0$). As expected, the geometric mean of the inductive and capacitive reflectances is relatively flat between roughly 94 and 96% within the EoR-Spec band. The reflectance drops most at the band edges, which is expected given the mesh geometry which had a bandwidth slightly under 2. The subtle variability within the bandpass is due to Fabry-Perot fringing inside the silicon substrate and is caused by the imperfect ARC. This variability is strongly

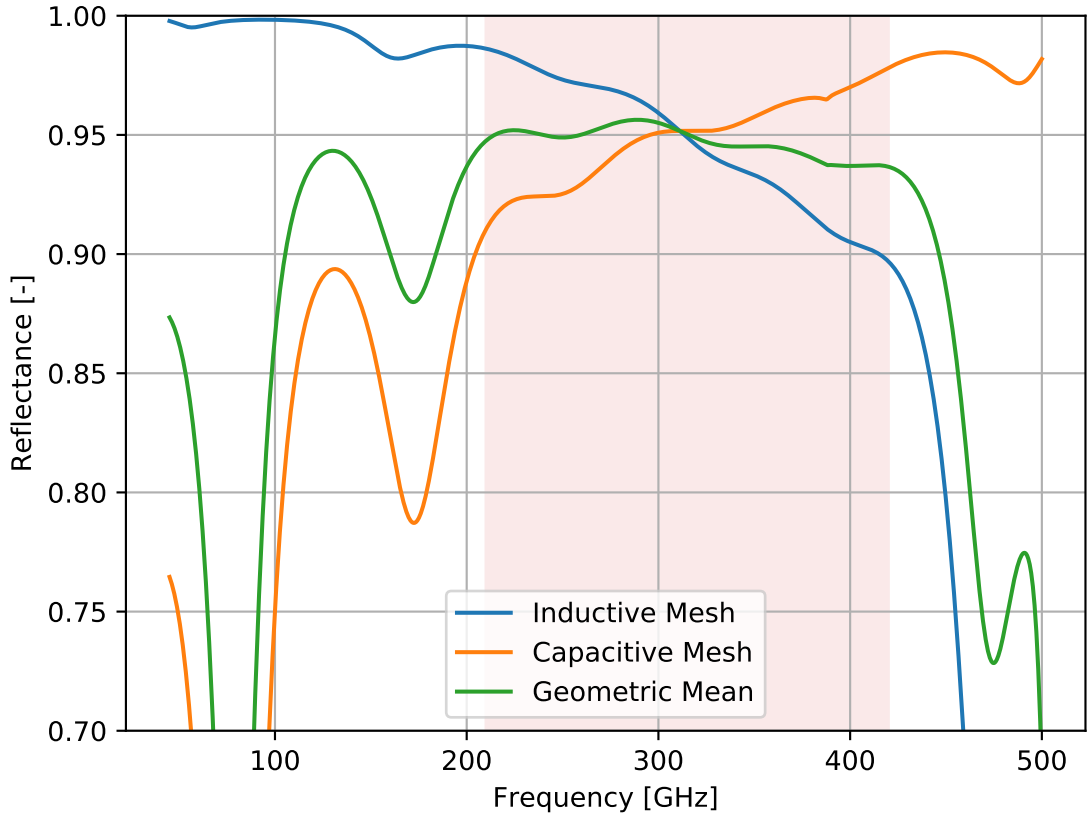


Figure 3.26: CST reflectance simulations of inductive and capacitive fold meshes on silicon substrates with double-layer ARCs. The ARC design uses the geometry specified in Table 3.1. The metal mesh geometries used correspond to the optimized mesh design from Section 3.4.2. The green line shows the geometric mean of the mirror reflectance which can be used as an approximation for the FPI mirror reflectance when estimating the expected finesse. Slight variations in the bandpass are due to fringing within the silicon substrate due to the imperfect ARC.

correlated with the thickness of the substrate. The variability and fringing seen here, where the substrate was assumed to be $600 \mu\text{m}$ thick (before etching the ARC layers), will be different from the variability and fringing from a $500 \mu\text{m}$ thick substrate. The thickness of the substrate must be chosen carefully. The performance of these mirrors should be adequate, but one could attempt the same optimization over w_{ind} and w_{cap} as detailed in the previous section for this full mirror model if the design requires modification.

3.4.4 Electromagnetic Simulations of Silicon Substrate-Based FPIs

The simplest silicon based interferometer is a bare silicon wafer with no coatings whatsoever. A standard silicon wafer is a resonating cavity and constitutes an etalon. The resonant frequency depends on the wafer thickness, the index of refraction in the wafer, and the angle of incidence (see Equation 3.5). The finesse is simply a function of the Fresnel reflections at the silicon-vacuum interfaces on either side of the wafer (see Equation 3.11). With an index $n_{\text{Si}} = 3.4$, we roughly expect a reflectance of $\mathcal{R} = 30\%$ corresponding to a low finesse of $\mathcal{F} = 2.5$.¹³ With $\mathcal{R} = 30\%$ at both surfaces, we expect the mean transmittance through the both surfaces to be $\mathcal{T}^2 = (1 - \mathcal{R})^2 \approx 50\%$. Figure 3.27 shows a CST simulation of the transmittance through a 500 μm thick silicon wafer. The Fabry-Perot fringes are evident, with the fundamental resonance at $f_{m=1} \approx 80$ GHz. Measuring the FWHM of the fringes confirms that the finesse is on the order $\mathcal{F} \sim 2.5$. The mean transmittance is also as expected, near 50%.

Figure 3.27 also plots the transmittance of a 500 μm thick silicon wafer with metalized surfaces. In this simulation, an inductive mesh and a capacitive mesh were placed on either side of the silicon wafer. The mesh geometry is identical to the one used in the previous section. The two main fringes in the EoR-Spec band give finesses between 70 and 80, consistent with expectations from the parameter sweep shown in Figure 3.24. The fringes outside of the EoR-Spec band have significantly reduced transmittance as expected from the high and low-pass filtering of the

¹³Note that when defining the FWHM of an Airy function peak, we made the assumption that $\mathcal{F} \gg \pi/2$ in Equation 3.10. Here, with the low reflectance of bare silicon, we have broken that assumption and so we do not expect the FWHM to perfectly match the expected reflective finesse.

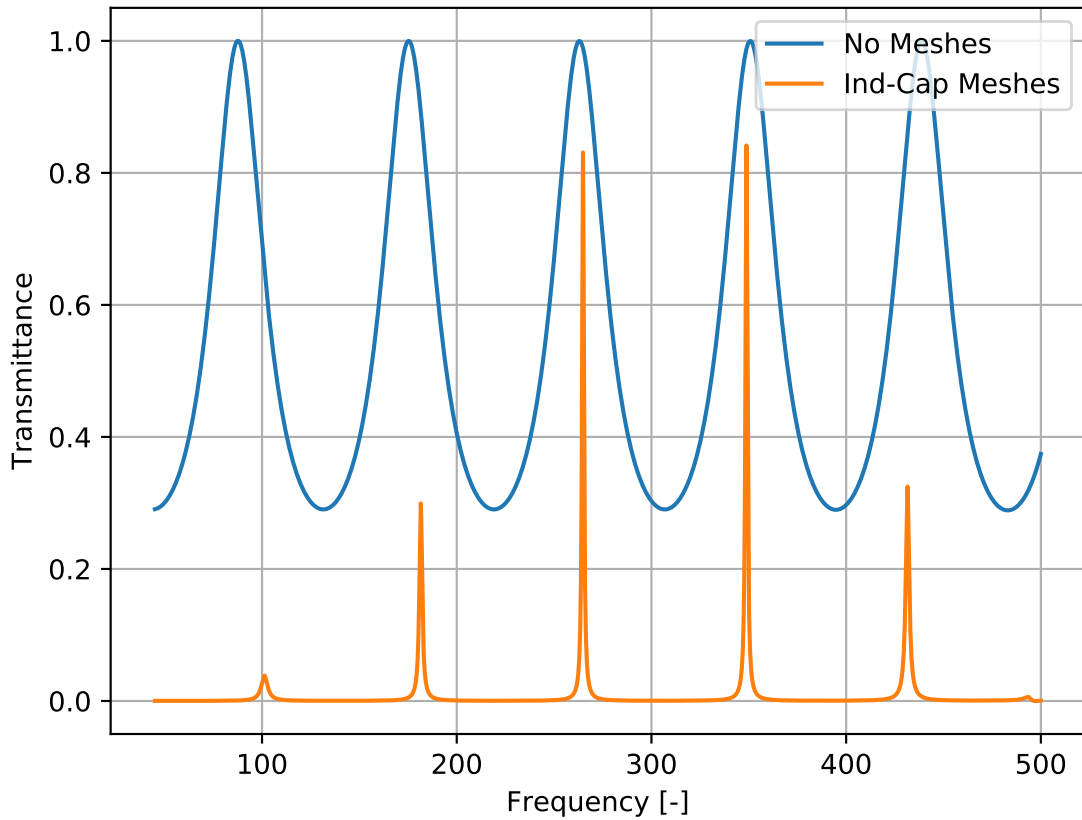


Figure 3.27: CST transmittance simulation through a bare and metalized silicon wafers. The mean transmittance of the blank wafer is $\approx 50\%$ as expected from the $\approx 30\%$ reflectance at each silicon surface. The metal mesh geometries used correspond to the optimized mesh design from Section 3.4.2. As expected, finesse between 70 and 80 are seen in the two main fringes in the middle of the EoR-Spec band.

inductive and capacitive meshes. This model includes dielectric losses in cryogenic silicon and metal mesh absorption in the cryogenic gold meshes. Note that the fringes of metalized silicon etalon do not line up with those of the bare silicon wafer. This is due to the frequency-dependent phase shift induced by the metal meshes upon reflections.

We now examine the performance of a full SSB FPI CST model. Figure 3.28 shows a screenshot of the dual SSB mirror FPI model in CST. The mirrors are

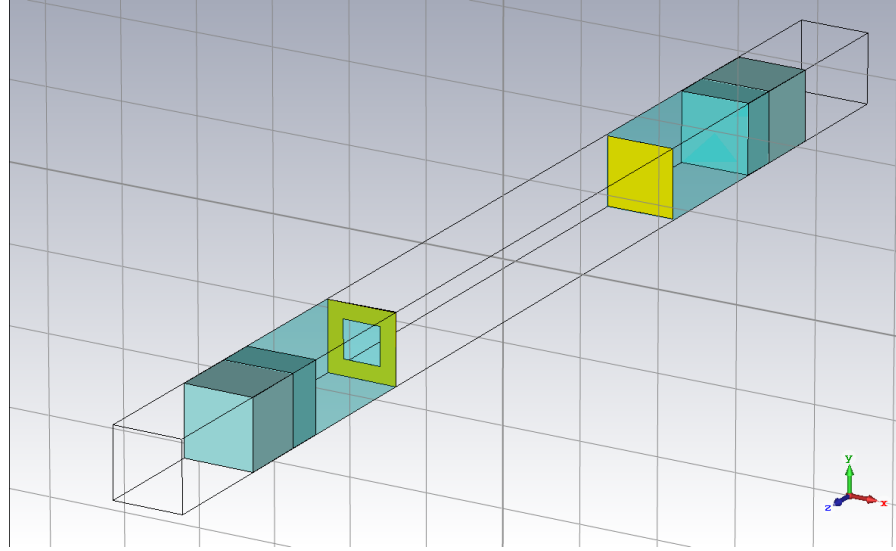


Figure 3.28: Screenshot of a full FPI model in CST including inductive and capacitive mirrors with homogeneous ARC. The free-space cavity between the two mirrors sets the resonant frequencies of the FPI. Periodic boundary conditions are set on the lateral sides of the unit cell. Floquet ports (hidden) are defined in free space some distance away from both surfaces.

the same mirrors that were examined in the previous section and in Figure 3.26. The mirror substrate thickness before etching the two-layer ARC is assumed to be 600 μm . The mirrors are oriented such that their reflective surfaces face each other, forming the vacuum gap resonance cavity. The spacing between the mirrors is set such that the second and third order FPI fringes are placed within the EoR-Spec band.

Figure 3.29 shows the results of this CST simulation for 15 different mirror separation distances. Changing the mirror separation scans the second and third order FPI fringes around the EoR-Spec band. By eye, the resolving power of the fringes appears to stay relatively constant across the EoR-Spec band. The peak transmittance is markedly better in the middle half of the band. This could be due in part to the un-even geometric mean reflectance of the mirrors shown in Figure

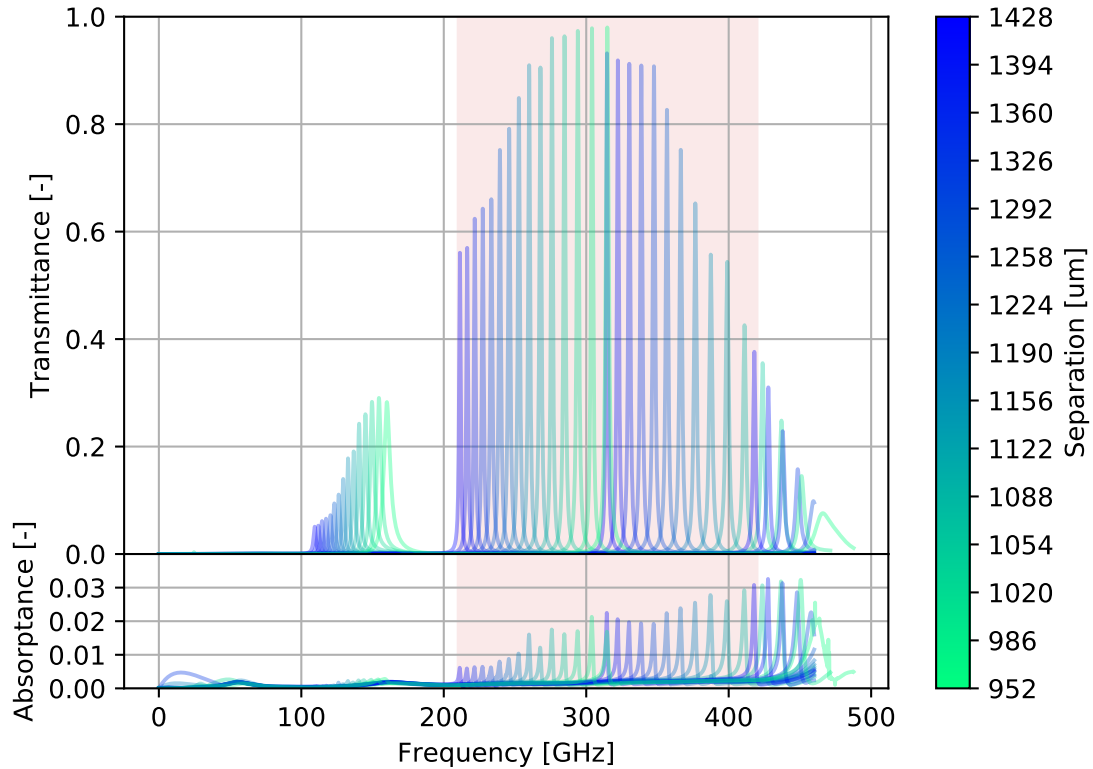


Figure 3.29: CST transmittance simulation for the full SSB FPI model, sweeping over the mirror separation. Absorptance ($\mathcal{A} = 1 - \mathcal{T} - \mathcal{R}$) is shown below the transmittance and is limited to a few percent. The parameters used in the model are given in Table 3.2. This model assumes cryogenic gold and silicon.

3.26. Optimizing the mirror substrate thickness and the mesh reflectance to create a more uniform 95% geometric mean reflectance may help bring power back into the higher end of the EoR-Spec band. By looking at the simulated reflectance as well as the transmittance, it is clear that the absorptance ($\mathcal{A} = 1 - \mathcal{T} - \mathcal{R}$) of the FPI is limited to a few percent. The absorptance is also greater on the high frequency side of the band. Assuming an absorptance of 2% and a reflectance of 94%, Equation 3.8 gives a max transmittance of $\approx 44\%$, which roughly agrees with the high frequency fringes. The CST model parameters for this SSB FPI model are given in Table 3.2

Description	Parameter	Value
Upper layer target dielectric constant	ϵ_1	1.9
Lower layer target dielectric constant	ϵ_2	5.82
Substrate dielectric constant	ϵ_{Si}	11.7
Upper layer ARC depth	d_1	167.48 μm
Lower layer ARC depth	d_2	100.63 μm
Substrate thickness	t_{si}	600 μm
Substrate dielectric loss tangent	$\tan \delta_{\text{Si}}$	3×10^{-6}
Metal mesh pitch	p	175 μm
Inductive mesh square width ratio	w_{ind}	0.54
Capacitive mesh square width ratio	w_{cap}	0.97
Metal mesh film thickness	t_{au}	100 nm
Metal mesh resistivity	ρ_{Au}	$0.022 \times 10^{-8} \Omega \cdot \text{m}$

Table 3.2: SSB FPI CST model parameters which generated the simulation results shown in Figure 3.29 and 3.30. Note that the ARC depths and widths are functions of the ARC target dielectric constant.

As EoR-Spec’s FPI is imaged onto its focal plane detector arrays, the resonant frequency observed at each detector will depend on its radius from the center of the focal plane. This is because the imaging optics will couple off-axis detectors to off-axis rays through the FPI. As we saw in Section 3.2.1 (Figure 3.3), off-axis rays in an FPI are blue-shifted and so off-axis detectors will see slightly blue-shifted resonances when compared to the central detectors. Therefore, it is important for us to know how the FPI performs for off-axis illumination. Figure 3.30 shows the transmittance of the full FPI model as a function of the angle of incidence for a fixed cavity spacing of 1258 μm . The maximum angle of the off-axis rays through EoR-Spec’s FPI, determined by the diameter of the Lyot stop which will be defined by the SSB FPI, will be about $27^\circ/2 = 13.5^\circ$. These simulations show that off-axis illumination of the silicon metamaterial-based FPI behaves as expected.

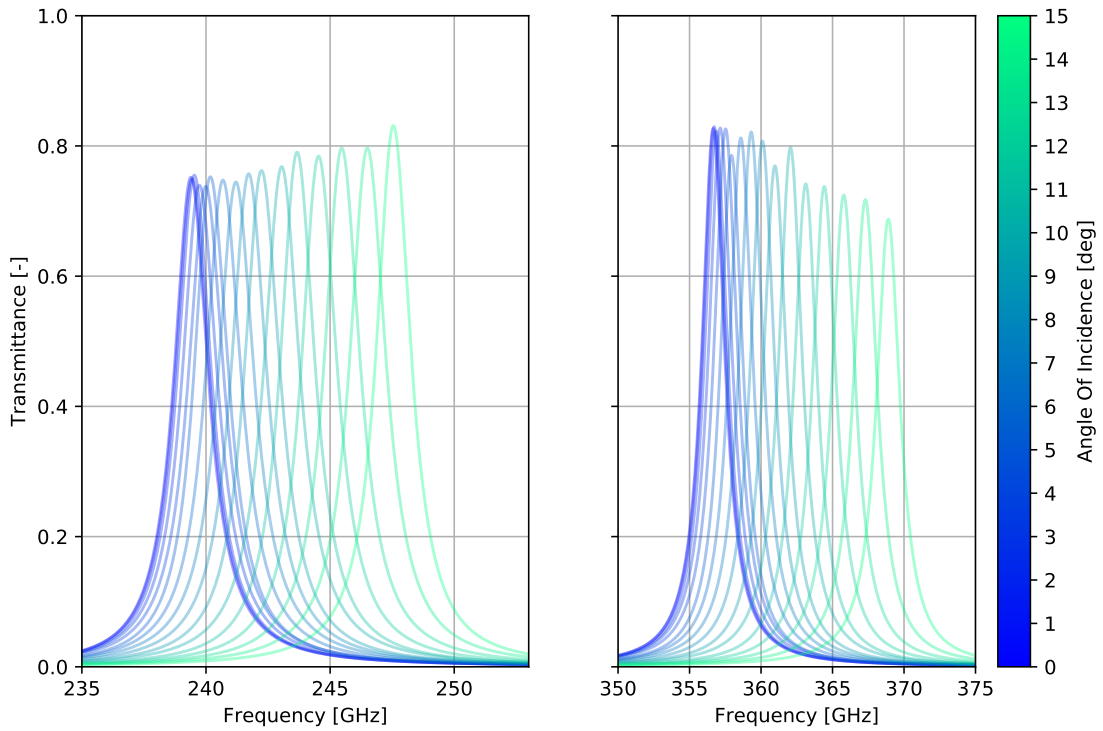


Figure 3.30: CST transmittance simulation for the full SSB FPI model, sweeping over angles of incidence for a constant mirror separation of $1258 \mu\text{m}$. The left and right plots zoom in on the second and third order fringes respectively. As the angle of incidence is increased, the fringes are blue-shifted, as expected. The fringe heights change with the angle of incidence as the mirror reflectances vary as a function of frequency and angle incidence.

3.4.5 Ohmic and Dielectric Losses

Ohmic losses in metal meshes

Metal mesh absorption, which occurs at every bounce within the EoR-Spec FPI cavity, degrades the amplitude of the fringe as described by Equation 3.8. Ulrich showed [147] that if the skin depth of a mesh is much less than the thickness of the mesh, then the fraction power dissipated by a single bounce off a mesh due to

the mesh surface impedance is approximately given by

$$\mathcal{A} = \mathcal{R}\eta\sqrt{4\pi\epsilon_0 f\rho}, \quad (3.35)$$

where f is the incident frequency, ρ is the mesh resistivity, and η is a form factor dependent on the mesh geometry. For inductive meshes $\eta = (1 - w/p)^{-1}$ and for capacitive meshes $\eta = p/w$. We see that the absorptance is a slow function of the frequency. This may explain why we saw the absorptance of the full FPI simulation increase at the higher frequency side of the EoR-Spec band in figure 3.29. The resistivity also affects the absorptance since it affects the surface impedance and skin depth. It is important to note that this model does not include any affects due to dielectric mesh substrates which could impact the surface currents of the mesh if the mesh is sufficiently thin. Choosing a material and/or mesh temperature with a lower resistivity will reduce the absorptance.

We now look at the mirrors examined for the EoR-Spec mirrors in Figure 3.26. For these meshes, we have $w_{\text{ind}} = 0.54$, $w_{\text{cap}} = 0.97$, $\mathcal{R}(315 \text{ GHz}) = 0.95$, and $\rho_{\text{Au},1\text{K}} = 0.022 \times 10^{-8} \Omega \cdot \text{m}$. Computing the absorptance for both meshes gives $\mathcal{A}_{\text{ind}} = 1.8 \times 10^{-4}$ and $\mathcal{A}_{\text{cap}} = 8.6 \times 10^{-5}$. With $\mathcal{R} = 0.95$ the finesse will be roughly 60 and so a photon can be expected to be reflected by both mirrors about 60 times. Thus the total absorbed power of each mirror will be roughly $60 \times (\mathcal{A}_{\text{ind}} + \mathcal{A}_{\text{cap}}) \approx 0.015$. This is roughly equivalent to few percent absorption we saw in Figure 3.29.

To visualize the effects of Ohmic absorption in metal meshes more dramatically, Figure 3.31 shows the transmittance of a fixed silicon etalon FPI tuned for operation in the terahertz. The etalon has two gold inductive meshes ($p = 17 \mu\text{m}$, $w_{\text{ind}} = 0.596$) patterned on either side of a $525 \mu\text{m}$ thick silicon substrate. The simulation was run using the resistivity of gold at 300 K, 80 K, and 1 K. The

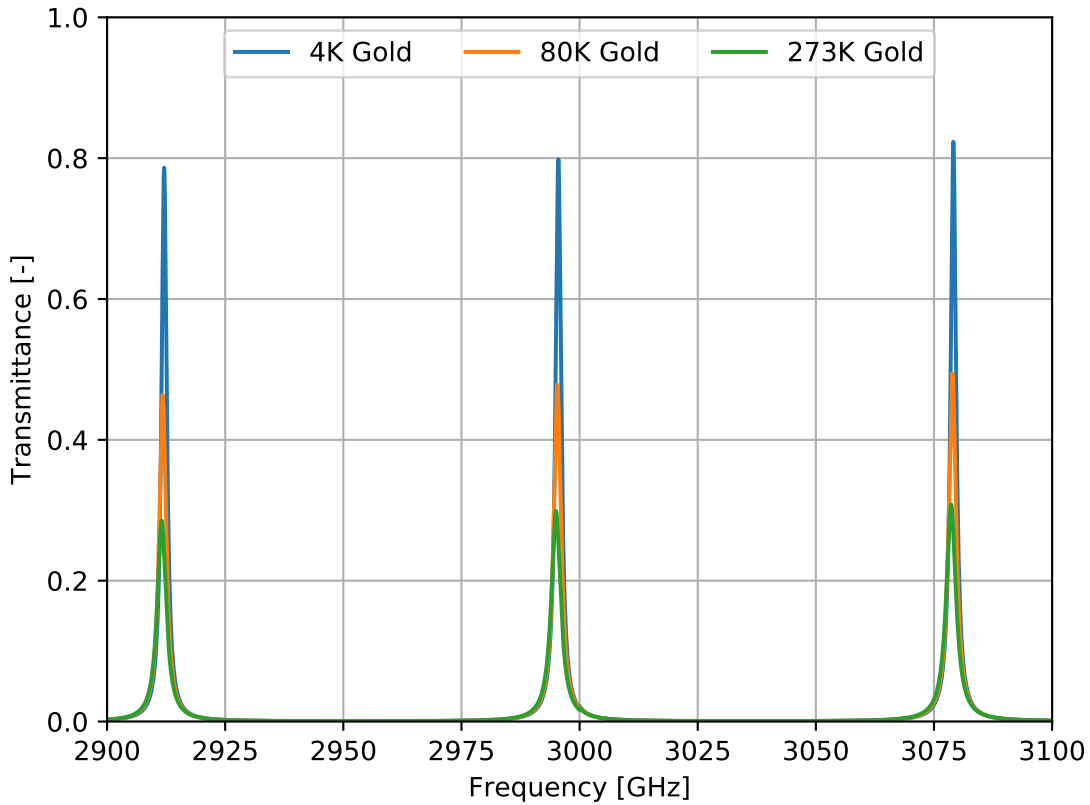


Figure 3.31: CST transmittance simulation of fixed silicon-cavity FPI demonstrating Ohmic loss by varying the gold mesh resistivity. The gold resistivity used correspond to different mesh temperatures and are $\rho_{\text{Au},273\text{K,SI}} = 2.193 \times 10^{-8} \Omega \cdot m$, $\rho_{\text{Au},80\text{K,SI}} = 0.481 \times 10^{-8} \Omega \cdot m$, and $\rho_{\text{Au},4\text{K,SI}} = 0.022 \times 10^{-8} \Omega \cdot m$.

increased loss due to the greater resistivities at warmer temperatures is evident from the strong amplitude reduction between simulations. Thus, it is important to choose the mesh material carefully and optimize the cryogenic design around the FPI to maintain low Ohmic losses.

Dielectric loss in silicon

In EoR-Spec, since the silicon substrates are outside the resonating cavity, dielectric absorption only occurs as the wave enters and exits the cavity. However, for

a silicon-based cavity such as the one described in Figure 3.27, dielectric absorption is much more important since resonating beams see a much longer path length through the silicon. In general, a dielectric with a complex index of refraction will dissipate power from a wave traveling through it. The complex index of refraction and dielectric constant of a material can be written as

$$\begin{aligned}\tilde{n} &= n + i\kappa \\ \tilde{\epsilon}_r &= \epsilon' + i\epsilon'',\end{aligned}\tag{3.36}$$

and using $\tilde{\epsilon}_r = \tilde{n}^2$, we have

$$\begin{aligned}\epsilon' &= n^2 - \kappa^2 \\ \epsilon'' &= 2n\kappa.\end{aligned}\tag{3.37}$$

Also note that the loss tangent is defined

$$\tan \delta = \frac{\epsilon''}{\epsilon'} = \frac{2n\kappa}{n^2 - \kappa^2}.\tag{3.38}$$

For low-loss dielectrics ($\kappa \ll n$), we can approximate

$$\tan \delta \approx \delta \approx \frac{2\kappa}{n}.\tag{3.39}$$

We now consider a plane wave in this lossy dielectric medium

$$E(z, t) = E_0 e^{ikz - i\omega t} = E_0 \exp\left[-\frac{\omega\kappa}{c}z\right] \exp\left[i\omega\left(\frac{n}{c}z - t\right)\right],\tag{3.40}$$

where we have used $k = \omega\tilde{n}/c$. We see that the wave is attenuated exponentially as a function of κ . The time-averaged transmitted power is proportional to the square of electric field such that

$$P(z) = P_0 \exp\left(-\frac{2\omega\kappa}{c}z\right) = P_0 \exp(-\alpha z),\tag{3.41}$$

where α is the attenuation constant. Using $\omega = 2\pi c/\lambda n$ and Equation 3.39, we can rewrite in terms of κ and δ :

$$\alpha = \frac{2\omega\kappa}{c} = \frac{4\pi\kappa}{\lambda n} = \frac{2\pi\delta}{\lambda} = \frac{2\pi n\delta}{\lambda_0},\tag{3.42}$$

where $\lambda = \lambda_0/n$ is the wavelength in the medium and λ_0 is the wavelength in free-space. Thus, the intensity attenuation of a wave with free-space wavelength λ_0 traveling through a low-loss dielectric can be written either in terms of δ or κ :

$$P(z) = P_0 \exp\left(-\frac{4\pi\kappa}{n^2} \frac{z}{\lambda_0}\right) = P_0 \exp\left(-2\pi\delta \frac{nz}{\lambda_0}\right). \quad (3.43)$$

Recent measurements by collaborator Ed Wollack determined \tilde{n} of a high purity silicon sample between 3 and 30 THz at 300 K and 10 K[157]. Wollack et al found \tilde{n} to be relatively constant below 9 THz at $\tilde{n}_{300K} = 3.417 + i8.9 \times 10^{-5}$ and $\tilde{n}_{10K} = 3.389 + i4.9 \times 10^{-6}$. Using Equation 3.39, these measurements correspond to $\delta_{300K} = 5.2 \times 10^{-5}$ and $\delta_{10K} = 2.9 \times 10^{-6}$. Figure 3.32 plots the amplitude attenuation (Equation 3.43) for both loss tangents as a function of the number of free-space wavelengths traveled in the medium.

This data is useful for developing a sense for the amount of dielectric loss due to transmission through silicon. For example, consider the silicon wafer etalon with metal mesh patterned surfaces described above in Figure 3.27. For this 500 μm thick etalon with a finesse of ~ 80 at 300 GHz, the average pathlength in the cavity of a photon is roughly 80 mm or roughly 80 wavelengths. For room temperature high-purity silicon, the amount of dielectric attenuation would be about 10% where as it would be only $\sim 1\%$ with cold silicon. It is important to note that this data is only true for high purity, high resistivity ($30 - 40 \text{ k}\Omega \cdot \text{cm}$) silicon. Lower purity silicon will have higher loss tangents due to increased charge carrier density and therefore will have significantly worse absorptance. It is therefore important to consider and characterize the type of silicon used for our silicon substrate-based devices at relevant temperatures.

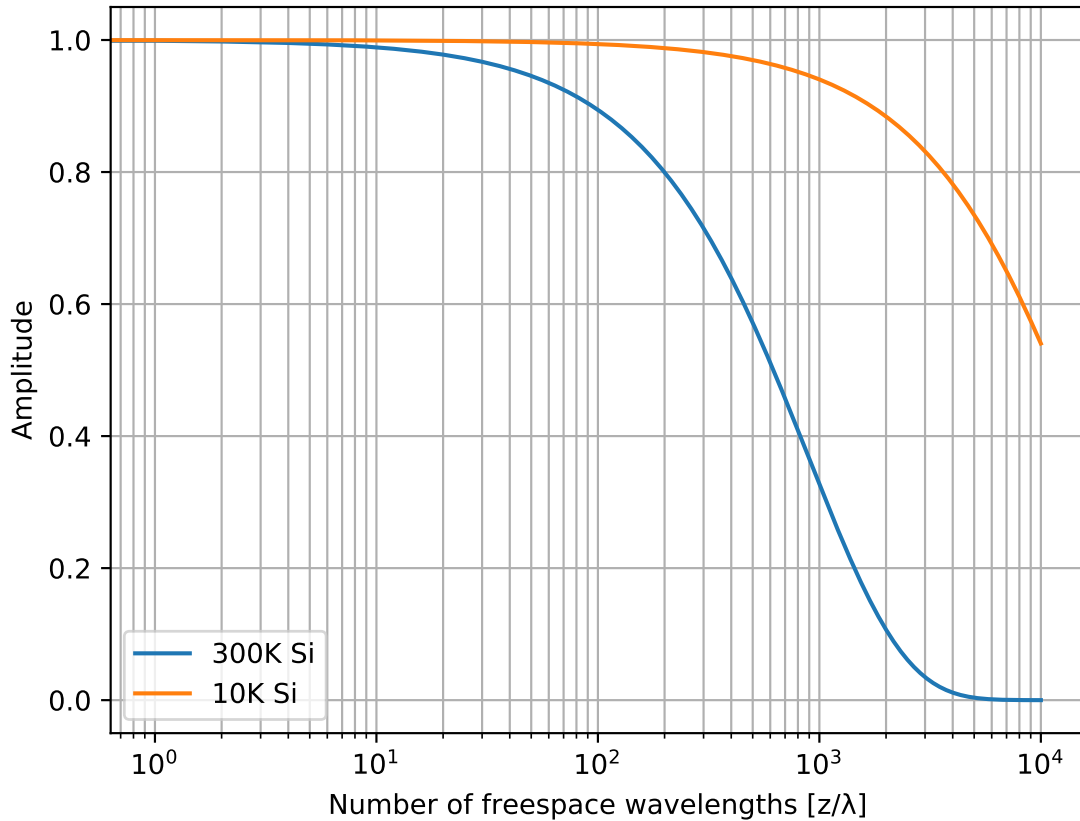


Figure 3.32: Intensity of a wave traveling through 300 K vs 10 K silicon as a function of the number of freespace wavelengths traveled in the medium. Losses are due to dielectric absorption. Loss tangents computed from \tilde{n} measurements in Wollack et al [157].

3.5 Prototype Device Fabrication and Characterization

In this section, we discuss fabrication methods that were developed for creating SSB FPI mirrors. The fabrication methods for plasma-etched ARCs and lithographically patterned metal meshes are presented, followed by a description of spectral characterization of early prototype silicon-based devices.

3.5.1 Deep Reactive Ion Etching for sub-mm ARCs

We use deep reactive ion etching (DRIE) to etch double-layer sub-mm metamaterial ARCs on silicon substrates. DRIE is an anisotropic plasma etching technique used to etch silicon in the microfabrication industry. DRIE tools rely on the Bosch process [158] which involves iteratively plasma etching fractions of a micron of silicon and then passivating the un-etched sidewalls to protect them during the next iteration. This process enables etching of high aspect ratio vertical structures in silicon to depths ranging from hundreds of nanometers to hundreds of microns. Metamaterial features can be etched into silicon wafers by applying etch masks to protect surface patterns of the silicon. Our group at Cornell developed a recipe for single-layer DRIE-based ARCs and published it with spectral measurements in Gallardo et al [61]. For a single layer ARC, we lithographically pattern an etch mask comprised of a square grid of photoresist which protects the silicon beneath it from being etched.

For a double layer ARC, we pattern and stack silicon dioxide and photoresist etch masks of different lateral dimensions before etching any silicon. The silicon is first etched once using the top etch mask (photoresist) and then a second time using the lower etch mask (silicon dioxide). Many challenges arise at various steps of the recipe, requiring additional steps to be added to improve the final double-layer geometry. Figure 3.33 outlines each major step of the double-layer recipe.

The recipe begins with depositing and patterning the silicon dioxide etch mask which defines the upper metamaterial layer geometry. The oxide is deposited using an Oxford plasma enhanced chemical vapor deposition (PECVD) tool. The thickness of the oxide etch mask depends on the depth of the ARC layer¹⁴. Once

¹⁴In a typical DRIE, SiO₂ is etched 100 to 150 times slower than silicon.

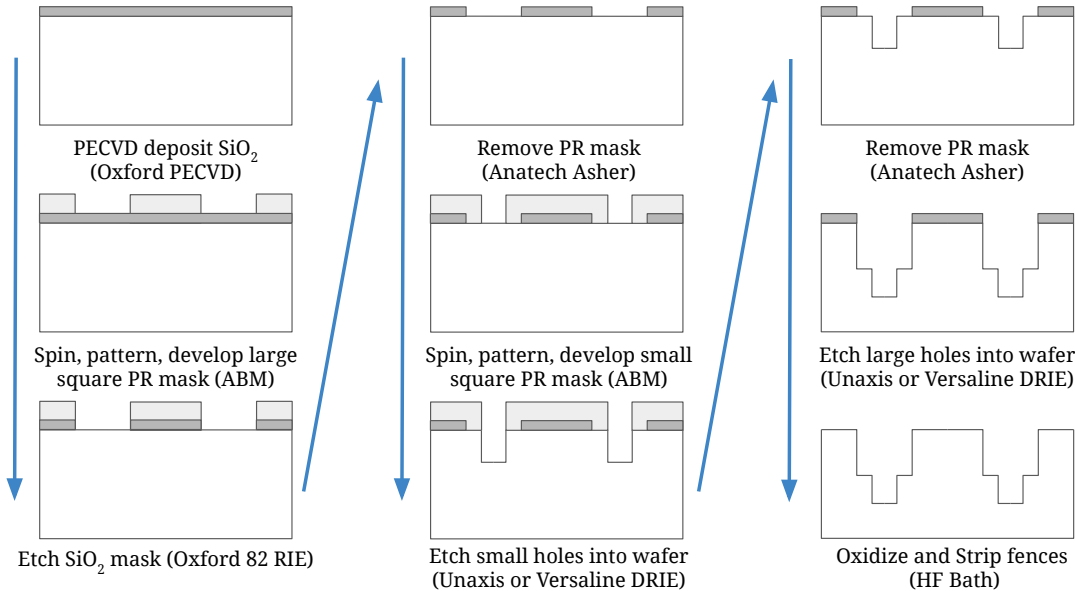


Figure 3.33: Micro-fabrication recipe for a double-layer metamaterial ARC using DRIE. SiO_2 and a photoresist etch masks are lithographically patterned onto the wafer. DRIE is used to etch the lower metamaterial layer into silicon through the etch masks. The photoresist mask is stripped and the SiO_2 etch mask is used to etch the upper metamaterial layer. Note both layers are etched simultaneously at different rates during the second DRIE etch.

enough oxide is deposited, it is lithographically patterned with the upper layer geometry and then etched using reactive ion etching to expose the areas where the silicon will be etched. The lithography steps are performed using an ABM contact aligner or an ASML stepper, depending on the metamaterial feature sizes. The ABM is limited to feature sizes of $\lesssim 1 \mu\text{m}$, making it adequate for work generally below 860 GHz. The ASML is slower, more complex, and more expensive to use than the ABM but can achieve much smaller resolutions of $\lesssim 200 \text{ nm}$, making it suitable for work in the THz. The photoresist is then stripped using an Anatech oxygen plasma barrel ash and a new layer of photoresist with the lower layer geometry is patterned, forming a second etch mask. The photoresist thickness also

depends on the depth of the ARC layer¹⁵.

With both etch masks patterned, the lower layer geometry is then etched into the silicon using either a Unaxis 770 or a PlasmaTherm Versaline DRIE tool. After etching for a given amount of time, the wafer is removed from the DRIE tool and the etch depths are measured using a Zygo optical profilometer. The Zygo profilometer measures the depth of the holes to sub-nm precision and enables a rough estimation of the DRIE etch rate. By iteratively etching and measuring the hole depths, it is possible to control the metamaterial layer depth to within a fraction of a micron. In general, however, we found that both metamaterial layers etch at different rates and that as the layers become deeper (their aspect ratio grows), their etch rates slow down. Characterizing the etch rates of both layers is therefore key to successfully fabricating both metamaterial layers with their proper depths.

After the lower layer is etched into the silicon, the photoresist etch mask is removed using an Anatech oxygen plasma ash. With only the upper layer SiO₂ etch mask remaining, the wafer is returned to the DRIE tool and both layers are simultaneously etched by the plasma at different rates. The target ARC layer depths are achieved by once again iteratively etching and measuring the layer depths using the profilometer. The oxide etch mask is then removed from the double-layer metamaterial coating using a buffered oxide etch of hydrofluoric acid.

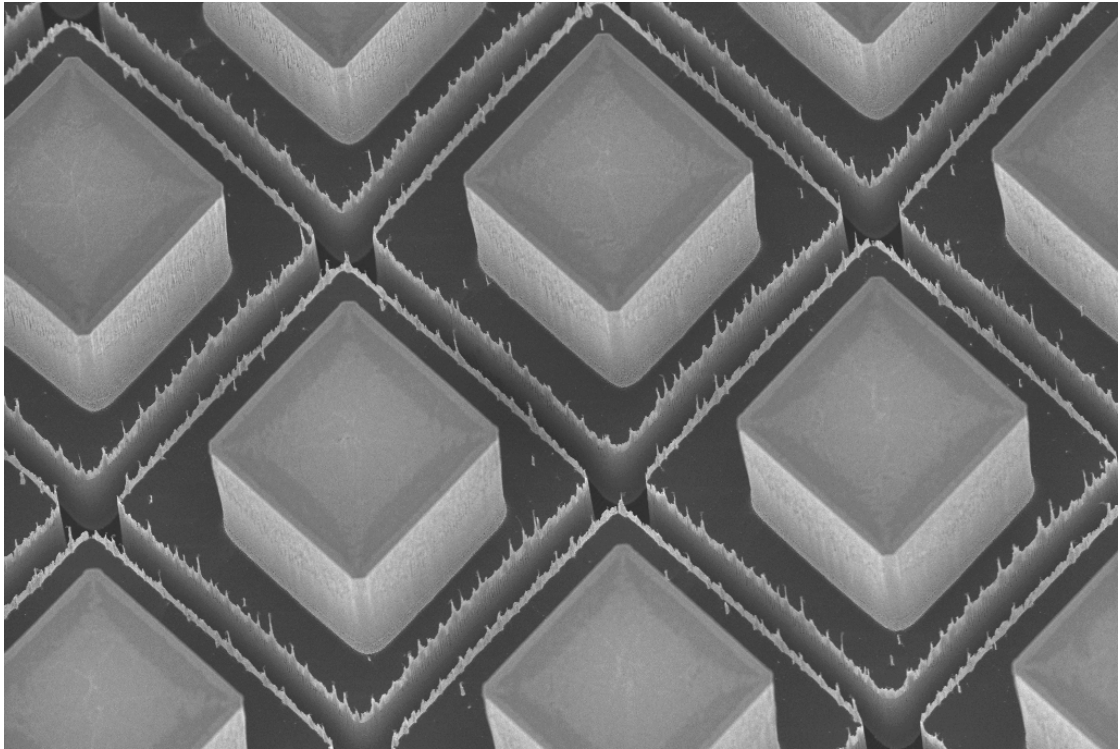


Figure 3.34: SEM image of first DRIE-based double-layer metamaterial ARC. This pillar-geometry design was optimized for operation around 860 GHz. Note the flat upper and middle surfaces. The lower surface in the trenches is obscured. Also note the small and likely negligible “fence”-like upward spikes on the shoulder of the middle layer above the trenches. Image taken with a Zeiss Ultra SEM.

3.5.2 DRIE ARC Characterization

Figure 3.34 shows a scanning electron microscope (SEM) image of our first double-layer DRIE-based metamaterial coating. This sample used the pillar metamaterial geometry and was designed for applications in the 860 GHz band. The resulting structure has vertical sidewalls and flat lateral geometries. However, note the small spike like features pointing up at the boundary between the upper and lower metamaterial layers. We called these features “fences”. Although small and likely negligible in this sample, we later found fences to be a common and sometimes

¹⁵In a typical DRIE, photoresist is etched as little as 50 times slower than silicon.

much larger concern, especially for higher frequency applications where they take up more of the silicon fill fraction.

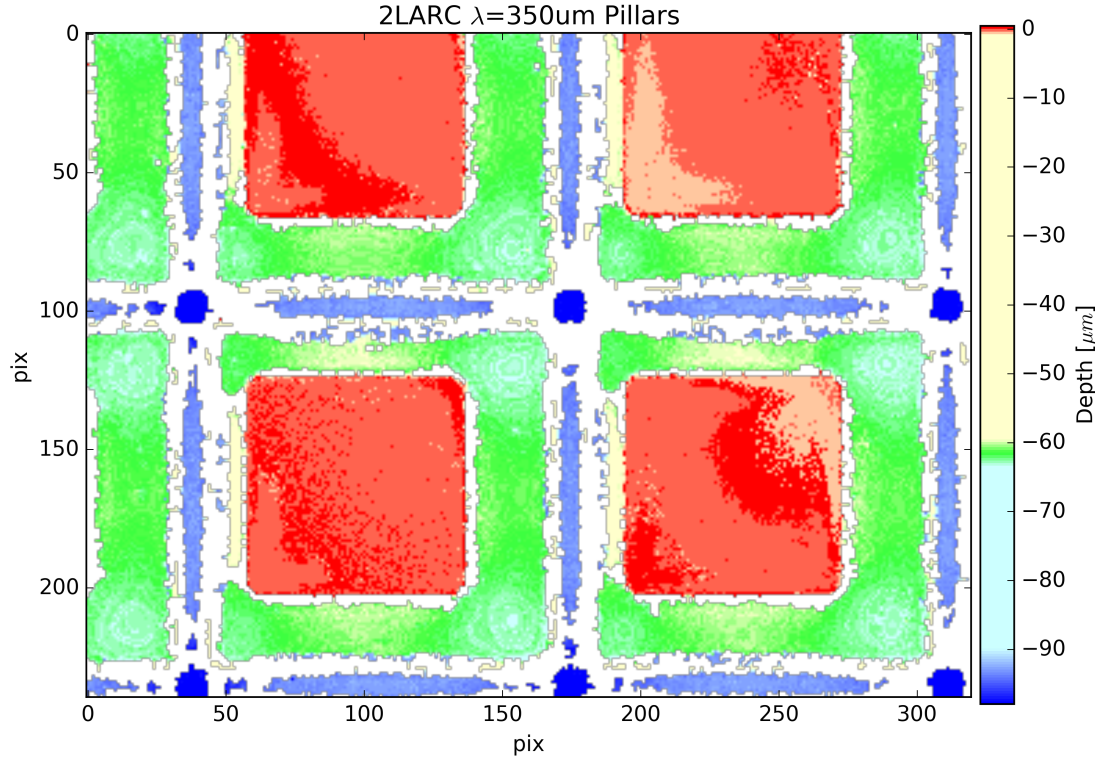


Figure 3.35: Zygo profilometer data of the first DRIE-based double-layer metamaterial ARC. The depth and flatness of each layer is evident. The top and middle level appear relatively flat while the lower layer is significantly higher in the middle of the trenches than at the trench intersections.

Figure 3.35 shows depth data from a Zygo profilometer the same double-layer metamaterial coating as in the SEM image. Notice that the top and middle surfaces are relatively flat but the lower layer is deepest at the intersection of trenches, and a few microns shallower in the middle of the trenches. This behavior was found to be common for high-aspect ratio features such as narrow trenches and so, we prefer to fabricate metamaterials with the hole geometry where the aspect ratio of the lower layer features is reduced. Notice also that the two layers were misaligned. This was due to user error during lithography. Misalignment of this order between

layers is not expected to affect the metamaterial performance except in polarization for far off-axis beams. We note that the fence is not visible in this data because on this sample, it was too thin and too steep to be measured by the profilometer.

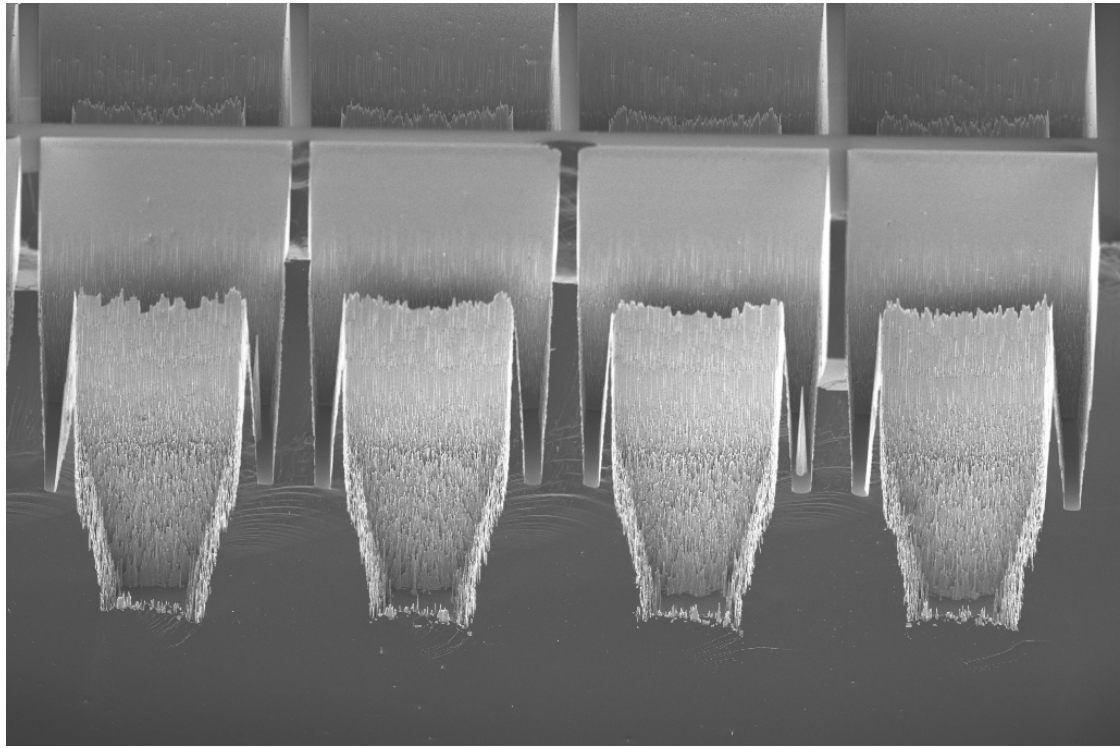


Figure 3.36: SEM cross-section image of a DRIE-based double-layer metamaterial ARC. This hole-based metamaterial geometry was designed for operation in the millimeter. Note the thick fences, sloped sidewalls, and micro-pitting and micro-grass on the lower layer sidewalls and floor.

After fabricating, the first double-layer prototype, the challenge remained to characterize the etch rates in order to produce accurately tuned layer depths. Multiple issues with the recipe were discovered while addressing this challenge. Figure 3.36 shows a cross-section SEM image of one of the worst-case results of the recipe. In this two-layer hole-geometry metamaterial coating, we see a number of complications. First, the fence is much worse in sample, with a height of about half the upper layer depth and a base width of almost half the upper layer wall width. Additionally, the upper and lower layer walls are significantly sloped. The

lower layer walls also have micro-pitting rather than a smooth surface. The bottom surface is covered with small “grass”-like spikes.

A large number of fabrication factors could have influenced all of these unwanted features. Potential causes of these features include, but are not limited to: (1) incomplete RIE etching of the SiO₂ etch mask, leaving residual micro masks which could generate grass, (2) sloped edges on both etch masks which could generate sloped sidewalls, (3) photoresist hardening during plasma etching which could leave residual material post-ashing which could cause micropitting and fences, and/or (4) the DRIE sidewall passivation build-up during the first DRIE etch could impact the second DRIE etch, leaving the fence. Many potential solutions were explored by multiple students in our group over the past few years including using different etchers and various pre- and post-etching cleaning steps.

Recently, fellow Applied Physics graduate student Bugao Zou developed a modified recipe of insuring clean sidewalls and minimal fences. In short, his method counteracts the potential causes by introducing aggressive post-etch clean cycles¹⁶, and using multiple shorter etches to improve substrate cooling. Figure 3.37 shows the result of this method. Note that the sidewalls are still sloped, but they are clean and sloped consistently. EM simulations can be used to optimize the layer depths for the consistent wall taper angle. We are continuing to optimize the recipe to achieve the target layer depths within a few percent.

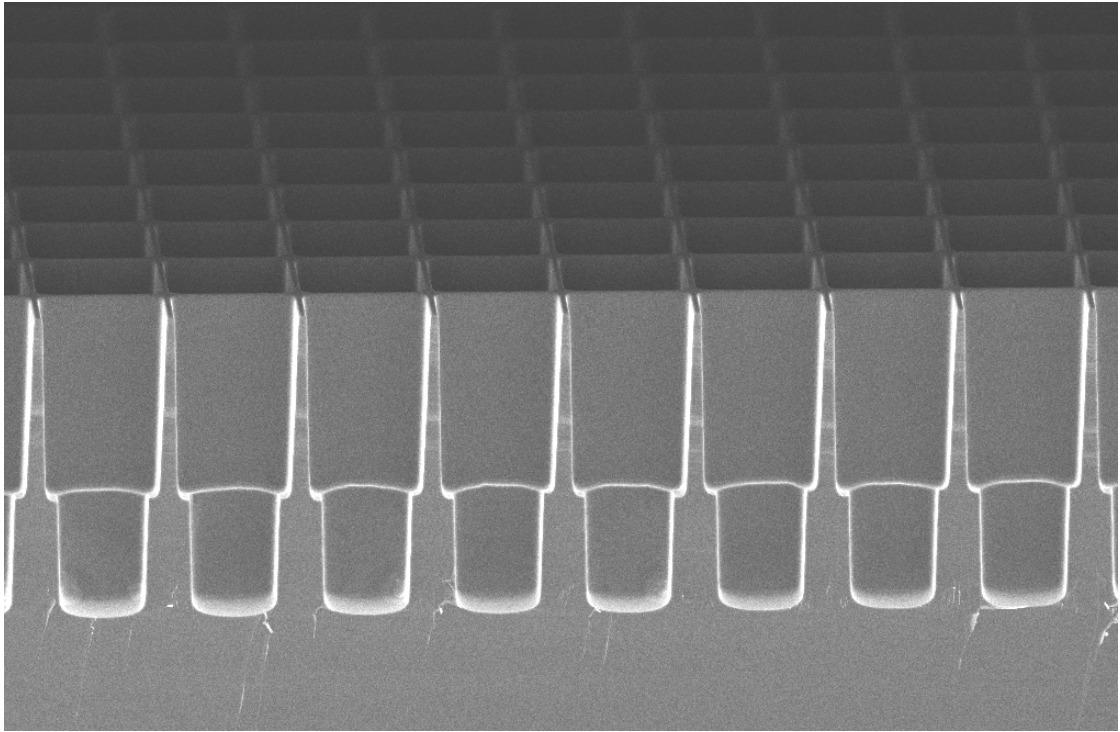


Figure 3.37: SEM cross-section of a DRIE-based double-layer metamaterial ARC. This hole-based metamaterial geometry was designed for operation between 88 and 112 μm . Note the lack of fences, clean lateral and vertical surfaces, and slightly sloped sidewalls.

3.5.3 Metal Mesh Fabrication

We fabricate metal mesh filters using standard evaporation and lift-off lithography techniques. Figure 3.38 illustrates the recipe. Negative lift-off resist (AZ nLOF 2020) is exposed with the mesh pattern using an ABM contact aligner and then developed. Since we use negative photoresist, the unexposed resist regions are removed with developer, leaving a slight undercut in the resist sidewall. The patterned resist is descummed using an Anatech oxygen plasma barrel ash to clean the silicon surface and improve the undercut. Next, 10 nm of a chromium adhesion layer and 100 nm of gold are evaporated onto the patterned wafer using

¹⁶The post etch geometry can be cleaned by oxidizing the exposed silicon surfaces and stripping away the outer layer with a buffered oxide hydrofluoric acid bath.

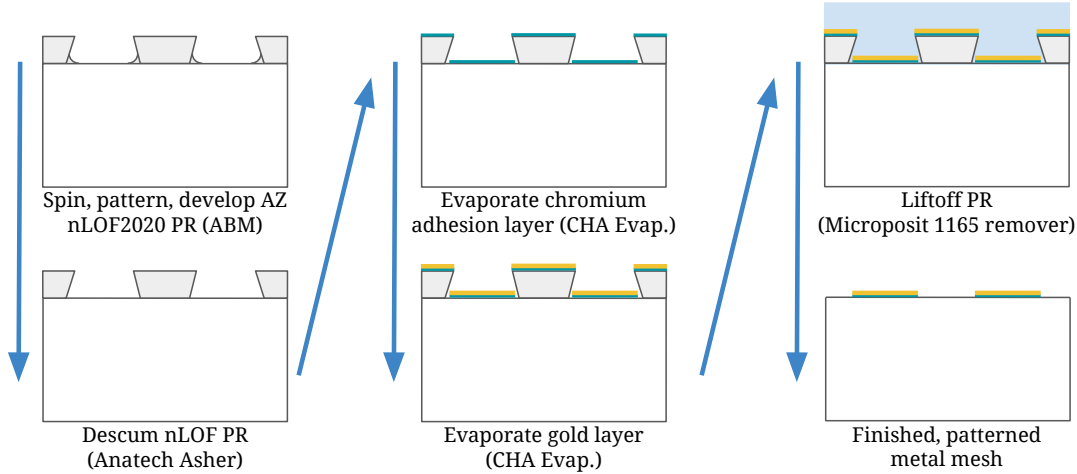


Figure 3.38: Micro-fabrication recipe for a gold metal meshes using negative lift-off (nLOF). nLOF photoresist is lithographically patterned with the inverse mesh design and then descummed in an oxygen plasma ash. A thin 10 nm chromium adhesion layer is evaporated before evaporating 100 nm of gold. The nLOF resist is then removed leaving the patterned mesh.

a CHA evaporator. Due to the undercut sidewalls of the negative photoresist, the gold film is discontinuous between the top of the silicon and the top of the resist. The wafer is then placed in a bath of Microposit 1165 remover and left for 24 hours or until the photoresist is fully released. After rinsing and drying, the patterned metal mesh is microscopically examined for uniformity and correct dimensions. Using contact lithography, feature sizes of $\lesssim 1 \mu\text{m}$ can be achieved. Using stepper lithography, feature sizes of $\lesssim 0.2 \mu\text{m}$ can be achieved.

This recipe was found to work well for capacitive style meshes, where the lift-off material consisted of a continuous sheet of negative resist. However, for inductive style meshes, where the removed material consisted of many patches of negative resist, it was sometimes found that a significant fraction of resist patches were left scattered and partially removed. We found that using a heated bath of the Microposit 1165 remover was generally able to solve this issue. Figure 3.39 shows

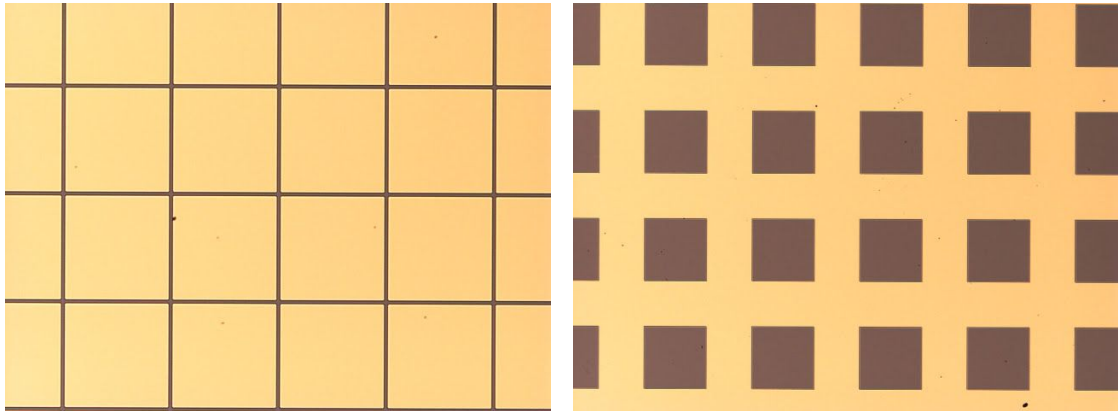


Figure 3.39: Microscope photos of capacitive (left) and inductive (gold) meshes deposited on silicon using negative lift-off. The silicon substrate is apparent as the brown material underneath the gold meshes. The gold is 100 nm thick and is on top of a 10 nm chromium adhesion layer. The pitch of both meshes is approximately 171 μm .

microscope photos of inductive and capacitive metal meshes designed for operation around 315 GHz with a pitch of 171 μm .

3.5.4 Early Device Measurements

Post-fabrication spectral characterization of our SSB devices is an extremely important feedback mechanism for fabrication and modeling development. In this subsection, we present some Fourier transform spectrometer (FTS) measurements of early prototype devices. Further measurements will be necessary with cryogenic testbeds as the fabrication develops and higher quality samples with high-purity silicon are made to more closely match the target ARC geometries (i.e. hole widths and depths).

Figure 3.40 shows FTS transmittance measurements of a mm-wave, silicon-cavity fixed-FPI with inductive and capacitive gold metal meshes on either side.

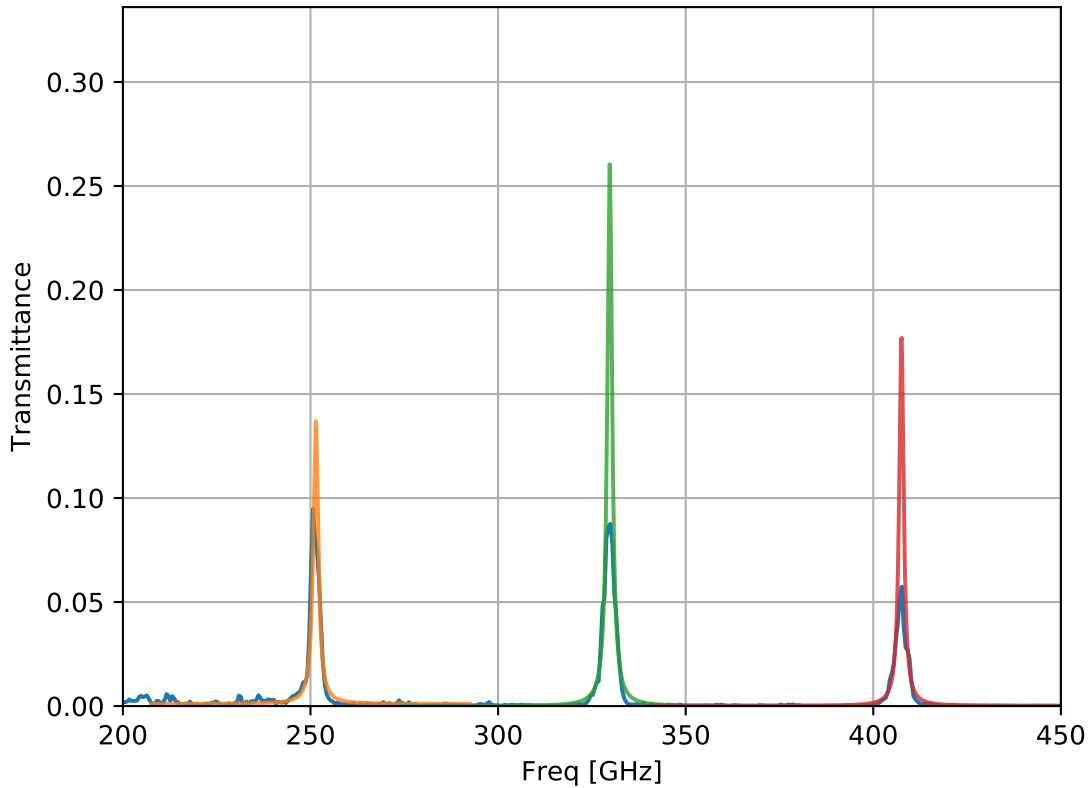


Figure 3.40: FTS measurements of a room temperature mm-wave silicon-cavity fixed-FPI. The $\sim 500 \mu\text{m}$ thick substrate has an inductive and a capacitive gold mesh on either side. Transmittance is expected to be low for this device at room temperature due to losses in the silicon and the gold meshes. The data is shown in blue and has been apodized with a triangle window function. Lorentzian fits are overplotted for each fringe. The finesse of each fit is approximately 55 as expected from the mesh design.

The blue line shows FTS data of the room temperature sample which has been apodized using a triangular window function. The shoulders of the fringes were fit to Lorentzian profiles¹⁷ as shown by the colored lines. For this $\sim 500\mu\text{m}$ thick piece of silicon, the fringes are at their expected frequencies. The width of the Lorentzian fits suggests a finesse of $\mathcal{F} \sim 55$ for all three fringes, which roughly matches expectations given the mesh designs. The transmittance peaks are low between 5 and

¹⁷The center data points were excluded from the fit on the basis that the FTS is unable to resolve the narrowest part of the Lorentzian

10%. Many factors could have contributed to the low transmittance. Absorption of silicon and gold at room temperature is significant. Cryogenic measurements of this device would hopefully yield much higher fringe peaks. The uncollimated optics of the FTS beam through the FPI is can also significantly reduce the fringe height by smearing the beam via walk-off. Nonetheless, this early measurement indicates that our fabrication methods are on track to produce working cryogenic mirrors.

Figure 3.41 shows cryogenic FTS transmittance measurements of sub-mm silicon-cavity fixed-FPI. This device was designed for operation near 3 THz and was cooled to about 18 K using a liquid helium cryostat. Inductive meshes on both side, give the overall transmittance a high-pass filter shape. The data is shown in orange and has been convolved with a Happ-Genzel window function¹⁸. Water lines are evident by the large spikes and noise in the data. A CST EM simulation using the 4 K resistivity of gold is overplotted in blue. The simulation was apodized with the same window function as the data. The unapodized simulation had fringe peaks between 80 and 90 %. The data and the model agree remarkably well on the fringe widths and heights. The substrate thickness used in the model was chosen to match the data and is set to 517.5 μm . The silicon wafer used for this measurement was a 525 μm thick, high resistivity ($> 10,000 \Omega \cdot \text{cm}$) wafer. The discrepancy between the CST and actual wafer thickness could be explained by percent-level deviations in the substrate index of refraction. The discrepancy can also be due to thickness variation in the substrate which should be $> 10\mu\text{m}$, for this wafer. The mesh geometry used in the CST model was chosen to match microscope measurements of the metal mesh with $p = 17.1 \mu\text{m}$ and $w_{\text{ind}} = 0.577$.

¹⁸The Happ-Genzel window function is also known as a Hamming window.

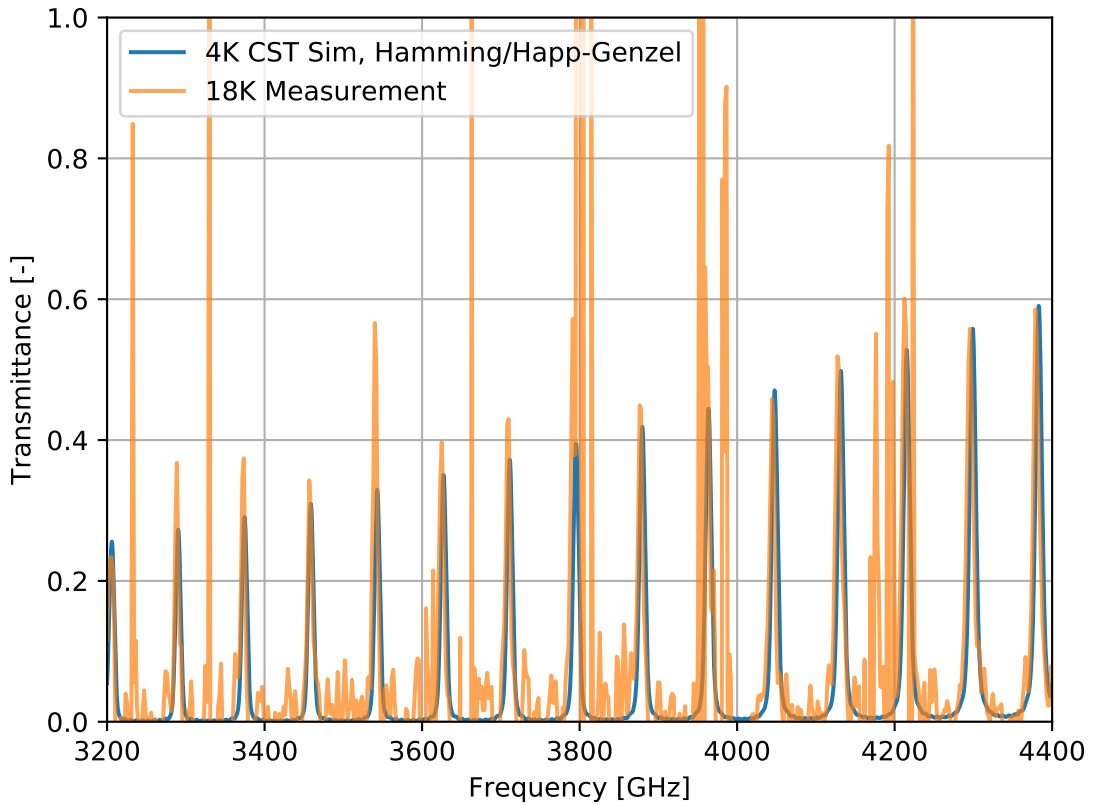


Figure 3.41: FTS measurements of a 18 K sub-mm silicon-cavity fixed-FPI. The $525 \mu\text{m}$ thick substrate has a pair of inductive gold meshes on either side of the silicon cavity. The FTS data has been apodized with a Happ-Genzel window function and is shown in orange. A CST EM simulation is overplotted in blue, uses the 4K resistivity of gold and is apodized with the same Happ-Genzel window to assist with comparison. The substrate thickness of CST simulation is $517.5 \mu\text{m}$. The nominal thickness of this wafer was advertised to be $525 \mu\text{m}$.

3.6 Future Paths

3.6.1 Next Steps Towards EoR-Spec

Many of the critical components required for testing and fielding EoR-Spec are well into development. In this subsection, we will briefly discuss the state and outlooks for cryogenic testbeds for small-scale SSB devices and for the full EoR-

Spec instrument module.

The spectral measurements described in the previous section were taken using two different FTSSs for the mm-wave and sub-mm bands. Both FTSSs can be equipped with cryogenic sample dewars to test SSB samples in low-loss conditions. These testbeds will continue to be useful for rapid testing of small-scale SSB ARC and mirror samples as they are fabricated. We are also developing a new cryogenic testbed that will feed the FPI samples with a more well-collimated beam than the FTSSs can currently achieve. The new testbed will be equipped with a heritage¹⁹ room-temperature, free-standing metal mesh, scanning FPI which will be used to survey the fringes of a liquid helium cooled SSB FPI. We have blackbody thermal sources, an arc lamp, and a 290 GHz laser that can each be coupled through collimating optics and the FPIs to a liquid helium bolometer. The 290 GHz laser and a room temperature mm-wave detector array will be used to parallelize the SSB mirrors. The liquid helium bolometer and broad band sources will provide spectral measurements across EoR-Spec’s band and will be used to characterize the performance of the SSB mirrors. These results will feedback to fabrication as the final EoR-Spec mirrors are finalized.

With full-size (6 inch diameter) FPI mirrors, EoR-Spec will be ready for full instrument module testing. The sources, FTSSs, and room temperature free-standing metal mesh FPIs will be used to test the full-scale FPI mirrors. Once the EoR-Spec MKID detectors are also ready, the FPI will be implemented into the module and tested in its scanning configuration. The separation between the SSB mirrors will be driven by cryogenic stepper motors and measured using capacitive sensors. Using heavily filtered beams from the previously mentioned sources, the

¹⁹We plan to use the low order FPI (LOFPI) from the South Pole Imaging FPI (SPIFI) [20] with existing mm-wave wire grids.

MKIDs beams will be confirmed and the scanning SSB FPI performance will be characterized in preparation for deployment on FYST.

3.6.2 Prospects for Future Silicon-based sub-mm Devices

The ability to pattern arbitrarily shaped metal meshes and etch metamaterial ARCs enables many sub-mm applications. Both broad and narrow band filters are extremely useful for sub-mm instrumentation. Low and high-pass filters are useful for broadband detector arrays where spectral shaping is important. Narrow bandpass filters are useful for order-sorting in spectrometer-based applications. In this subsection, we talk about a few device designs that the author explored via CST simulations for these types of applications.

Low and high pass filters

A single inductive or capacitive SSB mirror effectively constitutes a wideband high or low pass filter. Tuning the shape of the mesh designs to provide sharper cutoffs can enable band defining filtration. Placing multiple SSB filters in series (with the surfaces tilted in order to avoid FPI resonances) could generate wideband bandpass shapes. Peter Ade's group at Cardiff generates such filters using thin dielectric sheets [4] which are used throughout mm-wave and sub-mm instrumentation. SSB versions of these filters should incur lower dielectric losses and using the negative lift-off techniques described above, are relatively easy to make in University clean-rooms. The challenge remains the fabrication of ARCs on the silicon substrate. A single layer ARC which has been well demonstrated [61] can satisfy a large fraction of applications. Recent work by collaborators who were at the University of Michi-

gan made a reflective-absorptive IR-blocking (low-pass) filter [107]. This device used a pair of silicon wafers with single layer metamaterial ARCs and capacitive meshes to sandwich an IR absorbing powder. Single ARC-metal-mesh filters can therefore be used in a variety of broadband applications.

Narrow bandpass filters

By using mesh designs other than simple inductive and capacitive grids, single substrate filters can also be used as narrow bandpass filters. As described in Section 3.4.2, adding additional features to inductive and capacitive meshes tends to add narrowband resonant features. For example, loading an inductive mesh with a small capacitive patch (imagine the Target logo), or turning the square capacitive mesh into and array of capacitive pluses. The narrow bandpass filters that these designs produce can be used as band defining filters for detectors. They can also be used as order-sorting filters in spectrometers, which need low resolving power fixed filters to help reject unwanted spectrometer lines. These single substrate filters would need an ARC, but a single layer metamaterial is likely sufficient for such narrowband filters.

Fixed silicon cavity FPIs (very narrow bandpass filters)

It is also possible to create even narrower bandpass filters by creating a fixed-length silicon-cavity FPI with metal meshes on either side. Such a design does not require an ARC. These resonant cavities can be used as fixed narrow line filters which can be used as calibration etalons or order sorters for spectrometer applications. The robust silicon cavity and relatively simple lift-off metal mesh fabrication makes these devices easy to manufacture and use. The catch, however,

is that high-purity silicon must be used because the average path length through the etalon will be much greater than a single SSB mirror and is therefore much more susceptible to absorption.

Silicon-substrate Bragg mirrors

A Bragg mirror is purely dielectric and needs no metal meshes. The reflector is comprised of alternating quarter-wave layers of high (silicon) and low (vacuum) index of refraction materials. The number of alternating layers determines the peak reflectance. The reflective bandwidth of a Bragg mirror is limited to an octave of bandwidth (and harmonics of that octave). Outside the reflective octave, the mirror performance is highly variable (i.e. it is not purely transmissive). A prototypes of such a device has been fabricated by a group at SRON and has been shown to work reasonably well near 1 THz [152]. The benefit of dielectric-only mirrors is the lack of Ohmic losses from metal mesh reflectors. The downside is that Bragg reflectors tend towards high reflectances very quickly and so are more difficult to tune for lower finesse which require $R \sim 95\%$. Further, tuning the precise substrate thicknesses and vacuum gaps is challenging and requires careful characterization. The reflectivity of a Bragg mirror is a function of the number of alternatingly indexed layers and the contrast between the layer indices. One could imagine tuning the contrast of the layers by etching through the silicon layers, making it an artificial dielectric with an index of refraction closer to that of vacuum. Silicon Bragg mirrors remain a viable mirror technology that merits continued investigation.

Silicon-substrate virtually imaged phased arrays

A related application to that of a fixed silicon cavity FPI is a virtually imaged phased array (VIPA). A VIPA uses multi-beam interference (like a FPI) to angularly disperse different wavelengths (like a prism or grating). A silicon-based VIPA is composed of a thick (~ 10 mm) silicon block. Aside from an entrance slit, the first surface of the VIPA is coated with a 100% reflective film such as gold. The second surface is coated with a partially transmissive metal mesh. An off-axis cylindrically diverging beam²⁰ is input through the entrance slit. The diverging beam then bounces around the cavity as it is partially transmitted out through the second surface. The output beam behaves as if a phased array of sources existed behind the first surface of the cavity. Due to interference from the virtually phased array, the output beam will be collimated and its exit angle will be frequency dependent. Due to only needing metal mesh deposition, a silicon VIPA should be relatively simple to fabricate. The product would be a compact, high resolution spectrometer. We are currently working on fabricating a prototype silicon-based VIPA at CNF using our metal mesh fabrication techniques.

3.7 Conclusion

In this chapter, we discussed the design and status of silicon substrate-based technologies for EoR-Spec's high-throughput, wide bandwidth mm-wave FPI. We described the design of the EoR-Spec module in the context of Prime-Cam, FYST, and the CCAT-prime Collaboration's science goals. We presented models for FPIs, ARCs, and metal meshes, which gave us a nominal design for the EoR-Spec FPI.

²⁰In one axis, the beam is collimated, in the other, it is diverging

We improved the nominal design by optimizing design parameters with EM simulations. We demonstrated our fabrication recipes and capabilities and discussed early spectral characterization. The next steps towards deploying EoR-Spec are to characterize FPI mirrors with high-precision double-layer metamaterial ARCs and then couple a scanning SSB FPI to detector arrays for module characterization. With the development of the silicon models and fabrications methods presented here, many new silicon-substrate applications are within reach for mm-wave and sub-mm instrumentation and spectrometry.

CHAPTER 4

TRANSITION EDGE SENSORS FOR SIMONS OBSERVATORY

In this chapter, we present aspects of the detector development for the Simons Observatory¹ (SO). Section 4.1, provides a brief overview of SO’s telescopes and science goals. Section 4.2 describes the pixel and detector design and reviews the relevant theory to help guide our design and measurement processes. Multiple characterization methods and analyses that were used to optimize the SO single pixel designs are discussed in Section 4.3. Section 4.4 concludes the chapter with a brief discussion on the impacts of these measurements on SO and other collaborations.

4.1 Simons Observatory

SO is a suite of millimeter wave telescopes designed to map the polarization of the CMB. Multiple small aperture telescopes (SATs: ~ 0.5 m) and one large aperture telescope² (LAT: ~ 6 m) will comprise the Observatory [56, 83, 160]. The SATs will have a diffraction limited beam size roughly 12 times larger than the LAT. The telescopes are currently being developed, built, and tested off-site but will be installed at 5190 m in the Atacama Desert in northern Chile for first light in 2022. The observatory will share the same plateau on Cerro Toco as ACT (Section 2.1), CLASS, and the Simons Array, and is in the vicinity of ALMA and CCAT-prime (Section 3.1). The telescopes will be outfitted with cryogenic receivers containing many tens of thousands of TESs in six frequency bands. Figure 4.1 shows 3D renderings of the telescopes and receivers.

¹<https://simonobservatory.org/>

²The LAT design is nearly identical to CCAT-prime’s FYST. Since SO does not plan to observe in the sub-millimeter, the LAT has lower surface quality mirrors than FYST.

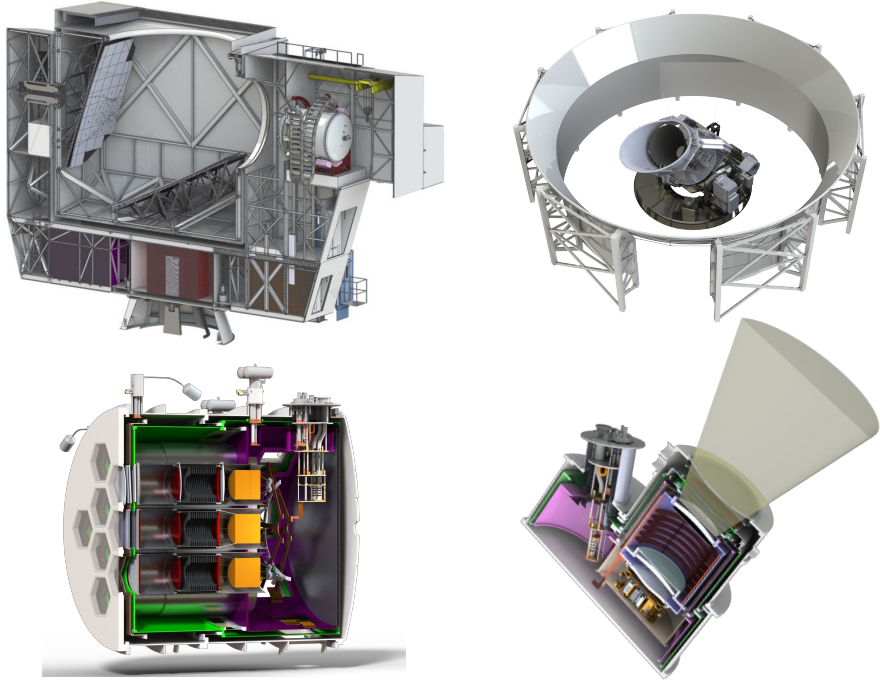


Figure 4.1: Renderings of the LAT (upper left), SAT-platform (SATp, upper right), LAT-receiver (LATR, lower left), and SAT (lower right). The cross-section of the LATR shows the optics modules and cryogenics. The LATR is also shown inside the LAT, in its upper right corner. The SATp is shown with a stationary and co-moving ground screen. A cross-section shows the mirror-less SAT, it's cryogenics, optics, and focal plane.

The combination of the dry site and the capability to measure multiple angular scales with two types of telescopes will enable many science goals using the same detector array technologies [3, 30]. At small angular scales, the LAT will probe both the primary and secondary anisotropies of the CMB including gravitational lensing and the SZ effects. At large angular scales, the SATs will map the CMB polarization signal on scales corresponding to the expected B-mode polarization imprint from primordial gravitational waves. Through these observations, SO will improve constraints on cosmological parameters, probe the sum of the neutrino masses, detect high-redshift galaxy clusters, use gravitational lensing to characterize the distribution of dark matter, and constrain the tensor to scalar ratio,

r.

In order to achieve its broad science goals, SO will deploy $\sim 70,000$ polarization sensitive AlMn TES bolometers in six frequency bands spanning 30 – 290 GHz. The number of detectors is almost an order of magnitude greater than has been deployed on a CMB instrument. Three dichroic, polarization-sensitive pixel designs will be used for the low-frequency (LF 30/40 GHz), mid-frequency (MF 90/150 GHz), and ultra-high-frequency (UHF 230/290 GHz) arrays. The LF arrays are being fabricated at the University of California at Berkeley (UCB) and will be optically coupled via sinuous antennas and silicon lenslets. The MF and UHF arrays are being fabricated at the National Institute of Standards and Technology at Boulder (NIST) and will be optically coupled via orthomode transducer antennas and gold-plated aluminum feedhorns. Figure 4.2 illustrates early prototype detector arrays and single pixels for all three bands.

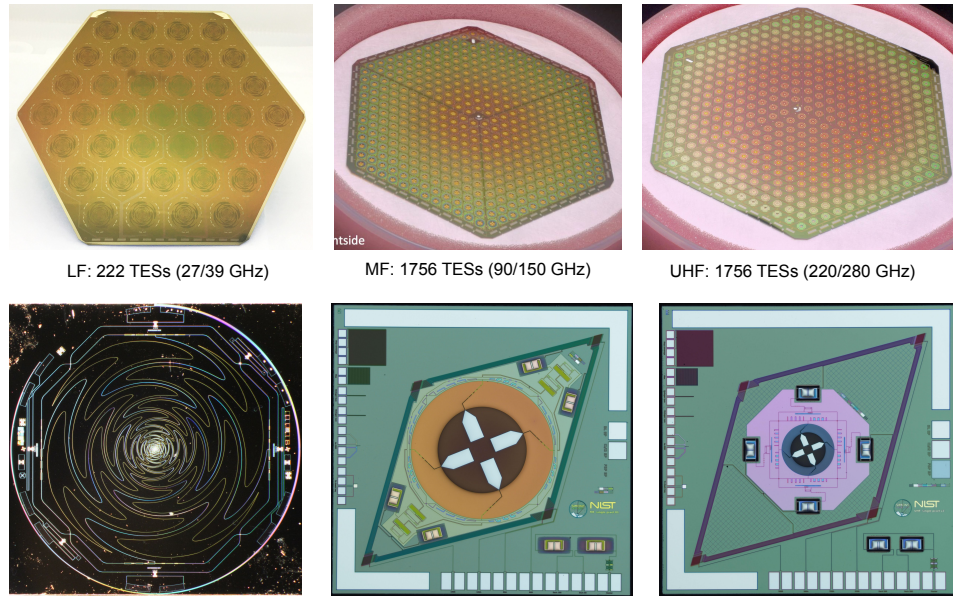


Figure 4.2: Photographs of early SO arrays (upper) and single pixels (lower). Each array is dichroic and polarization sensitive. Large-format hexagonal arrays enabling close array-packing on the focal plane, maximizing the number of detectors.

All detector arrays will be fabricated on large 150 mm diameter silicon wafers. Each pixel in the dichroic arrays will contain four TESs, two for each polarization and two for each frequency. All three types of detector arrays will utilize a common packaging called a universal focal-plane module (UFM) [69]. In each UFM, a detector array will be integrated with their feedhorns, and microwave-squid multiplexer (μ MUX) [44] readout components. The UFM design enables high-density hex-packing of arrays to fill the focal plane with as many detectors as possible.

The UFs are designed to provide a common detector array package for the LAT and SAT. This requires the detector arrays to be optimized for the observing conditions of both telescopes. This includes considering the different photon loadings of the telescopes, their beam shapes, and how they will operate during observations. Many detector parameters must be optimized including saturation powers, time constants, noise performance, polarization efficiency, and bandpasses. Here, we focus on saturation powers, time constants, and complex impedance TES measurements.

4.2 Transition Edge Sensor Design Overview

The deployment of SO’s \sim 70,000 detectors will require production-scale fabrication and testing of detectors and readout components. It is therefore critical to optimize the detector designs before large-scale production begins. This is accomplished by characterizing many prototype “single pixels” with varying TES designs.

4.2.1 TES Pixel Design

Incident radiation from the sky is focused by the telescope into the cryogenic receiver where it is then filtered and re-imaged onto the ~ 100 mK focal plane. The microwave radiation is then accepted by either a gold-plated aluminum feedhorn (MF and UHF arrays) or an AR coated silicon lenslet (LF arrays), and deposited onto a pixel with complex superconducting microwave circuitry.

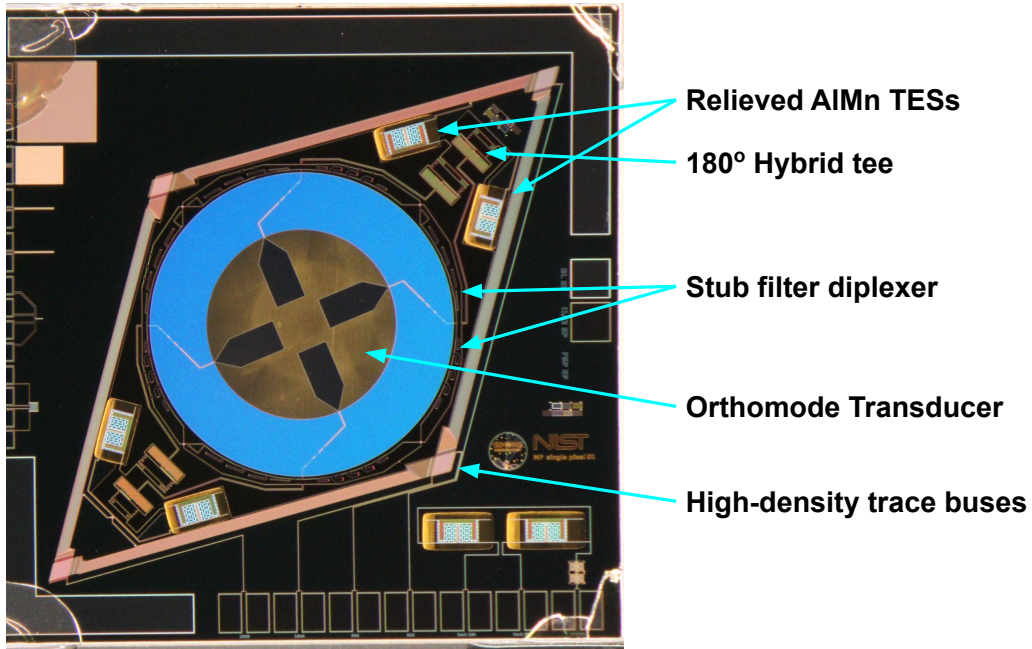


Figure 4.3: Photograph of a SO MF 90/150 GHz single pixel used for prototype TES characterization. The microwave structures which take radiation from the feedhorn to the TESs and readout are labeled.

Figure 4.3 shows a labeled SO MF single pixel. The design and fabrication of the NIST-style SO detectors is very similar to the AdvACT arrays, which are described in Duff et al (2016) [48]. Radiation from the horn is coupled to the polarization-sensitive plus-shaped orthomode transducer antenna (OMT). The OMT resides on a suspended nitride film which sits between a choke-coupled feedhorn and a quarter-wave backshort that optimizes the antenna efficiency [102].

The radiation is then transmitted via microstrip to on-chip diplexing stub-filters which define the TES bandpasses. Each band is then sent to a hybrid-tee which combines the signals from opposite OMT fins. The sum port of the hybrid-tee is terminated on the silicon chip while the difference port is sent on to the TES. This preserves polarization purity by selecting the 11 mode of the waveguide, at the cost of power³. The difference port of the hybrid-tee is terminated in a lossy meander on the TES bolometer island. All four TESs on the pixel are then connected to wire busses at perimeter of the detector which route the TESs to remainder of the TES circuit described below. The LF pixels from UCB follow a very similar pixel architecture except they use a sinuous antenna instead of an OMT and hybrid-tee [138, 156].

4.2.2 TES Model

Our TES bolometers are electrothermal devices. During operation, they are electrically biased onto the superconducting transition. Their resistance is a function of the bolometer temperature and the current through the TES. Therefore, they effectively behave as a very sensitive transducer. The bias circuit is designed such that the TES is approximately voltage biased. This gives rise to negative electrothermal feedback. For example, as incident radiation raises the temperature and resistance of the TES, the Joule heating bias power ($P_{\text{bias}} = V^2/R_{\text{TES}}$) decreases. This negative feedback maintains the TES on its transition, enabling its operation under a varying optical load.

Figure 4.4 (left) illustrates the single-body electrothermal model of a TES. In

³For an instrument that doesn't intend to measure polarization, such as EoR-spec, maximizing the number of photons absorbed by the detector is paramount to overall instrument sensitivity and mapping speed, and so a hybrid-tee would not be used.

the model, the TES resides on a thermal island with total heat capacity C and temperature T . Multi-body thermal models for the TES have been developed in the literature [35, 63, 96] but for our purposes, the simpler single-body model suffices. The island is weakly connected to the bath temperature T_{bath} via a thermal conductance G . Radiation that is terminated on the bolometer island with power P_γ raises the temperature of the bolometer and thus the resistance of the TES, R_{TES} . The TES bias circuit is also shown in the model. A bias current I_{bias} is applied through the circuit consisting of the parallel combination of the TES resistance and a shunt resistor, where $R_{\text{sh}} \ll R_{\text{TES}}$. This voltage-biases the TES with $V_{\text{bias}} = I_{\text{bias}}R_{\text{sh}}$. The TES branch of the bias circuit is inductively coupled to a superconducting quantum interference device (SQUID) readout system. The author’s different collaborations are using different SQUID-based multiplexed readout systems which are described in more detail in [71, 72]. The SQUID readout measures the change in current through the TES branch of the bias circuit.

Figure 4.4 (right) shows a microscope photo of an SO 150 GHz TES bolometer island fabricated at NIST. Details on the fabrication can be found in Duff et al (2016) [48]. The TES is suspended on a thin nitride film via four “legs” whose width and length control the thermal conductance G to the bath [84, 135]. The black areas surrounding the island are “open-to-below”, isolating the bolometer island from the bath except at the legs. On the island, a U-shaped gold meander is used to terminate radiation from the pixel’s antenna, transforming it into heat on the island. The thin rectangle in the middle of the island is the AlMn TES, which is coupled to the bias circuit via niobium traces that go through one of the bolometer legs. The rest of the island (pink area) is PdAu and AlMn which comprise the thermal ballast of the suspended island. The PdAu and AlMn volumes are adjusted to tune the total heat capacity C of the island (Section 4.3.5). The intrinsic time

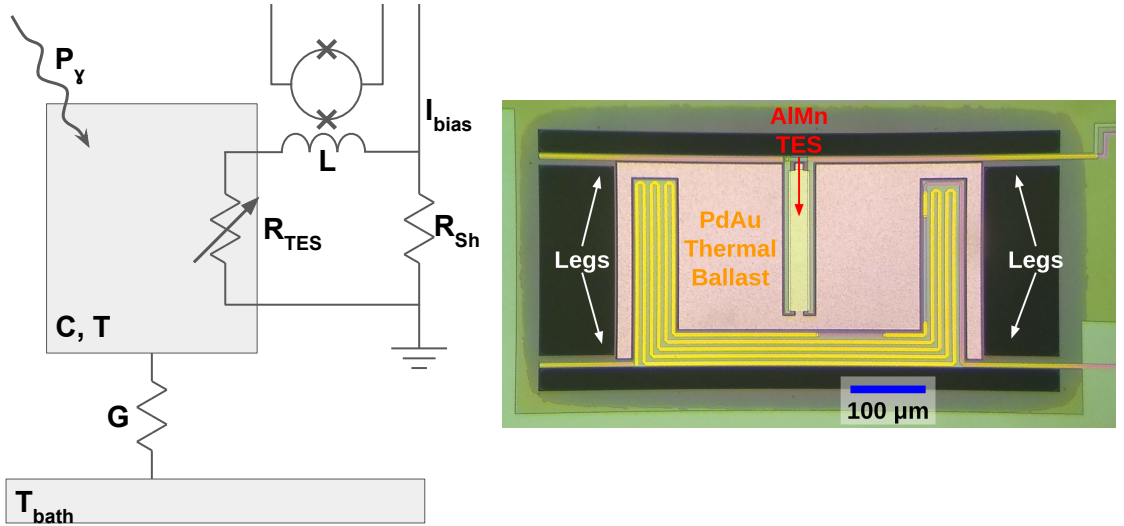


Figure 4.4: *Left:* Illustration of the coupled electrothermal TES system. A single-body thermal model is assumed. The bias circuit is shown along with an inductively-coupled SQUID for probing the current through the TES. *Right:* Microscope photograph of a prototype SO 150 GHz TES bolometer fabricated at NIST. Four legs support the floating island and define G . The pink thermal ballast comprised of AlMn and PdAu define C . The meandering line in the lower portion of the island is the resistive termination from the waveguide. The AlMn TES is the white rectangle in the middle of the island.

constant (in the absence of electrothermal feedback, $P_{bias} = 0$) of the bolometer is therefore driven by the geometry of the legs and the volume of the thermal ballast of the bolometer island, $\tau_{nat} \equiv C/G$.

Using the model presented above, we now develop a formalism for understanding the TES behavior in response to small changes in the photon loading and bias current. As an electrothermal system, the response of a TES can be described by two coupled differential equations. A detailed derivation is presented in Irwin & Hilton's chapter, *Transition-Edge Sensors* [78]. Here, we follow portions of their derivation, highlighting the equations that are most relevant to the TES measurements presented in Section 4.3.

The total power flowing into the TES can be written:

$$P_{\text{TES}} = P_{\text{bias}} + P_{\gamma} - P_{\text{bath}}, \quad (4.1)$$

where P_{bias} and P_{γ} are the bias and optical powers defined above and P_{bath} represents the power flowing from the TES to the bath. P_{bath} which is well described by a power law [100]:

$$P_{\text{bath}}(T) = k(T^n - T_{\text{bath}}^n), \quad (4.2)$$

where T is the temperature of the TES, n is the power law index and k is the coefficient of thermal conduction. We define the saturation power as the power flowing to the bath when the TES is at its critical temperature T_c such that

$$P_{\text{sat}} \equiv P_{\text{bath}}(T_c) = k(T_c^n - T_{\text{bath}}^n). \quad (4.3)$$

Note that P_{sat} is a function of the bath temperature and that lower bath temperatures mean higher saturation powers. From this, we also define the thermal conductance of the bolometer,

$$G \equiv \frac{dP_{\text{bath}}}{dT} = nkT^{n-1}. \quad (4.4)$$

During operation, when the TES is biased onto it's transition, we can make the approximation that $T \approx T_c$ since the transition is narrow⁴. These equations are useful for characterizing the saturation power and thermal conductance of a TES (Section 4.3.2).

The electrical and thermal differential equations of the TES are written as

$$L \frac{dI_{\text{TES}}}{dt} = V_{\text{bias}} - I_{\text{TES}}R_{\text{sh}} - I_{\text{TES}}R_{\text{TES}}(T, I_{\text{TES}}) \quad (4.5)$$

⁴The superconducting transition width is $\mathcal{O}(1\%)$ of the critical temperature, as is shown in Section 4.3.1 and Figure 4.7.

and

$$C \frac{dT}{dt} = P_{\text{TES}} = P_{\text{bias}} + P_{\gamma} - P_{\text{bath}}, \quad (4.6)$$

where the TES resistance R_{TES} is a function of the TES temperature, T , and the current flowing through the TES, I_{TES} .

We assume small signals and Taylor expand each of the terms around their steady state values (R_0 , T_0 , I_0) to first order. As such, the power to the bath can be expanded

$$P_{\text{bath}} \approx P_{\text{bath}0} + \frac{dP_{\text{bath}}}{dT} \delta T = P_{\text{bias}0} + P_{\gamma 0} + G \delta T, \quad (4.7)$$

where $P_{\text{bias}0} = I_0^2 R_0$ is the steady state bias power, $P_{\gamma 0}$ is the steady state optical power, and $\delta T \equiv T - T_0$. Similarly, the resistance can be expanded to first order:

$$R_{\text{TES}}(T, I_{\text{TES}}) \approx R_0 + \left. \frac{\partial R}{\partial T} \right|_{I_0} \delta T + \left. \frac{\partial R}{\partial I} \right|_{T_0} \delta I = R_0 + \alpha \frac{R_0}{T_0} \delta T + \beta \frac{R_0}{I_0} \delta I, \quad (4.8)$$

where $\delta I \equiv I_{\text{TES}} - I_0$ and we have defined the logarithmic temperature and current sensitivities, $\alpha \equiv \left. \frac{\partial \log R}{\partial \log T} \right|_{I_0}$ and $\beta \equiv \left. \frac{\partial \log R}{\partial \log I} \right|_{T_0}$, respectively. We can further expand the bias power to first order

$$P_{\text{bias}} = I_{\text{TES}}^2 R_{\text{TES}}(T, I_{\text{TES}}) \approx P_{\text{bias}0} + 2I_0 R_0 \delta I + \alpha \frac{P_{\text{bias}0}}{T_0} \delta T + \beta \frac{P_{\text{bias}0}}{I_0} \delta I. \quad (4.9)$$

We also define the constant current loop gain

$$\mathcal{L}_I = \frac{P_{\text{bias}0} \alpha}{G T_0}. \quad (4.10)$$

We now rewrite the governing differential equations (Eqs 4.5 and 4.6) and insert the expanded approximations. The DC terms cancel and second order terms are dropped such that

$$L \frac{d\delta I}{dt} = -[R_{\text{sh}} + R_0(1 + \beta)]\delta I - \frac{\mathcal{L}G}{I_0} \delta T + \delta V \quad (4.11)$$

$$C \frac{d\delta T}{dt} = I_0 R_0 (2 + \beta) \delta I - G(1 - \mathcal{L}) \delta T + \delta P, \quad (4.12)$$

where $\delta P \equiv P_\gamma - P_{\gamma 0}$ and $\delta V \equiv V_{\text{bias}} - V_0$ represent small changes in the optical load and bias voltage respectively.

Consider extreme cases for these equations. In the limit of $\delta V = 0$ (constant voltage bias) and $\mathcal{L} \rightarrow 0$ (small α or P_{bias}), then the current equation is easily integrable and gives an exponential decay with electrical time constant $\tau_{\text{el}} = L/[R_{\text{sh}} + R_0(1 + \beta)]$. Similarly, in the limit of $\delta I = 0$ (constant current bias) and $\delta P \rightarrow 0$ (small changes in the optical signals), then the thermal equation is easily integrable and gives the current-biased thermal time constant $\tau_I = \tau_{\text{nat}}/(1 - \mathcal{L})$.

We now follow Lindeman et al (2004) [94], writing the coupled differential equations in matrix format and taking their Fourier transform [51] to analyze the electrothermal system in frequency-space:

$$\begin{pmatrix} \left[\frac{1}{\tau_{\text{el}}} + i\omega \right] L & \frac{\mathcal{L}G}{I_0} \\ -I_0 R_0 (2 + \beta) & \left[\frac{1 - \mathcal{L}}{\tau_{\text{nat}}} + i\omega \right] C \end{pmatrix} \begin{pmatrix} I_\omega \\ T_\omega \end{pmatrix} = \begin{pmatrix} V_\omega \\ P_\omega \end{pmatrix}. \quad (4.13)$$

Alternatively, we can write this as

$$M \begin{pmatrix} I_\omega \\ T_\omega \end{pmatrix} = \begin{pmatrix} V_\omega \\ P_\omega \end{pmatrix}, \quad (4.14)$$

such that we can solve for the TES current and temperature as functions of small voltage and power inputs with

$$\begin{pmatrix} I_\omega \\ T_\omega \end{pmatrix} = M^{-1} \begin{pmatrix} V_\omega \\ P_\omega \end{pmatrix}. \quad (4.15)$$

The matrix M is often referred to as the generalized responsivity matrix because it describes the current and temperature responses to voltage and power inputs

[78]. In the time domain, the eigenvalues and eigenvectors of M can be used to diagonalize the matrix and find its homogeneous solution which is the sum of two decaying exponentials. The eigenvalues represent the time constants of the exponentials, corresponding to the “rise” and “fall” times after a delta-function impulse. Irwin & Hilton [78] provides a detailed time domain derivation but we skip to the result. In the small inductance limit, the rise time corresponds to τ_{el} and the fall time corresponds to an effective thermal time constant

$$\tau_{\text{eff}} = \tau_{\text{nat}} \frac{1 + \beta + R_{\text{sh}}/R_0}{1 + \beta + R_{\text{sh}}/R_0 + (1 - R_{\text{sh}}/R_0)\mathcal{L}}, \quad (4.16)$$

which is often rewritten as

$$f_{3\text{dB,eff}} = \frac{1}{2\pi\tau_{\text{eff}}} = f_{3\text{dB,nat}} \left(1 + \frac{(1 - R_{\text{sh}}/R_0)\mathcal{L}}{1 + \beta + R_{\text{sh}}/R_0} \right), \quad (4.17)$$

where $f_{3\text{dB,nat}} = 1/2\pi\tau_{\text{nat}} = G/2\pi C$. When $R_{\text{sh}}/R_0 \ll 1$, this reduces to

$$f_{3\text{dB,eff}} = f_{3\text{dB,nat}} \left(1 + \frac{\mathcal{L}}{1 + \beta} \right). \quad (4.18)$$

From this, we see that negative electrothermal feedback has the effect of speeding up the thermal time constant of the TES. From the standpoint of designing detectors for telescopes, this is the time constant we care most about and present in Section 4.3.3.

The advantage of writing the system of coupled equations (Equation 4.13) in the frequency domain is that the complex impedance of the circuit is easily extracted from M_{11}^{-1} [78, 94]:

$$Z_{\omega} = \frac{V_{\omega}}{I_{\omega}} = Z_{\text{eq}} + Z_{\text{TES}}, \quad (4.19)$$

where $Z_{\text{eq}} = R_{\text{sh}} + i\omega L$ is the equivalent impedance of the bias circuit elements and Z_{TES} is the impedance of the TES alone. Z_{TES} can be shown to be

$$Z_{\text{TES}}(\omega) = R_0(1 + \beta) + \frac{R_0\mathcal{L}(2 + \beta)}{1 - \mathcal{L} + i\omega\tau_{\text{nat}}}, \quad (4.20)$$

which can be rewritten as

$$Z_{\text{TES}}(f) = R_0(1 + \beta) + \frac{R_0\mathcal{L}(2 + \beta)}{1 - \mathcal{L} + if/f_{\text{nat}}}, \quad (4.21)$$

where $f = \omega/2\pi$ is the frequency of the incident radiation. $Z_{\text{TES}}(f)$ takes the form of a semi-circle in the lower half of the complex plane. By measuring the phase and amplitude response of a TES as a function of frequency, we can map out $Z_{\text{TES}}(f)$. The low frequency limit reduces to $Z_{\text{TES}} \approx -R_0$, while the high frequency limit goes to $Z_{\text{TES}} \approx R_0(1 + \beta)$. If the limits are properly probed, they can be used to constrain β . Further, if we expand the loopgain and natural time constant, we can rewrite as

$$Z_{\text{TES}}(f) = R_0(1 + \beta) + \frac{R_0(2 + \beta)\alpha P_{\text{bias}}}{(T_c G - \alpha P_{\text{bias}}) + 2\pi i f T_c C}, \quad (4.22)$$

where we have used the approximation $T_0 \approx T_c$. Thus, if we know R_0 , P_{bias} , T_c , and G , then we can fit $Z_{\text{TES}}(f)$ for α , β , and C . We do this using I-V curves (Section 4.3.2) to determine the prerequisite parameters before fitting complex impedance data (Section 4.3.4).

4.2.3 SO detector parameters

To optimize TES bolometer designs for SO at Cornell, we focus on tuning the saturation powers and time constants for each band to operate in the expected observing conditions. First, we set targets for the parameters which are constant between each band. The bath temperature and critical temperature targets are $T_{\text{bath}} = 100$ mK and $T_c = 160 \pm 10$ mK. The target TES normal resistance and the shunt resistance are $R_N = 8$ mΩ and $R_{\text{sh}} = 400$ μΩ.

Next, to set the target saturation powers, the photon loading on the detectors must be estimated. Many factors affect the photon loading including the pre-

cipitable water vapor (PWV), the throughput of the telescopes, the efficiencies of the optics, and the on-pixel microwave components. The photon loading has been estimated for each telescope and band using SO-specific sensitivity calculators which incorporate estimates for these components [74]. The LAT and SAT photon loading estimates differ but are similar enough that we typically take the average loading for our calculations. We apply a safety factor of 2.4 to the photon loading estimates (assuming 1 mm PWV, an elevation angle of 50°, and ambient temperature mirrors) to determine the target saturation powers. We allow $\pm 25\%$ variation in saturation powers. Table 4.1 lists the expected photon loading power for each band and the related target saturation power ranges.

Band	Freq.	$P_{\gamma,1\text{mm}}$	P_{sat} range	Min. $f_{3\text{dB,eff}}$	$f_{3\text{dB,eff}}$ Limit
LF-1	27 GHz	0.3 pW	0.6 – 1.0 pW	150 Hz	SAT CHWP
LF-2	39 GHz	1.5 pW	2.7 – 4.4 pW	150 Hz	SAT CHWP
MF-1	90 GHz	1.1 pW	2.0 – 3.3 pW	150 Hz	SAT CHWP
MF-2	150 GHz	3.0 pW	5.4 – 9.0 pW	166 Hz	LAT Nyquist
UHF-1	220 GHz	9.4 pW	17 – 28 pW	245 Hz	LAT Nyquist
UHF-2	280 GHz	12 pW	22 – 37 pW	279 Hz	LAT Nyquist

Table 4.1: Target saturation power ranges and time constant requirements for SO TESes given the estimated optical loading in each band.

To set the target time constants, we consider the operating mode of the telescopes. The LAT scans its diffraction limited beam width, $\theta \approx 1.22\lambda/(6 \text{ m})$, across the sky at some speed, $S \approx 1.5\text{deg/s}$. In order to properly Nyquist sample the sky, the effective time constant must be no slower than $1/2\pi\tau_{\text{eff}} = f_{3\text{dB,eff}} = 2.4S/\theta$ [126]. The LAT beam size is much smaller than the SAT and so the LAT drives the Nyquist limited time constant. However, the SATs are operated with a cryogenic half-wave plate (CHWP) to modulate the polarized signal [73, 83]. The CHWP will rotate at 2 Hz and so in order to deconvolve the polarization signal with sufficient accuracy, the detectors will need to be no slower than $f_{3\text{dB,eff}} = 150 \text{ Hz}$. This

requirement is faster than the LAT Nyquist requirement for SO’s lowest three frequency bands and so supersedes them. Table 4.1 summarizes the minimum $f_{3\text{dB},\text{eff}}$ (maximum τ_{eff}) requirements for each band. Note that the $f_{3\text{dB},\text{eff}}$ requirement for UHF-280 GHz is 279 Hz ($\tau_{\text{eff}} = 0.57$ ms), which is faster than most detectors previously fielded by our collaborations.

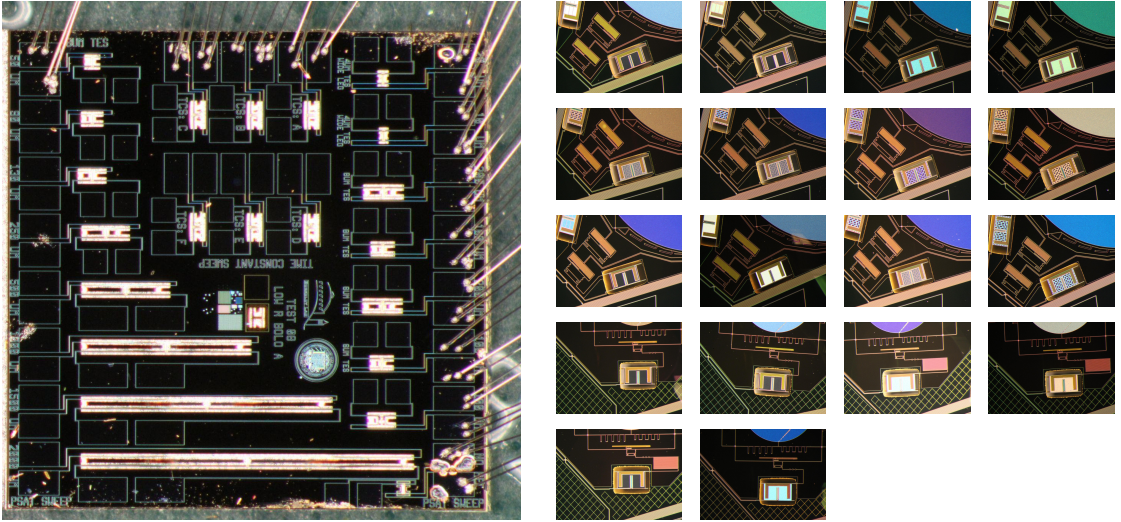


Figure 4.5: Microscope photographs of UCB TES test die (left) and NIST single pixels (right) illustrating the various leg length and heat capacity splits used to optimize G and C and thus P_{sat} and $f_{3\text{dB}}$.

To achieve these target parameters for full arrays of detectors, many prototype TESs are made first. Figure 4.5 shows photographs of UCB and NIST bolometer test chips and single pixels. To tune P_{sat} , we change G by modifying the leg lengths. The photo on the left shows a test die with TESs of varying leg lengths which are used to tune the saturation power by changing G . Once G is set for the target P_{sat} , we tune $f_{3\text{dB},\text{eff}}$ by changing C via the volumes of PdAu and AlMn on the island. The photos on the right show many TESs in single pixels with different amounts of PdAu and AlMn heat capacity volumes. In the next section, we will discuss how measurements of these different “spilts” are used to characterize their saturation powers and time constants.

Many iterations of SO bolometers have been characterized. At the time of this writing, there have been three iterations of UHF single pixels to tune their design heat capacities for the fast time constant requirements [33]. Similarly, multiple iterations of LF single pixels have been examined to tune their critical temperatures and normal resistances [135]. The MF detector designs are very similar to the AdvACT bolometers and thus have required less tuning to meet the target specifications [33]. Detectors from the most recent iteration of MF and UHF single pixels, called SO Single Pixels v3 (SOSP3), will be featured as examples throughout the remainder of the chapter. The characterization methods presented below were also used to examine prototype bolometers for commercialized TES fabrication [138, 139] and for other past and future collaborations such as AdvACT [84] and CMB Stage-4 (CMB-S4) [150].

4.3 TES Characterization Methods

We present four different TES characterization methods: four-wire R-T curves, I-V curves, bias steps, and complex impedance measurements. The first of these is performed with a Lakeshore AC resistance bridge (370/372) and is used as a fast method to probe T_c and R_N . The latter three measurements are performed using a multi-channel electronics (MCE) time division multiplexed (TDM) SQUID readout system [15] which is the same readout electronics used on AdvACT. A detailed description of our TDM system for single pixel characterization is presented in [72, 137].

Figure 4.6 shows how the single pixel TESs are coupled to the readout system. TESs are wire-bonded to different rows on an interface chip. The interface chip

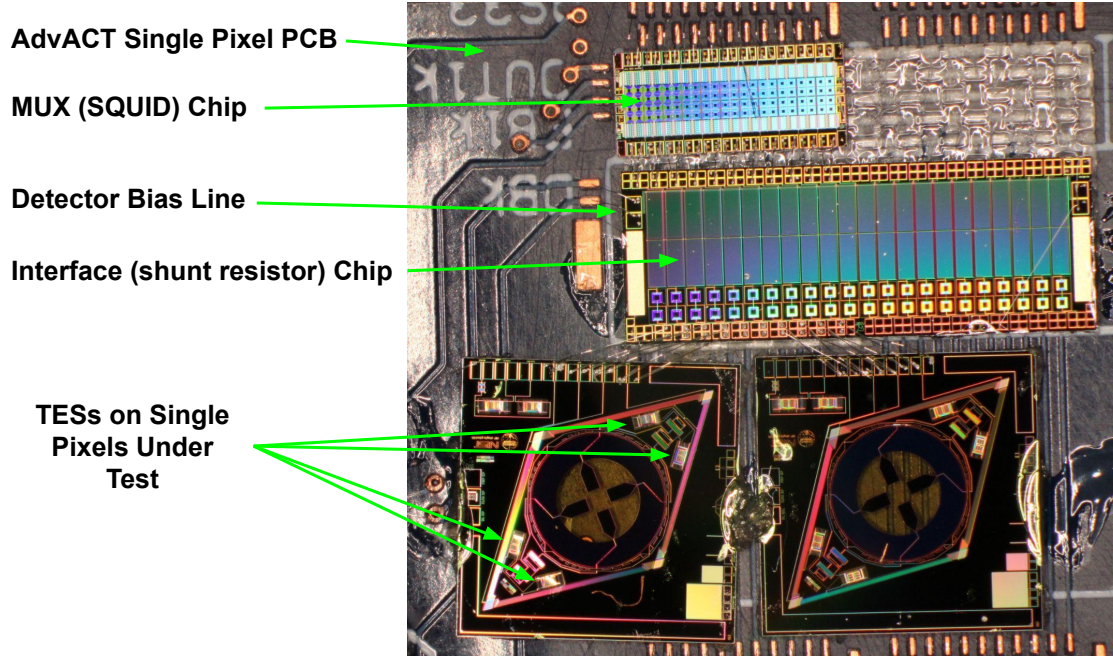


Figure 4.6: Photograph of NIST-style SO MF single pixels on the AdvACT TDM single-pixel test PCB. Each TES is wire-bonded to a row on the interface chip which contains the shunt resistors for each row and a single biasline. Each row is then bonded to a DC SQUID MUX chip where the rows are readout serially via TDM. The PCB is operated in a dark environment in our dilution refrigerator.

contains a single bias line which runs through a shunt resistor⁵ in each row. The interface chip also contains optional (wirebond selected) Nyquist inductors that can be used to tune the RL high-frequency roll-off of the TES circuit, which is important for aliasing [57]. Each detector/row is then wire-bonded to a DC SQUID multiplexer (MUX) chip which enables the TDM serialized readout of each row. More rows can be added by adding more MUX and interface chips in parallel. A column consists of all the chips connected to a single set of TES bias, SQUID bias, and SQUID feedback lines. The single pixel test PCB (blue, beneath the chips) contains wiring for multiple columns, enabling the screening of multiple

⁵Note that for the AdvACT style SQUID-based readout used here, we use $R_{sh} \approx 200 \mu\Omega$ instead of SO's target $400 \mu\Omega$.

MUX, interface, and TES chips. The PCB provides all of the necessary electrical interfaces to the rest of the MCE system.

Lastly, we note that the measurements presented in this section were performed in our Bluefors LD-400 dilution refrigerator (DR) at Cornell. The bath temperature on the DR mixing chamber plate was controlled with a Bluefors calibrated ROX thermometer and a servoed heater via a Lakeshore 370 AC resistance bridge. The DR was optically closed such that detectors on the mixing chamber plate operated in the “dark”, seeing only the 1 K copper shell that was cooled by the DR still.

4.3.1 R vs T Critical Temperatures

Confirming the target T_c and R_N of a prototype pixel is a critical first step for bolometer characterization. If either parameter is off-target, it can affect the results of subsequent measurements. For example, if T_c is too high, then the saturation power will be inflated via Equation 4.3. Further, if R_N is too high, the detector noise will increase relative to the readout noise. It is therefore prudent to perform simple checks on T_c and R_N for new TES designs.

Figure 4.7 shows two sets of four-wire resistance measurements from a NIST-style SO MF single pixel. The left plot shows measurements of a 150 GHz TES bolometer which consists of a 1/8th square of AlMn on a suspended bolometer island. The right plot shows measurements of a T_c -check pad that also resides on the single pixel, consists of a full square of AlMn, and is designed to make it easier to measure T_c with higher signal to noise than the TES.

The measurements were performed with a Lakeshore 372 AC resistance bridge

using multiple AC excitation currents. An Ruthenium oxide (ROX) thermometer was placed behind the TESs on the rear of the four-wire PCB that they were bonded to. During measurements, the temperature of the four-wire board was servoed using the ROX and a heater placed at the mixing chamber of the DR.

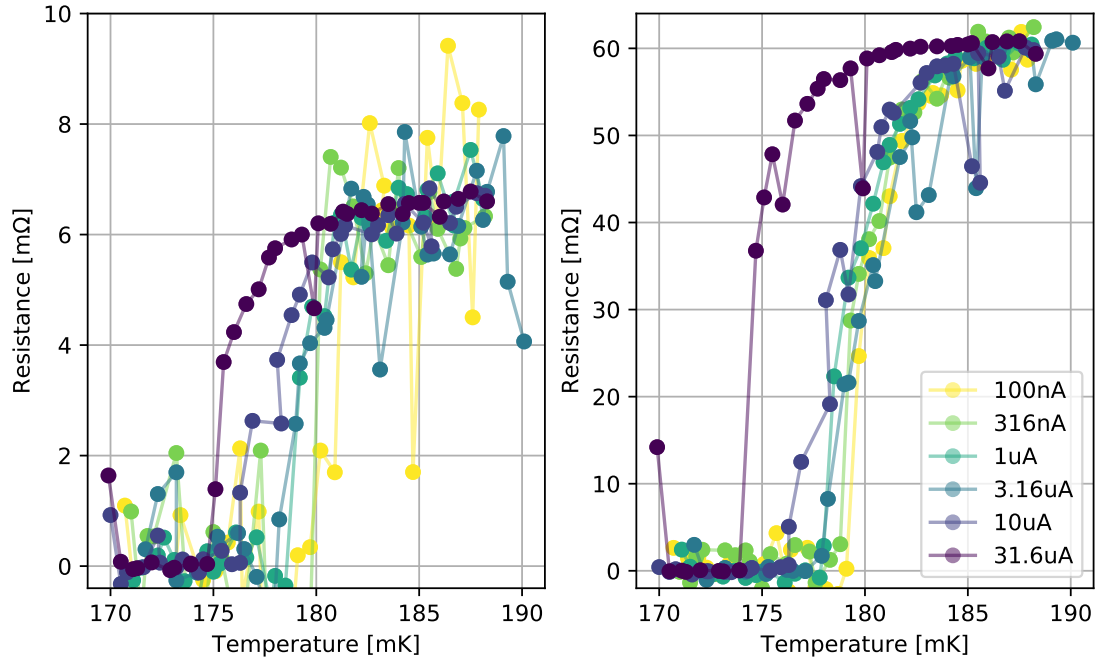


Figure 4.7: Critical temperature and normal resistance measurements of SOSP3 150 GHz TES (left) and SOSP3 T_c -check pad structure (right). Measurements were taken with a Lakeshore 372 AC resistance bridge. Measurements at multiple AC excitation currents were taken (see legend). T_c is deflated at higher excitation currents. The TES is 1/8th square AlMn and the check pad is a full square AlMn. The normal resistances roughly confirm this by scaling by a factor of ~ 8 . T_c is found to be ~ 179 mK for both samples.

For both samples, the critical temperature is deflated at excitation higher currents. However at lower excitation currents, the four-wire resistance measurements are noisier, making it more difficult to constrain T_c . Longer data integration times were used to increase the signal to noise ratio of low excitation measurements. The critical temperature of both samples is found to be ~ 179 mK. The normal

resistances are found to be $\sim 6.8 \text{ m}\Omega$ and $\sim 60 \text{ m}\Omega$ for the TES and T_c -check pad respectively. The TES resistance is slightly lower than expected when compared to the T_c check pad given the $1/8^{\text{th}}$ square geometry. Further, we find that T_c is higher than the $160 \pm 10 \text{ mK}$ target set by SO, indicating the need to tune this in fabrication more carefully during array fabrication.

4.3.2 I-V Curve Saturation Powers

I-V curves are one of the most useful characterization methods available to us. The measurements are relatively quick and provide a wealth of information about the detector and its photon loading environment. I-V curves are performed in the field (on AdvACT arrays) at regular intervals throughout each day/night of observing. The measurement begins by driving the TES normal with a large bias voltage, V_{bias} . The bias is then decreased and I_{TES} is measured as $R_{\text{TES}}(T, I_{\text{TES}})$ drops through its superconducting transition. In the field, it takes about a minute to run an I-V curve on all detectors in the array simultaneously. In the laboratory, we measure I-V curves at a variety of bath temperatures, enabling us to extract additional TES parameters. For prototype TES testing, we servo to a specific bath temperature, wait about 10 minutes for the single pixel board to thermalize with the DR, and then run an I-V curve before servoing to another bath temperature.

The left panel of Figure 4.8 overplots I-V curves of a single MF 150 GHz prototype SO TES at many bath temperatures. At high V_{bias} , the TES is normal and the slope gives the TES's normal resistance. The region with negative slope is the superconducting transition, and in the region below that at low V_{bias} , the TES is superconducting. From the I-V curves, we can extract the TES resistance and TES bias power by taking the ratio and product of the measured voltage

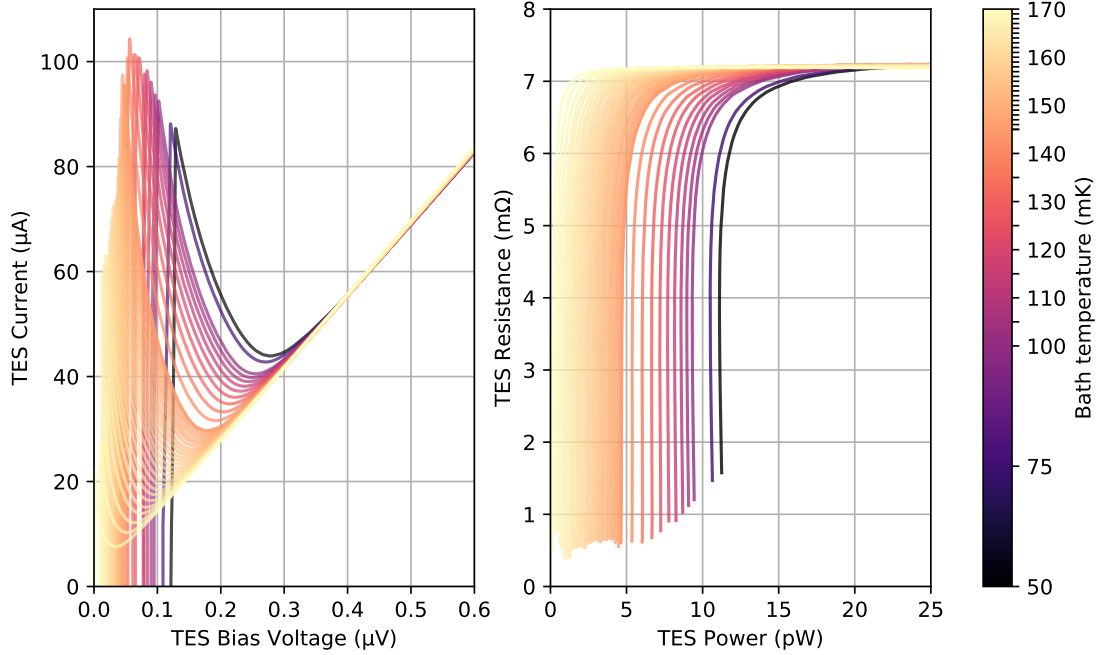


Figure 4.8: Left: I-V curves of a SO MF 150 GHz TES at many bath temperatures. Right: R-P curves calculated from the I-V data for the same TES. The ticks on the colorbar indicate the bath temperatures at which data were taken. We note that the TES normal resistance is independent of bath temperature while the saturation power decreases with increasing bath temperatures, as expected.

and current. The right panel of Figure 4.8 overplots R-P curves based on the I-V curves in the left panel. We see that regardless of bath temperature, at high bias power, the TES has a consistent normal resistance of ~ 7 mΩ. We also see that the amount of bias power that is required to drive the TES normal increases with decreasing temperature, as expected from Equation 4.3. From the R-P curves, we extract R_N and $P_{\text{sat}}(T_{\text{bath}})$

Figure 4.9 plots the saturation power as a function of bath temperature (blue dots) for the same device as shown in Figure 4.8. The data was fit⁶ to Equation 4.3 and is shown as the overplotted lines. The free parameters in Equation 4.3

⁶The IV analysis and P_{sat} fitting routing is based heavily on work done by Dr. Jason Stevens and others [135].

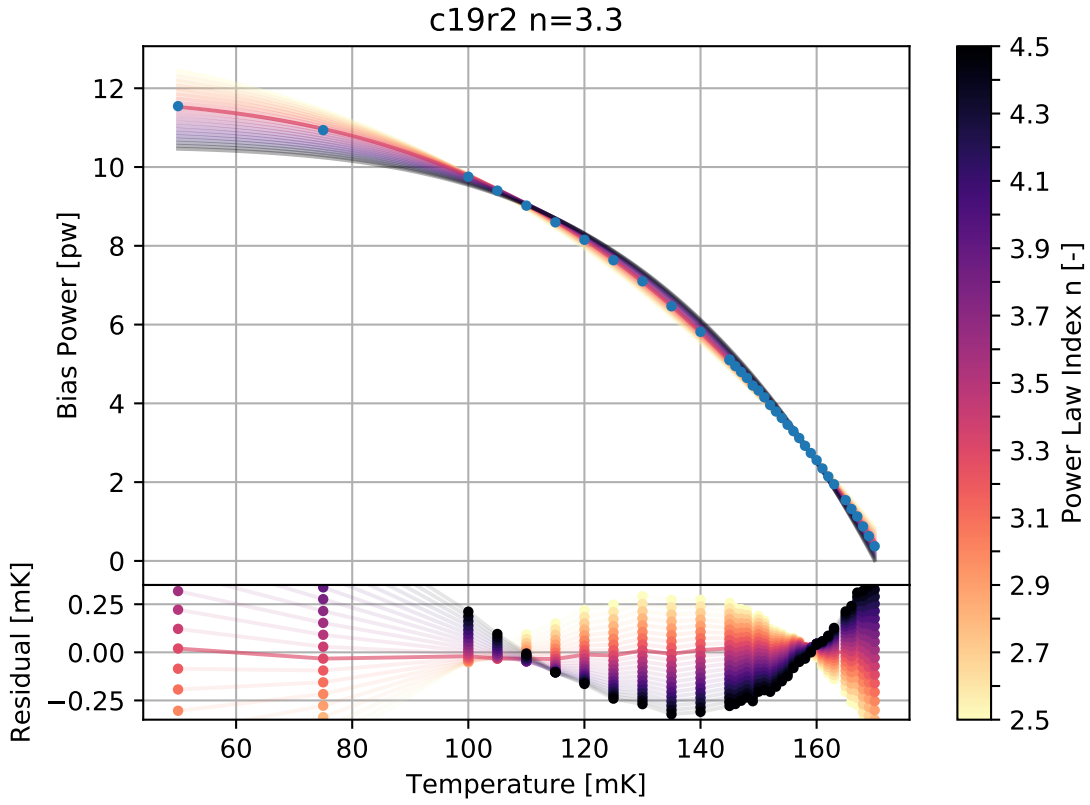


Figure 4.9: TES saturation power data as a function of bath temperature (blue dots, upper panel). Data corresponds to the I-V curves shown in Figure 4.8. The data is fit to Equation 4.3. We fit the data multiple times for fixed n in order to investigate degeneracy between n and k . The lower panel shows that $n = 3.3$ (bolded line) minimizes the residual for this detector. The ticks on the colorbar indicate the values of n that were used in the fits.

are n , k , and T_c but due to modest degeneracy between n and k , it was historically found to be simplest to fix n during the fit and manually search for n given the fit results [137]. In Stevens et al 2020 [135], $n = 3$ was used held constant. In Figure 4.9 the we plot the residuals for fits over a wide range of n from 2.5 to 4.5. For this detector, it is found that $n = 3.3$ (bolded line in Figure 4.9) minimizes the residuals well across all temperatures.

From the fit to Equation 4.3, we determine n , k , and T_c , and can then use

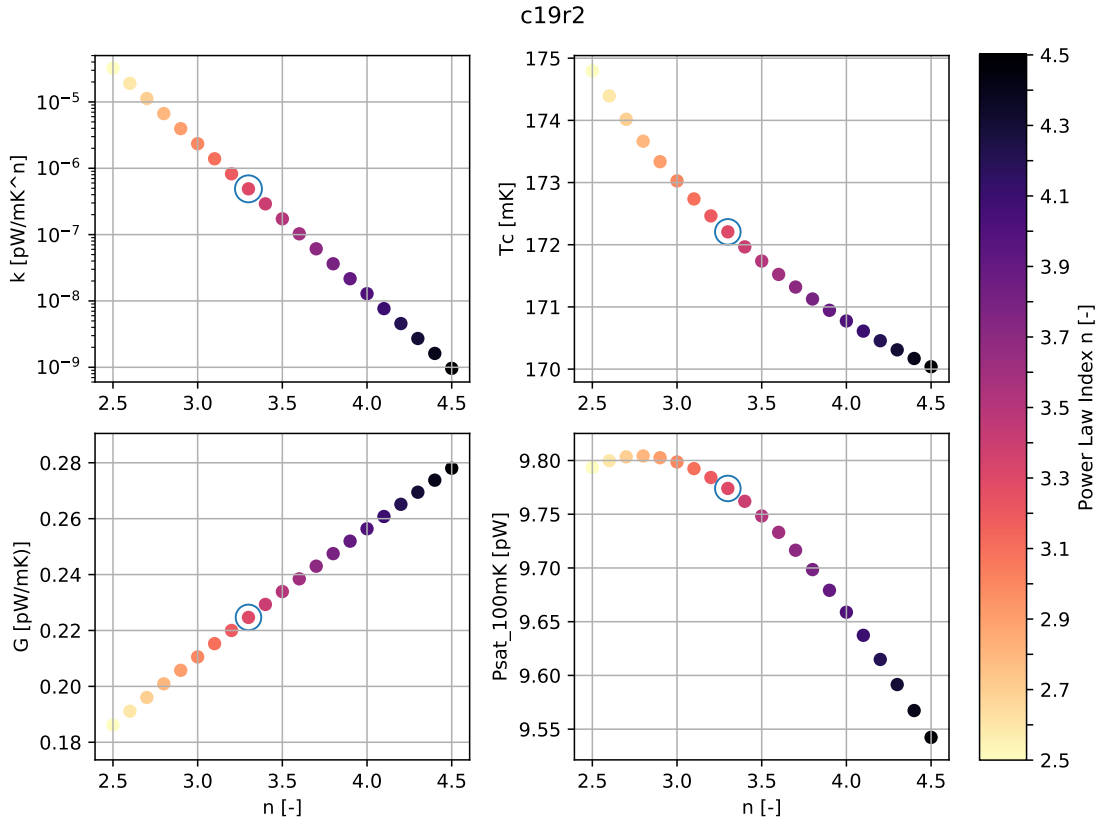


Figure 4.10: Extracted parameters from the fits shown in Figure 4.9 as a function of n . We see that k is highly dependent on n but different combinations of n and k yield significantly different T_c , G , and $P_{\text{sat},100\text{mK}}$, suggesting that an optimal n and k can be found. The fit-extracted parameters for $n = 3.3$ are circled and presented in Table 4.2.

them to determine T_c , $P_{\text{sat},100\text{mK}}$, and G . The critical temperature is found by extrapolating the fit to the x-intercept. The saturation power at 100 mK (the target bath temperature for the SO arrays), is calculated by evaluating the fit at $T_{\text{bath}} = 100$ mK. The thermal conductance is calculated by plugging in the previously fit parameters to Equation 4.4.

To further examine the degeneracy between n and k , we look at how the fit and calculated parameters k , T_c , G , and $P_{\text{sat},100\text{mK}}$ vary as a function of n . Figure 4.10 plots these parameters for each fit in Figure 4.9. As expected, k is highly

dependent on n . However, each of the other parameters is also relatively variable with n , suggesting that there is a combination of n and k which should sufficiently minimize the residuals of $P_{\text{sat}}(T_{\text{bath}})$. We see that depending on our choice of n between 2.5 and 4.5, the critical temperature can vary almost a percent and saturation powers can vary up to a few percent. Table 4.2 presents the best fit parameters for the I-V and P_{sat} analyses for this prototype detector.

R_N [mΩ]	n	k [pW/mK n]	T_c [mK]	G [pW/mK]	$P_{\text{sat},100\text{mK}}$ [pW]
7.2	3.3	5×10^{-7}	172.2	0.225	9.77

Table 4.2: Table of best-fit parameters from I-V and P_{sat} analysis for the SO MF 150 GHz TES data shown above.

During prototype TES characterization, we perform these I-V measurements and analyses on many TESs. These measurements help determine whether we are meeting the T_c and R_N targets and allow us to probe G for TESs with different leg lengths in order to set $P_{\text{sat},100\text{mK}}$ for our fieldable arrays. We report these measurements for SO in Stevens et al 2020 [135], and similar measurements for AdvACT in Koopman et al 2018 [84].

4.3.3 Bias Step Time Constants

A common way to measure the effective thermal time constant of TES bolometers is the bias step method. By applying a small amplitude square-wave to the TES bias, the thermal response of the TES can be observed. Like I-V curves, this measurement is frequently performed during observations on deployed AdvACT arrays. In the lab, we characterize the TES response as a function of simulated loading conditions by performing bias step time constant measurements at many T_{bath} and at multiple points in the superconducting transition, $\%R_N = R_0/R_N$. At

each bath temperature, I-V curve measurements are used to determine the P_{bias} required to bias the TES to a specific $\%R_N$.

In order to measure the time constant well, the data acquisition rate must be much faster than the detectors $f_{3\text{dB},\text{eff}}$. In normal operation, our MCE is setup to sample at ~ 400 Hz. To speed the MCE data acquisition up to this rate, we reduce the number of sampled rows. By default, our MCE serially samples 64 rows at 400 Hz. For these measurements, `num_rows` is decreased from 64 to 4, increasing the row-visit rate by a factor of 16, giving us an effective TES sampling rate of ~ 6400 Hz. This greatly increases the fidelity of the measurements but limits us to using only the first four rows of every column.⁷

Before a bias step measurement, a DC bias is applied to the TES, placing it on its transition at some fraction of its normal resistance, $\%R_N$. A square wave with an amplitude much smaller ($\sim 5\%$) than I_{bias} is then applied on top of the DC bias⁸. Roughly 30 periods of the square waves are repeated, building a statistical picture of the bolometer's stimulated response. To understand how the time constant varies at different points on the superconducting transition, the TES can then be re-biased to a different $\%R_N$ and another bias step can be acquired.

The left panel of Figure 4.11 shows an example bias step time stream in DAC units. The square wave response is evident. The spikes before each step represent the electrical response and are followed by a slower thermal decay. Before fitting the thermal response of the TES, the time stream is split into individual steps of the square wave. The colored lines in the right panel of Figure 4.11 show the individual steps stacked on top of each other. Each step is then fit to a single pole

⁷There are ways around this, such as changing the `row_order`, which the author has begun investigating and implementing into recent measurements.

⁸Data taken with smaller amplitude square waves were found to be consistent with these results. We use the larger amplitude to increase the signal to noise for our time-domain fits.

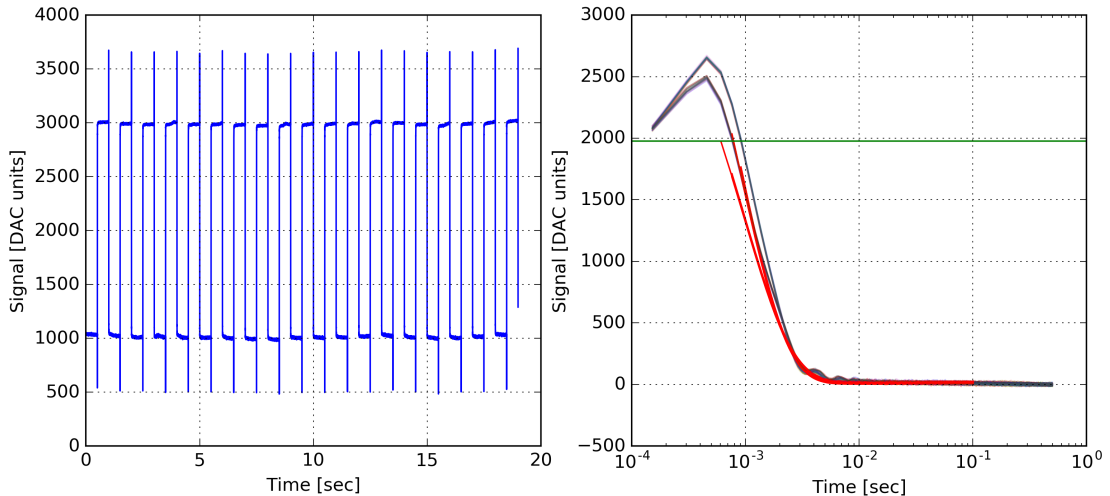


Figure 4.11: Example bias step acquisition (left). The data were split after each step and stacked (colored lines, right). Each step was fit (red lines, right) to a single pole exponential to determine the effective thermal time constant. The data shown is for the same SO NIST-style MF 150 GHz detector biased to 55 % R_N with a bath temperature of 130 mK. The mean time constant of the fits was found to be ≈ 165 Hz.

exponential of the form $f(t) = Ae^{-t/\tau_{\text{eff}}} + C$. In order to primarily fit the thermal response and not the electrical response, care is taken to choose the starting point of the fit. The exponential decay fit begins at the asymptotic value of the previous step (shown as the green horizontal line in the plot). Fitting prior to this would include the electrical response and no longer fit well to a single pole filter. Each step is fit (the fits are overplotted in red) after being split from the timestream, flipped such that the step is always downwards, and given a vertical offset such that the asymptotic value of each step is zero. For fast detectors, the exponential decay fits slightly underestimate the speed of the detector response in general. This is due to the limited amount of data on the decay and can be improved by sampling the detector faster. We see this effect in the Figure 4.11 where the red fits appear slightly slower than the colored data.

Time constants at different sky loading conditions can be simulated by measur-

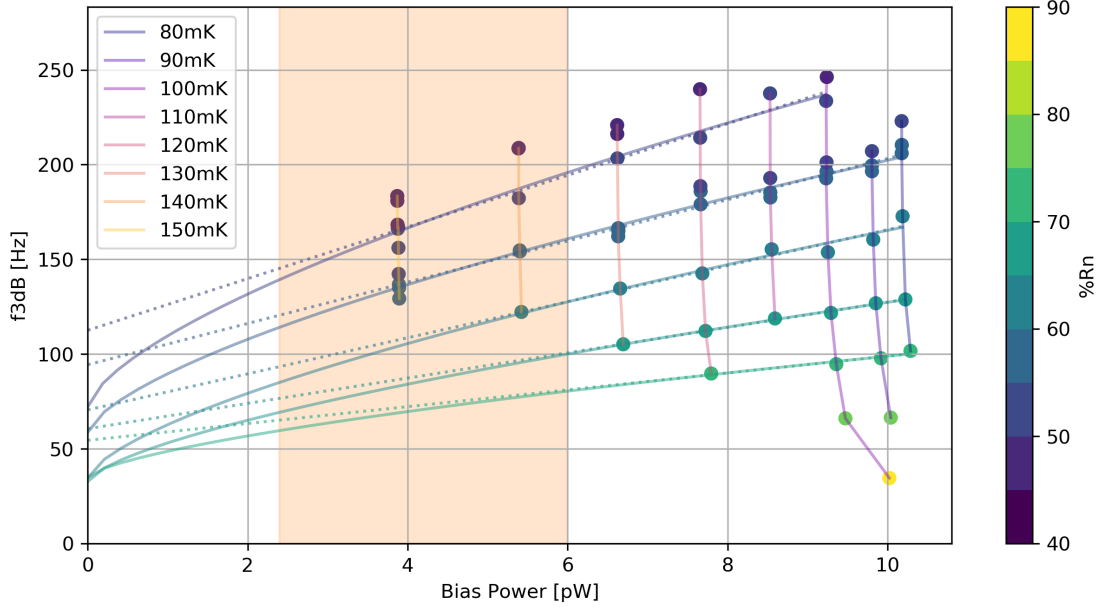


Figure 4.12: Bias step time constant measurements as a function of bias power and $\%R_N$ for the same prototype SO 150 GHz bolometer as presented above. Data were taken at many bath temperatures, simulating different loading conditions. The vertical orange band shows the expected bias power range for this band when on-sky. Below $\sim 50\%R_N$, the bolometer achieves the 166 Hz time constant specification of this band, over a broad range of bias powers. The natural time constant is estimated using the linear model (dotted lines) from the theory presented above and a two-fluid model (solid lines) [77] for fixed $\%R_N$. The two-fluid model estimates a natural time constant between 40 – 75 Hz.

ing bias steps at multiple bath temperatures. As bath temperature increases, P_{bias} decreases because P_{sat} decreases, simulating optical loading. Figure 4.12 shows effective time constants in f_{3dB} as a function of bias power and fraction of normal resistance. The data shown is for the same 150 GHz SOSP3 detector that was shown in previous sections. Each vertical grouping of data corresponds to a set of bias step measurements at one bath temperature and multiple $\%R_N$. At each bath temperature, we perform an I-V curve to determine the P_{bias} required to bias each detector to a given $\%R_N$. The orange highlighted band shows the expected range

of bias powers that will be used in the field, $P_{\text{bias}} = P_{\text{sat}} - P_{\gamma,1\text{mm}}$.

The natural time constant of the bolometer can be estimated by extrapolating these results to $P_{\text{bias}} = 0$, where the bolometer behavior is entirely thermal. A linear extrapolation follows the simple one-block model described by Equation 4.18 and is shown as the dotted lines in Figure 4.12 for fixed $\%R_N$. However, recent bias step time constant measurements [84] have found a two-fluid model [77] to fit better where $f_{3\text{dB}}(P_{\text{bias}}) = A + BP_{\text{bias}}^{2/3}$. Extrapolations following this model are shown as solid lines for fixed $\%R_N$. We see that the extrapolations of both models do not converge well to a natural time constant for this detector. However, we find that the natural time constants extrapolated using the two-fluid model have a smaller spread, with an average $f_{3\text{dB,nat}} \approx 50$ Hz.

Bias step measurements of SO and CMB-S4 effective thermal time constants are reported in [33, 135, 150]. As detectors become faster (such as for the fast SO 280 GHz bolometers), it becomes increasingly difficult to fit their thermal response due to fewer data points on the thermal decay. Fast detector sampling rates can improve this but require special and detailed tuning of the readout configuration. In order to determine if our current sampling rate is significantly affecting our time constant measurements, we compare the bias step time constants to those measured independently with via the bolometer’s complex impedance (Section 4.3.5).

4.3.4 Complex Impedance

In comparison to I-V curve and bias step measurements, complex impedance (CZ) measurements are time consuming and require the MCE to be placed in a non-standard readout mode. For this reason, CZ measurements are rarely performed

in the field. However, CZ measurements are able to access fundamental device parameters that the other measurement methods cannot and therefore can enable a deeper understanding of the bolometer performance. This is useful for our prototype device characterization. The data acquisition and analyses presented in this section closely follow methods described in [35, 36, 164].

The goal of CZ data acquisition is to measure the detector’s response to sinusoidally modulated detector bias voltages. The bolometer impedance is obtained by mapping the TES response as a function of stimulated frequency. The MCE is designed to perform time division multiplexing of entire detector arrays. However, for CZ measurements, we want to measure one detector at a time at high sampling rates. This is done by putting the MCE into “rectangle mode” which allows a single detector to be sampled repeatedly without switching between rows⁹. The MCE output data mode is also switched such that the user receives the unfiltered (anti-aliasing filter) SQUID feedback signal¹⁰.

To measure the complex impedance of a bolometer, small amplitude (< 1%) sine waves are applied on top of the DC operating bias point determined from I-V curves. The MCE’s arbitrary waveform generator (AWG) is used to apply digitized sine wave modulations to the DC biases. The frequency at which the AWG can update the bias registers sets the maximum sine frequency to 1/4th the sampling frequency. Faster sampling modes enable faster excitations. The data presented here were sampled at ~ 7.8 kHz and with about ~ 25 unique sine excitations ranging from 4 Hz to ~ 1.3 kHz.

CZ data acquisition was performed on 22 TESs from NIST’s SOSP3 MF and

⁹A detailed description of rectangle mode can be found at https://e-mode.phas.ubc.ca/mcewiki/index.php/Rectangle_Mode_Data

¹⁰We use data mode 4 for complex impedance acquisitions. Standard acquisitions on our MCE use data mode 10. More info: https://e-mode.phas.ubc.ca/mcewiki/index.php/Data_mode

UHF single pixels at three bath temperatures (100, 115, 130 mK), and at three bias points (40, 50, 60 % R_N). At each bath temperature, an I-V curve was measured to determine the bias powers necessary for the bias points of each detector individually. For each detector and each bias point, the MCE was switched to high-rate acquisition mode, the AWG was initiated, and the unfiltered SQUID feedback response was recorded. In addition to the three bias points at each bath temperature, each detector was also measured in their superconducting ($T_{\text{bath}} = 100$ mK, $P_{\text{bias}} = 0$ pW) and normal ($T_{\text{bath}} = 250$ mK, $P_{\text{bias}} = 0$) states. In total, about 275 time streams were collected for each detector, resulting in a massive dataset to analyze.

The amplitude and phase of the sinusoidal response in each time-stream was fit. Figure 4.13 shows example time streams and fits of a single detector for multiple applied sine waves and at different bias points. The detector shown is the same NIST-style SOSP3 MF-150 GHz TES that was analyzed in the previous sections. We see the orange fits recovering the amplitude and phase of the blue data with good accuracy. Note that since each time stream is at a different DC bias point, the amplitudes of the waves are not directly comparable.

As a function of the applied frequency, the relative amplitude and phase between the measured response and the input function forms a complex-valued transfer function, $\mathcal{T}(f)$. The transfer function is the ratio of the output and input sine wave voltages, or $V_{\text{SQUID-FB}}/V_{\text{bias}}$ and describes the TES circuit's complex response as a function of frequency. Since we know the amplitude of the input sine wave and the zero-phase offset of the AWG, we can extract the transfer function for each T_{bath} and % R_N (as well as for the superconducting and normal states). Figure 4.14 shows the magnitude and phase of the on-transition transfer functions

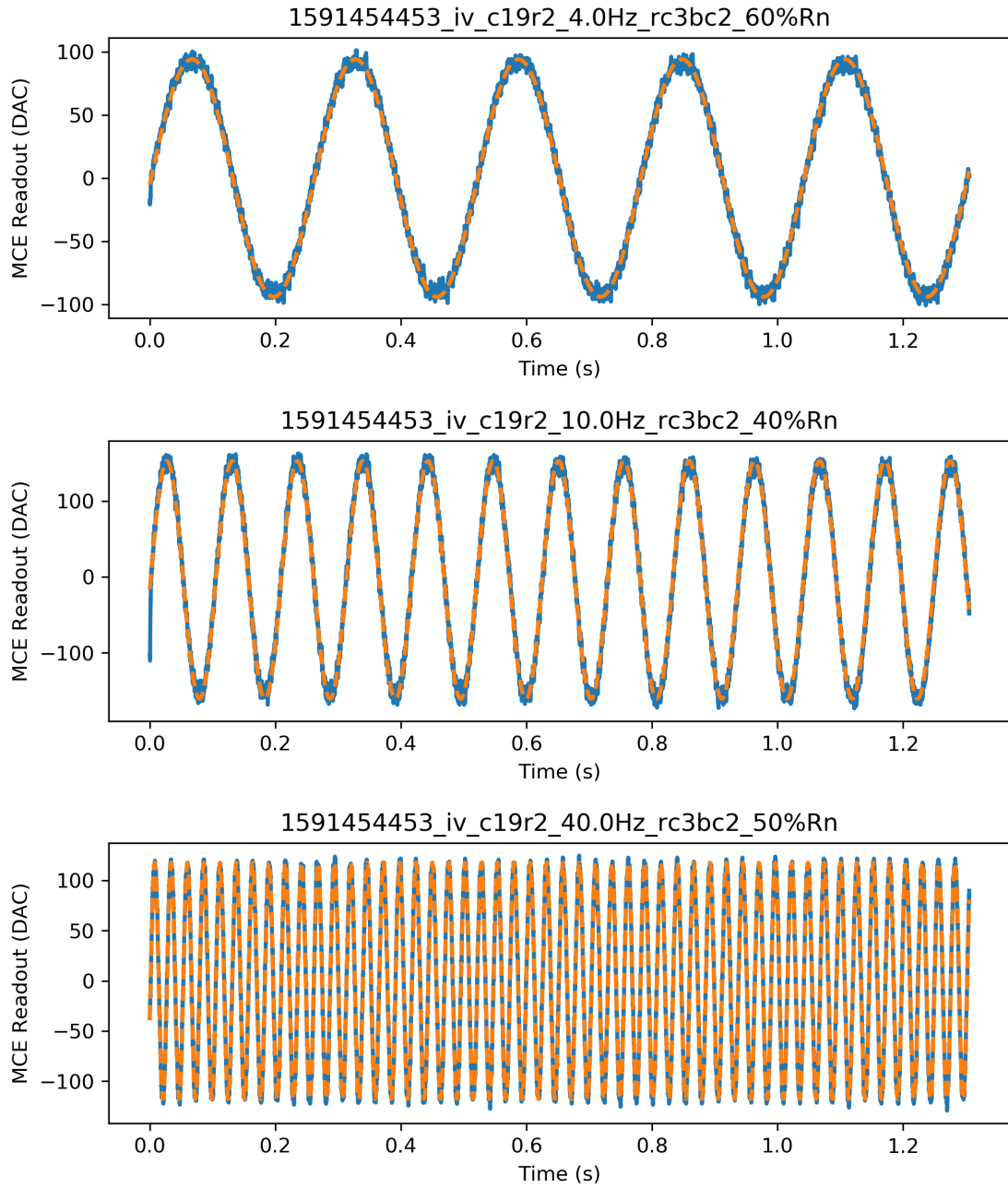


Figure 4.13: Example CZ acquisition time-streams for an SO MF-150 GHz bolometer at various excitation frequencies and DC bias points. The data in blue shows the TES response to a sine wave-modulated DC detector bias using the MCE's AWG. Sinusoidal fits shown in orange recover the amplitude and phase.

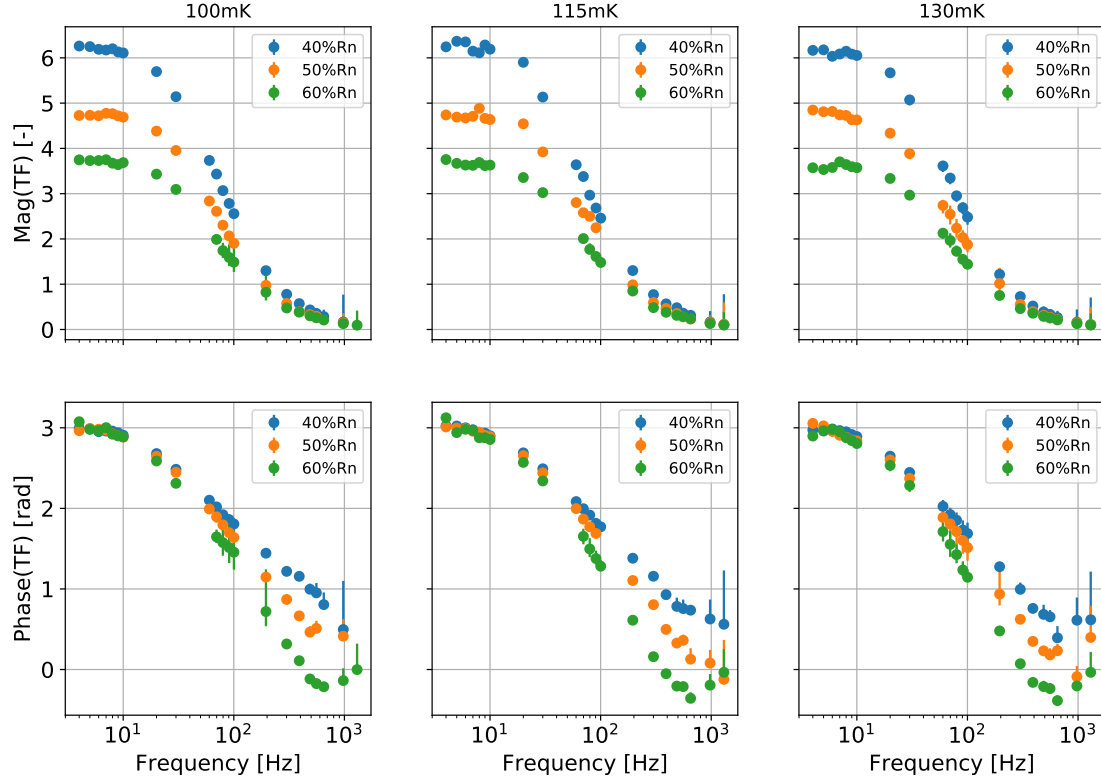


Figure 4.14: CZ transfer functions for a MF-150 GHz bolometer at multiple bath temperatures (each column: 100, 115, 130 mK) and bias points (each color). The complex valued transfer function represents the relative amplitude and phase of the detector circuit response to the input sine-wave, $V_{\text{SQUID-FB}}/V_{\text{bias}}$. Error bars represent the statistical error in the sine fitting algorithm.

for a SO MF-150 GHz bolometer at each bath temperature and bias point. At high frequencies, we see the amplitude dropping, indicating that the TES is less responsive to high-frequency impulses, as expected.

The transfer functions shown in Figure 4.14 incorporate the TES response as well as the TES bias circuitry response. Following [35], we extract the TES-only response, Z_{TES} , using the Thevenin equivalent voltage, \tilde{V}_{th} , and equivalent impedance, Z_{eq} which are computed from the normal and superconducting transfer

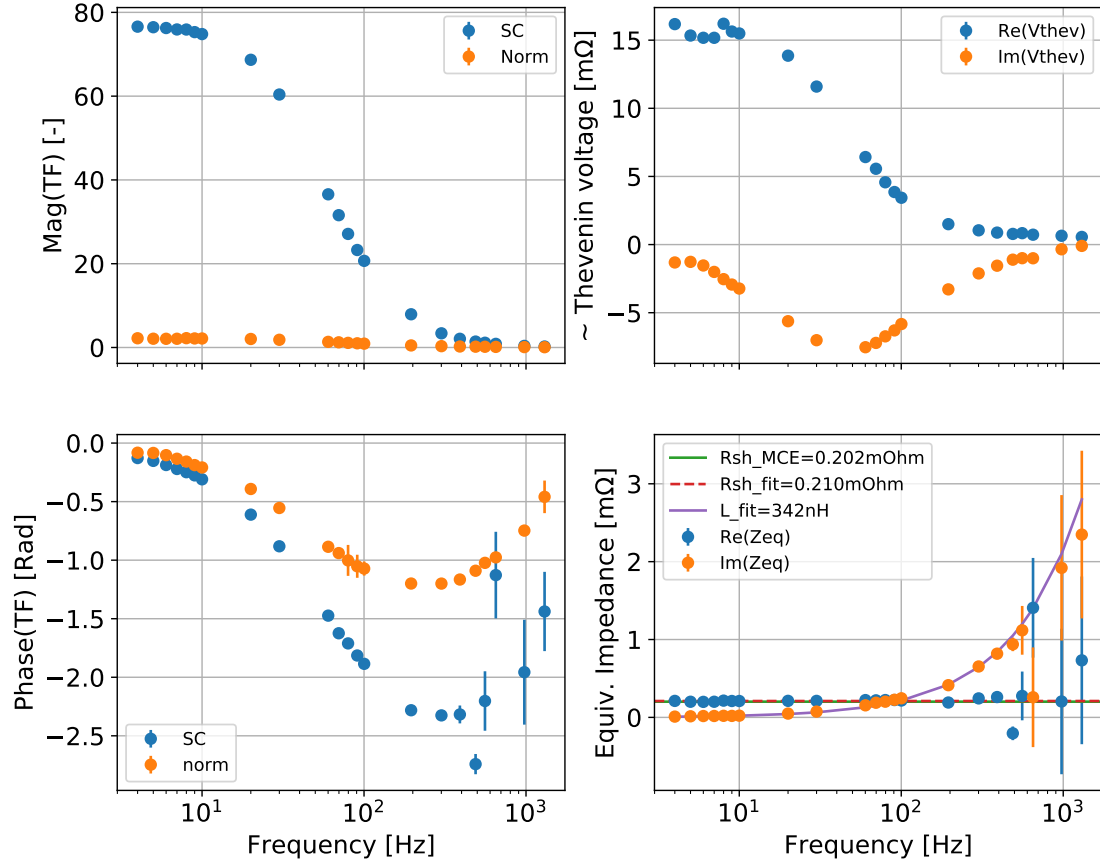


Figure 4.15: Left panels: the magnitude and phase of superconducting and normal transfer functions. Right panels: Thevenin equivalent voltage and bias circuit equivalent impedance calculated from the transfer functions. Fits to the real and imaginary portions of Z_{eq} give reasonable values for the shunt resistance and line inductance (shown in legend). The shunt resistance for this channel was independently measured to be 0.202 mΩ, where as the fitted value is 0.210 mΩ. Statistical errors from the sine-wave fits are propagated through to \tilde{V}_{th} and Z_{eq} .

functions (\mathcal{T}_N and \mathcal{T}_{SC} respectively):

$$\tilde{V}_{\text{th}} = \frac{R_N}{\mathcal{T}_N^{-1} - \mathcal{T}_{\text{SC}}^{-1}} \quad (4.23)$$

$$Z_{\text{eq}} = \frac{\tilde{V}_{\text{th}}}{\mathcal{T}_{\text{SC}}} \quad (4.24)$$

Note that since \mathcal{T} is dimensionless, \tilde{V}_{th} has units of Ohms instead of Volts because of omitted calibration constants. From Equation 4.19, we expect that Z_{eq} is dominated by the bias shunt resistor and parasitic line inductance in the superconducting wiring. Figure 4.15 plots the superconducting and normal transfer functions, \tilde{V}_{th} , and Z_{eq} , and confirms our expectations for Z_{eq} . Fitting Z_{eq} recovers reasonable values for the shunt resistance and line inductance.

Z_{TES} is computed using \tilde{V}_{th} , Z_{eq} , and the on-transition transfer functions [35]:

$$Z_{\text{TES}} = \frac{\tilde{V}_{\text{th}}}{\mathcal{T}_{T_{\text{bath}}, \%R_N}} - Z_{\text{eq}} \quad (4.25)$$

Uncertainties in Z_{TES} are propagated from statistical uncertainties in the sinusoidal fits. Figure 4.16 shows the complex valued Z_{TES} as a function of frequency (upper panels) and in the complex plane (lower panels). As expected, Z_{TES} traces semi-circles in the lower half of the complex plane.

Figure 4.16 also shows fits to Z_{TES} data using Equation 4.22. I-V curve measurements of R_N , T_c , G , and P_{bias} are used in the fitting and are assumed to have negligible uncertainties. The heat capacity is assumed to be constant as a function of $\%R_N$ and therefore is constrained as such between all fits at the same T_{bath} . The fitted parameters are α , β , and C . A rough fit of the data is performed with a SciPy implementation of the Nelder-Mead algorithm and then improved using the MIGRAD algorithm [35, 79]. The fits to Z_{TES} are over plotted as solid lines and also show that the data fits well to the model.

The top row of Figure 4.17 shows the fitted parameters as a function of T_{bath} and $\%R_N$. The high α seems generally acceptable and is within expectations.

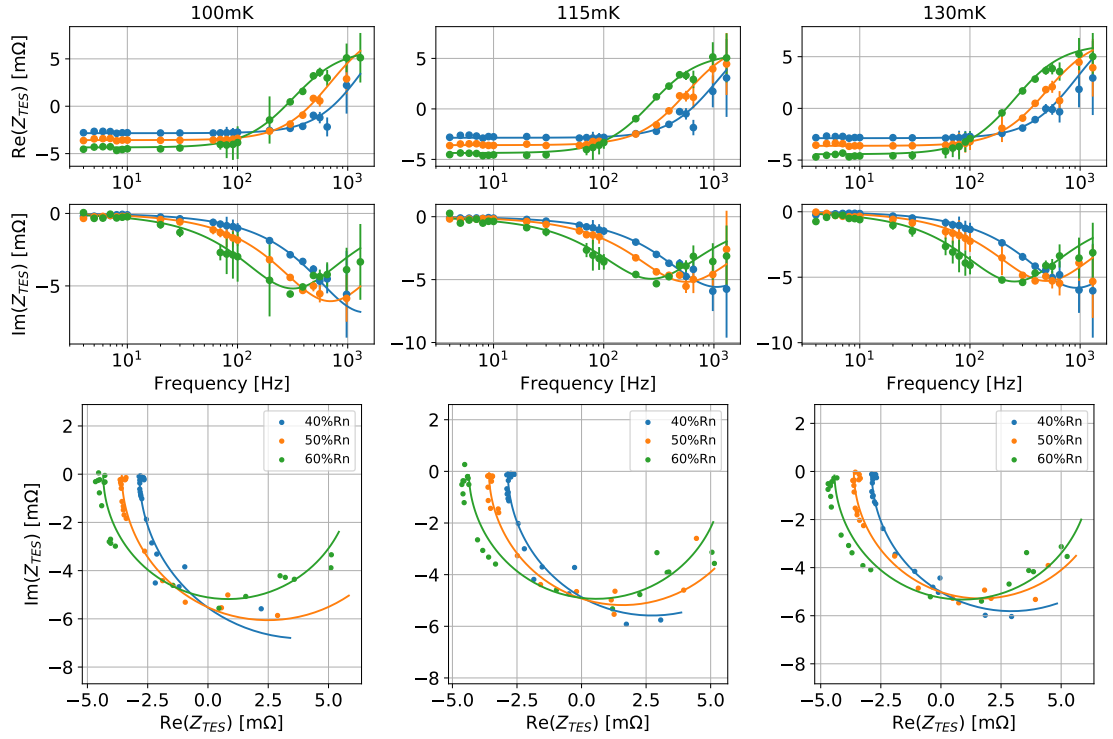


Figure 4.16: Complex impedance measurements and fits of an SO MF-150 GHz bolometer. Each column is a different bath temperature. Each color is a different bias point. The top two rows plot the complex valued impedance as a function of frequency while the lower row plots it on the complex plane. As expected, Z_{TES} appears as a semicircle in the lower half of the complex plane. The data were fit to Equation 4.22 for α , β , and C , while using I-V curve measurements for the other parameters.

However, $\beta \sim \mathcal{O}(1)$ borders on too high since we generally expect $\beta < 1$. From fabrication notes on the amount of PdAu and AlMn deposited on the island, we expect $C \sim 1 \text{ pJ/K}$. The heat capacity is expected to scale roughly linearly with the temperature of the bolometer. However, since the bolometer is biased onto its transition, its temperature is constant at T_c , so we expect the heat capacity to be flat with T_{bath} . The fitted value is modestly higher than expected and varies significantly with T_{bath} . This may be due to degeneracy between α and β .

The bottom row of Figure 4.17 shows inferred parameters that were calculated

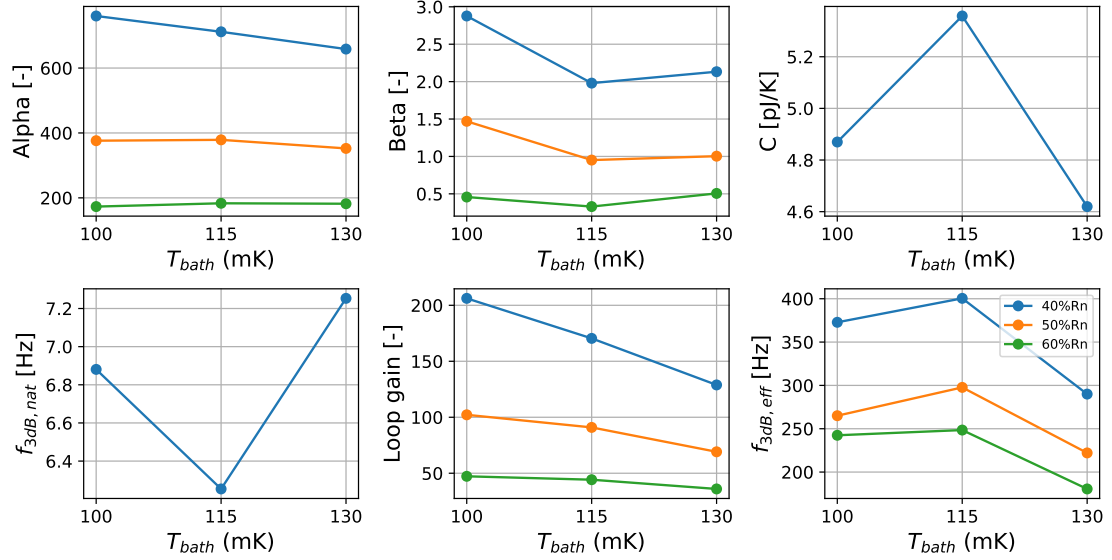


Figure 4.17: Extracted and calculated TES bolometer parameters from CZ fits as a function of T_{bath} and $\%R_{\text{N}}$. The top row shows the three parameters that were fit to the CZ data. The lower row shows calculated parameters using the CZ-fits and I-V data.

using the CZ fitted parameters and I-V results. The natural time constant follows the heat capacity with $f_{3dB,\text{nat}} = G/2\pi C$. The loop gain and effective thermal time constants are computed using Equations 4.10 and 4.18. The natural time constant is slower than expected given the linear and two-fluid extrapolations from the bias step measurements (Figure 4.12). The loop gain and $f_{3dB,\text{eff}}$ decline with bath temperature, as expected since at lower bath temperatures, P_{bias} is lower. Additionally, the time constant is faster at lower $\%R_{\text{N}}$, as expected due to the increase in α .

The fit parameters are expected to be degenerate. By forcing C to be constant for all $\%R_{\text{N}}$, we hope to relieve degeneracy between C and α . If the low and high frequency limits are probed well, β can be constrained. However, the MCE AWG high-frequency sine wave limit prevents us from measuring the high frequency

limit of the response of this detector. Thus modest degeneracy between α and β is expected. This may account for the higher than expected β , which may have also impacted the heat capacity. For future measurements, it is recommended that higher detector sampling rates and sine wave excitation frequencies are used.

4.3.5 Comparison of $f_{3\text{dB},\text{eff}}$ Measurements

Figure 4.18 compares the measured $f_{3\text{dB},\text{eff}}$ from the bias step and complex impedance methods presented above in the left panel. At each $\%R_N$, the three points represent the three bath temperatures that were surveyed. Note that the bolometer speeds up at lower $\%R_N$, as expected. Bias step and complex impedance data for this detector were in relative agreement.

The right panel of Figure 4.18 adds three more SOSP3 bolometers that were tested, but does not distinguish between $\%R_N$. The devices sampled include 90 and 150 GHz detectors with various amounts of heat capacities, controlled by the volume of thermal ballast on the island (Figure 4.4). These prototype bolometers were fabricated to explore the range of time constants achievable by tuning the bolometer heat capacities. Each point on the scatter plot corresponds to a given bolometer (denoted by color) at a given bias point and bath temperature.

From these data, it is clear that while the two methods are in general agreement, the bias step data may under estimate the effective time constant compared to the complex impedance measurements. The largest discrepancy occurs for the lowest heat capacity device (150 GHz Low C, red), which is expected to be the fastest and potentially least stable due to its low heat capacity. For this particular detector, as the heat capacity is lowered and the device is made faster, it becomes

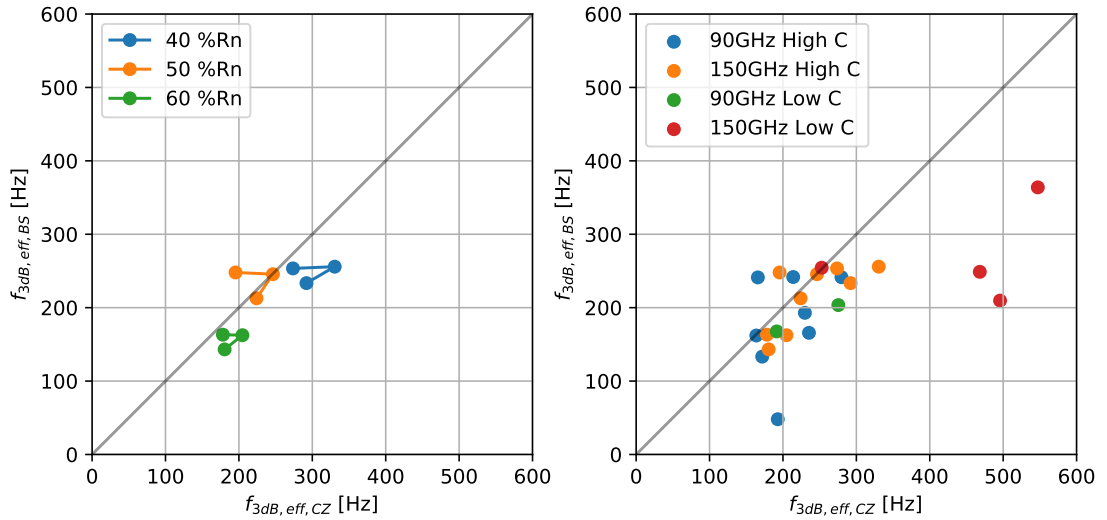


Figure 4.18: Comparison of time constants measured via bias steps (y-axis) and complex impedance (x-axis). The left plot shows a comparison for a single SOSP3 150 GHz bolometer at three bias points (colors) and three bath temperatures. For this bolometer, the two measurement methods are in relative agreement. In the right plot, three additional SOSP3 detectors are added (colors) and it is evident that the bias step method slightly under estimates the complex impedance method. The 150 GHz low heat capacity device (red) is very fast and so the CZ fits were unable to fully probe the complex plane.

more challenging to fully probe the complex plane of the device's impedance. The faster bolometer response requires faster excitation frequencies than we were able to generate to break degeneracies between the fitted parameters. Thus, for this particular detector, the fitted parameters and inferred time constant are poorly constrained. Inspecting Z_{TES} of the 150 GHz Low C device confirmed this by showing that the right hand side of the semicircle in the complex plane was not measured and thus the fitted parameters, especially β , were not well constrained. In the future, this could be improved by using data from other measurements, such as I-V curves, to place prior constraints on β , reducing the degeneracy in the CZ fits. Increasing the sampling and excitation rate of both the complex impedance and bias step methods would likely also improve the data and fits of fast devices.

4.4 Conclusion

In this chapter, we presented models and measurements of prototype SO TES bolometers which have been used to optimize the detector designs that will comprise SO’s $\sim 70,000$ detectors. SO detectors are progressing towards deployment for first light in 2022. MF and UHF arrays are being fabricated and multiple arrays have been assembled for array scale laboratory characterization [101]. Saturation power, time constant, and noise performance characterization of the LF detectors will take place in the coming months.

As full UFMAs are assembled, array scale characterization will be performed with the SLAC microresonator radio frequency (SMuRF) readout electronics using μ MUX. At Cornell, UFMs will be tested in the dark and with a cold load using a SMuRF. The SMuRF architecture will make future array scale complex impedance measurements simpler by enabling higher sampling and excitation frequencies. This could enable better laboratory and field characterizations, providing detailed knowledge of the bolometer parameters and performance.

The MCE-based TDM measurement methods presented above not only provided critical device parameters to SO’s fabrication teams, but also developed data acquisition procedures and analysis methods that will be useful for future applications. For example, at the time of this writing, CMB-S4 is base-lining TES arrays with TDM readout. Therefore, the work presented here will be directly portable for future projects. Similarly, before CCAT-prime selected MKIDs, significant work was done to design TES pixel architectures for EoR-spec and other multi-chroic CCAT-prime applications. CCAT-Prime prototype quad-chroic single pixels were fabricated at NIST and characterized at Cornell. Although CCAT-prime’s current efforts are focused on MKID characterization [47], the measurement methods and

analyses that were developed will no doubt remain useful for future TES applications.

CHAPTER 5

CONCLUSIONS

We conclude this dissertation with a brief discussion of a few of the expected cosmology and astrophysics products of the aforementioned collaborations.

5.1 The Atacama Cosmology Telescope

The Atacama Cosmology Telescope was described in Section 2.1, followed by a presentation of the beam measurements of one of AdvACT’s MF2 receiver. While this measurement has largely impacted the warm and cryogenic baffle designs of the future SO, CCAT-prime, and CMB-S4 instruments, it has also impacted ACT. As mentioned above, simulation studies were performed that relate the author’s measurements to telescope sidelobes on the sky [59]. These simulations were shown to agree empirically with sun and moon sidelobe maps generated with real data, thus closing a loop between expectations and data.

In Section 1.2.3, we showed the most recent power spectra measurements from ACTPol’s DR4 [25] and overviewed some of the recent data analyses that have been performed in the past few years. This pristine power spectra dataset has a significant amount of cosmological parameter constraining power. In combination with *Planck* data, DR4 sets tight constraints on Λ CDM [9]. However, as discussed in Section 1.2.4, there are many open questions to be investigated further.

Some preliminary data from ACT’s third generation receiver, AdvACT, which has been observing at high-efficiency every year since 2016, has already been released [109]. However, compared to DR4, there is expected to be at least four times as much data from AdvACT in the pipeline, for which analysis is underway.

The sheer amount of new data will certainly help improve cosmological constraints. Additionally, while ACTPol only observed at 90 and 150 GHz, AdvACT will add maps at 27, 39, and 220 GHz as well. The addition of these bands will significantly improve ACT’s ability to remove foreground contamination. The lower frequencies will access synchrotron and spinning dust emission while the high frequency will access galactic dust and dusty star-forming galaxies. In combination with SO data products, AdvACT will help search for inflationary B-mode signals by providing crucial data on foregrounds.

5.2 The Simons Observatory

The Simons Observatory was described in Section 4.1, followed by a presentation of the characterization and optimization of SO’s TES bolometers. The SO MF (90 and 150 GHz) and UHF (220 and 280 GHz) bolometer designs were iterated on until they met observing requirements. They are now mature enough to be tested on the array scale, and possibly fielded as is. The MF and UHF arrays are nearing production and are being tested individually at SO test institutions around the country. The SO LF (27 and 39 GHz) bolometer designs will be tested in the coming months and full array scale testing is scheduled to proceed shortly thereafter. SO plans for first light in 2022 using the detector designs characterized here.

With $\sim 70,000$ TESs, SO will over than an order of magnitude more number of detectors than AdvACT. Spread across the LAT and multiple SATs, these detectors will enable a multitude of data analyses. This will provide a stunning amount of cosmological constraining power and will enable highly sensitive probes

into the B-mode polarization spectra, constraints on the neutrino mass, extensions to Λ CDM, and more. The discussion below of a sample of SO forecasts is based largely on the extensive modeling and calculations presented in the SO Science Paper [3].

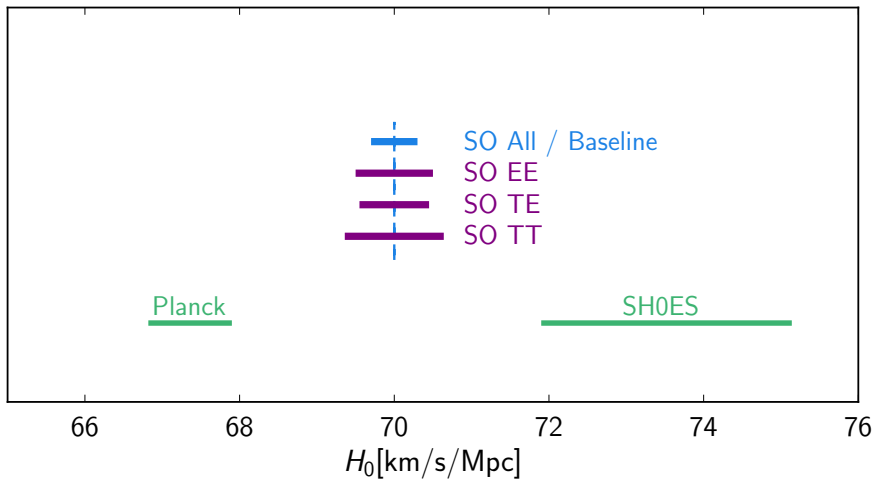


Figure 5.1: SO forecasted constraint on the Hubble constant. Data for recent early time (CMB, *Planck*) and late time (Cepheids, SH0ES) are also shown. The SO constraint is centered at the fiducial value between both measurements. The SO constraint could provide evidence for a departure from Λ CDM or other new physics in order to explain the Hubble tension. Figure from [3].

SO forecasts that it will reduce the current uncertainty on the Hubble constant, H_0 , to half a percent. This will help address the Hubble tension, which is the $> 3\sigma$ discrepancy between early time (CMB, BAO) and late time (Cepheid, supernovae) Hubble constant measurements. Figure 5.1 compares the expected SO uncertainty in a Λ CDM model to current estimates from *Planck* and the SH0ES collaboration which uses Cepheid variables to measure the late time Hubble constant [28, 120]. Clearly, when all channels are combined, the SO data will improve the *Planck* constraints by about a factor of two. SO will thus test *Planck* and early time measurements and could provide evidence for departures from Λ CDM or other

new physics.

SO also aims to constrain models of inflation by searching for the signature of primordial gravitational waves in the CMB polarization. The inflationary B-mode signal is dominated by lensing and dust contamination. This motivates a sophisticated combination of foreground removal and map-based cleaning methods. Figure 5.2 shows a simulated B-mode spectrum measurement (red) that was computed using map-level component separation to remove the foreground emission (gray band). The simulation input spectrum (black band) assumes $r=0$, and that the data is delensed by 50%. The SO baseline and goal uncertainties are shown in orange and blue for optimistic and pessimistic $1/f$ noise levels. The foreground residuals between the simulated measurements and the lensing is shown in yellow and is comparable to a tensor-to-scalar ratio $r = 0.0016$ (dashed). Marginalizing over the foreground residuals can reduce this bias, but increases the uncertainty on r . From this, SO forecasts that it will measure the tensor-to-scalar ratio to the level of $\sigma(r) = 0.003$. If primordial B-modes are detected with $r > 0.01$, this would enable a $> 3\sigma$ detection and would be a breakthrough result of modern cosmology.

The Sunyaev-Zel'dovich (SZ) effects are powerful probes of cosmology and astrophysics. CMB photons are scattered by energetic electrons in galaxy clusters, imprinting spectral distortions in the CMB. A wealth of information about the galaxy clusters and their large scale structure is thus contained in these secondary anisotropies. SO's extended frequency coverage and sensitivity will enable new detailed SZ analyses, improving our understanding of the growth of structure and galaxy properties at late times. For example, measurements of the abundance and motions of clusters will probe large-scale structure. Additionally, multi-spectral measurements and cross-correlations between the thermal and kinetic SZ effects

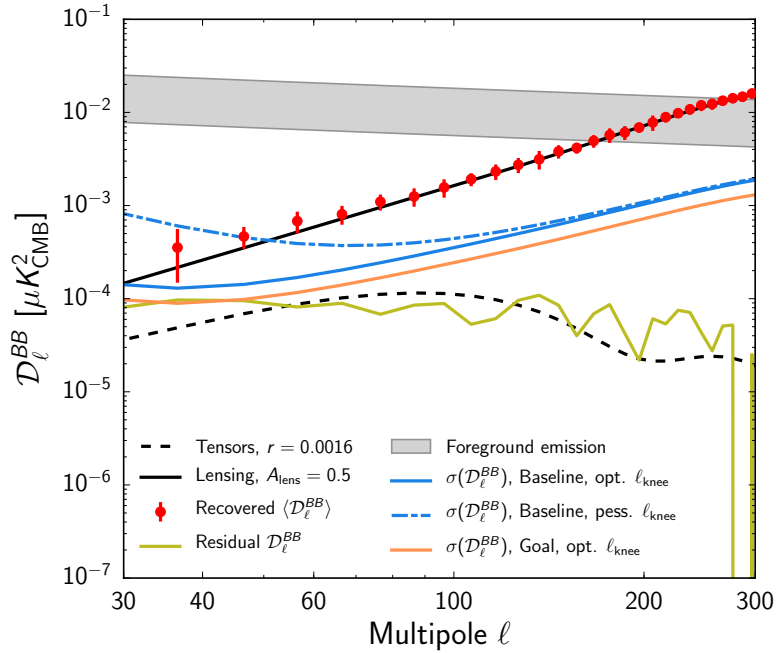


Figure 5.2: Simons Observatory simulated B-mode measurements (red) which have been component separated from simulated foreground emission (gray band). SO baseline and goal B-mode sensitivities are shown in orange and blue for optimistic and pessimistic $1/f$ noise. The residual between the simulated signal (red) and the input lensing spectrum (black) is shown in yellow and is comparable to an inflationary B-mode signal with $r = 0.0016$. Figure from [3].

will probe the astrophysical and thermodynamic properties of the clusters and their constituents. Further, SO forecasts that it will place constraints on the Epoch of Reionization by observing the redshift duration of the EoR and the ionization efficiency during the EoR.

These are just a few examples of the many forecasted science products from SO. More are presented in detail in the SO Science Paper [3]. The SO detector development described in Chapter 4 will undoubtedly contribute to opening new windows into cosmology and astrophysics.

5.3 The CCAT-Prime Collaboration

The CCAT-prime project and FYST were described in Section 3.1, followed by a presentation of models and fabrication methods of the silicon substrate FPI technologies that have been developed for EoR-Spec. The EoR-spec FPI mirror designs were optimized for observing the [CII] line emission during the EoR between redshifts 3.5 to 8. Fabrication development is nearing completion and FPI testbeds await samples for characterization. Following successful characterization, full-scale mirrors will be fabricated and characterized before fielding in EoR-Spec on FYST in late 2023. In addition to EoR-Spec, Prime-Cam will also contain multiple broadband KID modules for a variety of cosmology and astrophysics observations. Below we describe a few of the many science goals that CCAT-prime will pursue with Prime-Cam. Forecasts and constraints for these applications will be presented in great detail in CCAT-prime’s upcoming Science Paper [27].

In combination with SO, CCAT-prime will help constrain measurements of the tensor-to-scalar ratio r . Prime-Cam measurements at many millimeter and sub-millimeter wavelengths will dramatically improve our understanding of polarized dust foregrounds. At current sensitivities, the foregrounds are well modeled by a single temperature “grey body” spectrum [29]. Prime-Cam’s measurements at higher frequencies will help constrain the dust model parameters and could provide evidence of extensions to the single temperature grey body model. In combination with SO’s SAT B-mode forecasts, these measurements are forecasted to improve the SO’s B-mode foreground bias discussed above while maintaining a similar $\sigma(r)$. This could reduce the need for SO’s marginalisation, which otherwise roughly doubles their forecasted $\sigma(r)$. By reducing foreground bias, Prime-Cam therefore can aid in constraining models of inflation.

Prime-Cam’s high frequency maps will also contribute significantly to SZ measurements. In combination with the large cluster catalogs that will be identified by ACT and SO, CCAT-prime will probe more of the SZ spectral distortions by adding high-frequency coverage. These additions will be valuable for enabling clean separations of signals from the different SZ effects. Current cosmological constraints from SZ measurements are limited by uncertainties in cluster properties such as their temperature, density, and pressure profiles. The component separations enabled by Prime-Cam will improve these uncertainties by providing windows into the thermodynamic properties of the clusters, enabling astrophysical characterization. Further, spectroscopic measurements of a small subset of the brightest SZ clusters using EoR-Spec will provide unprecedented spectral characterization and component separation of SZ clusters.

EoR-Spec’s primary objective is to explore the Epoch of Reionization via the redshifted $158\text{ }\mu\text{m}$ [CII] fine structure line from early star forming galaxies between redshifts 3.5 to 8 corresponding to frequencies between 420 and 210 GHz. As described in Section 1.3.2, [CII] will be used to probe cooling radiation around the early star-forming regions of the EoR, enabling characterization of the ionization sources. The bright [CII] line efficiently traces the history of reionization process and the evolution of the underlying dark matter structure. Using the SSB FPI mirrors developed in Chapter 3, EoR-Spec will perform LIM of this emission as a function of redshift, tomographically measuring the evolution of the EoR. EoR-Spec will therefore produce a 3D mapping of the EoR, probing the evolution of and processes within the first star forming galaxies through cosmic time.

Figure 5.3 *left* shows an example simulated redshift slice, similar to what will be observed by EoR-Spec. This figure shows a simulated 16 square degree field,

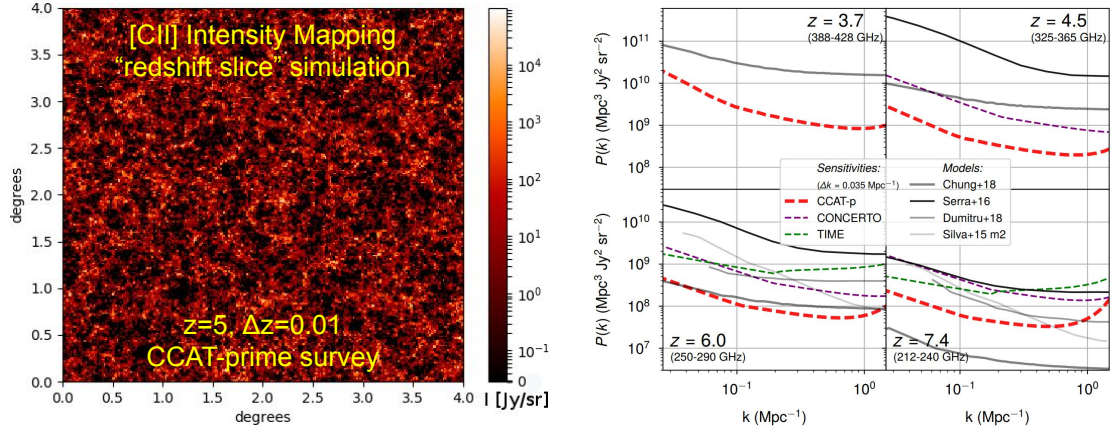


Figure 5.3: *Left:* simulated redshift slice of [CII] emission at $z \sim 5$ from a 16 deg^2 survey showing the clustering signal [82]. Represented is a single spectral bin of the spatial-spectral intensity mapping data cube. *Right:* Sensitivity curves for the power spectrum of the [CII] emission at multiple redshifts [26]. Plotted are multiple power spectra predictions which differ by factors of 10 to 50. Over plotted are predicted EoR-Spec sensitivity curves for the first generation 16 deg^2 survey as well as sensitivity curves for other upcoming experiments. Note that since the generation of this figure EoR-Spec's survey areas have halved to $\sim 8 \text{ deg}^2$, as described in [27].

although the the actual observing fields will be more like 8 square degrees. The simulated slice at $z = 5$ corresponds to an observed [CII] frequency of $\sim 315 \text{ GHz}$ ($950\mu\text{m}$). At this frequency, rotational CO lines and the [OIII] fine structure line will be simultaneously imaged. However, they will not be as bright as the [CII] line and they will be at different redshifts, tracing different large-scale structure. For the [CII] LIM measurements, these lines are essentially a foreground that is important to remove carefully. Details for multiple proposed methods of foreground removal for [CII] analyses will be presented in the upcoming CCAT-prime Science Paper [27].

The CO and [OIII] also contain a great deal of astrophysics and cosmology, and will enable many additional studies once separated from the [CII] emission.

The [OIII] line for example, like [CII], will trace early star forming regions but at redshifts $z > 7$ within the EoR-Spec frequency coverage. At lower redshifts, between $0 < z < 2$, the CO rotational lines will trace molecular gas clouds and can be used to improve our understanding of gas properties in the interstellar medium and their evolution.

By intensity mapping the aggregate [CII] emission over large co-moving spatial scales, EoR-Spec will be a cosmological probe, revealing the growth of density fluctuations and the primordial power spectrum. With sufficiently precise measurements, constraints could be placed on fundamental physics including models of inflation, dark energy, and the sum of the neutrino masses. Figure 5.3 *right* shows multiple power spectrum predictions. Compared to each other, the models vary significantly by roughly an order of magnitude. The figure also shows the expected EoR-Spec sensitivity and suggests that EoR-Spec will enable detections of [CII] regions of the EoR out to at least $z \approx 5$, and should provide significant constraining power at higher redshifts.

Lastly, one of the greatest features of LIM is the natural ability to perform cross correlations between different probes. EoR-Spec's fields are being carefully chosen to optimize the ability to cross-correlate with multiple other surveys. Details on the survey areas chosen will be well described in CCAT-prime's Science Paper [27]. Cross correlations will not only reveal large-scale structure but will also enable powerful comparisons on the interactions between different components and processes during the EoR.

CCAT-prime's spectrometer, powered by the SSB FPI developed here, will probe the growth of structure, the reionization process, and the evolution of galaxies, thus opening new windows to one of the remaining relatively unexplored epochs

of the cosmos.

5.4 Conclusion

This dissertation reports the author’s significant technical contributions to the ACT, CCAT-prime, and SO collaborations. The technical works that are discussed are over a broad range of topics within experimental cosmology and astrophysics. In Chapter 2, we present optical spillover measurements which have had significant influence over the design of many upcoming mm-wave and sub-mm telescopes and receivers. In Chapter 3, we present models and fabrication methods for silicon substrate FPIs that will enable new probes into the Epoch of Reionization. In Chapter 4, we present prototype TES characterization measurements and analysis methods which have been used to optimize the design of what will be the largest-fielded number of bolometers in a CMB observatory. Observations enabled by these technologies will continue to inform and surprise us as we explore our universe.

BIBLIOGRAPHY

- [1] Kevork N. Abazajian, Peter Adshead, Zeeshan Ahmed, Steven W. Allen, David Alonso, Kam S. Arnold, Carlo Baccigalupi, James G. Bartlett, Nicholas Battaglia, Bradford A. Benson, Colin A. Bischoff, Julian Borrill, Victor Buza, Erminia Calabrese, Robert Caldwell, John E. Carlstrom, Clarence L. Chang, Thomas M. Crawford, Francis-Yan Cyr-Racine, Francesco De Bernardis, Tijmen de Haan, Sperello di Serego Alighieri, Joanna Dunkley, Cora Dvorkin, Josquin Errard, Giulio Fabbian, Stephen Feeney, Simone Ferraro, Jeffrey P. Filippini, Raphael Flauger, George M. Fuller, Vera Gluscevic, Daniel Green, Daniel Grin, Evan Grohs, Jason W. Henning, J. Colin Hill, Renee Hlozek, Gilbert Holder, William Holzapfel, Wayne Hu, Kevin M. Huffenberger, Reijo Keskitalo, Lloyd Knox, Arthur Kosowsky, John Kovac, Ely D. Kovetz, Chao-Lin Kuo, Akito Kusaka, Maude Le Jeune, Adrian T. Lee, Marc Lilley, Marilena Loverde, Mathew S. Madhavacheril, Adam Mantz, David J. E. Marsh, Jeffrey McMahon, Pieter Daniel Meerburg, Joel Meyers, Amber D. Miller, Julian B. Munoz, Ho Nam Nguyen, Michael D. Niemack, Marco Peloso, Julien Peloton, Levon Pogosian, Clement Pryke, Marco Raveri, Christian L. Reichardt, Graca Rocha, Aditya Rotti, Emmanuel Schaan, Marcel M. Schmittfull, Douglas Scott, Neelima Sehgal, Sarah Shandera, Blake D. Sherwin, Tristan L. Smith, Lorenzo Sorbo, Glenn D. Starkman, Kyle T. Story, Alexander van Engelen, Joaquin D. Vieira, Scott Watson, Nathan Whitehorn, and W. L. Kimmy Wu. CMB-S4 Science Book, First Edition. *arXiv:1610.02743 [astroph, physics:gr-qc, physics:hep-ph, physics:hep-th]*, October 2016. arXiv: 1610.02743.

- [2] P. A. R. Ade, R. W. Aikin, D. Barkats, S. J. Benton, C. A. Bischoff, J. J. Bock, J. A. Brevik, I. Buder, E. Bullock, C. D. Dowell, L. Duband, J. P. Filippini, S. Fliescher, S. R. Golwala, M. Halpern, M. Hasselfield, S. R. Hildebrandt, G. C. Hilton, V. V. Hristov, K. D. Irwin, K. S. Karkare, J. P. Kaufman, B. G. Keating, S. A. Kernasovskiy, J. M. Kovac, C. L. Kuo, E. M. Leitch, M. Lueker, P. Mason, C. B. Netterfield, H. T. Nguyen, R. O'Brient, R. W. Ogburn IV, A. Orlando, C. Pryke, C. D. Reintsema, S. Richter, R. Schwarz, C. D. Sheehy, Z. K. Staniszewski, R. V. Sudiwala, G. P. Teply, J. E. Tolan, A. D. Turner, A. G. Vieregg, C. L. Wong, and K. W. Yoon. BICEP2 I: Detection Of B-mode Polarization at Degree Angular Scales. *Physical Review Letters*, 112(24):241101, June 2014. arXiv: 1403.3985.
- [3] Peter Ade, James Aguirre, Zeeshan Ahmed, Simone Aiola, Aamir Ali, David Alonso, Marcelo A. Alvarez, Kam Arnold, Peter Ashton, Jason Austermann, Humna Awan, Carlo Baccigalupi, Taylor Baildon, Darcy Barron, Nick Battaglia, Richard Battye, Eric Baxter, Andrew Bazarko, James A. Beall, Rachel Bean, Dominic Beck, Shawn Beckman, Benjamin Beringue, Federico Bianchini, Steven Boada, David Boettger, J. Richard Bond, Julian Borrill, Michael L. Brown, Sarah Marie Bruno, Sean Bryan, Erminia Calabrese, Victoria Calafut, Paolo Calisse, Julien Carron, Anthony Challinor, Grace Chesmore, Yuji Chinone, Jens Chluba, Hsiao-Mei Sherry Cho, Steve Choi, Gabriele Coppi, Nicholas F. Cothard, Kevin Coughlin, Devin Crichton, Kevin D. Crowley, Kevin T. Crowley, Ari Cukierman, John M. D'Ewart, Rolando Dünner, Tijmen de Haan, Mark Devlin, Simon Dicker, Joy Didier, Matt Dobbs, Bradley Dober, Cody J. Duell, Shannon Duff, Adri Duivenvoorden, Jo Dunkley, John Dusatko, Josquin Errard, Giulio Fabbian, Stephen Feeney, Simone Ferraro, Pedro Fluxà, Katherine

ine Freese, Josef C. Frisch, Andrei Frolov, George Fuller, Brittany Fuzia, Nicholas Galitzki, Patricio A. Gallardo, Jose Tomas Galvez Ghersi, Jian-song Gao, Eric Gawiser, Martina Gerbino, Vera Gluscevic, Neil Goeckner-Wald, Joseph Golec, Sam Gordon, Megan Gralla, Daniel Green, Arpi Grigorian, John Groh, Chris Groppi, Yilun Guan, Jon E. Gudmundsson, Dongwon Han, Peter Hargrave, Masaya Hasegawa, Matthew Hasselfield, Makoto Hattori, Victor Haynes, Masashi Hazumi, Yizhou He, Erin Healy, Shawn W. Henderson, Carlos Hervias-Caimapo, Charles A. Hill, J. Colin Hill, Gene Hilton, Matt Hilton, Adam D. Hincks, Gary Hinshaw, Renée Hložek, Shirley Ho, Shuay-Pwu Patty Ho, Logan Howe, Zhiqi Huang, Johannes Hubmayr, Kevin Huffenberger, John P. Hughes, Anna Iijas, Margaret Ikape, Kent Irwin, Andrew H. Jaffe, Bhuvnesh Jain, Oliver Jeong, Daisuke Kaneko, Ethan D. Karpel, Nobuhiko Katayama, Brian Keating, Sarah S. Kernasovskiy, Reijo Keskitalo, Theodore Kisner, Kenji Kiuchi, Jeff Klein, Kenda Knowles, Brian Koopman, Arthur Kosowsky, Nicoletta Krachmalnicoff, Stephen E. Kuenstner, Chao-Lin Kuo, Akito Kusaka, Jacob Lashner, Adrian Lee, Eunseong Lee, David Leon, Jason S.-Y. Leung, Antony Lewis, Yaqiong Li, Zack Li, Michele Limon, Eric Linder, Carlos Lopez-Caraballo, Thibaut Louis, Lindsay Lowry, Marius Lungu, Mathew Madhavacheril, Daisy Mak, Felipe Maldonado, Hamdi Mani, Ben Mates, Frederick Matsuda, Loïc Maurin, Phil Mauskopf, Andrew May, Nialh McCallum, Chris McKenney, Jeff McMahon, P. Daniel Meerburg, Joel Meyers, Amber Miller, Mark Mirmelstein, Kavilan Moodley, Moritz Munchmeyer, Charles Munson, Sigurd Naess, Federico Nati, Martin Navaroli, Laura Newburgh, Ho Nam Nguyen, Michael Niemack, Haruki Nishino, John Orlowski-Scherer, Lyman Page, Bruce Partridge, Julien Peloton, Francesca Perrotta, Lucio Pic-

cirillo, Giampaolo Pisano, Davide Poletti, Roberto Puddu, Giuseppe Puglisi, Chris Raum, Christian L. Reichardt, Mathieu Remazeilles, Yoel Rephaeli, Dominik Riechers, Felipe Rojas, Anirban Roy, Sharon Sadeh, Yuki Sakurai, Maria Salatino, Mayuri Sathyaranayana Rao, Emmanuel Schaan, Marcel Schmittfull, Neelima Sehgal, Joseph Seibert, Uros Seljak, Blake Sherwin, Meir Shimon, Carlos Sierra, Jonathan Sievers, Precious Sikhosana, Maximiliano Silva-Feaver, Sara M. Simon, Adrian Sinclair, Praween Siritanasak, Kendrick Smith, Stephen R. Smith, David Spergel, Suzanne T. Staggs, George Stein, Jason R. Stevens, Radek Stompor, Aritoki Suzuki, Osamu Tajima, Satoru Takakura, Grant Teply, Daniel B. Thomas, Ben Thorne, Robert Thornton, Hy Trac, Calvin Tsai, Carole Tucker, Joel Ullom, Sunny Vagnozzi, Alexander van Engelen, Jeff Van Lanen, Daniel D. Van Winkle, Eve M. Vavagiakis, Clara Vergès, Michael Vissers, Kasey Wagoner, Samantha Walker, Jon Ward, Ben Westbrook, Nathan Whitehorn, Jason Williams, Joel Williams, Edward J. Wollack, Zhilei Xu, Byeonghee Yu, Cyndia Yu, Fernando Zago, Hezi Zhang, and Ningfeng Zhu and. The Simons Observatory: science goals and forecasts. *Journal of Cosmology and Astroparticle Physics*, 2019(02):056–056, February 2019.

- [4] Peter A. R. Ade, Giampaolo Pisano, Carole Tucker, and Samuel Weaver. A review of metal mesh filters. In *Millimeter and Submillimeter Detectors and Instrumentation for Astronomy III*, volume 6275, page 62750U. International Society for Optics and Photonics, June 2006.
- [5] M. N. Afsar. Precision millimeter-wave measurements of complex refractive index, complex dielectric permittivity, and loss tangent of common polymers. *IEEE Transactions on Instrumentation and Measurement*, IM-36(2):530–536, June 1987.

- [6] Mohamed Nurul Afsar and Hua Chi. Millimeter wave complex refractive index, complex dielectric permittivity and loss tangent of extra high purity and compensated silicon. *International Journal of Infrared and Millimeter Waves*, 15(7):1181–1188, July 1994.
- [7] N. Aghanim, Y. Akrami, F. Arroja, M. Ashdown, J. Aumont, C. Baccigalupi, M. Ballardini, A. J. Banday, R. B. Barreiro, N. Bartolo, S. Basak, R. Battye, K. Benabed, J.-P. Bernard, M. Bersanelli, P. Bielewicz, J. J. Bock, J. R. Bond, J. Borrill, F. R. Bouchet, F. Boulanger, M. Bucher, C. Burigana, R. C. Butler, E. Calabrese, J.-F. Cardoso, J. Carron, B. Casaponsa, A. Challinor, H. C. Chiang, L. P. L. Colombo, C. Combet, D. Contreras, B. P. Crill, F. Cuttaia, P. de Bernardis, G. de Zotti, J. Delabrouille, J.-M. Delouis, F.-X. Désert, E. Di Valentino, C. Dickinson, J. M. Diego, S. Donzelli, O. Doré, M. Douspis, A. Ducout, X. Dupac, G. Efstathiou, F. Elsner, T. A. Enßlin, H. K. Eriksen, E. Falgarone, Y. Fantaye, J. Ferguson, R. Fernandez-Cobos, F. Finelli, F. Forastieri, M. Frailis, E. Franceschi, A. Frolov, S. Galeotta, S. Galli, K. Ganga, R. T. Génova-Santos, M. Gerbino, T. Ghosh, J. González-Nuevo, K. M. Górski, S. Gratton, A. Gruppuso, J. E. Gudmundsson, J. Hamann, W. Handley, F. K. Hansen, G. Helou, D. Herranz, S. R. Hildebrandt, E. Hivon, Z. Huang, A. H. Jaffe, W. C. Jones, A. Karakci, E. Keihänen, R. Keskitalo, K. Kiiveri, J. Kim, T. S. Kisner, L. Knox, N. Krachmalnicoff, M. Kunz, H. Kurki-Suonio, G. Lagache, J.-M. Lamarre, M. Langer, A. Lasenby, M. Lattanzi, C. R. Lawrence, M. Le Jeune, J. P. Leahy, J. Lesgourgues, F. Levrier, A. Lewis, M. Liguori, P. B. Lilje, M. Lilley, V. Lindholm, M. López-Caniego, P. M. Lubin, Y.-Z. Ma, J. F. Macías-Pérez, G. Maggio, D. Maino, N. Mandolesi, A. Mangilli, A. Marcos-Caballero, M. Maris, P. G. Martin, M. Martinelli, E. Martínez-

González, S. Matarrese, N. Mauri, J. D. McEwen, P. D. Meerburg, P. R. Meinholt, A. Melchiorri, A. Mennella, M. Migliaccio, M. Millea, S. Mitra, M.-A. Miville-Deschénes, D. Molinari, A. Moneti, L. Montier, G. Morgante, A. Moss, S. Mottet, M. Münchmeyer, P. Natoli, H. U. Nørgaard-Nielsen, C. A. Oxborrow, L. Pagano, D. Paoletti, B. Partridge, G. Patanchon, T. J. Pearson, M. Peel, H. V. Peiris, F. Perrotta, V. Pettorino, F. Piacentini, L. Polastri, G. Polenta, J.-L. Puget, J. P. Rachen, M. Reinecke, M. Remazeilles, C. Renault, A. Renzi, G. Rocha, C. Rosset, G. Roudier, J. A. Rubiño-Martín, B. Ruiz-Granados, L. Salvati, M. Sandri, M. Savelainen, D. Scott, E. P. S. Shellard, M. Shiraishi, C. Sirignano, G. Sirri, L. D. Spencer, R. Sunyaev, A.-S. Suur-Uski, J. A. Tauber, D. Tavagnacco, M. Tenti, L. Terenzi, L. Toffolatti, M. Tomasi, T. Trombetti, J. Valiviita, B. Van Tent, L. Vibert, P. Vielva, F. Villa, N. Vittorio, B. D. Wandelt, I. K. Wehus, M. White, S. D. M. White, A. Zacchei, and A. Zonca. Planck 2018 results - I. Overview and the cosmological legacy of Planck. *Astronomy & Astrophysics*, 641:A1, September 2020. Publisher: EDP Sciences.

- [8] N. Aghanim, Y. Akrami, M. Ashdown, J. Aumont, C. Baccigalupi, M. Ballardini, A. J. Banday, R. B. Barreiro, N. Bartolo, S. Basak, R. Battye, K. Benabed, J.-P. Bernard, M. Bersanelli, P. Bielewicz, J. J. Bock, J. R. Bond, J. Borrill, F. R. Bouchet, F. Boulanger, M. Bucher, C. Burigana, R. C. Butler, E. Calabrese, J.-F. Cardoso, J. Carron, A. Challinor, H. C. Chiang, J. Chluba, L. P. L. Colombo, C. Combet, D. Contreras, B. P. Crill, F. Cuttaia, P. de Bernardis, G. de Zotti, J. Delabrouille, J.-M. Delouis, E. Di Valentino, J. M. Diego, O. Doré, M. Douspis, A. Ducout, X. Dupac, S. Dusini, G. Efstathiou, F. Elsner, T. A. Enßlin, H. K. Eriksson, Y. Fantaye, M. Farhang, J. Fergusson, R. Fernandez-Cobos, F. Finelli,

F. Forastieri, M. Frailis, A. A. Fraisse, E. Franceschi, A. Frolov, S. Galeotta, S. Galli, K. Ganga, R. T. Génova-Santos, M. Gerbino, T. Ghosh, J. González-Nuevo, K. M. Górski, S. Gratton, A. Gruppuso, J. E. Gudmundsson, J. Hamann, W. Handley, F. K. Hansen, D. Herranz, S. R. Hildebrandt, E. Hivon, Z. Huang, A. H. Jaffe, W. C. Jones, A. Karakci, E. Keihänen, R. Keskitalo, K. Kiiveri, J. Kim, T. S. Kisner, L. Knox, N. Krachmalnicoff, M. Kunz, H. Kurki-Suonio, G. Lagache, J.-M. Lamarre, A. Lasenby, M. Latanzi, C. R. Lawrence, M. Le Jeune, P. Lemos, J. Lesgourgues, F. Levrier, A. Lewis, M. Liguori, P. B. Lilje, M. Lilley, V. Lindholm, M. López-Caniego, P. M. Lubin, Y.-Z. Ma, J. F. Macías-Pérez, G. Maggio, D. Maino, N. Mandlesi, A. Mangilli, A. Marcos-Caballero, M. Maris, P. G. Martin, M. Martinelli, E. Martínez-González, S. Matarrese, N. Mauri, J. D. McEwen, P. R. Meinholt, A. Melchiorri, A. Mennella, M. Migliaccio, M. Millea, S. Mitra, M.-A. Miville-Deschénes, D. Molinari, L. Montier, G. Morgante, A. Moss, P. Natoli, H. U. Nørgaard-Nielsen, L. Pagano, D. Paoletti, B. Partridge, G. Patanchon, H. V. Peiris, F. Perrotta, V. Pettorino, F. Piacentini, L. Polastri, G. Polenta, J.-L. Puget, J. P. Rachen, M. Reinecke, M. Remazeilles, A. Renzi, G. Rocha, C. Rosset, G. Roudier, J. A. Rubiño-Martín, B. Ruiz-Granados, L. Salvati, M. Sandri, M. Savelainen, D. Scott, E. P. S. Shellard, C. Sirignano, G. Sirri, L. D. Spencer, R. Sunyaev, A.-S. Suur-Uski, J. A. Tauber, D. Tavagnacco, M. Tenti, L. Toffolatti, M. Tomasi, T. Trombetti, L. Valenziano, J. Valiviita, B. Van Tent, L. Vibert, P. Vielva, F. Villa, N. Vittorio, B. D. Wandelt, I. K. Wehus, M. White, S. D. M. White, A. Zacchei, and A. Zonca. Planck 2018 results - VI. Cosmological parameters. *Astronomy & Astrophysics*, 641:A6, September 2020. Publisher: EDP Sciences.

- [9] Simone Aiola, Erminia Calabrese, Loïc Maurin, Sigurd Naess, Benjamin L.

Schmitt, Maximilian H. Abitbol, Graeme E. Addison, Peter A. R. Ade, David Alonso, Mandana Amiri, Stefania Amodeo, Elio Angile, Jason E. Austermann, Taylor Baildon, Nick Battaglia, James A. Beall, Rachel Bean, Daniel T. Becker, J. Richard Bond, Sarah Marie Bruno, Victoria Calafut, Luis E. Campusano, Felipe Carrero, Grace E. Chesmore, Hsiao-mei Cho., Steve K. Choi, Susan E. Clark, Nicholas F. Cothard, Devin Crichton, Kevin T. Crowley, Omar Darwish, Rahul Datta, Edward V. Denison, Mark J. Devlin, Cody J. Duell, Shannon M. Duff, Adriaan J. Duivenvoorden, Jo Dunkley, Rolando Dünner, Thomas Essinger-Hileman, Max Fankhanel, Simone Ferraro, Anna E. Fox, Brittany Fuzia, Patricio A. Gallardo, Vera Gluscevic, Joseph E. Golec, Emily Grace, Megan Gralla, Yilun Guan, Kirsten Hall, Mark Halpern, Dongwon Han, Peter Hargrave, Matthew Hasselfield, Jakob M. Helton, Shawn Henderson, Brandon Hensley, J. Colin Hill, Gene C. Hilton, Matt Hilton, Adam D. Hincks, Renée Hložek, Shuay-Pwu Patty Ho, Johannes Hubmayr, Kevin M. Huffenberger, John P. Hughes, Leopoldo Infante, Kent Irwin, Rebecca Jackson, Jeff Klein, Kenda Knowles, Brian Koopman, Arthur Kosowsky, Vincent Lakey, Dale Li, Yaqiong Li, Zack Li, Martine Lokken, Thibaut Louis, Marius Lungu, Amanda MacInnis, Mathew Madhavacheril, Felipe Maldonado, Maya Mallaby-Kay, Danica Marsden, Jeff McMahon, Felipe Menanteau, Kavilan Moodley, Tim Morton, Toshiya Namikawa, Federico Nati, Laura Newburgh, John P. Nibarger, Andrina Nicola, Michael D. Niemack, Michael R. Nolta, John Orlowski-Sherer, Lyman A. Page, Christine G. Pappas, Bruce Partridge, Phumlani Phakathi, Heather Prince, Roberto Puddu, Frank J. Qu, Jesus Rivera, Naomi Robertson, Felipe Rojas, Maria Salatino, Emmanuel Schaan, Alessandro Schillaci, Neelima Sehgal, Blake D. Sherwin, Carlos Sierra, Jon Sievers, Cristobal Si-

fon, Precious Sikhosana, Sara Simon, David N. Spergel, Suzanne T. Staggs, Jason Stevens, Emilie Storer, Dhaneshwar D. Sunder, Eric R. Switzer, Ben Thorne, Robert Thornton, Hy Trac, Jesse Treu, Carole Tucker, Leila R. Vale, Alexander Van Engelen, Jeff Van Lanen, Eve M. Vavagiakis, Kasey Wagoner, Yuhan Wang, Jonathan T. Ward, Edward J. Wollack, Zhilei Xu, Fernando Zago, and Ningfeng Zhu. The Atacama Cosmology Telescope: DR4 Maps and Cosmological Parameters. *arXiv:2007.07288 [astro-ph]*, July 2020. arXiv: 2007.07288.

- [10] G. B. Airy. VI. On the phænomena of Newton's rings when formed between two transparent substances of different refractive powers. *The London, Edinburgh, and Dublin Philosophical Magazine and Journal of Science*, 2(7):20–30, January 1833. Publisher: Taylor & Francis eprint: <https://doi.org/10.1080/14786443308647959>.
- [11] Y. Akrami, F. Arroja, M. Ashdown, J. Aumont, C. Baccigalupi, M. Ballardini, A. J. Banday, R. B. Barreiro, N. Bartolo, S. Basak, K. Benabed, J.-P. Bernard, M. Bersanelli, P. Bielewicz, J. J. Bock, J. R. Bond, J. Borrill, F. R. Bouchet, F. Boulanger, M. Bucher, C. Burigana, R. C. Butler, E. Calabrese, J.-F. Cardoso, J. Carron, A. Challinor, H. C. Chiang, L. P. L. Colombo, C. Combet, D. Contreras, B. P. Crill, F. Cuttaia, P. de Bernardis, G. de Zotti, J. Delabrouille, J.-M. Delouis, E. Di Valentino, J. M. Diego, S. Donzelli, O. Doré, M. Douspis, A. Ducout, X. Dupac, S. Dusini, G. Efstathiou, F. Elsner, T. A. Enßlin, H. K. Eriksen, Y. Fantaye, J. Fergusson, R. Fernandez-Cobos, F. Finelli, F. Forastieri, M. Frailis, E. Franceschi, A. Frolov, S. Galeotta, S. Galli, K. Ganga, C. Gauthier, R. T. Génova-Santos, M. Gerbino, T. Ghosh, J. González-Nuevo, K. M. Górska, S. Gratton, A. Gruppuso, J. E. Gudmundsson, J. Hamann, W. Handley, F. K. Hansen, D. Herranz,

E. Hivon, D. C. Hooper, Z. Huang, A. H. Jaffe, W. C. Jones, E. Keihänen, R. Keskitalo, K. Kiiveri, J. Kim, T. S. Kisner, N. Krachmalnicoff, M. Kunz, H. Kurki-Suonio, G. Lagache, J.-M. Lamarre, A. Lasenby, M. Lattanzi, C. R. Lawrence, M. Le Jeune, J. Lesgourgues, F. Levrier, A. Lewis, M. Liguori, P. B. Lilje, V. Lindholm, M. López-Caniego, P. M. Lubin, Y.-Z. Ma, J. F. Macías-Pérez, G. Maggio, D. Maino, N. Mandolesi, A. Mangilli, A. Marcos-Caballero, M. Maris, P. G. Martin, E. Martínez-González, S. Matarrese, N. Mauri, J. D. McEwen, P. D. Meerburg, P. R. Meinhold, A. Melchiorri, A. Mennella, M. Migliaccio, S. Mitra, M.-A. Miville-Deschénes, D. Molinari, A. Moneti, L. Montier, G. Morgante, A. Moss, M. Münchmeyer, P. Natoli, H. U. Nørgaard-Nielsen, L. Pagano, D. Paoletti, B. Partridge, G. Patanchon, H. V. Peiris, F. Perrotta, V. Pettorino, F. Piacentini, L. Polastri, G. Polenta, J.-L. Puget, J. P. Rachén, M. Reinecke, M. Remazeilles, A. Renzi, G. Rocha, C. Rosset, G. Roudier, J. A. Rubiño-Martín, B. Ruiz-Granados, L. Salvati, M. Sandri, M. Savelainen, D. Scott, E. P. S. Shellard, M. Shiraishi, C. Sirignano, G. Sirri, L. D. Spencer, R. Sunyaev, A.-S. Suur-Uski, J. A. Tauber, D. Tavagnacco, M. Tenti, L. Toffolatti, M. Tomasi, T. Trombetti, J. Valiviita, B. Van Tent, P. Vielva, F. Villa, N. Vittorio, B. D. Wandelt, I. K. Wehus, S. D. M. White, A. Zacchei, J. P. Zibin, and A. Zonca. Planck 2018 results - X. Constraints on inflation. *Astronomy & Astrophysics*, 641:A10, September 2020. Publisher: EDP Sciences,, hello.

- [12] Y. Akrami, M. Ashdown, J. Aumont, C. Baccigalupi, M. Ballardini, A. J. Banday, R. B. Barreiro, N. Bartolo, S. Basak, K. Benabed, M. Bersanelli, P. Bielewicz, J. J. Bock, J. R. Bond, J. Borrill, F. R. Bouchet, F. Boulanger, M. Bucher, C. Burigana, R. C. Butler, E. Calabrese, J.-F. Cardoso, B. Casaponsa, H. C. Chiang, L. P. L. Colombo, C. Combet, D. Contreras,

B. P. Crill, P. de Bernardis, G. de Zotti, J. Delabrouille, J.-M. Delouis, E. Di Valentino, J. M. Diego, O. Doré, M. Douspis, A. Ducout, X. Dupac, G. Efstathiou, F. Elsner, T. A. Enßlin, H. K. Eriksen, Y. Fantaye, R. Fernandez-Cobos, F. Finelli, M. Frailis, A. A. Fraisse, E. Franceschi, A. Frolov, S. Galeotta, S. Galli, K. Ganga, R. T. Génova-Santos, M. Gerbino, T. Ghosh, J. González-Nuevo, K. M. Górski, A. Gruppuso, J. E. Gudmundsson, J. Hamann, W. Handley, F. K. Hansen, D. Herranz, E. Hivon, Z. Huang, A. H. Jaffe, W. C. Jones, E. Keihänen, R. Keskitalo, K. Kiiveri, J. Kim, N. Krachmalnicoff, M. Kunz, H. Kurki-Suonio, G. Lagache, J.-M. Lamarre, A. Lasenby, M. Lattanzi, C. R. Lawrence, M. Le Jeune, F. Levrier, M. Liguori, P. B. Lilje, V. Lindholm, M. López-Caniego, Y.-Z. Ma, J. F. Macías-Pérez, G. Maggio, D. Maino, N. Mandolesi, A. Mangilli, A. Marcos-Caballero, M. Maris, P. G. Martin, E. Martínez-González, S. Matarrese, N. Mauri, J. D. McEwen, P. R. Meinhold, A. Mennella, M. Migliaccio, M.-A. Miville-Deschénes, D. Molinari, A. Moneti, L. Montier, G. Morgante, A. Moss, P. Natoli, L. Pagano, D. Paoletti, B. Partridge, F. Perrotta, V. Pettorino, F. Piacentini, G. Polenta, J.-L. Puget, J. P. Rachén, M. Reinecke, M. Remazeilles, A. Renzi, G. Rocha, C. Rosset, G. Roudier, J. A. Rubiño-Martín, B. Ruiz-Granados, L. Salvati, M. Savelainen, D. Scott, E. P. S. Shellard, C. Sirignano, R. Sunyaev, A.-S. Suur-Uski, J. A. Tauber, D. Tavagnacco, M. Tenti, L. Toffolatti, M. Tomasi, T. Trombetti, L. Valenziano, J. Valiviita, B. Van Tent, P. Vielva, F. Villa, N. Vittorio, B. D. Wandelt, I. K. Wehus, A. Zacchei, J. P. Zibin, and A. Zonca. Planck 2018 results - VII. Isotropy and statistics of the CMB. *Astronomy & Astrophysics*, 641:A7, September 2020. Publisher: EDP Sciences, hello.

[13] Atacama Cosmology Telescope Collaboration, Mathew Madhavacheril, Nee-

lima Sehgal, Rupert Allison, Nick Battaglia, J. Richard Bond, Erminia Calabrese, Jerod Caligiuri, Kevin Coughlin, Devin Crichton, Rahul Datta, Mark J. Devlin, Joanna Dunkley, Rolando Dünner, Kevin Fogarty, Emily Grace, Amir Hajian, Matthew Hasselfield, J. Colin Hill, Matt Hilton, Adam D. Hincks, Renée Hlozek, John P. Hughes, Arthur Kosowsky, Thibaut Louis, Marius Lungu, Jeff McMahon, Kavilan Moodley, Charles Munson, Sigurd Naess, Federico Nati, Laura Newburgh, Michael D. Niemack, Lyman A. Page, Bruce Partridge, Benjamin Schmitt, Blake D. Sherwin, Jon Sievers, David N. Spergel, Suzanne T. Staggs, Robert Thornton, Alexander Van Engelen, Jonathan T. Ward, and Edward J. Wollack. Evidence of Lensing of the Cosmic Microwave Background by Dark Matter Halos. *Physical Review Letters*, 114(15):151302, April 2015. Publisher: American Physical Society.

- [14] Rennan Barkana and Abraham Loeb. In the Beginning: The First Sources of Light and the Reionization of the Universe. *Physics Reports*, 349(2):125–238, July 2001. arXiv: astro-ph/0010468.
- [15] E. S. Battistelli, M. Amiri, B. Burger, M. Halpern, S. Knotek, M. Ellis, X. Gao, D. Kelly, M. MacIntosh, K. Irwin, and C. Reintsema. Functional Description of Read-out Electronics for Time-Domain Multiplexed Bolometers for Millimeter and Sub-millimeter Astronomy. *Journal of Low Temperature Physics*, 151(3):908–914, May 2008.
- [16] B. A. Belyaev, V. V. Tyurnev, and N. V. Volkov. Scattering of Electromagnetic Waves on a Subwave Lattice of Square Strip Conductors. *Journal of Communications Technology and Electronics*, 64(7):664–674, July 2019.
- [17] José Luis Bernal, Patrick C. Breysse, and Ely D. Kovetz. The Cosmic

Expansion History from Line-Intensity Mapping. *Physical Review Letters*, 123(25):251301, December 2019. arXiv: 1907.10065.

- [18] S. Biber, J. Richter, S. Martius, and L. P. Schmidt. Design of Artificial Dielectrics for Anti-Reflection-Coatings. In *2003 33rd European Microwave Conference*, pages 1115–1118, October 2003.
- [19] Max Born and Emil Wolf. *Principles of Optics*. Cambridge University Press, Cambridge ; New York, 7th edition edition, October 1999.
- [20] C. Matt Bradford, Gordon J. Stacey, Mark R. Swain, Thomas Nikola, Alberto D. Bolatto, James M. Jackson, Maureen L. Savage, Jacqueline A. Davidson, and Peter A. R. Ade. SPIFI: a direct-detection imaging spectrometer for submillimeter wavelengths. *Applied Optics*, 41(13):2561–2574, May 2002. Publisher: Optical Society of America.
- [21] Victoria Calafut, Patricio A. Gallardo, Eve M. Vavagiakis, Stefania Amodeo, Simone Aiola, Jason E. Austermann, Nicholas Battaglia, Elia S. Battistelli, James A. Beall, Rachel Bean, J. Richard Bond, Erminia Calabrese, Steve K. Choi, Nicholas F. Cothard, Mark J. Devlin, Cody J. Duell, Adriaan J. Duivenvoorden, Jo Dunkley, Rolando Dunner, Simone Ferraro, Yilun Guan, J. Colin Hill, Matt Hilton, Renee Hlozek, Zachary B. Huber, Johannes Hubmayr, Kevin M. Huffenberger, John P. Hughes, Brian J. Koopman, Arthur Kosowsky, Yaqiong Li, Martine Lokken, Mathew Madhavacheril, Jeff McMahon, Kavilan Moodley, Sigurd Naess, Federico Nati, Laura B. Newburgh, Michael D. Niemack, Bruce Partridge, Emmanuel Schaan, Alessandro Schillaci, Cristobal Sifon, David N. Spergel, Suzanne T. Staggs, Joel N. Ullom, Leila R. Vale, Alexander Van Engelen, Edward J. Wollack, and Zhilei Xu. The Atacama Cosmology Telescope: Detection of

the Pairwise Kinematic Sunyaev-Zel'dovich Effect with SDSS DR15 Galaxies. *arXiv:2101.08374 [astro-ph]*, January 2021. arXiv: 2101.08374.

- [22] John Ernest Chamberlain. *The principles of interferometric spectroscopy*. Wiley, Chichester, England, 1979. <http://newcatalog.library.cornell.edu/catalog/729078>.
- [23] S. K. Choi, J. Austermann, K. Basu, N. Battaglia, F. Bertoldi, D. T. Chung, N. F. Cothard, S. Duff, C. J. Duell, P. A. Gallardo, J. Gao, T. Herter, J. Hubmayr, M. D. Niemack, T. Nikola, D. Riechers, K. Rossi, G. J. Stacey, J. R. Stevens, E. M. Vavagiakis, M. Vissers, and S. Walker. Sensitivity of the Prime-Cam Instrument on the CCAT-Prime Telescope. *Journal of Low Temperature Physics*, 199(3):1089–1097, May 2020.
- [24] S. K. Choi, J. Austermann, J. A. Beall, K. T. Crowley, R. Datta, S. M. Duff, P. A. Gallardo, S. P. Ho, J. Hubmayr, B. J. Koopman, Y. Li, F. Nati, M. D. Niemack, L. A. Page, M. Salatino, S. M. Simon, S. T. Staggs, J. Stevens, J. Ullom, and E. J. Wollack. Characterization of the Mid-Frequency Arrays for Advanced ACTPol. *Journal of Low Temperature Physics*, 193(3):267–275, November 2018.
- [25] Steve K. Choi, Matthew Hasselfield, Shuay-Pwu Patty Ho, Brian Koopman, Marius Lungu, Maximilian H. Abitbol, Graeme E. Addison, Peter A. R. Ade, Simone Aiola, David Alonso, Mandana Amiri, Stefania Amodeo, Elio Angile, Jason E. Austermann, Taylor Baildon, Nick Battaglia, James A. Beall, Rachel Bean, Daniel T. Becker, J. Richard Bond, Sarah Marie Bruno, Erminia Calabrese, Victoria Calafut, Luis E. Campusano, Felipe Carrero, Grace E. Chesmore, Hsiao-meい Cho., Susan E. Clark, Nicholas F. Cothard, Devin Crichton, Kevin T. Crowley, Omar Darwish, Rahul Datta, Edward V.

Denison, Mark J. Devlin, Cody J. Duell, Shannon M. Duff, Adriaan J. Duivenvoorden, Jo Dunkley, Rolando Dünner, Thomas Essinger-Hileman, Max Fankhanel, Simone Ferraro, Anna E. Fox, Brittany Fuzia, Patricio A. Gallardo, Vera Gluscevic, Joseph E. Golec, Emily Grace, Megan Gralla, Yilun Guan, Kirsten Hall, Mark Halpern, Dongwon Han, Peter Hargrave, Shawn Henderson, Brandon Hensley, J. Colin Hill, Gene C. Hilton, Matt Hilton, Adam D. Hincks, Renée Hložek, Johannes Hubmayr, Kevin M. Huffenberger, John P. Hughes, Leopoldo Infante, Kent Irwin, Rebecca Jackson, Jeff Klein, Kenda Knowles, Arthur Kosowsky, Vincent Lakey, Dale Li, Yaqiong Li, Zack Li, Martine Lokken, Thibaut Louis, Amanda MacInnis, Mathew Madhavacheril, Felipe Maldonado, Maya Mallaby-Kay, Danica Marsden, Loïc Maurin, Jeff McMahon, Felipe Menanteau, Kavilan Moodley, Tim Morton, Sigurd Naess, Toshiya Namikawa, Federico Nati, Laura Newburgh, John P. Nibarger, Andrina Nicola, Michael D. Niemack, Michael R. Nolta, John Orlowski-Sherer, Lyman A. Page, Christine G. Pappas, Bruce Partridge, Phumlani Phakathi, Heather Prince, Roberto Puddu, Frank J. Qu, Jesus Rivera, Naomi Robertson, Felipe Rojas, Maria Salatino, Emmanuel Schaan, Alessandro Schillaci, Benjamin L. Schmitt, Neelima Sehgal, Blake D. Sherwin, Carlos Sierra, Jon Sievers, Cristobal Sifon, Precious Sikhosana, Sara Simon, David N. Spergel, Suzanne T. Staggs, Jason Stevens, Emilie Storer, Dhaneshwar D. Sunder, Eric R. Switzer, Ben Thorne, Robert Thornton, Hy Trac, Jesse Treu, Carole Tucker, Leila R. Vale, Alexander Van Engelen, Jeff Van Lanen, Eve M. Vavagiakis, Kasey Wagoner, Yuhan Wang, Jonathan T. Ward, Edward J. Wollack, Zhilei Xu, Fernando Zago, and Ningfeng Zhu. The Atacama Cosmology Telescope: A Measurement of the Cosmic Microwave Background Power Spectra at 98 and 150 GHz.

arXiv:2007.07289 [astro-ph], July 2020. arXiv: 2007.07289.

- [26] Dongwoo Chung. Personal Communication.
- [27] CCAT-Prime collaboration, M. Aravena, J. E. Austermann, K. Basu, N. Battaglia, B. Beringue, F. Bertoldi, F. Bigiel, J. R. Bond, P. C. Breysse, C. Broughton, R. Bustos, S. C. Chapman, M. Charmetant, S. K. Choi, D. T. Chung, S. E. Clark, N. F. Cothard, A. Dev, K. Douglas, C. J. Duell, H. Ebina, J. Erler, M. Fich, L. M. Fissel, S. Foreman, J. Gao, Pablo García, R. Giovanelli, M. P. Haynes, B. Hensley, T. Herter, R. Higgins, Z. Huber, J. Hubmayr, D. Johnstone, C. Karoumpis, Laura C. Keating, E. Komatsu, Y. Li, Benjamin Magnelli, B. C. Matthews, P. D. Meerburg, J. Meyers, V. Muralidhara, N. W. Murray, M. D. Niemack, T. Nikola, Y. Okada, D. A. Riechers, E. Rosolowsky, A. Roy, S. I. Sadavoy, R. Schaaf, P. Schilke, D. Scott, R. Simon, Adrian K. Sinclair, G. R. Sivakoff, G. J. Stacey, Amelia M. Stutz, J. Stutzki, M. Tahani, K. Thanjavur, R. A. Timmermann, J. N. Ullom, A. van Engelen, E. M. Vavagiakis, M. R. Vissers, J. D. Wheeler, S. D. M. White, Y. Zhu, and B. Zou. CCAT-prime Collaboration: Science Goals and Forecasts with Prime-Cam on the Fred Young Submillimeter Telescope. *arXiv:2107.10364 [astro-ph]*, July 2021. arXiv: 2107.10364.
- [28] Planck Collaboration, N. Aghanim, Y. Akrami, M. Ashdown, J. Aumont, C. Baccigalupi, M. Ballardini, A. J. Banday, R. B. Barreiro, N. Bartolo, S. Basak, R. Battye, K. Benabed, J.-P. Bernard, M. Bersanelli, P. Bielewicz, J. J. Bock, J. R. Bond, J. Borrill, F. R. Bouchet, F. Boulanger, M. Bucher, C. Burigana, R. C. Butler, E. Calabrese, J.-F. Cardoso, J. Carron, A. Challinor, H. C. Chiang, J. Chluba, L. P. L. Colombo, C. Combet, D. Contreras, B. P. Crill, F. Cuttaia, P. de Bernardis, G. de Zotti, J. Delabrouille, J.-M. De

louis, E. Di Valentino, J. M. Diego, O. Doré, M. Douspis, A. Ducout, X. Dupac, S. Dusini, G. Efstathiou, F. Elsner, T. A. Enßlin, H. K. Eriksen, Y. Fantaye, M. Farhang, J. Fergusson, R. Fernandez-Cobos, F. Finelli, F. Forastieri, M. Frailis, E. Franceschi, A. Frolov, S. Galeotta, S. Galli, K. Ganga, R. T. Génova-Santos, M. Gerbino, T. Ghosh, J. González-Nuevo, K. M. Górski, S. Gratton, A. Gruppuso, J. E. Gudmundsson, J. Hamann, W. Handley, D. Herranz, E. Hivon, Z. Huang, A. H. Jaffe, W. C. Jones, A. Karakci, E. Keihänen, R. Keskitalo, K. Kiiveri, J. Kim, T. S. Kisner, L. Knox, N. Krachmalnicoff, M. Kunz, H. Kurki-Suonio, G. Lagache, J.-M. Lamarre, A. Lasenby, M. Lattanzi, C. R. Lawrence, M. Le Jeune, P. Lemos, J. Lesgourges, F. Levrier, A. Lewis, M. Liguori, P. B. Lilje, M. Lilley, V. Lindholm, M. López-Caniego, P. M. Lubin, Y.-Z. Ma, J. F. Macías-Pérez, G. Maggio, D. Maino, N. Mandolesi, A. Mangilli, A. Marcos-Caballero, M. Maris, P. G. Martin, M. Martinelli, E. Martínez-González, S. Matarrese, N. Mauri, J. D. McEwen, P. R. Meinholt, A. Melchiorri, A. Mennella, M. Migliaccio, M. Millea, S. Mitra, M.-A. Miville-Deschénes, D. Molinari, L. Montier, G. Morgante, A. Moss, P. Natoli, H. U. Nørgaard-Nielsen, L. Pagano, D. Paoletti, B. Partridge, G. Patanchon, H. V. Peiris, F. Perrotta, V. Pettorino, F. Pisacentini, L. Polastri, G. Polenta, J.-L. Puget, J. P. Rachen, M. Reinecke, M. Remazeilles, A. Renzi, G. Rocha, C. Rosset, G. Roudier, J. A. Rubiño-Martín, B. Ruiz-Granados, L. Salvati, M. Sandri, M. Savelainen, D. Scott, E. P. S. Shellard, C. Sirignano, G. Sirri, L. D. Spencer, R. Sunyaev, A.-S. Suur-Uski, J. A. Tauber, D. Tavagnacco, M. Tenti, L. Toffolatti, M. Tomasi, T. Trombetti, L. Valenziano, J. Valiviita, B. Van Tent, L. Vibert, P. Vielva, F. Villa, N. Vittorio, B. D. Wandelt, I. K. Wehus, M. White, S. D. M. White, A. Zacchei, and A. Zonca. Planck 2018 results. VI. Cosmological parameters.

- [29] Planck Collaboration, Y. Akrami, M. Ashdown, J. Aumont, C. Baccigalupi, M. Ballardini, A. J. Banday, R. B. Barreiro, N. Bartolo, S. Basak, K. Benabed, J.-P. Bernard, M. Bersanelli, P. Bielewicz, J. R. Bond, J. Borrill, F. R. Bouchet, F. Boulanger, A. Bracco, M. Bucher, C. Burigana, E. Calabrese, J.-F. Cardoso, J. Carron, H. C. Chiang, C. Combet, B. P. Crill, P. de Bernardis, G. de Zotti, J. Delabrouille, J.-M. Delouis, E. Di Valentino, C. Dickinson, J. M. Diego, A. Ducout, X. Dupac, G. Efstathiou, F. Elsner, T. A. Enßlin, E. Falgarone, Y. Fantaye, K. Ferrière, F. Finelli, F. Forastieri, M. Frailis, A. A. Fraisse, E. Franceschi, A. Frolov, S. Galeotta, S. Galli, K. Ganga, R. T. Génova-Santos, T. Ghosh, J. González-Nuevo, K. M. Górski, A. Gruppuso, J. E. Gudmundsson, V. Guillet, W. Handley, F. K. Hansen, D. Herranz, Z. Huang, A. H. Jaffe, W. C. Jones, E. Keihänen, R. Keskitalo, K. Kiiveri, J. Kim, N. Krachmalnicoff, M. Kunz, H. Kurki-Suonio, J.-M. Lamarre, A. Lasenby, M. Le Jeune, F. Levrier, M. Liguori, P. B. Lilje, V. Lindholm, M. López-Caniego, P. M. Lubin, Y.-Z. Ma, J. F. Macías-Pérez, G. Maggio, D. Maino, N. Mandolcsi, A. Mangilli, P. G. Martin, E. Martínez-González, S. Matarrese, J. D. McEwen, P. R. Meinhold, A. Melchiorri, M. Migliaccio, M.-A. Miville-Deschénes, D. Molinari, A. Moneti, L. Montier, G. Morgante, P. Natoli, L. Pagano, D. Paoletti, V. Pettorino, F. Piacentini, G. Polenta, J.-L. Puget, J. P. Rachen, M. Reinecke, M. Remazeilles, A. Renzi, G. Rocha, C. Rosset, G. Roudier, J. A. Rubiño-Martín, B. Ruiz-Granados, L. Salvati, M. Sandri, M. Savelainen, D. Scott, J. D. Soler, L. D. Spencer, J. A. Tauber, D. Tavagnacco, L. Toffolatti, M. Tomasi, T. Trombetti, J. Valiviita, F. Van-syngel, F. Van Tent, P. Vielva, F. Villa, N. Vittorio, I. K. Wehus, A. Zacchei, and A. Zonca. Planck 2018 results. XI. Polarized dust foregrounds. *Astron-*

- [30] The Simons Observatory Collaboration, Maximilian H. Abitbol, Shunsuke Adachi, Peter Ade, James Aguirre, Zeeshan Ahmed, Simone Aiola, Aamir Ali, David Alonso, Marcelo A. Alvarez, Kam Arnold, Peter Ashton, Zachary Atkins, Jason Austermann, Humna Awan, Carlo Baccigalupi, Taylor Baildon, Anton Baleato Lizancos, Darcy Barron, Nick Battaglia, Richard Battye, Eric Baxter, Andrew Bazarko, James A. Beall, Rachel Bean, Dominic Beck, Shawn Beckman, Benjamin Beringue, Tanay Bhandarkar, Sanah Bhimani, Federico Bianchini, Steven Boada, David Boettger, Boris Bolliet, J. Richard Bond, Julian Borrill, Michael L. Brown, Sarah Marie Bruno, Sean Bryan, Erminia Calabrese, Victoria Calafut, Paolo Calisse, Julien Carron, Fred M. Carl, Juan Cayuso, Anthony Challinor, Grace Chesmore, Yuji Chinone, Jens Chluba, Hsiao-Mei Sherry Cho, Steve Choi, Susan Clark, Philip Clarke, Carlo Contaldi, Gabriele Coppi, Nicholas F. Cothard, Kevin Coughlin, Will Coulton, Devin Crichton, Kevin D. Crowley, Kevin T. Crowley, Ari Cukierman, John M. D'Ewart, Rolando Dünner, Tijmen de Haan, Mark Devlin, Simon Dicker, Bradley Dober, Cody J. Duell, Shannon Duff, Adri Duivenvoorden, Jo Dunkley, Hamza El Bouhargani, Josquin Errard, Giulio Fabbian, Stephen Feeney, James Fergusson, Simone Ferraro, Pedro Fluxà, Katherine Freese, Josef C. Frisch, Andrei Frolov, George Fuller, Nicholas Galitzki, Patricio A. Gallardo, Jose Tomas Galvez Ghersi, Jiansong Gao, Eric Gawiser, Martina Gerbino, Vera Gluscevic, Neil Goeckner-Wald, Joseph Golec, Sam Gordon, Megan Gralla, Daniel Green, Arpi Grigorian, John Groh, Chris Groppi, Yilun Guan, Jon E. Gudmundsson, Mark Halpern, Dongwon Han, Peter Hargrave, Kathleen Harrington, Masaya Hasegawa, Matthew Hasselfield, Makoto Hattori, Victor Haynes, Masashi Hazumi, Erin

Healy, Shawn W. Henderson, Brandon Hensley, Carlos Hervias-Caimapo, Charles A. Hill, J. Colin Hill, Gene Hilton, Matt Hilton, Adam D. Hincks, Gary Hinshaw, Renée Hložek, Shirley Ho, Shuay-Pwu Patty Ho, Thuong D. Hoang, Jonathan Hoh, Selim C. Hotinli, Zhiqi Huang, Johannes Hubmayr, Kevin Huffenberger, John P. Hughes, Anna Iijas, Margaret Ikape, Kent Irwin, Andrew H. Jaffe, Bhuvnesh Jain, Oliver Jeong, Matthew Johnson, Daisuke Kaneko, Ethan D. Karpel, Nobuhiko Katayama, Brian Keating, Reijo Keskitalo, Theodore Kisner, Kenji Kiuchi, Jeff Klein, Kenda Knowles, Anna Kofman, Brian Koopman, Arthur Kosowsky, Nicoletta Krachmalnicoff, Akito Kusaka, Phil LaPlante, Jacob Lashner, Adrian Lee, Eunseong Lee, Antony Lewis, Yaqiong Li, Zack Li, Michele Limon, Eric Linder, Jia Liu, Carlos Lopez-Caraballo, Thibaut Louis, Marius Lungu, Mathew Madhavacheril, Daisy Mak, Felipe Maldonado, Hamdi Mani, Ben Mates, Frederick Matsuda, Loïc Maurin, Phil Mauskopf, Andrew May, Niall McCallum, Heather McCarrick, Chris McKenney, Jeff McMahon, P. Daniel Meerburg, James Mertens, Joel Meyers, Amber Miller, Mark Mirmelstein, Kavilan Moodley, Jenna Moore, Moritz Munchmeyer, Charles Munson, Masaaki Murata, Sigurd Naess, Toshiya Namikawa, Federico Nati, Martin Navaroli, Laura Newburgh, Ho Nam Nguyen, Andrina Nicola, Mike Niemack, Haruki Nishino, Yume Nishinomiya, John Orlowski-Scherer, Luca Pagano, Bruce Partridge, Francesca Perrotta, Phumlani Phakathi, Lucio Piccirillo, Elena Pierpaoli, Giampaolo Pisano, Davide Poletti, Roberto Puddu, Giuseppe Puglisi, Chris Raum, Christian L. Reichardt, Mathieu Remazeilles, Yoel Rephaeli, Dominik Riechers, Felipe Rojas, Aditya Rotti, Anirban Roy, Sharon Sadeh, Yuki Sakurai, Maria Salatino, Mayuri Sathyaranayana Rao, Lauren Saunders, Emmanuel Schaan, Marcel Schmittfull, Neelima Sehgal, Joseph Seib-

ert, Uros Seljak, Paul Shellard, Blake Sherwin, Meir Shimon, Carlos Sierra, Jonathan Sievers, Cristobal Sifon, Precious Sikhosana, Maximiliano Silva-Feaver, Sara M. Simon, Adrian Sinclair, Kendrick Smith, Wuhyun Sohn, Rita Sonka, David Spergel, Jacob Spisak, Suzanne T. Staggs, George Stein, Jason R. Stevens, Radek Stompor, Aritoki Suzuki, Osamu Tajima, Satoru Takakura, Grant Teply, Daniel B. Thomas, Ben Thorne, Robert Thornton, Hy Trac, Jesse Treu, Calvin Tsai, Carole Tucker, Joel Ullom, Sunny Vagnozzi, Alexander van Engelen, Jeff Van Lanen, Daniel D. Van Winkle, Eve M. Vavagiakis, Clara Vergès, Michael Vissers, Kasey Wagoner, Samantha Walker, Yuhan Wang, Jon Ward, Ben Westbrook, Nathan Whitehorn, Jason Williams, Joel Williams, Edward Wollack, Zhilei Xu, Siavash Yasini, Edward Young, Byeonghee Yu, Cyndia Yu, Fernando Zago, Mario Zannoni, Hezi Zhang, Kaiwen Zheng, Ningfeng Zhu, and Andrea Zonca. The Simons Observatory: Astro2020 Decadal Project Whitepaper. *arXiv:1907.08284 [astro-ph]*, July 2019. arXiv: 1907.08284.

- [31] Filippo Costa, Agostino Monorchio, and Giuliano Manara. An Overview of Equivalent Circuit Modeling Techniques of Frequency Selective Surfaces and Metasurfaces. *Applied Computational Electromagnetics Society Journal*, 29, December 2014.
- [32] N. F. Cothard, S. K. Choi, C. J. Duell, T. Herter, J. Hubmayr, J. McMahon, M. D. Niemack, T. Nikola, C. Sierra, G. J. Stacey, E. M. Vavagiakis, E. J. Wollack, and B. Zou. The Design of the CCAT-prime Epoch of Reionization Spectrometer Instrument. *Journal of Low Temperature Physics*, 199(3):898–907, May 2020.
- [33] Nicholas F. Cothard, Aamir M. Ali, Jason E. Austermann, Steve K. Choi,

Kevin T. Crowley, Bradley J. Dober, Cody J. Duell, Shannon M. Duff, Patricio Gallardo, Gene C. Hilton, Shuay-Pwu Patty Ho, Johannes Hubmayr, Michael D. Niemack, Rita F. Sonka, Suzanne T. Staggs, Eve M. Vavagiakis, Edward J. Wollack, and Zhilei Xu. Comparing complex impedance and bias step measurements of Simons Observatory transition edge sensors. In *Millimeter, Submillimeter, and Far-Infrared Detectors and Instrumentation for Astronomy X*, volume 11453, page 1145325. International Society for Optics and Photonics, December 2020.

- [34] K. Coughlin. *Metamaterial Optics for Precision Cosmic Microwave Background Observation*. Ph.D., University of Michigan, 2018.
- [35] Kevin T. Crowley. *In Search of Inflation: Tools for Cosmic Microwave Background Polarimetry*. {Ph.D Thesis}, Princeton University, 2018.
- [36] Kevin T. Crowley, Jason E. Austermann, Steve K. Choi, Shannon M. Duff, Patricio A. Gallardo, Shuay-Pwu Patty Ho, Johannes Hubmayr, Brian J. Koopman, Federico Nati, Michael D. Niemack, Maria Salatino, Sara M. Simon, Suzanne T. Staggs, Jason R. Stevens, Joel N. Ullom, Eve M. Vavagiakis, and Edward J. Wollack. Advanced ACTPol TES Device Parameters and Noise Performance in Fielded Arrays. *Journal of Low Temperature Physics*, 193(3-4):328–336, November 2018. arXiv: 1807.07496.
- [37] A. Dalgarno and R. A. McCray. Heating and Ionization of HI Regions. *Annual Review of Astronomy and Astrophysics*, 10:375, 1972.
- [38] R. Datta, J. Austermann, J. A. Beall, D. Becker, K. P. Coughlin, S. M. Duff, P. A. Gallardo, E. Grace, M. Hasselfield, S. W. Henderson, G. C. Hilton, S. P. Ho, J. Hubmayr, B. J. Koopman, J. V. Lanen, D. Li, J. McMahon, C. D. Munson, F. Nati, M. D. Niemack, L. Page, C. G. Pappas, M. Salatino,

B. L. Schmitt, A. Schillaci, S. M. Simon, S. T. Staggs, J. R. Stevens, E. M. Vavagiakis, J. T. Ward, and E. J. Wollack. Design and Deployment of a Multichroic Polarimeter Array on the Atacama Cosmology Telescope. *Journal of Low Temperature Physics*, 184(3):568–575, August 2016.

- [39] R. Datta, C. D. Munson, M. D. Niemack, J. J. McMahon, J. Britton, E. J. Wollack, J. Beall, M. J. Devlin, J. Fowler, P. Gallardo, J. Hubmayr, K. Irwin, L. Newburgh, J. P. Nibarger, L. Page, M. A. Quijada, B. L. Schmitt, S. T. Staggs, R. Thornton, and L. Zhang. Large-aperture wide-bandwidth antireflection-coated silicon lenses for millimeter wavelengths. *Applied Optics*, 52(36):8747–8758, December 2013.
- [40] Fabien Defrance, Cecile Jung-Kubiak, Jack Sayers, Jake Connors, Clare deYoung, Matthew I. Hollister, Hiroshige Yoshida, Goutam Chattopadhyay, Sunil R. Golwala, and Simon J. E. Radford. 1.6:1 bandwidth two-layer antireflection structure for silicon matched to the 190-310 GHz atmospheric window. *Applied Optics*, 57(18):5196–5209, June 2018.
- [41] R. H. Dicke, P. J. E. Peebles, P. G. Roll, and D. T. Wilkinson. Cosmic Black-Body Radiation. *The Astrophysical Journal*, 142:414–419, July 1965.
- [42] S. R. Dicker, P. A. Gallardo, J. E. Gudmundsson, P. D. Mauskopf, A. Ali, P. C. Ashton, G. Coppi, M. J. Devlin, N. Galitzki, S. P. Ho, C. A. Hill, J. Hubmayr, B. Keating, A. T. Lee, M. Limon, F. Matsuda, J. McMahon, M. D. Niemack, J. L. Orlowski-Scherer, L. Piccirillo, M. Salatino, S. M. Simon, S. T. Staggs, R. Thornton, J. N. Ullom, E. M. Vavagiakis, E. J. Wollack, Z. Xu, and N. Zhu. Cold optical design for the large aperture Simons’ Observatory telescope. In *Ground-based and Airborne Telescopes VII*, vol-

ume 10700, page 107003E. International Society for Optics and Photonics, July 2018.

- [43] Azadeh Moradinezhad Dizgah and Garrett K. Keating. Line intensity mapping with [CII] and CO(1-0) as probes of primordial non-Gaussianity. *The Astrophysical Journal*, 872(2):126, February 2019. arXiv: 1810.02850.
- [44] B. Dober, Z. Ahmed, K. Arnold, D. T. Becker, D. A. Bennett, J. A. Connors, A. Cukierman, J. M. D'Ewart, S. M. Duff, J. E. Dusatko, J. C. Frisch, J. D. Gard, S. W. Henderson, R. Herbst, G. C. Hilton, J. Hubmayr, Y. Li, J. a. B. Mates, H. McCarrick, C. D. Reintsema, M. Silva-Feaver, L. Ruckman, J. N. Ullom, L. R. Vale, D. D. Van Winkle, J. Vasquez, Y. Wang, E. Young, C. Yu, and K. Zheng. A microwave SQUID multiplexer optimized for bolometric applications. *Applied Physics Letters*, 118(6):062601, February 2021. Publisher: American Institute of Physics.
- [45] Scott Dodelson. *Modern Cosmology*. Academic Press, San Diego, Calif., 2003.
- [46] Olivier Doré, Jamie Bock, Matthew Ashby, Peter Capak, Asantha Cooray, Roland de Putter, Tim Eifler, Nicolas Flagey, Yan Gong, Salman Habib, Katrin Heitmann, Chris Hirata, Woong-Seob Jeong, Raj Katti, Phil Korngut, Elisabeth Krause, Dae-Hee Lee, Daniel Masters, Phil Mauskopf, Gary Melnick, Bertrand Mennesson, Hien Nguyen, Karin Öberg, Anthony Pullen, Alvise Raccanelli, Roger Smith, Yong-Seon Song, Volker Tolls, Steve Unwin, Tejaswi Venumadhav, Marco Viero, Mike Werner, and Mike Zemcov. Cosmology with the SPHEREX All-Sky Spectral Survey. *arXiv:1412.4872 [astro-ph]*, December 2014. arXiv: 1412.4872.
- [47] Cody J. Duell, Eve M. Vavagiakis, Jason Austermann, Scott C. Chapman,

Steve K. Choi, Nicholas F. Cothard, Brad Dober, Patricio Gallardo, Jiansong Gao, Christopher Groppi, Terry L. Herter, Gordon J. Stacey, Zachary Huber, Johannes Hubmayr, Doug Johnstone, Yaqiong Li, Philip Mauskopf, Jeff McMahon, Michael D. Niemack, Thomas Nikola, Kayla Rossi, Sara Simon, Adrian K. Sinclair, Michael Vissers, Jordan Wheeler, and Bugao Zou. CCAT-prime: Designs and status of the first light 280 GHz MKID array and mod-cam receiver. In *Millimeter, Submillimeter, and Far-Infrared Detectors and Instrumentation for Astronomy X*, volume 11453, page 114531F. International Society for Optics and Photonics, December 2020.

- [48] S. M. Duff, J. Austermann, J. A. Beall, D. Becker, R. Datta, P. A. Gallardo, S. W. Henderson, G. C. Hilton, S. P. Ho, J. Hubmayr, B. J. Koopman, D. Li, J. McMahon, F. Nati, M. D. Niemack, C. G. Pappas, M. Salatino, B. L. Schmitt, S. M. Simon, S. T. Staggs, J. R. Stevens, J. Van Lanen, E. M. Vavagiakis, J. T. Ward, and E. J. Wollack. Advanced ACTPol Multichroic Polarimeter Array Fabrication Process for 150 mm Wafers. *Journal of Low Temperature Physics*, 184(3-4):634–641, August 2016.
- [49] Alexander van Engelen, Blake D. Sherwin, Neelima Sehgal, Graeme E. Addison, Rupert Allison, Nick Battaglia, Francesco de Bernardis, J. Richard Bond, Erminia Calabrese, Kevin Coughlin, Devin Crichton, Rahul Datta, Mark J. Devlin, Joanna Dunkley, Rolando Dünner, Patricio Gallardo, Emily Grace, Megan Gralla, Amir Hajian, Matthew Hasselfield, Shawn Henderson, J. Colin Hill, Matt Hilton, Adam D. Hincks, Renée Hlozek, Kevin M. Huffenberger, John P. Hughes, Brian Koopman, Arthur Kosowsky, Thibaut Louis, Marius Lungu, Mathew Madhavacheril, Loïc Maurin, Jeff McMahon, Kavilan Moodley, Charles Munson, Sigurd Naess, Federico Nati, Laura Newburgh, Michael D. Niemack, Michael R. Nolta, Lyman A. Page, Christine Pappas,

Bruce Partridge, Benjamin L. Schmitt, Jonathan L. Sievers, Sara Simon, David N. Spergel, Suzanne T. Staggs, Eric R. Switzer, Jonathan T. Ward, and Edward J. Wollack. The Atacama Cosmology Telescope: Lensing of CMB Temperature and Polarization Derived from Cosmic Infrared Background Cross-Correlation. *The Astrophysical Journal*, 808(1):7, July 2015. Publisher: American Astronomical Society.

- [50] Xiaohui Fan, C. L. Carilli, and B. Keating. Observational constraints on Cosmic Reionization. *Annual Review of Astronomy and Astrophysics*, 44(1):415–462, September 2006. arXiv: astro-ph/0602375.
- [51] Enectali Figueroa Feliciano. *Theory and development of position-sensitive quantum calorimeters*. Ph.D., Stanford University, United States – California, 2001. ISBN: 9780493403885.
- [52] D. J. Fixsen. The Temperature of the Cosmic Microwave Background. *The Astrophysical Journal*, 707(2):916–920, December 2009. arXiv: 0911.1955.
- [53] D. J. Fixsen, E. S. Cheng, J. M. Gales, J. C. Mather, R. A. Shafer, and E. L. Wright. The Cosmic Microwave Background Spectrum from the Full COBE* FIRAS Data Set. *The Astrophysical Journal*, 473(2):576, December 1996. Publisher: IOP Publishing.
- [54] J. W. Fowler, M. D. Niemack, S. R. Dicker, A. M. Aboobaker, P. a. R. Ade, E. S. Battistelli, M. J. Devlin, R. P. Fisher, M. Halpern, P. C. Hargrave, A. D. Hincks, M. Kaul, J. Klein, J. M. Lau, M. Limon, T. A. Marriage, P. D. Mauskopf, L. Page, S. T. Staggs, D. S. Swetz, E. R. Switzer, R. J. Thornton, and C. E. Tucker. Optical design of the Atacama Cosmology Telescope and the Millimeter Bolometric Array Camera. *Applied Optics*, 46(17):3444–3454, June 2007. Publisher: Optical Society of America.

- [55] A. Friedman. On the Curvature of Space. *General Relativity and Gravitation*, 31(12):1991–2000, December 1999.
- [56] Nicholas Galitzki, Aamir Ali, Kam S. Arnold, Peter C. Ashton, Jason E. Austermann, Carlo Baccigalupi, Taylor Baildon, Darcy Barron, James A. Beall, Shawn Beckman, Sarah Marie M. Bruno, Sean Bryan, Paolo G. Calisse, Grace E. Chesmore, Yuji Chinone, Steve K. Choi, Gabriele Coppi, Kevin D. Crowley, Kevin T. Crowley, Ari Cukierman, Mark J. Devlin, Simon Dicker, Bradley Dober, Shannon M. Duff, Jo Dunkley, Giulio Fabbian, Patricio A. Gallardo, Martina Gerbino, Neil Goeckner-Wald, Joseph E. Golec, Jon E. Gudmundsson, Erin E. Healy, Shawn Henderson, Charles A. Hill, Gene C. Hilton, Shuay-Pwu Patty Ho, Logan A. Howe, Johannes Hubmayr, Oliver Jeong, Brian Keating, Brian J. Koopman, Kenji Kiuchi, Akito Kusaka, Jacob Lashner, Adrian T. Lee, Yaqiong Li, Michele Limon, Marius Lungu, Frederick Matsuda, Philip D. Mauskopf, Andrew J. May, Nialh McCallum, Jeff McMahon, Federico Nati, Michael D. Niemack, John L. Orlowski-Scherer, Stephen C. Parshley, Lucio Piccirillo, Mayuri Sathyanarayana Rao, Christopher Raum, Maria Salatino, Joseph S. Seibert, Carlos Sierra, Max Silva-Feaver, Sara M. Simon, Suzanne T. Staggs, Jason R. Stevens, Aritoki Suzuki, Grant Teply, Robert Thornton, Calvin Tsai, Joel N. Ullom, Eve M. Vavagiakis, Michael R. Vissers, Benjamin Westbrook, Edward J. Wollack, Zhilei Xu, and Ningfeng Zhu. The Simons Observatory: instrument overview. In *Millimeter, Submillimeter, and Far-Infrared Detectors and Instrumentation for Astronomy IX*, volume 10708, page 1070804. International Society for Optics and Photonics, July 2018.
- [57] P. A. Gallardo, M. D. Niemack, J. E. Austermann, J. Beall, N. F. Cothard, C. J. Duell, S. M. Duff, S. W. Henderson, G. C. Hilton, S. P. Ho, J. Hubmayr,

C. D. Reintsema, M. Salatino, J. N. Ullom, J. Van Lanen, M. R. Vissers, and E. J. Wollack. Characterization of Aliased Noise in the Advanced ACTPol Receiver. *Journal of Low Temperature Physics*, 199(3):762–770, May 2020.

- [58] Patricio Gallardo, Rolando Dünner, Edward Wollack, Fernando Henriquez, and Carlos Jerez-Hanckes. Mirror illumination and spillover measurements of the Atacama Cosmology Telescope. In *Millimeter, Submillimeter, and Far-Infrared Detectors and Instrumentation for Astronomy VI*, volume 8452, page 845224. International Society for Optics and Photonics, September 2012.
- [59] Patricio A. Gallardo, Nicholas F. Cothard, Roberto Puddu, Rolando Dünner, Brian J. Koopman, Michael D. Niemack, Sara M. Simon, and Edward J. Wollack. Far sidelobes from baffles and telescope support structures in the Atacama Cosmology Telescope. In *Millimeter, Submillimeter, and Far-Infrared Detectors and Instrumentation for Astronomy IX*, volume 10708, page 107082L. International Society for Optics and Photonics, August 2018.
- [60] Patricio A. Gallardo, Jon Gudmundsson, Brian J. Koopman, Frederick T. Matsuda, Sara M. Simon, Aamir Ali, Sean Bryan, Yuji Chinone, Gabriele Coppi, Nicholas Cothard, Mark J. Devlin, Simon Dicker, Giulio Fabbian, Nicholas Galitzki, Charles A. Hill, Brian Keating, Akito Kusaka, Jacob Lashner, Adrian T. Lee, Michele Limon, Philip D. Mauskopf, Jeff McMahon, Federico Nati, Michael D. Niemack, John L. Orlowski-Scherer, Stephen C. Parshley, Giuseppe Puglisi, Christian L. Reichardt, Maria Salatino, Suzanne Staggs, Aritoki Suzuki, Eve M. Vavagiakis, Edward J. Wollack, Zhilei Xu, and Ningfeng Zhu. Systematic uncertainties in the Simons Observatory: optical effects and sensitivity considerations. In *Millimeter, Submillimeter,*

and Far-Infrared Detectors and Instrumentation for Astronomy IX, volume 10708, page 107083Y. International Society for Optics and Photonics, August 2018.

- [61] Patricio A. Gallardo, Brian J. Koopman, Nicholas F. Cothard, Sarah Marie M. Bruno, German Cortes-Medellin, Galen Marchetti, Kevin H. Miller, Brenna Mockler, Michael D. Niemack, Gordon Stacey, and Edward J. Wollack. Deep reactive ion etched anti-reflection coatings for sub-millimeter silicon optics. *Applied Optics*, 56(10):2796–2803, April 2017.
- [62] Patricio Andres Gallardo Matamala. *Optimizing future CMB observatories and measuring galaxy cluster motions with the Atacama Cosmology Telescope*. Ph.D., Cornell University, United States – New York, December 2019.
Accepted: 2020-06-23T18:02:56Z.
- [63] E. M. George, J. E. Austermann, J. A. Beall, D. Becker, B. A. Benson, L. E. Bleem, J. E. Carlstrom, C. L. Chang, H.-M. Cho, A. T. Crites, M. A. Dobbs, W. Everett, N. W. Halverson, J. W. Henning, G. C. Hilton, W. L. Holzapfel, J. Hubmayr, K. D. Irwin, D. Li, M. Lueker, J. J. McMahon, J. Mehl, J. Montgomery, T. Natoli, J. P. Nibarger, M. D. Niemack, V. Novosad, J. E. Ruhl, J. T. Sayre, E. Shirokoff, K. T. Story, G. Wang, V. Yefremenko, K. W. Yoon, and E. Young. A Study of Al–Mn Transition Edge Sensor Engineering for Stability. *Journal of Low Temperature Physics*, 176(3):383–391, August 2014.
- [64] Joseph E. Golec, Jeffrey J. McMahon, Aamire Ali, Simon Dicker, Nicholas Galitzki, Kathleen Harrington, Benjamin Westbrook, Edward J. Wollack, Zhilei Xu, and Ningfeng Zhu. Design and fabrication of metamaterial anti-reflection coatings for the Simons Observatory. In *Advances in Optical*

and Mechanical Technologies for Telescopes and Instrumentation IV, volume 11451, page 114515T. International Society for Optics and Photonics, December 2020.

- [65] Yilun Guan, Susan E. Clark, Brandon S. Hensley, Patricio A. Gallardo, Sigurd Naess, Cody J. Duell, Simone Aiola, Zachary Atkins, Erminia Calabrese, Steve K. Choi, Nicholas F. Cothard, Mark Devlin, Adriaan J. Duivenvoorden, Jo Dunkley, Rolando Dünner, Simone Ferraro, Matthew Hasselfield, John P. Hughes, Brian J. Koopman, Arthur B. Kosowsky, Mathew S. Madhavacheril, Jeff McMahon, Federico Nati, Michael D. Niemack, Lyman A. Page, Maria Salatino, Emmanuel Schaan, Neelima Sehgal, Cristóbal Sifón, Suzanne Staggs, Eve M. Vavagiakis, Edward J. Wollack, and Zhilei Xu. The Atacama Cosmology Telescope: Microwave Intensity and Polarization Maps of the Galactic Center. *arXiv:2105.05267 [astro-ph]*, May 2021. arXiv: 2105.05267.
- [66] Jon E. Gudmundsson, Patricio A. Gallardo, Roberto Puddu, Simon R. Dicker, Alexandre E. Adler, Aamir M. Ali, Andrew Bazarko, Grace E. Chesmore, Gabriele Coppi, Nicholas F. Cothard, Nadia Dachlythra, Mark Devlin, Rolando Dünner, Giulio Fabbian, Nicholas Galitzki, Joseph E. Golec, Shuay-Pwu Patty Ho, Peter C. Hargrave, Anna M. Kofman, Adrian T. Lee, Michele Limon, Frederick T. Matsuda, Philip D. Mauskopf, Kavilan Moodley, Federico Nati, Michael D. Niemack, John Orlowski-Scherer, Lyman A. Page, Bruce Partridge, Giuseppe Puglisi, Christian L. Reichardt, Carlos E. Sierra, Sara M. Simon, Grant P. Teply, Carole Tucker, Edward J. Wollack, Zhilei Xu, and Ningfeng Zhu. The Simons Observatory: Modeling Optical Systematics in the Large Aperture Telescope. *arXiv:2009.10138 [astro-ph]*, September 2020. arXiv: 2009.10138.

- [67] Matthew Hasselfield, Kavilan Moodley, J. Richard Bond, Sudeep Das, Mark J. Devlin, Joanna Dunkley, Rolando Dünner, Joseph W. Fowler, Patricio Gallardo, Megan B. Gralla, Amir Hajian, Mark Halpern, Adam D. Hincks, Tobias A. Marriage, Danica Marsden, Michael D. Niemack, Michael R. Nolta, Lyman A. Page, Bruce Partridge, Benjamin L. Schmitt, Neelima Sehgal, Jon Sievers, Suzanne T. Staggs, Daniel S. Swetz, Eric R. Switzer, and Edward J. Wollack. The Atacama Cosmology Telescope: Beam Measurements and the Microwave Brightness Temperatures of Uranus and Saturn. *The Astrophysical Journal Supplement Series*, 209(1):17, October 2013. Publisher: American Astronomical Society.
- [68] William M. Haynes, Thomas J. Bruno, and David R. Lide, editors. *CRC handbook of chemistry and physics: a ready-reference book of chemical and physical data*. CRC Press, Boca Raton, 97th edition. edition, 2016.
- [69] Erin Healy, Aamir M. Ali, Kam Arnold, Jason E. Austermann, James A. Beall, Sarah Marie Bruno, Steve K. Choi, Jake Connors, Nicholas F. Cothard, Bradley Dober, Shannon M. Duff, Nicholas Galitzki, Gene Hilton, Shuay-Pwu Patty Ho, Johannes Hubmayr, Bradley R. Johnson, Yaqiong Li, Michael J. Link, Tammy J. Lucas, Heather McCarrick, Michael D. Niemack, Maximiliano Silva-Feaver, Rita F. Sonka, Suzanne Staggs, Eve M. Vavagiakis, Michael R. Vissers, Yuhan Wang, Edward J. Wollack, Zhilei Xu, Benjamin Westbrook, and Kaiwen Zheng. Assembly development for the Simons Observatory focal plane readout module. In *Millimeter, Submillimeter, and Far-Infrared Detectors and Instrumentation for Astronomy X*, volume 11453, page 1145317. International Society for Optics and Photonics, December 2020.

- [70] S. W. Henderson, R. Allison, J. Austermann, T. Baildon, N. Battaglia, J. A. Beall, D. Becker, F. De Bernardis, J. R. Bond, E. Calabrese, S. K. Choi, K. P. Coughlin, K. T. Crowley, R. Datta, M. J. Devlin, S. M. Duff, J. Dunkley, R. Dünner, A. van Engelen, P. A. Gallardo, E. Grace, M. Hasselfield, F. Hills, G. C. Hilton, A. D. Hincks, R. Hlozek, S. P. Ho, J. Hubmayr, K. Huffenberger, J. P. Hughes, K. D. Irwin, B. J. Koopman, A. B. Kosowsky, D. Li, J. McMahon, C. Munson, F. Nati, L. Newburgh, M. D. Niemack, P. Niraula, L. A. Page, C. G. Pappas, M. Salatino, A. Schillaci, B. L. Schmitt, N. Sehgal, B. D. Sherwin, J. L. Sievers, S. M. Simon, D. N. Spergel, S. T. Staggs, J. R. Stevens, R. Thornton, J. Van Lanen, E. M. Vavagiakis, J. T. Ward, and E. J. Wollack. Advanced ACTPol Cryogenic Detector Arrays and Readout. *Journal of Low Temperature Physics*, 184(3):772–779, August 2016.
- [71] Shawn W. Henderson, Zeeshan Ahmed, Jason Austermann, Daniel Becker, Douglas A. Bennett, David Brown, Saptarshi Chaudhuri, Hsiao-Mei Sherry Cho, John M. D’Ewart, Bradley Dober, Shannon M. Duff, John E. Dusatko, Sofia Fatigoni, Josef C. Frisch, Jonathon D. Gard, Mark Halpern, Gene C. Hilton, Johannes Hubmayr, Kent D. Irwin, Ethan D. Karpel, Sarah S. Kerinasovskiy, Stephen E. Kuenstner, Chao-Lin Kuo, Dale Li, John A. B. Mates, Carl D. Reintsema, Stephen R. Smith, Joel Ullom, Leila R. Vale, Daniel D. Van Winkle, Michael Vissers, and Cyndia Yu. Highly-multiplexed microwave SQUID readout using the SLAC Microresonator Radio Frequency (SMuRF) electronics for future CMB and sub-millimeter surveys. In *Millimeter, Submillimeter, and Far-Infrared Detectors and Instrumentation for Astronomy IX*, volume 10708, page 1070819. International Society for Optics and Photonics, July 2018.
- [72] Shawn W. Henderson, Jason R. Stevens, Mandana Amiri, Jason Auster-

mann, James A. Beall, Saptarshi Chaudhuri, Hsiao-Mei Cho, Steve K. Choi, Nicholas F. Cothard, Kevin T. Crowley, Shannon M. Duff, Colin P. Fitzgerald, Patricio A. Gallardo, Mark Halpern, Matthew Hasselfield, Gene Hilton, Shuay-Pwu Patty Ho, Johannes Hubmayr, Kent D. Irwin, Brian J. Koopman, Dale Li, Yaqiong Li, Jeff McMahon, Federico Nati, Michael Niemack, Carl D. Reintsema, Maria Salatino, Alessandro Schillaci, Benjamin L. Schmitt, Sara M. Simon, Suzanne T. Staggs, Eve M. Vavagiakis, and Jonathan T. Ward. Readout of two-kilopixel transition-edge sensor arrays for Advanced ACTPol. In *Millimeter, Submillimeter, and Far-Infrared Detectors and Instrumentation for Astronomy VIII*, volume 9914, page 99141G. International Society for Optics and Photonics, July 2016.

- [73] C. A. Hill, A. Kusaka, P. Ashton, P. Barton, T. Adkins, K. Arnold, B. Bixler, S. Ganjam, A. T. Lee, F. Matsuda, T. Matsumura, Y. Sakurai, R. Tat, and Y. Zhou. A cryogenic continuously rotating half-wave plate for the POLARBEAR-2b cosmic microwave background receiver. *Review of Scientific Instruments*, 91(12):124503, December 2020. arXiv: 2009.03972.
- [74] Charles A. Hill, Sarah Marie M. Bruno, Sara M. Simon, Aamir Ali, Kam S. Arnold, Peter C. Ashton, Darcy Barron, Sean Bryan, Yuji Chinone, Gabriele Coppi, Kevin T. Crowley, Ari Cukierman, Simon Dicker, Jo Dunkley, Giulio Fabbian, Nicholas Galitzki, Patricio A. Gallardo, Jon E. Gudmundsson, Johannes Hubmayr, Brian Keating, Akito Kusaka, Adrian T. Lee, Frederick Matsuda, Philip D. Mauskopf, Jeffrey McMahon, Michael D. Niemack, Giuseppe Puglisi, Mayuri Sathyaranayana Rao, Maria Salatino, Carlos Sierra, Suzanne Staggs, Aritoki Suzuki, Grant Teply, Joel N. Ullom, Benjamin Westbrook, Zhilei Xu, and Ningfeng Zhu. BoloCalc: a sensitivity calculator for the design of Simons Observatory. In *Millimeter, Submillimeter,*

and Far-Infrared Detectors and Instrumentation for Astronomy IX, volume 10708, page 1070842. International Society for Optics and Photonics, July 2018.

- [75] Shuay-Pwu Patty Ho, Jason Austermann, James A. Beall, Steve K. Choi, Nicholas F. Cothard, Kevin T. Crowley, Rahul Datta, Mark J. Devlin, Shannon M. Duff, Patricio A. Gallardo, Matthew Hasselfield, Shawn W. Henderson, Gene Hilton, Johannes Hubmayr, Brian J. Koopman, Yaqiong Li, Jeffrey McMahon, Michael D. Niemack, Maria Salatino, Sara M. Simon, Suzanne T. Staggs, Jonathan T. Ward, Joel N. Ullom, Eve M. Vavagiakis, and Edward J. Wollack. Highly uniform 150 mm diameter multichroic polarimeter array deployed for CMB detection. In *Millimeter, Submillimeter, and Far-Infrared Detectors and Instrumentation for Astronomy VIII*, volume 9914, page 991418. International Society for Optics and Photonics, March 2017.
- [76] Edwin Hubble. A relation between distance and radial velocity among extra-galactic nebulae. *Proceedings of the National Academy of Sciences*, 15(3):168–173, March 1929.
- [77] K. D. Irwin, G. C. Hilton, D. A. Wollman, and John M. Martinis. Thermal-response time of superconducting transition-edge microcalorimeters. *Journal of Applied Physics*, 83(8):3978–3985, April 1998.
- [78] K.D. Irwin and G.C. Hilton. Transition-Edge Sensors. In Christian Enss, editor, *Cryogenic Particle Detection*, Topics in Applied Physics, pages 63–150. Springer, Berlin, Heidelberg, 2005.
- [79] F. James and M. Roos. Minuit - a system for function minimization and

analysis of the parameter errors and correlations. *Computer Physics Communications*, 10(6):343–367, December 1975.

- [80] O. Jeong, A. Lee, C. Raum, and A. Suzuki. Broadband Plasma-Sprayed Anti-reflection Coating for Millimeter-Wave Astrophysics Experiments. *Journal of Low Temperature Physics*, 184(3):621–626, August 2016.
- [81] Marc Kamionkowski and Ely D. Kovetz. The Quest for B Modes from Inflationary Gravitational Waves. *Annual Review of Astronomy and Astrophysics*, 54(1):227–269, September 2016. Publisher: Annual Reviews.
- [82] Christos Karoumpis. 2019 in Prep.
- [83] Kenji Kiuchi, Shunsuke Adachi, Aamir M. Ali, Kam Arnold, Peter Ashton, Jason E. Austermann, Andrew Bazako, James A. Beall, Yuji Chinone, Gabriele Coppi, Kevin D. Crowley, Kevin T. Crowley, Simon Dicker, Bradley Dober, Shannon M. Duff, Giulio Fabbian, Nicholas Galitzki, Joseph E. Golec, Jon E. Gudmundsson, Kathleen Harrington, Masaya Hasegawa, Makoto Hattori, Charles A. Hill, Shuay-Pwu Patty Ho, Johannes Hubmayr, Bradley R. Johnson, Daisuke Kaneko, Nobuhiko Katayama, Brian Keating, Akito Kusaka, Jack Lashner, Adrian T. Lee, Frederick Matsuda, Heather McCarrick, Masaaki Murata, Federico Nati, Yume Nishinomiya, Lyman Page, Mayuri Sathyaranayana Rao, Christian L. Reichardt, Kana Sakaguri, Yuki Sakurai, Joseph Sibert, Jacob Spisak, Osamu Tajima, Grant P. Teply, Tomoki Terasaki, Tran Tsan, Samantha Walker, Edward J. Wollack, Zhilei Xu, Kyohei Yamada, Mario Zannoni, and Ningfeng Zhu. Simons Observatory Small Aperture Telescope overview. In *Ground-based and Airborne Telescopes VIII*, volume 11445, page 114457L. International Society for Optics and Photonics, December 2020.

- [84] B. J. Koopman, N. F. Cothard, S. K. Choi, K. T. Crowley, S. M. Duff, S. W. Henderson, S. P. Ho, J. Hubmayr, P. A. Gallardo, F. Nati, M. D. Niemack, S. M. Simon, S. T. Staggs, J. R. Stevens, E. M. Vavagiakis, and E. J. Wollack. Advanced ACTPol Low-Frequency Array: Readout and Characterization of Prototype 27 and 39 GHz Transition Edge Sensors. *Journal of Low Temperature Physics*, 193(5):1103–1111, December 2018.
- [85] Ely D. Kovetz, Patrick C. Breysse, Adam Lidz, Jamie Bock, Charles M. Bradford, Tzu-Ching Chang, Simon Foreman, Hamsa Padmanabhan, Anthony Pullen, Dominik Reichers, Marta B. Silva, and Eric Switzer. Astrophysics and Cosmology with Line-Intensity Mapping. *arXiv:1903.04496 [astro-ph]*, March 2019. arXiv: 1903.04496.
- [86] Ely D. Kovetz, Marco P. Viero, Adam Lidz, Laura Newburgh, Mubdi Rahaman, Eric Switzer, Marc Kamionkowski, James Aguirre, Marcelo Alvarez, James Bock, J. Richard Bond, Geoffry Bower, C. Matt Bradford, Patrick C. Breysse, Philip Bull, Tzu-Ching Chang, Yun-Ting Cheng, Dongwoo Chung, Kieran Cleary, Asantha Corray, Abigail Crites, Rupert Croft, Olivier Doré, Michael Eastwood, Andrea Ferrara, José Fonseca, Daniel Jacobs, Garrett K. Keating, Guilaine Lagache, Gunjan Lakhani, Adrian Liu, Kavilan Moodley, Norm Murray, Aurélie Pénin, Gergö Popping, Anthony Pullen, Dominik Reichers, Shun Saito, Ben Saliwanchik, Mario Santos, Rachel Somerville, Gordon Stacey, George Stein, Francesco Villaescusa-Navarro, Eli Visbal, Amanda Weltman, Laura Wolz, and Micheal Zemcov. Line-Intensity Mapping: 2017 Status Report. *arXiv:1709.09066 [astro-ph]*, September 2017. arXiv: 1709.09066.
- [87] M. Kowalski, D. Rubin, G. Aldering, R. J. Agostinho, A. Amadon, R. Aman-

ullah, C. Balland, K. Barbary, G. Blanc, P. J. Challis, A. Conley, N. V. Connolly, R. Covarrubias, K. S. Dawson, S. E. Deustua, R. Ellis, S. Fabbro, V. Fadeyev, X. Fan, B. Farris, G. Folatelli, B. L. Frye, G. Garavini, E. L. Gates, L. Germany, G. Goldhaber, B. Goldman, A. Goobar, D. E. Groom, J. Haissinski, D. Hardin, I. Hook, S. Kent, A. G. Kim, R. A. Knop, C. Lidman, E. V. Linder, J. Mendez, J. Meyers, G. J. Miller, M. Moniez, A. M. Mourao, H. Newberg, S. Nobili, P. E. Nugent, R. Pain, O. Perdereau, S. Perlmutter, M. M. Phillips, V. Prasad, R. Quimby, N. Regnault, J. Rich, E. P. Rubenstein, P. Ruiz-Lapuente, F. D. Santos, B. E. Schaefer, R. A. Schommer, R. C. Smith, A. M. Soderberg, A. L. Spadafora, L.-G. Strolger, M. Strovink, N. B. Suntzeff, N. Suzuki, R. C. Thomas, N. A. Walton, L. Wang, W. M. Wood-Vasey, and J. L. Yun. Improved Cosmological Constraints from New, Old and Combined Supernova Datasets. *The Astrophysical Journal*, 686(2):749–778, October 2008. arXiv: 0804.4142.

- [88] J. M. Lau, J. W. Fowler, T. A. Marriage, L. Page, J. Leong, E. Wishnow, R. Henry, E. Wollck, M. Halpern, D. Marsden, and G. Marsden. A millimeter-wave antireflection coating for cryogenic silicon lenses. *Applied Optics*, 45(16):3746, June 2006. arXiv: astro-ph/0701091.
- [89] Henrietta S. Leavitt and Edward C. Pickering. Periods of 25 Variable Stars in the Small Magellanic Cloud. *Harvard College Observatory Circular*, 173:1–3, March 1912.
- [90] Adrian Lee, P. a. R. Ade, Y. Akiba, D. Alonso, K. Arnold, J. Aumont, J. Austermann, C. Baccigalupi, A. J. Banday, R. Banerji, R. B. Barreiro, S. Basak, J. Beall, S. Beckman, M. Bersanelli, J. Borrill, F. Boulanger, M. L. Brown, M. Bucher, A. Buzzelli, E. Calabrese, F. J. Casas, A. Challinor,

V. Chan, Y. Chinone, J.-F. Cliche, F. Columbro, A. Cukierman, D. Curtis, P. Danto, P. de Bernardis, T. de Haan, M. De Petris, C. Dickinson, M. Dobbs, T. Dotani, L. Duband, A. Ducout, S. Duff, A. Duivenvoorden, J.-M. Duval, K. Ebisawa, T. Ellefot, H. Enokida, H. K. Eriksen, J. Errard, T. Essinger-Hileman, F. Finelli, R. Flauger, C. Franceschet, U. Fuskeland, K. Ganga, J.-R. Gao, R. Genova-Santos, T. Ghigna, A. Gomez, M. L. Gradziel, J. Grain, F. Grupp, A. Gruppuso, J. E. Gudmundsson, N. W. Halverson, P. Hargrave, T. Hasebe, M. Hasegawa, M. Hattori, M. Hazumi, S. Henrot-Versille, D. Herranz, C. Hill, G. Hilton, Y. Hirota, E. Hivon, R. Hložek, D.-T. Hoang, J. Hubmayr, K. Ichiki, T. Iida, H. Imada, K. Ishimura, H. Ishino, G. C. Jaehnig, M. Jones, T. Kaga, S. Kashima, Y. Kataoka, N. Katayama, T. Kawasaki, R. Keskitalo, A. Kibayashi, T. Kikuchi, K. Kimura, T. Kisner, Y. Kobayashi, N. Kogiso, A. Kogut, K. Kohri, E. Komatsu, K. Komatsu, K. Konishi, N. Krachmalnicoff, C. L. Kuo, N. Kurinsky, A. Kushino, M. Kuwata-Gonokami, L. Lamagna, M. Lattanzi, A. T. Lee, E. Linder, B. Maffei, D. Maino, M. Maki, A. Mangilli, E. Martínez-Gonzalez, S. Masi, R. Mathon, T. Matsumura, A. Mennella, M. Migliaccio, Y. Minami, K. Mistuda, D. Molinari, L. Montier, G. Morgante, B. Mot, Y. Murata, J. A. Murphy, M. Nagai, R. Nagata, S. Nakamura, T. Namikawa, P. Natoli, S. Nerval, T. Nishibori, H. Nishino, Y. Nomura, F. Noviello, C. O'Sullivan, H. Ochi, H. Ogawa, H. Ogawa, H. Ohsaki, I. Ohta, N. Okada, N. Okada, L. Pagano, A. Paiella, D. Paoletti, G. Patanchon, F. Piacentini, G. Pisano, G. Polenta, D. Poletti, T. Prouvé, G. Puglisi, D. Rambaud, C. Raum, S. Realini, M. Remazeilles, G. Roudil, J. A. Rubiño-Martín, M. Russell, H. Sakurai, Y. Sakurai, M. Sandri, G. Savini, D. Scott, Y. Sekimoto, B. D. Sherwin, K. Shinozaki, M. Shiraishi, P. Shirron, G. Signorelli, G. Smecher, P. Spizzi, S. L. Stever, R. Stom-

por, H. Sugai, S. Sugiyama, A. Suzuki, J. Suzuki, E. Switzer, R. Takaku, H. Takakura, S. Takakura, Y. Takeda, A. Taylor, E. Taylor, Y. Terao, K. L. Thompson, B. Thorne, M. Tomasi, H. Tomida, N. Trappe, M. Tristram, M. Tsuji, M. Tsujimoto, C. Tucker, J. Ullom, S. Uozumi, S. Utsunomiya, J. Van Lanen, G. Vermeulen, P. Vielva, F. Villa, M. Vissers, N. Vittorio, F. Voisin, I. Walker, N. Watanabe, I. Wehus, J. Weller, B. Westbrook, B. Winter, E. Wollack, R. Yamamoto, N. Y. Yamasaki, M. Yanagisawa, T. Yoshida, J. Yumoto, M. Zannoni, and A. Zonca. LiteBIRD: an all-sky cosmic microwave background probe of inflation. *Bulletin of the AAS*, 51(7), September 2019. Publisher: PubPub.

- [91] Abbé G. Lemaître. A Homogeneous Universe of Constant Mass and Increasing Radius accounting for the Radial Velocity of Extra-galactic Nebulæ. *Monthly Notices of the Royal Astronomical Society*, 91(5):483–490, March 1931.
- [92] Yaqiong Li, Jason E. Austermann, James A. Beall, Sarah Marie Bruno, Steve K. Choi, Nicholas F. Cothard, Kevin T. Crowley, Shannon M. Duff, Patricio A. Gallardo, Shawn W. Henderson, Shuay-Pwu Patty Ho, Johannes Hubmayr, Brian J. Koopman, Jeff J. McMahon, Michael D. Niemack, Maria Salatino, Sara M. Simon, Suzanne T. Staggs, Jason R. Stevens, Joel N. Ullom, Jonathan Ward, and Edward J. Wollack. Performance of the advanced ACTPol low frequency array. In *Millimeter, Submillimeter, and Far-Infrared Detectors and Instrumentation for Astronomy IX*, volume 10708, page 107080A. International Society for Optics and Photonics, July 2018.
- [93] Adam Lidz, Steven R. Furlanetto, S. Peng Oh, James Aguirre, Tzu-Ching Chang, Olivier Doré, and Jonathan R. Pritchard. Intensity Mapping with

Carbon Monoxide Emission Lines and the Redshifted 21 cm Line. *The Astrophysical Journal*, 741(2):70, November 2011. arXiv: 1104.4800.

- [94] Mark A. Lindeman, Simon Bandler, Regis P. Brekosky, James A. Chervenak, Enectali Figueiroa-Feliciano, Fred M. Finkbeiner, Mary J. Li, and Caroline A. Kilbourne. Impedance measurements and modeling of a transition-edge-sensor calorimeter. *Review of Scientific Instruments*, 75(5):1283–1289, April 2004. Publisher: American Institute of Physics.
- [95] Olli Luukkonen, Constantin Simovski, Gérard Granet, George Goussetis, Dmitri Lioubtchenko, Antti V. Räisänen, and Sergei Tretyakov. Simple and accurate analytical model of planar grids and high-impedance surfaces comprising metal strips or patches. *IEEE Transactions on Antennas and Propagation*, 56(6):1624–1632, June 2008. arXiv: 0705.3548.
- [96] I. J. Maasilta. Complex impedance, responsivity and noise of transition-edge sensors: Analytical solutions for two- and three-block thermal models. *AIP Advances*, 2(4):042110, October 2012. Publisher: American Institute of Physics.
- [97] Mathew S. Madhavacheril, Cristóbal Sifón, Nicholas Battaglia, Simone Aiola, Stefania Amodeo, Jason E. Austermann, James A. Beall, Daniel T. Becker, J. Richard Bond, Erminia Calabrese, Steve K. Choi, Edward V. Denison, Mark J. Devlin, Simon R. Dicker, Shannon M. Duff, Adriaan J. Duivenvoorden, Jo Dunkley, Rolando Dünner, Simone Ferraro, Patricio A. Gallardo, Yilun Guan, Dongwon Han, J. Colin Hill, Gene C. Hilton, Matt Hilton, Johannes Hubmayr, Kevin M. Huffenberger, John P. Hughes, Brian J. Koopman, Arthur Kosowsky, Jeff Van Lanen, Eunseong Lee, Thibaut Louis, Amanda MacInnis, Jeffrey McMahon, Kavilan Moodley, Sigurd Naess,

Toshiya Namikawa, Federico Nati, Laura Newburgh, Michael D. Niemack, Lyman A. Page, Bruce Partridge, Frank J. Qu, Naomi C. Robertson, Maria Salatino, Emmanuel Schaan, Alessandro Schillaci, Benjamin L. Schmitt, Neelima Sehgal, Blake D. Sherwin, Sara M. Simon, David N. Spergel, Suzanne Staggs, Emilie R. Storer, Joel N. Ullom, Leila R. Vale, Alexander van Engelen, Eve M. Vavagiakis, Edward J. Wollack, and Zhilei Xu. The Atacama Cosmology Telescope: Weighing distant clusters with the most ancient light. *The Astrophysical Journal*, 903(1):L13, October 2020. arXiv: 2009.07772.

- [98] Nathan Marcuvitz. *Waveguide handbook*. P. Peregrinus on behalf of the Institution of Electrical Engineers, London, UK, 1986.
- [99] J. C. Mather, D. J. Fixsen, R. A. Shafer, C. Mosier, and D. T. Wilkinson. Calibrator Design for the COBE Far Infrared Absolute Spectrophotometer (FIRAS). *The Astrophysical Journal*, 512(2):511, 1999.
- [100] D. McCammon. Thermal Equilibrium Calorimeters – An Introduction. In Christian Enss, editor, *Cryogenic Particle Detection*, Topics in Applied Physics, pages 1–34. Springer, Berlin, Heidelberg, 2005.
- [101] Heather McCarrick, Erin Healy, Zeeshan Ahmed, Kam Arnold, Zachary Atkins, Jason E. Austermann, Tanay Bhandarkar, Jim A. Beall, Sarah Marie Bruno, Steve K. Choi, Jake Connors, Nicholas F. Cothard, Kevin D. Crowley, Simon Dicker, Bradley Dober, Cody J. Duell, Shannon M. Duff, Daniel Dutcher, Josef C. Frisch, Nicholas Galitzki, Megan B. Gralla, Jon E. Gundmundsson, Shawn W. Henderson, Gene C. Hilton, Shuay-Pwu Patty Ho, Zachary B. Huber, Johannes Hubmayr, Jeffrey Iuliano, Bradley R. Johnson, Anna M. Kofman, Akito Kusaka, Jack Lashner, Adrian T. Lee, Yaqiong Li, Michael J. Link, Tammy J. Lucas, Marius Lungu, J. A. B. Mates,

- Jeffrey J. McMahon, Michael D. Niemack, John Orlowski-Scherer, Joseph Seibert, Maximiliano Silva-Feaver, Sara M. Simon, Suzanne Staggs, Aritoki Suzuki, Tomoki Terasaki, Joel N. Ullom, Eve M. Vavagiakis, Leila R. Vale, Jeff Van Lanen, Michael R. Vissers, Yuhan Wang, Edward J. Wollack, Zhilei Xu, Edward Young, Cyndia Yu, Kaiwen Zheng, and Ningfeng Zhu. The Simons Observatory microwave SQUID multiplexing detector module design. *arXiv:2106.14797 [astro-ph]*, June 2021. arXiv: 2106.14797.
- [102] J. McMahon, J. W. Appel, J. E. Austermann, J. A. Beall, D. Becker, B. A. Benson, L. E. Bleem, J. Britton, C. L. Chang, J. E. Carlstrom, H. M. Cho, A. T. Crites, T. Essinger-Hileman, W. Everett, N. W. Halverson, J. W. Henning, G. C. Hilton, K. D. Irwin, J. Mehl, S. S. Meyer, S. Mossley, M. D. Niemack, L. P. Parker, S. M. Simon, S. T. Staggs, C. Visnjic, E. Wollack, K. U.-Yen, K. W. Yoon, Y. Zhao, Betty Young, Blas Cabrera, and Aaron Miller. Planar Orthomode Transducers for Feedhorn-coupled TES Polarimeters. In *AIP Conference Proceedings*, pages 490–493, Stanford (California), 2009.
- [103] B. K. Minhas, W. Fan, K. Agi, S. R. J. Brueck, and K. J. Malloy. Metallic inductive and capacitive grids: theory and experiment. *JOSA A*, 19(7):1352–1359, July 2002. Publisher: Optical Society of America.
- [104] Eva-Maria Mueller, Francesco de Bernardis, Rachel Bean, and Michael Niemack. Constraints on gravity and dark energy from the pairwise kinematic Sunyaev-Zeldovich effect. *The Astrophysical Journal*, 808(1):47, July 2015. arXiv: 1408.6248.
- [105] Eva-Maria Mueller, Francesco de Bernardis, Rachel Bean, and Michael D. Niemack. Constraints on massive neutrinos from the pairwise kinematic

- Sunyaev-Zel'dovich effect. *Physical Review D*, 92(6):063501, September 2015.
arXiv: 1412.0592.
- [106] Ben A. Munk. *Frequency Selective Surfaces: Theory and Design*. John Wiley & Sons, March 2005.
- [107] C. D. Munson, S. K. Choi, K. P. Coughlin, J. J. McMahon, K. H. Miller, L. A. Page, and E. J. Wollack. Composite reflective/absorptive IR-blocking filters embedded in metamaterial antireflection-coated silicon. *Applied Optics*, 56(19):5349–5354, July 2017.
- [108] Karl Dieter Möller. *Far-infrared spectroscopy*. Wiley-Interscience, New York, 1971.
- [109] Sigurd Naess, Simone Aiola, Jason E. Austermann, Nick Battaglia, James A. Beall, Daniel T. Becker, Richard J. Bond, Erminia Calabrese, Steve K. Choi, Nicholas F. Cothard, Kevin T. Crowley, Omar Darwish, Rahul Datta, Edward V. Denison, Mark Devlin, Cody J. Duell, Shannon M. Duff, Adriaan J. Duivenvoorden, Jo Dunkley, Rolando Dünner, Anna E. Fox, Patricio A. Gallardo, Mark Halpern, Dongwon Han, Matthew Hasselfield, J. Colin Hill, Gene C. Hilton, Matt Hilton, Adam D. Hincks, Renée Hložek, Shuay-Pwu Patty Ho, Johannes Hubmayr, Kevin Huffenberger, John P. Hughes, Arthur B. Kosowsky, Thibaut Louis, Mathew S. Madhavacheril, Jeff McMahon, Kavilan Moodley, Federico Nati, John P. Nibarger, Michael D. Niemack, Lyman Page, Bruce Partridge, Maria Salatino, Emmanuel Schaan, Alessandro Schillaci, Benjamin Schmitt, Blake D. Sherwin, Neelima Sehgal, Cristóbal Sifón, David Spergel, Suzanne Staggs, Jason Stevens, Emilie Storer, Joel N. Ullom, Leila R. Vale, Alexander Van Engelen, Jeff Van Lanen, Eve M. Vavagiakis, Edward J. Wollack, and Zhilei Xu. The Atacama

Cosmology Telescope: arcminute-resolution maps of 18,000 square degrees of the microwave sky from ACT 2008-2018 data combined with Planck. *arXiv:2007.07290 [astro-ph]*, July 2020. arXiv: 2007.07290, hello.

- [110] Sigurd Naess, Simone Aiola, Nick Battaglia, Richard J. Bond, Erminia Calabrese, Steve K. Choi, Nicholas F. Cothard, Mark Halpern, J. Colin Hill, Brian J. Koopman, Mark Devlin, Jeff McMahon, Simon Dicker, Adriaan J. Duivenvoorden, Jo Dunkley, Alexander Van Engelen, Valentina Fanfani, Simone Ferraro, Patricio A. Gallardo, Yilun Guan, Dongwon Han, Matthew Hasselfield, Adam D. Hincks, Kevin Huffenberger, Arthur B. Kosowsky, Thibaut Louis, Amanda Macinnis, Mathew S. Madhavacheril, Federico Nati, Michael D. Niemack, Lyman Page, Maria Salatino, Emmanuel Schaan, John Orlowski-Scherer, Alessandro Schillaci, Benjamin Schmitt, Neelima Sehgal, Cristóbal Sifón, Suzanne Staggs, and Edward J. Wollack. The Atacama Cosmology Telescope: A search for Planet 9. *arXiv:2104.10264 [astro-ph]*, May 2021. arXiv: 2104.10264.
- [111] Sigurd Naess, Nick Battaglia, J. Richard Bond, Erminia Calabrese, Steve K. Choi, Nicholas F. Cothard, Mark Devlin, Cody J. Duell, Adriaan J. Duivenvoorden, Jo Dunkley, Rolando Dünner, Patricio A. Gallardo, Megan Gralla, Yilun Guan, Mark Halpern, J. Colin Hill, Matt Hilton, Kevin M. Huffenberger, Brian J. Koopman, Arthur B. Kosowsky, Mathew S. Madhavacheril, Jeff McMahon, Federico Nati, Michael D. Niemack, Lyman Page, Bruce Partridge, Maria Salatino, Neelima Sehgal, David Spergel, Suzanne Staggs, Edward J. Wollack, and Zhilei Xu. The Atacama Cosmology Telescope: Detection of mm-wave transient sources. *arXiv:2012.14347 [astro-ph]*, December 2020. arXiv: 2012.14347, hello.

- [112] Michael D. Niemack. Designs for a large-aperture telescope to map the CMB 10x faster. *Applied Optics*, 55(7):1688–1696, March 2016. Publisher: Optical Society of America.
- [113] L. Page, M. R. Nolta, C. Barnes, C. L. Bennett, M. Halpern, G. Hinshaw, N. Jarosik, A. Kogut, M. Limon, S. S. Meyer, H. V. Peiris, D. N. Spergel, G. S. Tucker, E. Wollack, and E. L. Wright. First-Year Wilkinson Microwave Anisotropy Probe (WMAP)* Observations: Interpretation of the TT and TE Angular Power Spectrum Peaks. *The Astrophysical Journal Supplement Series*, 148(1):233, September 2003. Publisher: IOP Publishing.
- [114] Stephen C. Parshley, Jörg Kronshage, James Blair, Terry Herter, Mike Nolta, Gordon J. Stacey, Andrew Bazarko, Frank Bertoldi, Ricardo Bustos, Donald B. Campbell, Scott Chapman, Nicolas Cothard, Mark Devlin, Jens Erler, Michel Fich, Patricio A. Gallardo, Riccardo Giovanelli, Urs Graf, Scott Gramke, Martha P. Haynes, Richard Hills, Michele Limon, Jeffrey G. Mangum, Jeff McMahon, Michael D. Niemack, Thomas Nikola, Markus Omolor, Dominik A. Riechers, Karl Steeger, Jürgen Stutzki, and Eve M. Vavagiakis. CCAT-prime: a novel telescope for sub-millimeter astronomy. In *Ground-based and Airborne Telescopes VII*, volume 10700, page 107005X. International Society for Optics and Photonics, July 2018.
- [115] A. A. Penzias and R. W. Wilson. A Measurement of Excess Antenna Temperature at 4080 Mc/s. *The Astrophysical Journal*, 142:419–421, July 1965.
- [116] A. Perot and Charles Fabry. On the Application of Interference Phenomena to the Solution of Various Problems of Spectroscopy and Metrology. *The Astrophysical Journal*, 9:87, February 1899.

- [117] K. F. Renk and L. Genzel. Interference filters and Fabry-Perot interferometers for the far infrared. *Applied Optics*, 1(5):643–648, 1962.
- [118] Dominik A. Riechers, Christopher L. Carilli, Peter L. Capak, Nicholas Z. Scoville, Vernes Smolčić, Eva Schinnerer, Min Yun, Pierre Cox, Frank Bertoldi, Alexander Karim, and Lin Yan. ALMA IMAGING OF GAS AND DUST IN A GALAXY PROTOCLUSTER AT REDSHIFT 5.3: [C II] EMISSION IN “TYPICAL” GALAXIES AND DUSTY STARBURSTS \approx 1 BILLION YEARS AFTER THE BIG BANG. *The Astrophysical Journal*, 796(2):84, November 2014. Publisher: American Astronomical Society.
- [119] Adam G. Riess. The Expansion of the Universe is Faster than Expected. *Nature Reviews Physics*, 2(1):10–12, January 2020. arXiv: 2001.03624.
- [120] Adam G. Riess, Stefano Casertano, Wenlong Yuan, Lucas M. Macri, and Dan Scolnic. Large Magellanic Cloud Cepheid Standards Provide a 1% Foundation for the Determination of the Hubble Constant and Stronger Evidence for Physics Beyond LambdaCDM. *The Astrophysical Journal*, 876(1):85, May 2019. arXiv: 1903.07603.
- [121] H. P. Robertson. Kinematics and World-Structure. *The Astrophysical Journal*, 82:284, November 1935.
- [122] Darin Rosen, Aritoki Suzuki, Brian Keating, William Krantz, Adrian T. Lee, Erin Quealy, Paul L. Richards, Praween Siritanasak, and William Walker. Epoxy-based broadband anti-reflection coating for millimeter-wave optics. *Applied Optics*, 52(33):8102, November 2013. arXiv: 1307.7827.
- [123] Barbara Sue Ryden. *Introduction to cosmology*. Cambridge University Press, Cambridge, 2016.

- sity Press, Cambridge, United Kingdom, second edition. edition, 2017.
<http://newcatalog.library.cornell.edu/catalog/9900130>.
- [124] Kiyomi Sakai and Ludwig Genzel. Far Infrared Metal Mesh Filters and Fabry-Perot Interferometry. In *Reviews of Infrared and Millimeter Waves*, pages 155–247. Springer, Boston, MA, 1983.
- [125] Emmanuel Schaan and Martin White. Astrophysics & Cosmology from Line Intensity Mapping vs Galaxy Surveys. *arXiv:2103.01971 [astro-ph]*, March 2021. arXiv: 2103.01971.
- [126] Martin Shepherd. Correct Sampling of Diffraction Limited Images. Memo CCAT-TM-109, California Institute of Technology, November 2012.
- [127] Sara M. Simon, Jason Austermann, James A. Beall, Steve K. Choi, Kevin P. Coughlin, Shannon M. Duff, Patricio A. Gallardo, Shawn W. Henderson, Felicity B. Hills, Shuay-Pwu Patty Ho, Johannes Hubmayr, Alec Josaitis, Brian J. Koopman, Jeff J. McMahon, Federico Nati, Laura Newburgh, Michael D. Niemack, Maria Salatino, Alessandro Schillaci, Benjamin L. Schmitt, Suzanne T. Staggs, Eve M. Vavagiakis, Jonathan Ward, and Edward J. Wollack. The design and characterization of wideband spline-profiled feedhorns for Advanced ACTPol. In *Millimeter, Submillimeter, and Far-Infrared Detectors and Instrumentation for Astronomy VIII*, volume 9914, page 991416. International Society for Optics and Photonics, July 2016.
- [128] V. M. Slipher. The radial velocity of the Andromeda Nebula. *Lowell Observatory Bulletin*, 2:56–57, 1913.
- [129] V. M. Slipher. Spectrographic Observations of Nebulae. *Popular Astronomy*, 23:21–24, January 1915.

- [130] G. F. Smoot, C. L. Bennett, A. Kogut, E. L. Wright, J. Aymon, N. W. Boggess, E. S. Cheng, G. de Amici, S. Gulkis, M. G. Hauser, G. Hinshaw, P. D. Jackson, M. Janssen, E. Kaita, T. Kelsall, P. Keegstra, C. Lineweaver, K. Loewenstein, P. Lubin, J. Mather, S. S. Meyer, S. H. Moseley, T. Murdock, L. Rokke, R. F. Silverberg, L. Tenorio, R. Weiss, and D. T. Wilkinson. Structure in the COBE differential microwave radiometer first-year maps. *The Astrophysical Journal*, 396:L1–L5, September 1992.
- [131] G. J. Stacey, M. Aravena, K. Basu, N. Battaglia, B. Beringue, F. Bertoldi, J. R. Bond, P. Breysse, R. Bustos, S. Chapman, D. T. Chung, N. Cothard, J. Erler, M. Fich, S. Foreman, P. Gallardo, R. Giovanelli, U. U. Graf, M. P. Haynes, R. Herrera-Camus, T. L. Herter, R. Hložek, D. Johnstone, L. Keating, B. Magnelli, D. Meerburg, J. Meyers, N. Murray, M. Niemack, T. Nikola, M. Nolta, S. C. Parshley, D. A. Riechers, P. Schilke, D. Scott, G. Stein, J. Stevens, J. Stutzki, E. M. Vavagiakis, and M. P. Viero. CCAT-Prime: science with an ultra-widefield submillimeter observatory on Cerro Chajnantor. In *Ground-based and Airborne Telescopes VII*, volume 10700, page 107001M. International Society for Optics and Photonics, July 2018.
- [132] G. J. Stacey, N. Geis, R. Genzel, J. B. Lugten, A. Poglitsch, A. Sternberg, and C. H. Townes. The 158 micron [C II] line - A measure of global star formation activity in galaxies. *The Astrophysical Journal*, 373:423–444, June 1991.
- [133] G. J. Stacey, S. Hailey-Dunsheath, C. Ferkinhoff, T. Nikola, S. C. Parshley, D. J. Benford, J. G. Staguhn, and N. Fiolet. A 158 micron [CII] line survey of galaxies at $z \sim 1$ to 2: An indicator of star formation in the early universe. *The Astrophysical Journal*, 724(2):957–974, November 2010.

- [134] Gordon J. Stacey, Frank Bertoldi, A.W. Blain, C.M. Bradford, Riccardo Giovanelli, Jason Glenn, Paul Goldsmith, Sunil Golwala, Thomas Nikola, and Jonas Zmuidzinas. Star Formation Through Cosmic Time: From Local Galaxies to the Early Universe. *Astro2010: The Astronomy and Astrophysics Decadal Survey*, 2010, 2009. Conference Name: astro2010: The Astronomy and Astrophysics Decadal Survey.
- [135] Jason R. Stevens, Nicholas F. Cothard, Eve M. Vavagiakis, Aamir Ali, Kam Arnold, Jason E. Austermann, Steve K. Choi, Bradley J. Dober, Cody Duelle, Shannon M. Duff, Gene C. Hilton, Shuay-Pwu Patty Ho, Thuong D. Hoang, Johannes Hubmayr, Adrian T. Lee, Aashrita Mangu, Federico Nati, Michael D. Niemack, Christopher Raum, Mario Renzullo, Maria Salatino, Trevor Sasse, Sara M. Simon, Suzanne Staggs, Aritoki Suzuki, Patrick Truitt, Joel Ullom, John Vivalda, Michael R. Vissers, Samantha Walker, Benjamin Westbrook, Edward J. Wollack, Zhilei Xu, and Daniel Yohannes. Characterization of Transition Edge Sensors for the Simons Observatory. *Journal of Low Temperature Physics*, 199(3):672–680, May 2020.
- [136] Jason R. Stevens, Neil Goeckner-Wald, Reijo Keskitalo, Nialh McCallum, Aamir Ali, Julian Borrill, Michael L. Brown, Yuji Chinone, Patricio A. Gallardo, Akito Kusaka, Adrian T. Lee, Jeff McMahon, Michael D. Niemack, Lyman Page, Giuseppe Puglisi, Maria Salatino, Suet Ying D. Mak, Grant Teply, Daniel B. Thomas, Eve M. Vavagiakis, Edward J. Wollack, Zhilei Xu, and Ningfeng Zhu. Designs for next generation CMB survey strategies from Chile. In *Millimeter, Submillimeter, and Far-Infrared Detectors and Instrumentation for Astronomy IX*, volume 10708, page 1070841. International Society for Optics and Photonics, July 2018.

- [137] Jason Roland Stevens. *Measuring the Cosmic Microwave Background Radiation from Chile*. Ph.D., Cornell University, United States – New York, December 2020. Accepted: 2021-03-15T13:32:29Z.
- [138] Aritoki Suzuki, Nicholas Cothard, Adrian T. Lee, Michael D. Niemack, Christopher Raum, Mario Renzullo, Trevor Sasse, Jason Stevens, Patrick Truitt, Eve Vavagiakis, John Vivalda, Benjamin Westrook, and Daniel Yohannes. Commercially Fabricated Antenna-Coupled Transition Edge Sensor Bolometer Detectors for Next-Generation Cosmic Microwave Background Polarimetry Experiment. *Journal of Low Temperature Physics*, 199(3):1158–1166, May 2020.
- [139] Aritoki Suzuki, Jason R. Stevens, Daniel Yohannes, Patrick Truitt, Michael D. Niemack, Eve M. Vavagiakis, Akito Kusaka, Yume Nishinomiya, Kenji Kiuchi, Logan Foote, Shawn Beckman, Adrian Lee, Ben Westbrook, Chris Raum, Trevor Sasse, John Vivalda, Mario Renzullo, Nicholas F. Cothard, and Mayuri Sathyaranayana Rao. Recent developments and optimization of commercially fabricated antenna-coupled transition edge sensor bolometer detectors for next generation cosmic microwave background polarimetry experiments. In *Millimeter, Submillimeter, and Far-Infrared Detectors and Instrumentation for Astronomy X*, volume 11453, page 1145324. International Society for Optics and Photonics, December 2020.
- [140] D. S. Swetz, P. a. R. Ade, C. Allen, M. Amiri, J. W. Appel, E. S. Battistelli, B. Burger, J. A. Chervenak, A. J. Dahlen, S. Das, S. Denny, M. J. Devlin, S. R. Dicker, W. B. Doriese, R. Dünner, T. Essinger-Hileman, R. P. Fisher, J. W. Fowler, X. Gao, A. Hajian, M. Halpern, P. C. Hargrave, M. Hasselfield, G. C. Hilton, A. D. Hincks, K. D. Irwin, N. Jarosik, M. Kaul, J. Klein,

S. Knotek, J. M. Lau, M. Limon, R. H. Lupton, T. A. Marriage, K. L. Martocci, P. Mauskopf, S. H. Moseley, C. B. Netterfield, M. D. Niemack, M. R. Nolta, L. Page, L. P. Parker, B. A. Reid, C. D. Reintsema, A. J. Sederberg, N. Sehgal, J. L. Sievers, D. N. Spergel, S. T. Staggs, O. R. Stryzak, E. R. Switzer, R. J. Thornton, C. Tucker, E. J. Wollack, and Y. Zhao. Instrument design and characterization of the Millimeter Bolometer Array Camera on the Atacama Cosmology Telescope. In *Millimeter and Submillimeter Detectors and Instrumentation for Astronomy IV*, volume 7020, page 702008. International Society for Optics and Photonics, July 2008.

- [141] D. S. Swetz, P. A. R. Ade, M. Amiri, J. W. Appel, E. S. Battistelli, B. Burger, J. Chervenak, M. J. Devlin, S. R. Dicker, W. B. Doriese, R. Dünner, T. Essinger-Hileman, R. P. Fisher, J. W. Fowler, M. Halpern, M. Hasselfield, G. C. Hilton, A. D. Hincks, K. D. Irwin, N. Jarosik, M. Kaul, J. Klein, J. M. Lau, M. Limon, T. A. Marriage, D. Marsden, K. Martocci, P. Mauskopf, H. Moseley, C. B. Netterfield, M. D. Niemack, M. R. Nolta, L. A. Page, L. Parker, S. T. Staggs, O. Stryzak, E. R. Switzer, R. Thornton, C. Tucker, E. Wollack, and Y. Zhao. Overview of the Atacama Cosmology Telescope: Receiver, Instrumentation, and Telescope Systems. *The Astrophysical Journal Supplement Series*, 194(2):41, June 2011. Publisher: American Astronomical Society.
- [142] Jonathan A. Thompson and Giampaolo Pisano. Use of evolutionary computing algorithms in the design of millimetre-wave metamaterial devices. In *Millimeter, Submillimeter, and Far-Infrared Detectors and Instrumentation for Astronomy IX*, volume 10708, page 107083H. International Society for Optics and Photonics, July 2018.

- [143] Jonathan A. Thompson, Giampaolo Pisano, and Carole Tucker. Mesh low-pass filters for millimeter-wave applications: is the square capacitive shape optimal? *Journal of Astronomical Telescopes, Instruments, and Systems*, 6(3):036003, August 2020. Publisher: International Society for Optics and Photonics.
- [144] R. J. Thornton, P. A. R. Ade, S. Aiola, F. E. Angilè, M. Amiri, J. A. Beall, D. T. Becker, H-M. Cho, S. K. Choi, P. Corlies, K. P. Coughlin, R. Datta, M. J. Devlin, S. R. Dicker, R. Dünner, J. W. Fowler, A. E. Fox, P. A. Gallardo, J. Gao, E. Grace, M. Halpern, M. Hasselfield, S. W. Henderson, G. C. Hilton, A. D. Hincks, S. P. Ho, J. Hubmayr, K. D. Irwin, J. Klein, B. Koopman, Dale Li, T. Louis, M. Lungu, L. Maurin, J. McMahon, C. D. Munson, S. Naess, F. Nati, L. Newburgh, J. Nibarger, M. D. Niemack, P. Niraula, M. R. Nolta, L. A. Page, C. G. Pappas, A. Schillaci, B. L. Schmitt, N. Sehgal, J. L. Sievers, S. M. Simon, S. T. Staggs, C. Tucker, M. Uehara, J. van Lanen, J. T. Ward, and E. J. Wollack. The Atacama Cosmology Telescope: The polarization-sensitive ACTPol instrument. *The Astrophysical Journal Supplement Series*, 227(2):21, December 2016.
- [145] M. Tristram, A. J. Banday, K. M. Górski, R. Keskitalo, C. R. Lawrence, K. J. Andersen, R. B. Barreiro, J. Borrill, H. K. Eriksen, R. Fernandez-Cobos, T. S. Kisner, E. Martínez-González, B. Partridge, D. Scott, T. L. Svalheim, H. Thommesen, and I. K. Wehus. Planck constraints on the tensor-to-scalar ratio. *Astronomy & Astrophysics*, 647:A128, March 2021. arXiv: 2010.01139.
- [146] R. Ulrich. Effective low-pass filters for far infrared frequencies. *Infrared Physics*, 7(2):65–74, June 1967.

- [147] Reinhard Ulrich. Far-infrared properties of metallic mesh and its complementary structure. *Infrared Physics*, 7(1):37–55, March 1967.
- [148] eleonora di valentino, olga mena, Supriya Pan, Luca Visinelli, Weiqiang Yang, Alessandro Melchiorri, David Fonseca Mota, Adam G. Riess, and Joseph Silk. In the realm of the Hubble tension - a review of solutions. *Classical and Quantum Gravity*, 2021.
- [149] E. M. Vavagiakis, Z. Ahmed, A. Ali, K. Basu, N. Battaglia, F. Bertoldi, R. Bond, R. Bustos, S. C. Chapman, D. Chung, G. Coppi, N. F. Cothard, S. Dicker, C. J. Duell, S. M. Duff, J. Erler, M. Fich, N. Galitzki, P. A. Gallardo, S. W. Henderson, T. L. Herter, G. Hilton, J. Hubmayr, K. D. Irwin, B. J. Koopman, J. McMahon, N. Murray, M. D. Niemack, T. Nikola, M. Nolta, J. Orlowski-Scherer, S. C. Parshley, D. A. Riechers, K. Rossi, D. Scott, C. Sierra, M. Silva-Feaver, S. M. Simon, G. J. Stacey, J. R. Stevens, J. N. Ullom, M. R. Vissers, S. Walker, E. J. Wollack, Z. Xu, and N. Zhu. Prime-Cam: a first-light instrument for the CCAT-prime telescope. In *Millimeter, Submillimeter, and Far-Infrared Detectors and Instrumentation for Astronomy IX*, volume 10708, page 107081U. International Society for Optics and Photonics, July 2018.
- [150] E. M. Vavagiakis, N. F. Cothard, J. R. Stevens, C. L. Chang, M. D. Niemack, G. Wang, V. G. Yefremenko, and J. Zhang. Developing AlMn Films for Argonne TES Fabrication. *Journal of Low Temperature Physics*, 199(1):408–415, April 2020.
- [151] Eve M. Vavagiakis, Patricio A. Gallardo, Victoria Calafut, Stefania Amodeo, Simone Aiola, Jason E. Austermann, Nicholas Battaglia, Elia S. Battistelli, James A. Beall, Rachel Bean, J. Richard Bond, Erminia Calabrese,

- Steve K. Choi, Nicholas F. Cothard, Mark J. Devlin, Cody J. Duell, Adriaan J. Duivenvoorden, Jo Dunkley, Rolando Dunner, Simone Ferraro, Yilun Guan, J. Colin Hill, Matt Hilton, Renee Hlozek, Zachary B. Huber, Johannes Hubmayr, Kevin M. Huffenberger, John P. Hughes, Brian J. Koopman, Arthur Kosowsky, Yaqiong Li, Martine Lokken, Mathew Madhavacheril, Jeff McMahon, Kavilan Moodley, Sigurd Naess, Federico Nati, Laura B. Newburgh, Michael D. Niemack, Bruce Partridge, Emmanuel Schaan, Alessandro Schillaci, Cristobal Sifon, David N. Spergel, Suzanne T. Staggs, Joel N. Ulom, Leila R. Vale, Alexander Van Engelen, Edward J. Wollack, and Zhilei Xu. The Atacama Cosmology Telescope: Probing the Baryon Content of SDSS DR15 Galaxies with the Thermal and Kinematic Sunyaev-Zel'dovich Effects. *arXiv:2101.08373 [astro-ph]*, January 2021. arXiv: 2101.08373.
- [152] Ian Veenendaal, David Naylor, Brad Gom, Adam Christiansen, Willem Jellema, Carolien Feenstra, Marcel Ridder, Martin Eggens, and Peter Ade. An angle-scanned cryogenic Fabry–Pérot interferometer for far-infrared astronomy. *Review of Scientific Instruments*, 91(8):083108, August 2020. Publisher: American Institute of Physics.
- [153] A. G. Walker. On Milne’s Theory of World-Structure*. *Proceedings of the London Mathematical Society*, s2-42(1):90–127, 1937. eprint: <https://londmathsoc.onlinelibrary.wiley.com/doi/pdf/10.1112/plms/s2-42.1.90>.
- [154] Steven Weinberg. *Cosmology*. Oxford University Press, Oxford, 2008. <http://newcatalog.library.cornell.edu/catalog/6279632>.
- [155] Qi Wen, Elena Fadeeva, Shaul Hanany, Jurgen Koch, Tomotake Matsumura, Ryota Takaku, and Karl Young. Picosecond Laser Ablation of Millimeter-

Wave Subwavelength Structures on Alumina and Sapphire. *arXiv:2103.06974 [astro-ph, physics:physics]*, March 2021. arXiv: 2103.06974.

- [156] B. Westbrook, P. A. R. Ade, M. Aguilar, Y. Akiba, K. Arnold, C. Bacigalupi, D. Barron, D. Beck, S. Beckman, A. N. Bender, F. Bianchini, D. Boettger, J. Borrill, S. Chapman, Y. Chinone, G. Coppi, K. Crowley, A. Cukierman, T. de Haan, R. Dünner, M. Dobbs, T. Ellefot, J. Errard, G. Fabbian, S. M. Feeney, C. Feng, G. Fuller, N. Galitzki, A. Gilbert, N. Goeckner-Wald, J. Groh, N. W. Halverson, T. Hamada, M. Hasegawa, M. Hazumi, C. A. Hill, W. Holzapfel, L. Howe, Y. Inoue, G. Jaehnig, A. Jaffe, O. Jeong, D. Kaneko, N. Katayama, B. Keating, R. Keskitalo, T. Kisner, N. Krachmalnicoff, A. Kusaka, M. Le Jeune, A. T. Lee, D. Leon, E. Linder, L. Lowry, A. Madurowicz, D. Mak, F. Matsuda, A. May, N. J. Miller, Y. Minami, J. Montgomery, M. Navaroli, H. Nishino, J. Peloton, A. Pham, L. Piccirillo, D. Plambeck, D. Poletti, G. Puglisi, C. Raum, G. Rebeiz, C. L. Reichardt, P. L. Richards, H. Roberts, C. Ross, K. M. Rothermund, Y. Segawa, B. Sherwin, M. Silva-Feaver, P. Siritanasak, R. Stompor, A. Suzuki, O. Tajima, S. Takakura, S. Takatori, D. Tanabe, R. Tat, G. P. Teply, A. Tikhomirov, T. Tomaru, C. Tsai, N. Whitehorn, and A. Zahn. The POLARBEAR-2 and Simons Array Focal Plane Fabrication Status. *Journal of Low Temperature Physics*, 193(5):758–770, December 2018.
- [157] Edward J. Wollack, Giuseppe Cataldo, Kevin H. Miller, and Manuel A. Quijada. Infrared properties of high-purity silicon. *Optics Letters*, 45(17):4935–4938, September 2020. Publisher: Optical Society of America.
- [158] Banqiu Wu, Ajay Kumar, and Sharma Pamarthi. High aspect ratio silicon etch: A review. *Journal of Applied Physics*, 108(5):051101, September 2010.

- [159] Zhilei Xu, Shunsuke Adachi, Peter Ade, J. A. Beall, Tanay Bhandarkar, J. Richard Bond, Grace E. Chesmore, Yuji Chinone, Steve K. Choi, Jake A. Connors, Gabriele Coppi, Nicholas F. Cothard, Kevin D. Crowley, Mark Devlin, Simon Dicker, Bradley Dober, Shannon M. Duff, Nicholas Galitzki, Patricio A. Gallardo, Joseph E. Golec, Jon E. Gudmundsson, Saianeesh K. Haridas, Kathleen Harrington, Carlos Hervias-Caimapo, Shuay-Pwu Patty Ho, Zachary B. Huber, Johannes Hubmayr, Jeffrey Iuliano, Daisuke Kaneko, Anna M. Kofman, Brian J. Koopman, Jack Lashner, Michele Limon, Michael J. Link, Tammy J. Lucas, Frederick Matsuda, Heather McCarrick, Federico Nati, Michael D. Niemack, John Orlowski-Scherer, Lucio Piccirillo, Karen Perez Sarmiento, Emmanuel Schaan, Maximiliano Silva-Feaver, Rita Sonka, Shreya Sutariya, Osamu Tajima, Grant P. Teply, Tomoki Terasaki, Robert Thornton, Carole Tucker, Joel Ullom, Eve M. Vavagiakis, Michael R. Vissers, Samantha Walker, Zachary Whipps, Edward J. Wollack, Mario Zannoni, Ningfeng Zhu, and Andrea Zonca. The Simons Observatory: the Large Aperture Telescope (LAT). *Research Notes of the AAS*, 5(4):100, April 2021. arXiv: 2104.09511.
- [160] Zhilei Xu, Zhilei Xu, Grace E. Chesmore, Shunsuke Adachi, Aamir M. Ali, Andrew Bazarko, Gabriele Coppi, Gabriele Coppi, Mark Devlin, Tom Devlin, Simon R. Dicker, Patricio A. Gallardo, Joseph E. Golec, Jon E. Gudmundsson, Kathleen Harrington, Makoto Hattori, Anna Kofman, Kenji Kuchi, Akito Kusaka, Akito Kusaka, Akito Kusaka, Akito Kusaka, Michele Limon, Frederick Matsuda, Jeff McMahon, Jeff McMahon, Jeff McMahon, Jeff McMahon, Federico Nati, Michael D. Niemack, Michael D. Niemack, Aritoki Suzuki, Grant P. Teply, Robert J. Thornton, Robert J. Thornton, Edward J. Wollack, Mario Zannoni, and Ningfeng Zhu. The Simons Ob-

servatory: metamaterial microwave absorber and its cryogenic applications. *Applied Optics*, 60(4):864–874, February 2021. Publisher: Optical Society of America.

- [161] Pochi Yeh. *Optical waves in layered media*. Wiley, New York, 1988.
- [162] Karl Young, Qi Wen, Shaul Hanany, Hiroaki Imada, Jürgen Koch, Tomotake Matsumura, Oliver Suttmann, and Viktor Schütz. Broadband millimeter-wave anti-reflection coatings on silicon using pyramidal sub-wavelength structures. *Journal of Applied Physics*, 121(21):213103, June 2017. Publisher: American Institute of Physics.
- [163] Matias Zaldarriaga. Nature of the $E\backslash ensuremath{-}B$ decomposition of CMB polarization. *Physical Review D*, 64(10):103001, October 2001.
- [164] Yue Zhao. *Characterization of Transition Edge Sensors for the Millimeter Bolometer Array Camera on the Atacama Cosmology Telescope*. Ph.D., Princeton University, United States – New Jersey, 2010. ISBN: 9781124351070 Publication Title: ProQuest Dissertations and Theses Section: 0181.